Molecular Engineering of Tetrabenzoporphyrin toward Efficient Organic Semiconductor Devices

Dissertation

Kohtaro Takahashi

2017

Laboratory for Photofunctional Organic Chemistry

Graduate School of Materials Science

Nara Institute of Science and Technology

Table of Contents

Abbreviations

ADF: Amsterdam density functional

AFM: Atomic force microscopy

BP: Tetrabenzoporphyrin

BCOD: Bicyclo[2.2.2]octadieno

BCP: Bathociproine

BHJ: Bulk heterojunction

CP: 1,4:8,11:15,18:22,25-Tetraethano-29*H*,31*H*-tetrabenzo[*b,g,l,q*]porphyrin

DMF: *N*,*N*-Dimethylformamide

DFT: Density functional theory

DDQ: 2,3-Dichloro-5,6-dicyano-1,4-benzoquinone

EQE: External quantum efficiency

ESI: Electronspray ionization

FF: Fill factor

FWHM: Full-width at half-maximum

GIWAXD: Grazing- incident wide-angle X-ray diffractometry

GPC: Gel permeation chromatography

HMDS: Hexamethyldisilazane

HOMO: Highest occupied molecular orbital

HRMS: High-resolution mass spectrometry

ITO: Indium–tin oxide

J_{SC}: Short-circuit current density

L_{D}: Exciton diffusion length

LUMO: Lowest unoccupied molecular orbital

μ: Charge-carrier mobility

μ_{h}: Charge-carrier hole-mobility

MALDI: Matrix-assisted laser desorption/ionization

NBS: *N*-Bromosuccinimide

NMR: Nuclear magnetic resonance

OFETs: Organic field-effect transistors

OLEDs: Organic light-emitting diodes

OPVs: Organic photovoltaics

OTMS: Octadecyltrimethoxysilane

PCBNB: [6,6]-Phenyl-C$_{61}$-butyric acid *n*-butyl ester

PCE: Power conversion efficiency

PC$_{61}$BM: [6,6]-Phenyl-C$_{61}$-butyric acid methyl ester

PC$_{71}$BM: [6,6]-Phenyl-C$_{71}$-butyric acid methyl ester

PEDOT:PSS: Poly(3,4-ethylenedioxy thiophene):poly(4-styrenesulfonate)

SIMEF: Bis(dimethylphenylsilylmethyl) [60]fullerene

SIMEF-Ph, *o*-An: (*o*-Anisylsilylmethyl)(phenylsilylmethyl)[60]fullerene

SAM: Self-assembled monolayer

TFA: Trifluoroacetic acid

TGA: Thermogravimetric analysis

THF: Tetrahydrofuran

TIPS: Triisopropylsilyl

TLC: Thin-layer chromatography

TMS: Trimethylsilyl

V_{OC}: Open-circuit voltage

XRD: X-ray diffraction

Chapter 1

General Introduction

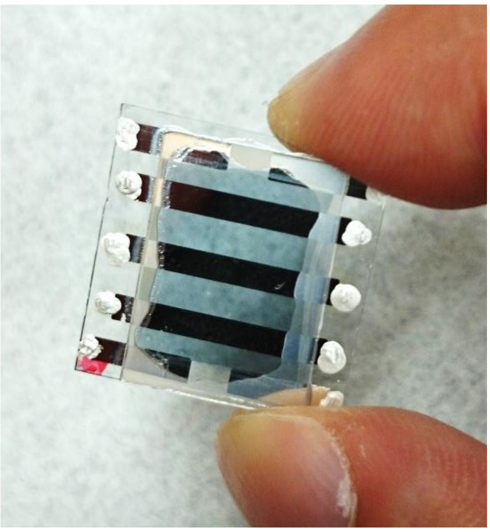

In this chapter, the general introduction of organic semiconductor devices is described.

1-1. Introduction to Organic Semiconductor Devices

Organic semiconductor devices such as organic light-emitting diodes (OLEDs),[1,2] organic field-effect transistors (OFETs),[3] and organic photovoltaics (OPVs)[4,5] have a possibility to provide us with flexible, light-weight, large area, and low cost electronic devices.[6] These features of organic semiconductor devices originate from the nature of organic materials; namely, the flexibility, solution- and ambient temperature-processabilities. However, the performance, stability, reproducibility and reliability of organic semiconductor devices are still lower than those of inorganic counterparts. Thus, a large number of researchers in various scientific fields search for solutions to overcome these problems associated with organic semiconductor devices.

1-2. Organic Field-Effect Transistors (OFETs)

Figure 1-1 shows the general device structure of bottom-gate-top-contact (BGTC) OFETs. A BGTC device consists of a gate electrode, a dielectric insulating layer, an organic semiconductor layer, and source–drain electrodes. Heavily doped silicon wafer is often used as both the substrate and gate electrode. A thermally grown SiO_2 layer of 100–300-nm thick is usually used as an insulating layer on the silicon surface. The organic active layer is deposited on the dielectric surface, and then the source and drain electrodes are deposited on top by vacuum evaporation through a shadow mask to give an OFET device.

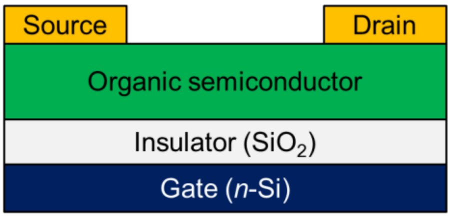

Figure 1-1. Illustration of bottom-gate-top-contact OFET devices.

Figure 1-2 shows the working mechanism of p-channel OFETs. When a negative bias is applied on the gate, an electronic field is produced at the semiconductor–dielectric surface, forming a conducting channel which is the path of holes. Holes are injected into the HOMO of organic semiconductor and transported via the overlap between HOMOs. The most important parameter in evaluation of OFETs is the charge-carrier mobility (μ), which quantifies the average charge-carrier drift velocity per unit of electric field.

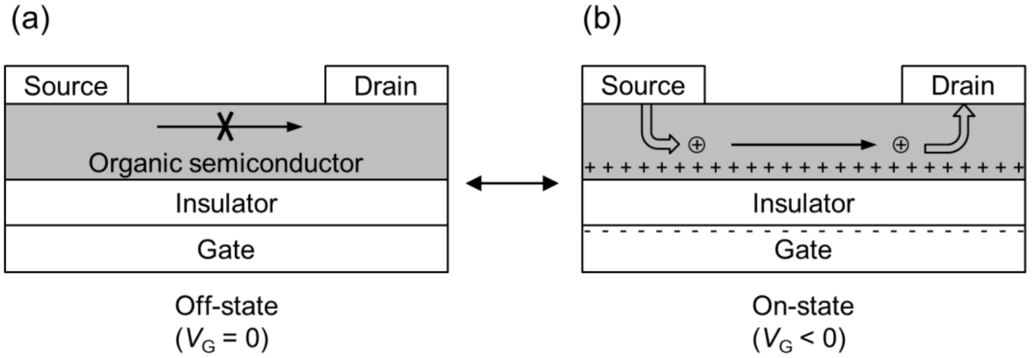

Figure 1-2. Working mechanism of p-channel OFET devices: (a) off-state and (b) on-state.

The first example of OFET was reported in 1970.[7] Since then, a large number of organic semiconductor materials for OFETs have been reported,[8] and the μ solution-processed OFETs has been remarkably improved. As described in Figure 1-2, the direction of charge-carrier path in the organic active layer of OFETs is parallel to the substrate. As the charge carriers move along π-overlap between molecules, controlling the anisotropy in molecular arrangement of organic semiconductor materials is important for improving the μ in OFETs. From this standpoint, solution-based deposition processes such as drop-casting,[9–11] dip-coating,[12,13] and solution-sharing[14,15] are highly effective, because the anisotropy of crystal growth is controllable by the direction of solvent evaporation. In fact, several groups have recently reported solution-processed OFETs which show μ values of over 10 cm^2 V^{-1} s^{-1}.[15–18]

1-3. Organic Photovoltaics (OPVs)

Figure 1-3 shows the working mechanism of OPVs. First, the solar light is absorbed by the p-type material to generate excitons (step 1). In this case, a mterial with a wide absorption range and high absorption coefficients is favorable in order for generating a large amount of excitions from the solar light. And then, the generated excitons diffuse to the interface of p-type and n-type materials (step 2). Since the exciton diffusion length (L_D) in organic materials is about 5–20 nanometers,[19] the grain size of p- and n-type materials should be controlled within the twice of L_D (10–40 nm) for efficient charge generation. At the interface of p- and n-type materials, the excitons in the p-type material give electrons to the n-type material to generate holes and electrons (step 3). It has been widely accepted that the energy-level difference between LUMOs of p- and n-type materials needs to be about 0.2–0.3 eV for efficient charge seperation (Figure 1-3b). It is also worth noting that the open-circuit voltage (V_{OC}) of OPV is konwn to be proportinal to the energy difference between the HOMO of p-type material and the LUMO of n-type materials (Figure 1-3b). In this regard, the ideal HOMO and LUMO levels of p-type materials are about –5.2~–5.4 eV and –3.8~–4.0 eV, respectively, when $PC_{61}BM$ (LUMO = ca. –4.3 eV) is employed as an n-type material.[20] Next, the holes and electrons are transported to the electrodes through p- and n-type materials, respectively (step 4). In this process, materials that show high μs to the out-of-plane direction are favorable. Lastly, the holes and electrons are collected at the electrodes to generate

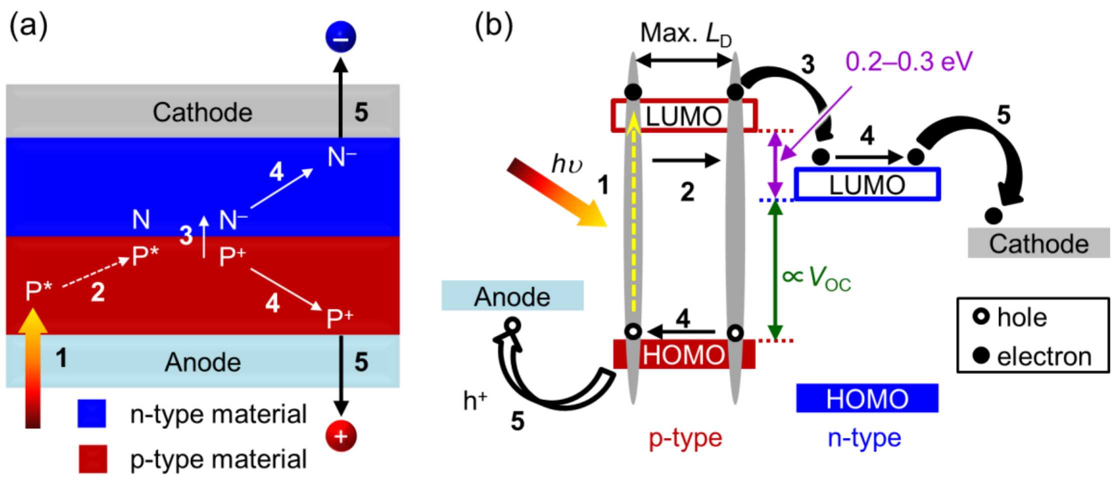

Figure 1-3. (a) Fundamental processes of bilayer heterojunction OPVs. (b) Typical HOMO–LUMO energy diagram of OPV.

photovoltaic current.

To satisfy the requirements for achieving efficient photovoltaic process, various types of highly π-conjugated organic semicondoctor materials have been developed.[21,22] Because of the low solubilies of pristine π-frameworks, long and bulky alkyl side-chains are generally introduced to such materials in order for ensuring high-enough solubilities in processing solvents and for tuning the miscibility with other materials in the acitve layer.[23–27] Recently, solution-processed bulk heterojunction (BHJ) OPVs based on polymer[28–33] and small-molecule[23,34] p-type materials have achieved over 10% of power conversion efficencies (PCEs). These achievements are owing to the development of OPV materials having high photoabsorption capability, suitable orbital energy levels, favorable film morphology, and excellent charge-transport property. However, the stability of the active-layer morphology and thus the performance of the OPVs comprising those materials with bulkyl side-chains are considered to be low against long-time thermal stress.[35] Thus, the introduction of bulky side chains to OPV materials should be avoided or minimized to improve the long-term device stability.

1-4. Tetrabenzoporphyrins for Organic Semiconductor Devices

Tetrabenzoporphyrin (BP) has a large, rigid π-framework, excellent stability, and the maximum absorption coefficient over 10^5 M^{-1} cm^{-1} around 450–500 nm in which the solar light intensity is strongest.[36] These structural and optical characteristics make BP attractive as an active-layer component in organic semiconductor devices such as OFETs and OPVs. On the other hand, BP shows extremely poor solubility owing to the large and rigid π-framework, and thus, its direct application to cost-effective solution-processed devices is severely limited. This issue has been evaded via a stepwise pathway so-called "precursor approach", in which a soluble precursor 1,4:8,11:15,18:22,25-Tetraethano-29*H*,31*H*-tetrabenzo[*b,g,l,q*]porphyrin

(CP) is solution-deposited and then converted to BP in situ by thermally induced retro-Diels–Alder reaction in situ (Figure 1-4 and 1-5).[37]

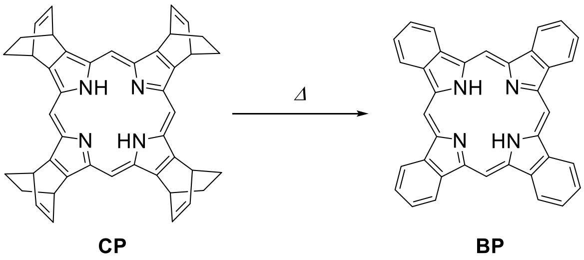

Figure 1-4. Thermal conversion of CP to BP.

Matsuo et al. judiciously employed this CP-to-BP conversion in the preparation of p–i–n-type organic photovoltaic active layers comprising BP and a fullerene-based acceptor named SIMEF achieving respectable PCEs of 5.2–5.4%.[38,39] These efficiency was among the best obtained in small-molecule OPVs at that time, and still remains one of the highest reported for the devices with BP or its derivative as an active-layer component.

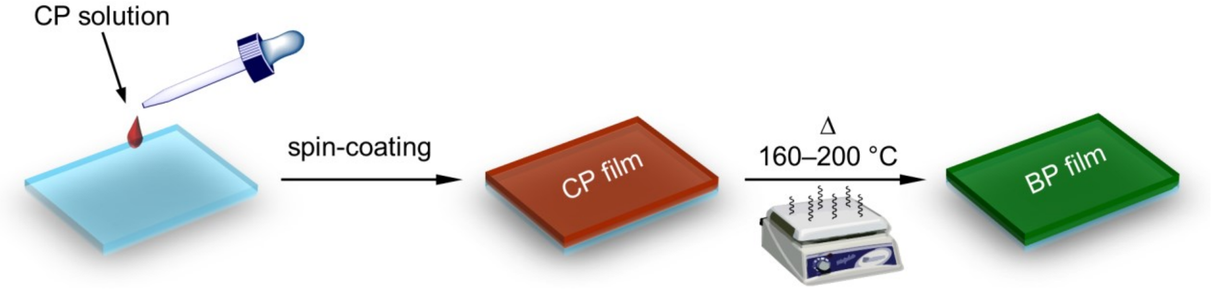

Figure 1-5. Description of the precursor approach using CP-to-BP conversion.

Several other groups also used the same approach in the preparation of OFET having BP or its metal complexes as an active-layer material.[40–43] The highest mobilities achieved thus far in free-base and metal-incorporated BPs are 0.070 and 0.22 cm^2 V^{-1} s^{-1}, respectively.[40,43] Since BP does not have any solubilizing groups, it is assumed that the stability of the BP-based OPVs and OFETs is higher as compared to those devices employing highly soluble materials with bulky side chains.

1-5. Aims and Outline

As mentioned in the previous section, BP has a great potential to be an excellent p-type material for organic semiconductor devices. However, the reported device performances of OFETs and OPVs comprising pristine BP and its derivatives are still much lower than those of the state-of-the-art organic semiconductor materials, indicating their great potentials have not been fully exploited until now. The reason for this stagnated performance can be ascribed to some drawbacks associated with BP, such as the limited photoabsorption range, too high HOMO level, and poor miscibility with other materials. A conceptually straightforward strategy for overcoming these drawbacks, is the structural tuning by chemical modification introduction. However, systematic investigation on the relationship between molecular structure and device performance among BP derivatives has been scarce, probably because of the limited synthetic accessibility to BP derivatives as well as the absence of the definite guideline for molecular design. In order to fully exploit the great potential of BP as a material for organic semiconductor devices, the author decided to develop new BP derivatives which show excellent device performance by introducing suitable substituents on the BP framework (Figure 1-6). The aims of this dissertation are to provide a desig guideline of BP derivatives which paves the way to achieve BP-based high-performance organic semiconductor devices.

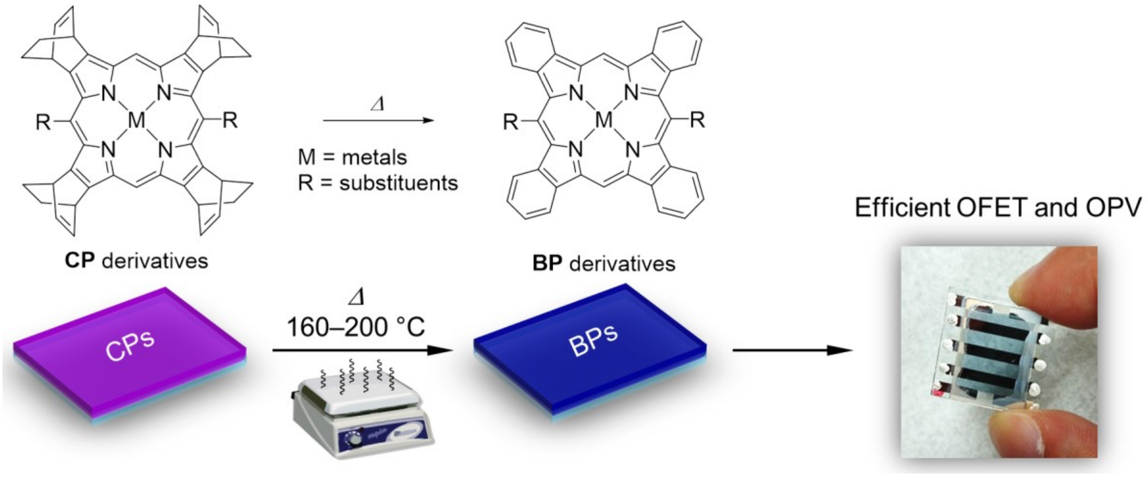

Figure 1-6. Schematic description of this study.

This project is started with the investigation of the basic properties, including OFET and OPV performances of 5,15-bis(trialkylsilylethynyl)-substituted BPs and their metal complexes are as described in **Chapter 2**. Both the size of substituents and the type of incorporated metal ion have considerable impacts on the crystal-packing behavior, energy levels, and device performance. The maximum μ_h and PCE of 0.12 cm^2 V^{-1} s^{-1} and 1.51% are obtained in OFET and BHJ OPV, respectively.

Chapter 3 focuses on improving the performance of OFETs based on a soluble BP derivative 5,15-bis(triisopropylsilylethynyl)tetrabenzoporphyrin (TIPS-BP) through polymorph and device engineering. TIPS-BP shows two different packing motifs in the single-crystalline state, named “1D π-stack” and “2D π-stack”, respectively. Theoretical calculations indicate that 2D π-stack has a potential to show excellent μ_hs in OFET. By careful optimization of deposition conditions, the molecular packing of “2D π-stack” is reproduced in the thin-film state, which affords the maximum μ_h of 1.1 cm^2 V^{-1} s^{-1}. This mobility is higher than any reported values with BP derivatives so far.

Chapter 4 focuses on the molecular engineering of BP for use as the p-type material in OPVs. A series of new BP derivatives having dithienyldiketopyrrolopyrroles (DPPs) units with different lengths of *N*-alkyl groups (C*n*-DPP–BPs) are designed toward improving the photocurrent-generation efficiency in BHJ layers. Systematic investigation of C*n*-DPP–BPs reveals the significant substituent impact on short-circuit current density (J_{SC}); C10-DPP–BP gives 0.88 mA cm^{-2}, while C4-DPP–BP affords 15.19 mA cm^{-2}, resulting in PCEs of 0.2 and 5.2 %, respectively. The fluorescence decay measurements, atomic force microscopy (AFM), and two-dimensional grazing-incident wide-angle X-ray diffractometry (2D-GIWAXD) images indicate that the introduction of shorter alkyl chains on the C*n*-DPP–BP framework leads to higher miscibility, finer grains, and more preferable molecular orientation.

Chapter 5 describes the general conclusion of this dissertation. The relationship between molecular structure and device performance among the BP derivatives is summarized. In addition, future directions for developing new BP derivatives toward high device performance are suggested.

1-6. References

(1) Sekitani, T.; Nakajima, H.; Maeda, H.; Fukushima, T.; Aida, T.; Hata, K.; Someya, T. Stretchable Active-Matrix Organic Light-Emitting Diode Display Using Printable Elastic Conductors. *Nat. Mater.* **2009**, *8*, 494–499.

(2) Xu, R.-P.; Li, Y.-Q.; Tang, J.-X. Recent Advances in Flexible Organic Light-Emitting Diodes. *J. Mater. Chem. C* **2016**, *4*, 9116–9142.

(3) Kaltenbrunner, M.; Sekitani, T.; Reeder, J.; Yokota, T.; Kuribara, K.; Tokuhara, T.; Drack, M.; Schwödiauer, R.; Graz, I.; Bauer-Gogonea, S.; Bauer, S.; Someya, T. An Ultra-Lightweight Design for Imperceptible Plastic Electronics. *Nature* **2013**, *499*, 458–463.

(4) Lipomi, D. J.; Tee, B. C.-K.; Vosgueritchian, M.; Bao, Z. Stretchable Organic Solar Cells. *Adv. Mater.* **2011**, *23*, 1771–1775.

(5) Kaltenbrunner, M.; White, M. S.; Głowacki, E. D.; Sekitani, T.; Someya, T.; Sariciftci, N. S.; Bauer, S. Ultrathin and Lightweight Organic Solar Cells with High Flexibility. *Nat. Commun.* **2012**, *3*, 770.

(6) Qian, Y.; Zhang, X.; Xie, L.; Qi, D.; Chandran, B. K.; Chen, X.; Huang, W. Stretchable Organic Semiconductor Devices. *Adv. Mater.* **2016**, *28*, 9243–9265.

(7) Tsumura, A.; Koezuka, H.; Ando, T. Macromolecular Electronic Device: Field-Effect Transistor with a Polythiophene Thin Film. *Appl. Phys. Lett.* **1986**, *49*, 1210–1212.

(8) Wang, C.; Dong, H.; Hu, W.; Liu, Y.; Zhu, D. Semiconducting π-Conjugated Systems in Field-Effect Transistors: A Material Odyssey of Organic Electronics. *Chem. Rev.* **2012**, *112*, 2208–2267.

(9) James, D. T.; Kjellander, B. K. C.; Smaal, W. T. T.; Gelinck, G. H.; Combe, C.; McCulloch, I.; Wilson, R.; Burroughes, J. H.; Bradley, D. D. C.; Kim, J.-S. Thin-Film Morphology of Inkjet-Printed Single-Droplet Organic Transistors Using Polarized Raman Spectroscopy: Effect of Blending TIPS-Pentacene with Insulating Polymer.

ACS Nano **2011**, *5*, 9824–9835.

(10) Lee, M. W.; Ryu, G. S.; Lee, Y. U.; Pearson, C.; Petty, M. C.; Song, C. K. Control of Droplet Morphology for Inkjet-Printed TIPS-Pentacene Transistors. *Microelectron. Eng.* **2012**, *95*, 1–4.

(11) Liu, D.; Xu, X.; Su, Y.; He, Z.; Xu, J.; Miao, Q. Self-Assembled Monolayers of Phosphonic Acids with Enhanced Surface Energy for High-Performance Solution-Processed n-Channel Organic Thin-Film Transistors. *Angew. Chem. Int. Ed.* **2013**, *52*, 6222–6227.

(12) Jang, J.; Nam, S.; Im, K.; Hur, J.; Cha, S. N.; Kim, J.; Son, H. B.; Suh, H.; Loth, M. A.; Anthony, J. E.; Park, J.-J.; Park, C. E.; Kim, J. M.; Kim, K. Highly Crystalline Soluble Acene Crystal Arrays for Organic Transistors: Mechanism of Crystal Growth During Dip-Coating. *Adv. Funct. Mater.* **2012**, *22*, 1005–1014.

(13) Nam, S.; Jang, J.; Anthony, J. E.; Park, J.-J.; Park, C. E.; Kim, K. High-Performance Triethylsilylethynyl Anthradithiophene Transistors Prepared without Solvent Vapor Annealing: The Effects of Self-Assembly during Dip-Coating. *ACS Appl. Mater. Interfaces* **2013**, *5*, 2146–2154.

(14) Giri, G.; Verploegen, E.; Mannsfeld, S. C. B.; Atahan-Evrenk, S.; Kim, D. H.; Lee, S. Y.; Becerril, H. A.; Aspuru-Guzik, A.; Toney, M. F.; Bao, Z. Tuning Charge Transport in Solution-Sheared Organic Semiconductors Using Lattice Strain. *Nature* **2011**, *480*, 504–508.

(15) Diao, Y.; Tee, B. C.-K.; Giri, G.; Xu, J.; Kim, D. H.; Becerril, H. A.; Stoltenberg, R. M.; Lee, T. H.; Xue, G.; Mannsfeld, S. C. B.; Bao, Z. Solution Coating of Large-Area Organic Semiconductor Thin Films with Aligned Single-Crystalline Domains. *Nat. Mater.* **2013**, *12*, 665–671.

(16) Minemawari, H.; Yamada, T.; Matsui, H.; Tsutsumi, J.; Haas, S.; Chiba, R.; Kumai, R.; Hasegawa, T. Inkjet Printing of Single-Crystal Films. *Nature* **2011**, *475*, 364–367.

(17) Yuan, Y.; Giri, G.; Ayzner, A. L.; Zoombelt, A. P.; Mannsfeld, S. C. B.; Chen, J.; Nordlund, D.; Toney, M. F.; Huang, J.; Bao, Z. Ultra-High Mobility Transparent Organic Thin Film Transistors Grown by an Off-Centre Spin-Coating Method. *Nat. Commun.* **2014**, *5*, 3005.

(18) Xu, X.; Yao, Y.; Shan, B.; Gu, X.; Liu, D.; Liu, J.; Xu, J.; Zhao, N.; Hu, W.; Miao, Q. Electron Mobility Exceeding 10 cm^2 V^{-1} s^{-1} and Band-Like Charge Transport in Solution-Processed n-Channel Organic Thin-Film Transistors. *Adv. Mater.* **2016**, *28*, 5276–5283.

(19) Mikhnenko, O. V.; Blom, P. W. M.; Nguyen, T.-Q. Exciton Diffusion in Organic Semiconductors. *Energy Environ. Sci.* **2015**, *8*, 1867–1888.

(20) Scharber, M. C.; Mühlbacher, D.; Koppe, M.; Denk, P.; Waldauf, C.; Heeger, A. J.; Brabec, C. J. Design Rules for Donors in Bulk-Heterojunction Solar Cells—Towards 10 % Energy-Conversion Efficiency. *Adv. Mater.* **2006**, *18*, 789–794.

(21) Mishra, A.; Bäuerle, P. Small Molecule Organic Semiconductors on the Move: Promises for Future Solar Energy Technology. *Angew. Chem. Int. Ed.* **2012**, *51*, 2020–2067.

(22) Roncali, J.; Leriche, P.; Blanchard, P. Molecular Materials for Organic Photovoltaics: Small Is Beautiful. *Adv. Mater.* **2014**, *26*, 3821–3838.

(23) Kan, B.; Li, M.; Zhang, Q.; Liu, F.; Wan, X.; Wang, Y.; Ni, W.; Long, G.; Yang, X.; Feng, H.; Zuo, Y.; Zhang, M.; Huang, F.; Cao, Y.; Russell, T. P.; Chen, Y. A Series of Simple Oligomer-like Small Molecules Based on Oligothiophenes for Solution-Processed Solar Cells with High Efficiency. *J. Am. Chem. Soc.* **2015**, *137*, 3886–3893.

(24) Sun, K.; Xiao, Z.; Lu, S.; Zajaczkowski, W.; Pisula, W.; Hanssen, E.; White, J. M.; Williamson, R. M.; Subbiah, J.; Ouyang, J.; Holmes, A. B.; Wong, W. W. H.; Jones, D. J. A Molecular Nematic Liquid Crystalline Material for High-Performance Organic

Photovoltaics. *Nat. Commun.* **2015**, *6*, 6013.

(25) Gao, K.; Li, L.; Lai, T.; Xiao, L.; Huang, Y.; Huang, F.; Peng, J.; Cao, Y.; Liu, F.; Russell, T. P.; Janssen, R. A. J.; Peng, X. Deep Absorbing Porphyrin Small Molecule for High-Performance Organic Solar Cells with Very Low Energy Losses. *J. Am. Chem. Soc.* **2015**, *137*, 7282–7285.

(26) Gupta, V.; Kyaw, A. K. K.; Wang, D. H.; Chand, S.; Bazan, G. C.; Heeger, A. J. Barium: An Efficient Cathode Layer for Bulk-Heterojunction Solar Cells. *Sci. Rep.* **2013**, *3*, 1965.

(27) Kan, B.; Zhang, Q.; Li, M.; Wan, X.; Ni, W.; Long, G.; Wang, Y.; Yang, X.; Feng, H.; Chen, Y. Solution-Processed Organic Solar Cells Based on Dialkylthiol-Substituted Benzodithiophene Unit with Efficiency near 10%. *J. Am. Chem. Soc.* **2014**, *136*, 15529–15532.

(28) Liu, Y.; Zhao, J.; Li, Z.; Mu, C.; Ma, W.; Hu, H.; Jiang, K.; Lin, H.; Ade, H.; Yan, H. Aggregation and Morphology Control Enables Multiple Cases of High-Efficiency Polymer Solar Cells. *Nat. Commun.* **2014**, *5*, 5293.

(29) Vohra, V.; Kawashima, K.; Kakara, T.; Koganezawa, T.; Osaka, I.; Takimiya, K.; Murata, H. Efficient Inverted Polymer Solar Cells Employing Favourable Molecular Orientation. *Nat. Photonics* **2015**, *9*, 403–408.

(30) Zhao, W.; Qian, D.; Zhang, S.; Li, S.; Inganäs, O.; Gao, F.; Hou, J. Fullerene-Free Polymer Solar Cells with over 11% Efficiency and Excellent Thermal Stability. *Adv. Mater.* **2016**, *28*, 4734–4739.

(31) Jin, Y.; Chen, Z.; Dong, S.; Zheng, N.; Ying, L.; Jiang, X.-F.; Liu, F.; Huang, F.; Cao, Y. A Novel Naphtho[1,2-*c*:5,6-*c*′]Bis([1,2,5]Thiadiazole)-Based Narrow-Bandgap π-Conjugated Polymer with Power Conversion Efficiency Over 10%. *Adv. Mater.* **2016**, *28*, 9811–9818.

(32) Qin, Y.; Uddin, M. A.; Chen, Y.; Jang, B.; Zhao, K.; Zheng, Z.; Yu, R.; Shin, T. J.; Woo,

H. Y.; Hou, J. Highly Efficient Fullerene-Free Polymer Solar Cells Fabricated with Polythiophene Derivative. *Adv. Mater.* **2016**.

(33) Li, S.; Ye, L.; Zhao, W.; Zhang, S.; Mukherjee, S.; Ade, H.; Hou, J. Energy-Level Modulation of Small-Molecule Electron Acceptors to Achieve over 12% Efficiency in Polymer Solar Cells. *Adv. Mater.* **2016**, *28*, 9423–9429.

(34) Deng, D.; Zhang, Y.; Zhang, J.; Wang, Z.; Zhu, L.; Fang, J.; Xia, B.; Wang, Z.; Lu, K.; Ma, W.; Wei, Z. Fluorination-Enabled Optimal Morphology Leads to over 11% Efficiency for Inverted Small-Molecule Organic Solar Cells. *Nat. Commun.* **2016**, *7*, 13740.

(35) Liao, H.-C.; Chen, P.-H.; Chang, R. P. H.; Su, W.-F. Morphological Control Agent in Ternary Blend Bulk Heterojunction Solar Cells. *Polymers* **2014**, *6*, 2784–2802.

(36) Berezin, D. S.; Toldina, O. V.; Kudrik, E. V. Complex Formation and Spectral Properties of *meso*-Phenyltetrabenzoporphyrins in Pyridine and *N*,*N*-Dimethylformamide. *Russ. J. Gen. Chem.* **2003**, *73*, 1309–1314.

(37) Ono, N.; Ito, S.; Ochi, N.; Murashima, T.; Uno, H. A New Synthesis of Benzoporphyrins Using 4,7-Dihydro-4,7-Ethano-2*H*-Isoindole as an Isoindole Equivalent. *Heterocycles* **2000**, *52*, 399–411.

(38) Matsuo, Y.; Sato, Y.; Niinomi, T.; Soga, I.; Tanaka, H.; Nakamura, E. Columnar Structure in Bulk Heterojunction in Solution-Processable Three-Layered p-i-n Organic Photovoltaic Devices Using Tetrabenzoporphyrin Precursor and Silylmethyl[60]fullerene. *J. Am. Chem. Soc.* **2009**, *131*, 16048–16050.

(39) Tanaka, H.; Abe, Y.; Matsuo, Y.; Kawai, J.; Soga, I.; Sato, Y.; Nakamura, E. An Amorphous Mesophase Generated by Thermal Annealing for High-Performance Organic Photovoltaic Devices. *Adv. Mater.* **2012**, *24*, 3521–3525.

(40) Noguchi, N.; Junwei, S.; Asatani, H.; Matsuoka, M. Control of Morphology and Orientation of a Thin Film Tetrabenzoporphyrin (TBP) Organic Semiconductor by

Solid-State Crystallization. *Cryst. Growth Des.* **2010**, *10*, 1848–1853.

(41) Shea, P. B.; Yamada, H.; Ono, N.; Kanicki, J. Solution-Processed Zinc Tetrabenzoporphyrin Thin-Films and Transistors. *Thin Solid Films* **2012**, *520*, 4031–4035.

(42) Shea, P. B.; Pattison, L. R.; Kawano, M.; Chen, C.; Chen, J.; Petroff, P.; Martin, D. C.; Yamada, H.; Ono, N.; Kanicki, J. Solution-Processed Polycrystalline Copper Tetrabenzoporphyrin Thin-Film Transistors. *Synth. Met.* **2007**, *157*, 190–197.

(43) Shea, P. B.; Kanicki, J.; Pattison, L. R.; Petroff, P.; Kawano, M.; Yamada, H.; Ono, N. Solution-Processed Nickel Tetrabenzoporphyrin Thin-Film Transistors. *J. Appl. Phys.* **2006**, *100*, 34502.

Chapter 2

Effect of Alkyl Substituents: 5,15-Bis(trimethylsilylethynyl) vs. 5,15-Bis(triisopropylsilylethynyl) tetrabenzoporphyrins and Their Metal Complexes

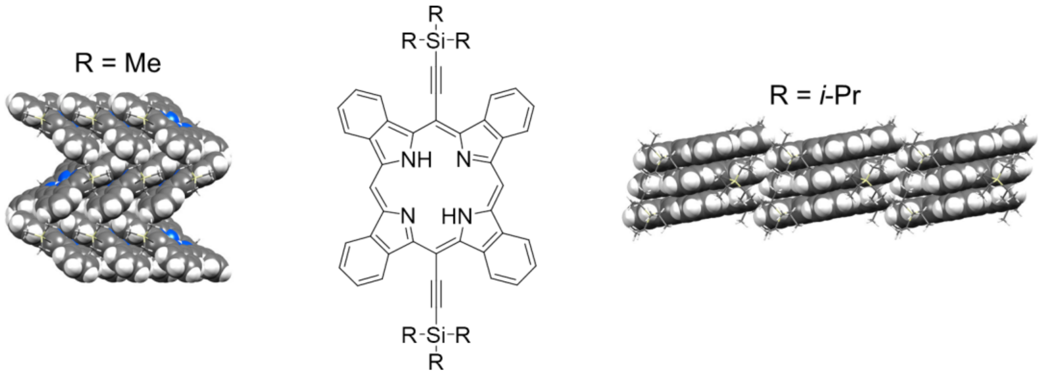

In this chapter, the basic property and device performance (OFETs and OPVs) of 5,15-trialkylethynyl substituted tetrabenzoporphyrins and their metal complexes are described.

2-1. Introduction

As mentioned in the previous chapter, BP has a great potential as a p-type organic semiconductor material for solution-processed OFETs and OPVs. However, BP still has some room as a p-type material for organic semiconductor devices. In case of BP-based OFETs, precursor approach is the only choice to deposit organic active layer by solution process, making its direct solution deposition essentially impossible to control the anisotropy of crystal growth. Thus, the μ_hs of BP-based OFETs (0.2–0.07 cm^2 V^{-1} s^{-1})[1–4] are still lower than those of state-of-the-art OFETs (>10 cm^2 V^{-1} s^{-1})[5–9] in which active layers deposited via fine-tuned solution processes. To improve the μ_hs of BP-based OFETs, the strategy of molecular design for a 6,13-triisopropylsililethynyl-pentacene (TIPS-PEN)[10] is a good model (Figure 2-1). Pentacene is one of the most promising organic p-type semiconductor materials showing good carrier mobilities of over 1 cm^2 V^{-1} s^{-1} in OFETs, but it is hardly soluble in common organic solvents and unstable in ambient conditions. In contrast, TIPS-PEN shows a good solubility and chemical stability owing to the introduction of the bulky TIPS-ethynyl groups to the most reactive 6,13-positions.[11] The pristine pentacene packs to form a herringbone motif, while TIPS-PEN forms a brickwork motif.[10] Anthony et al. have reported the molecular packing of molecular organic semiconductors can be tuned by changing the diameter of substituents at the end of ethynyl groups.[10,12,13] TIPS-PEN-based OFETs show superior carrier mobilities of up to 11 cm^2 V^{-1} s^{-1} in solution-processed single-crystalline film.[14]

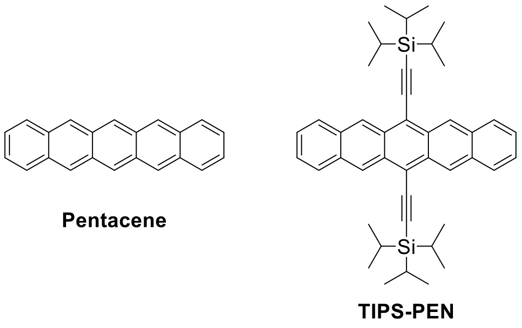

Figure 2-1. Chemical structure of pentacene and TIPS-PEN.

In case of BP-based OPVs, BP has three main drawbacks to improve the OPV performance as a p-type material. The first is the limited absorption capability. BP can't absorb the light over 700 nm and has the absorption valley at 500–600 nm.[15] The second is the extremely poor miscibility with other materials. The size of BP crystals in blend film is quite larger than the L_D of BP[16] because of the strong intermolecular interaction[17] yielding the BHJ OPV based on BP:$PC_{61}BM$ system shows a low power PCE of 0.02%.[18] The third is a high lying HOMO level. The V_{OC} of BP-based OPV (0.55–0.75 V) is still lower than state of the art OPV based on small molecular materials which show the excellent PCE of over 10% (ca. 0.9–1.0 V).[19,20]

A conceptually straightforward approach to fill room of BP is the introduction of proper substituents into a BP framework. However, systematic investigation of BP derivatives for OFETs and OPVs has been scarce probably because of the limited synthetic accessibility. Meanwhile, Yamada's group reported that 5,15-bis(trimethylsilylethynyl)tetrabenzoporphyrin (TMS-BP) could be formed in good yields via the corresponding CP-type precursors named TMS-CP (i.e., through the precursor approach).[21] This report demonstrated that the introduction of ethynyl groups at 5,15-positions of a BP framework is effective to expand π-conjugation. However, physical properties such as crystal structures and energy levels as well as device performance of TMS-BP were not investigated. In addition, several groups have reported the internal metal ions of BP have great impacts on the performance of both OFETs and OPVs.[1–4,22]

In this regard, the author decided to investigate the crystal structures, energy levels, and device performance (OFETs and OPVs) of TMS-BP, 5,15-bis(triisopropylsilylethynyl)tetrabenzoporphyrin (TIPS-BP) and their zinc, copper and nickel complexes (Figure 2-2).

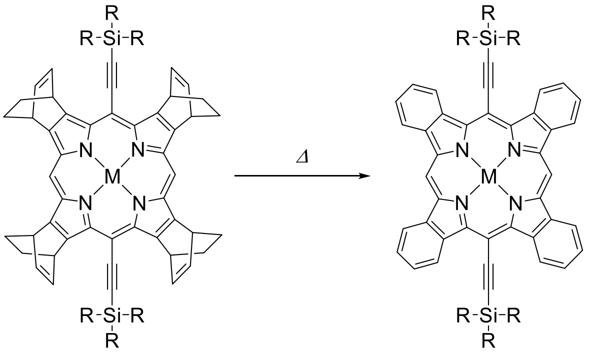

TMS-CP (R = Me, M =2H)
TMS-ZnCP (R = Me, M = Zn)
TMS-CuCP (R = Me, M = Cu)
TMS-NiCP (R = Me, M = Ni)
TIPS-CP (R = *i*-Pr, M = 2H)
TIPS-ZnCP (R = *i*-Pr, M = Zn)
TIPS-CuCP (R = *i*-Pr, M = Cu)
TIPS-NiCP (R = *i*-Pr, M = Ni)

TMS-BP (R = Me, M =2H)
TMS-ZnBP (R = Me, M = Zn)
TMS-CuBP (R = Me, M = Cu)
TMS-NiBP (R = Me, M = Ni)
TIPS-BP (R = *i*-Pr, M = 2H)
TIPS-ZnBP (R = *i*-Pr, M = Zn)
TIPS-CuBP (R = *i*-Pr, M = Cu)
TIPS-NiBP (R = *i*-Pr, M = Ni)

Figure 2-2. Molecular structures of TMS-, TIPS-BP, and their metal complexes.

2-2. Synthesis and Thermal Properties

The synthesis of TMS-BP, TIPS-BP their metal complexes is shown in Scheme 2-1.

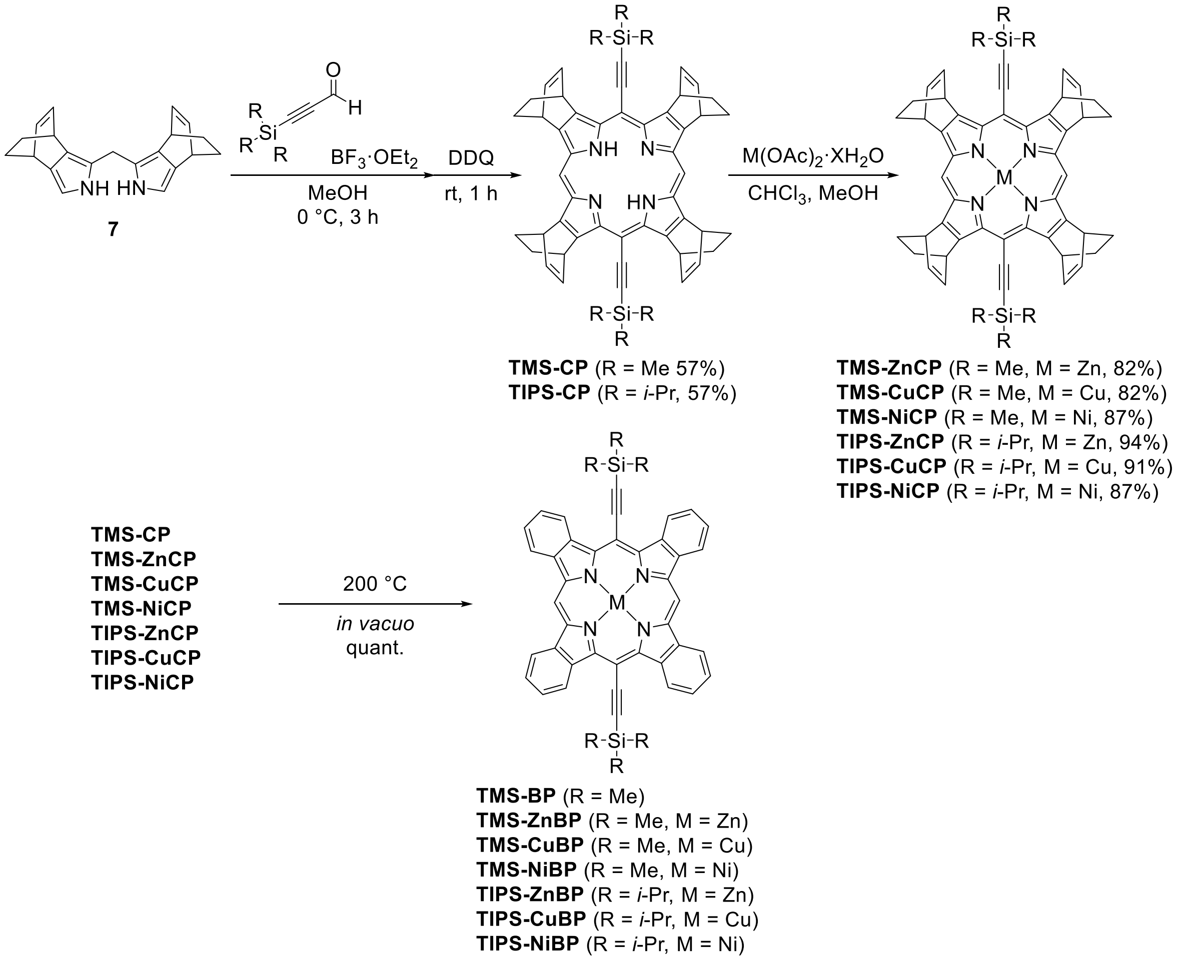

Scheme 2-1. Synthesis of TMS-, TIPS-BP, and their metal complexes.

TMS-CP and TIPS-CP were obtained by a MacDonald-type condensation of BCOD-fused dipyrromethane (1)[21] and 3-(triisopropylsilyl)propiolaldehyde. Dipyrromethane (1) was synthesized from *cis*-1,2-dichloromethane for 6 steps (Scheme S2-1). TMS-ZnCP, TMS-CuCP, TMS-NiCP, TIPS-ZnCP, TIPS-CuCP, and TIPS-NiCP were synthesized from TMS-CP and TIPS-CP by general metal insertion methods.[21]

Thermal behavior of CP, TMS-CP, TIPS-CP, and their metal complexes was observed by thermogravimetric analysis (TGA) (Figure 2-3). The temperature of thermally induced retro Diels–Alder reaction temperature (T_r), decomposition temperature (T_d), theoretical and observed mass losses of all precursors are summarized in Table 2-1. The mass loss of all precursors started at around 140–160 ºC and finished at around 200 ºC. The observed mass

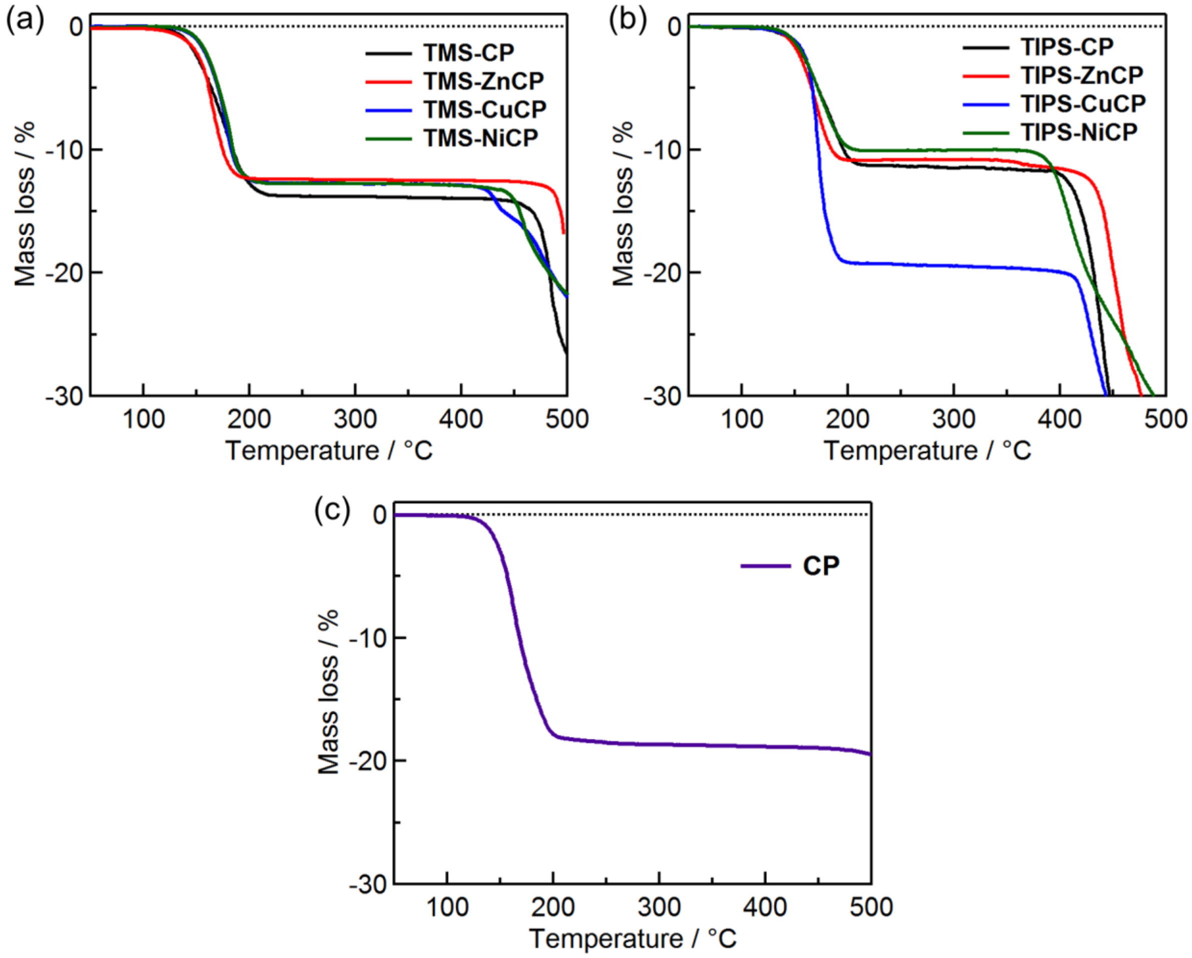

Figure 2-3. TGA curves of (a) TMS-CP, TMS-CuCP, TMS-NiCP, (b) TIPS-CP, TIPS-ZnCP, TIPS-CuCP, TIPS-NiCP, and (c) CP.

loss of all precursors except for TIPS-CuCP is in agreement with the calculated value of the mass loss of four ethylene molecules per molecule. On the other hand, the observed mass loss of TIPS-CuCP is 19.7%, which is consistent with the loss of four ethylene molecules and a chloroform molecule per TIPS-CuCP molecule. It is presumed that the chloroform was contaminated during recrystallization ($CHCl_3$/MeOH) of TIPS-CuCP. The TGA results suggested that the precursors could be converted to the corresponding BPs quantitatively by heating at 200 ºC in the solid state. The average T_d of TMS- and TIPS-BPs are 458 and 415 °C, respectively, indicating the thermal stability of TMS-BPs are higher than those of of TIPS-BPs, but lower than that of BP (T_d = 534 °C).

Table 2-1. Summary of TGA.

Materials	T_r^a / °C	Mass loss (calcd) / %	Mass loss (found)^b / %	T_d / °C
TMS-CP	141	13.8	13.8	472
TMS-ZnCP	151	12.8	12.4	488
TMS-CuCP	154	12.8	12.7	424
TMS-NiCP	155	12.9	12.8	449
TIPS-CP	147	11.4	11.4	417
TIPS-ZnCP	148	10.7	10.9	435
TIPS-CuCP	160	19.9^c	19.2	417
TIPS-NiCP	149	10.9	10.1	390
CP	146	18.0	18.5	534

^{a}Temperature of retro Diels–Alder reactions.; ^{b}at 250 °C, ^{c}with a $CHCl_3$ per one TIPS-CuCP.

2-3. Crystal Structures

Single crystal structures of TMS-BP and their metal complexes are shown in Figure 2-3 and Figure S2-1. Single crystals of TMS-BP, TMS-ZnBP, TMS-CuBP and TMS-NiBP suitable for X-ray analysis were obtained by recrystallization in *o*-dichlorobenzene (TMS-BP, TMS-ZnBP and TMS-CuBP) or slow diffusion of heptane into a chlorobenzene solution (TMS-NiBP). Specifically, recrystallization of TMS-BP, TMS-ZnBP, and TMS-CuBP were performed in boiling *o*-dichlorobenzene to dissolve compounds followed by cooling solutions to room temperature slowly in an oil bath. TMS-BP, TMS-ZnBP, and TMS-CuBP adopt

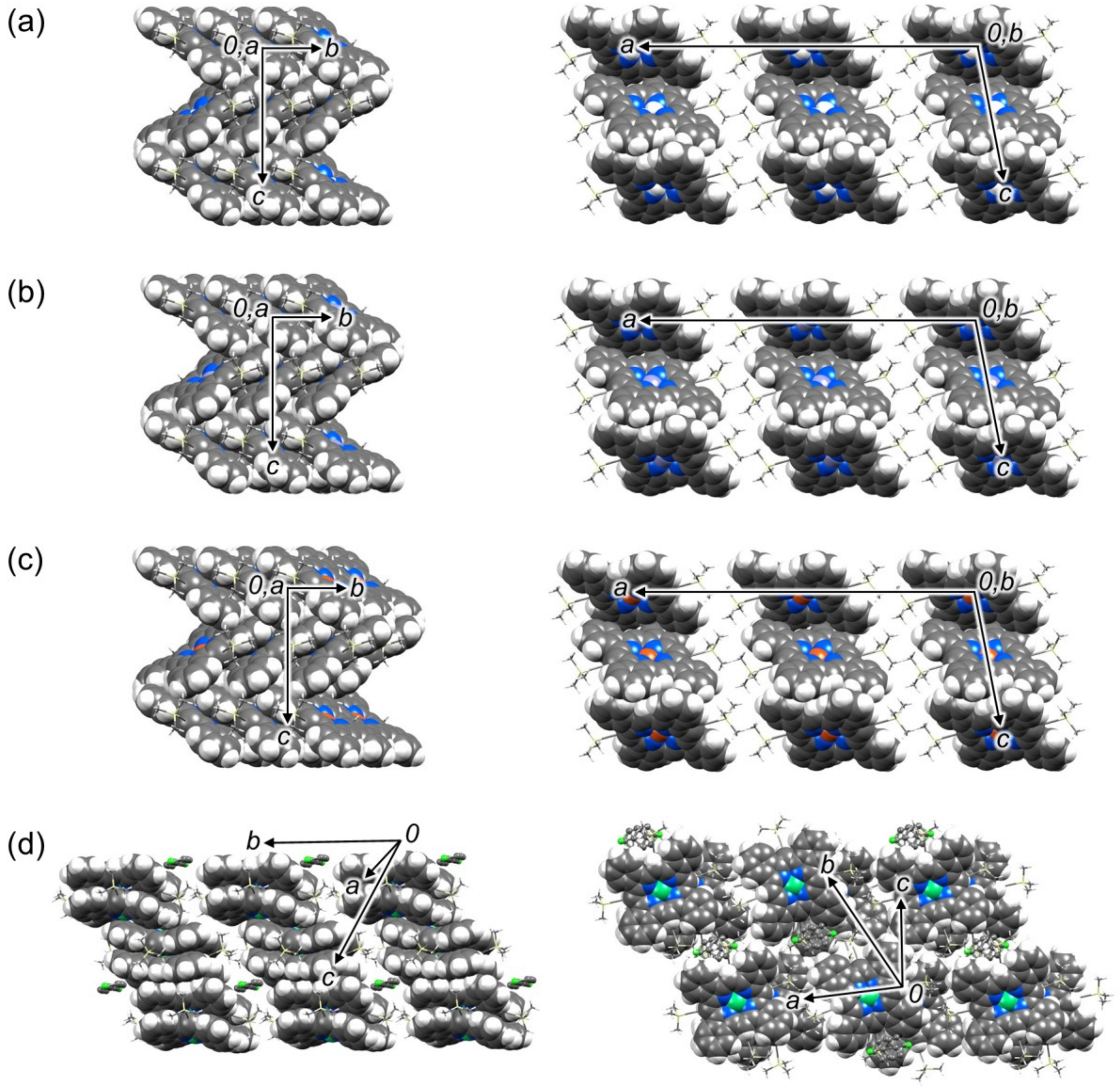

Figure 2-4. Crystal structures of (a) TMS-BP, (b) TMS-ZnBP, (c) TMS-CuBP, and (d) TMS-NiBP. Packing views from the side (left line) and top (right line) of π-stack colums.

herringbone motifs which are similar that of BP (Figure S2-2).[24] The distance associated with the π–π stacking between BP frameworks is 3.21 Å, 3.18 Å, and 3.21 Å for TMS-BP, TMS-ZnBP, and TMS-CuBP, respectively (Figure S2-3). These π–π stacking distances are longer than that of pristine BP crystal (3.15 Å, Figure S2-4) and each π–π stacking column is separated with insulate TMS-groups. On the other hand, the BP framework in TMS-NiBP adopts a saddle-shaped conformation reflecting the small radius of nickel(II) cation in comparison with the cavity size of porphyrin core. The TMS substituents orient to the same direction so that the overall molecular conformation is V-shaped (Figure S2-1d). Molecules of

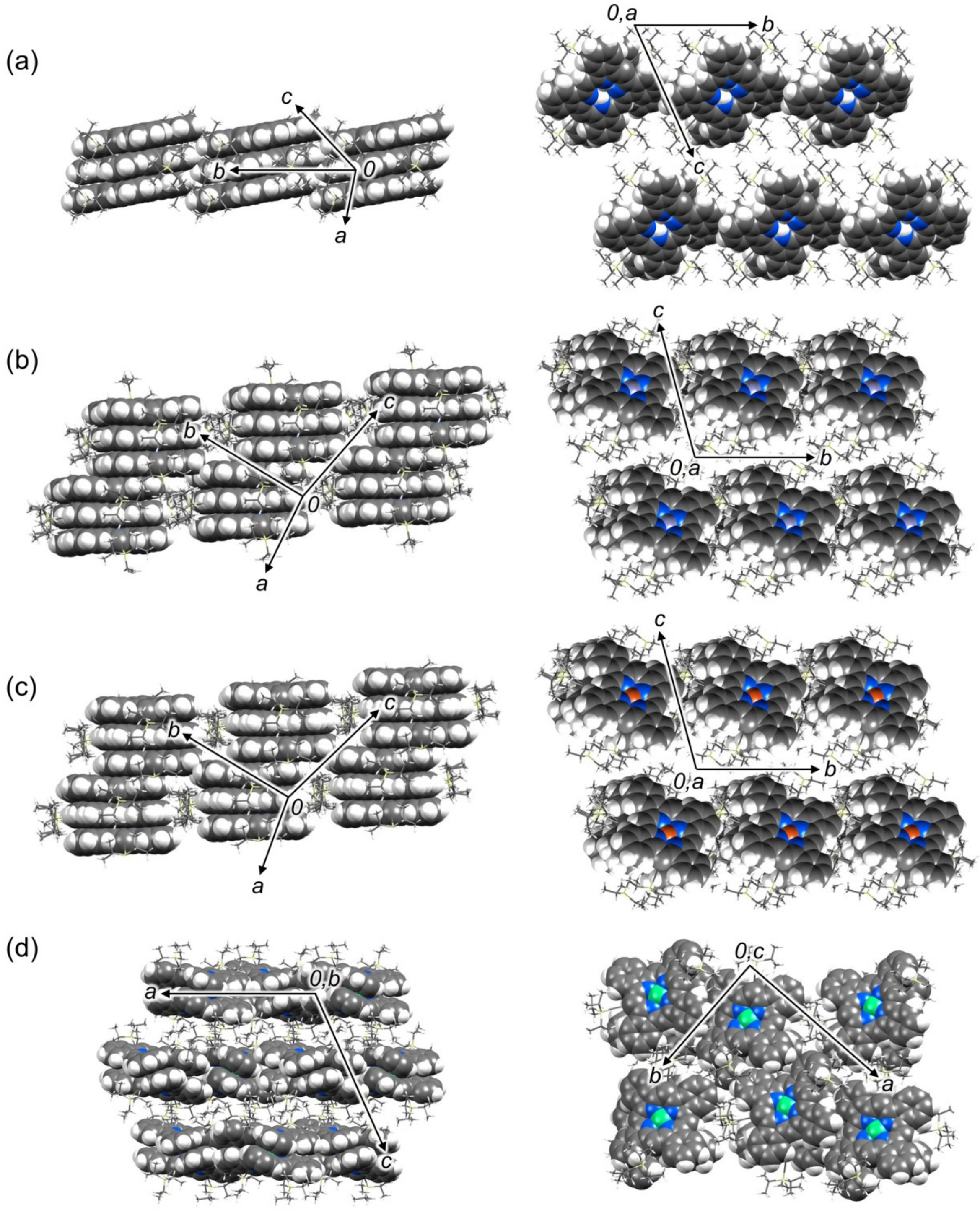

Figure 2-5. Crystal structures of (a) TIPS-BP, (b) TIPS-ZnBP, (c) TIPS-CuBP, and (d) TIPS-NiBP. Packing views from the side (left line) and top (right line) of π-stack colums.

TMS-NiBP form a face–to–face dimeric motif, in which the two molecules are stacked orthogonally with their curved porphyrin surfaces fitting well to each other. Two chlorobenzene molecules are located in the unit cell to occupy the space between the face–to–face dimeric motifs. The associated Ni–Ni distance in the dimer is 3.45 Å.

Single crystal structures of TIPS-BP and their metal complexes are shown in Figure 2-5 and Figure S2-5. Single crystals of TIPS-BP, TIPS-ZnBP, TIPS-CuBP, and TIPS-NiBP were obtained by slow diffusion of poor solvents into good solvent solutions of TIPS-BPs. The crystallization conditions (good/poor solvents) are described as follows: $CHCl_3$/MeOH (TIPS-BP), chlorobenzene/heptane (TIPS-ZnBP), $CHCl_3$/MeOH (TIPS-CuBP), and 1,2-dichloroethane/EtOH (TIPS-NiBP). The crystal structure of TIPS-BP consists of two crystallographically independent molecules in a unit cell. These molecules adopt orthogonal positions each other to form a one-dimensionally extended columnar π-stacking motif with an average interplane spacing of 3.30 Å (Figure S2-6). TIPS-ZnBP and TIPS-CuBP have a planar BP framework and two ethynyl groups bent from the BP framework sigmoidally as similar to the case of TIPS-BP (Figure S2-5b,c). In the packing structures of TIPS-ZnBP and TIPS-CuBP, molecules form a triad-like structures and the molecules are stacked orthogonally. The minimum plane–to–plane distance of each molecule is 3.25 Å for both TIPS-ZnBP and TIPS-CuBP, the distance of which is shorter than that of TIPS-BP (3.30 Å). The triad units are packed parallel to form one-dimensionally extended columnar π-stacking motifs with the plane–to–plane distances of 3.08 Å for TIPS-ZnBP and 3.11 Å for TIPS-CuBP, respectively. On the other hand, TIPS-NiBP molecules show a saddle-shaped conformation and form a face–to–face dimeric motif which is similar with that of TMS-NiBP. The curved porphyrin surfaces are fitted to each other, but TIPS groups of each molecule are oriented against its partner in the dimeric structure. It is indicated that this crystal structure is not suitable for organic electronic devices because of the absence of continuous π-overlap to transport charge-carriers.

The author evaluated the intermolecular electronic coupling of HOMO by calculating charge-transfer integrals (t_{HOMO}) based on the single-crystal structure of TMS-BP and

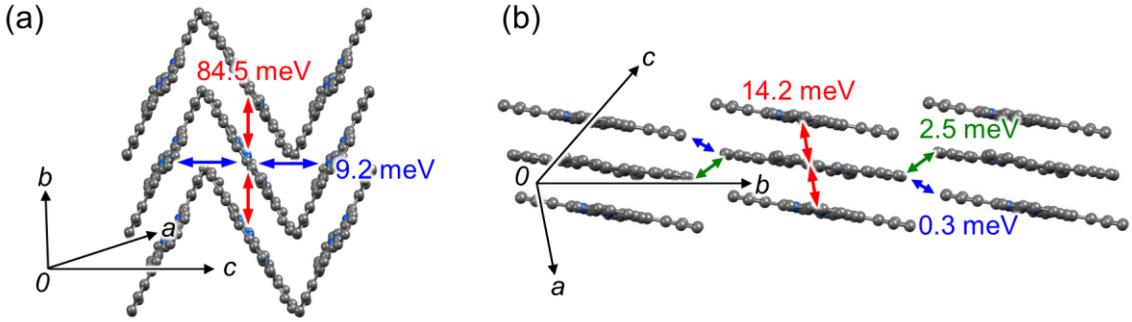

Figure 2-6. Transfer integrals in (a) TMS-BP and (b) TIPS-BP single-crystal structures: Substituents and hydrogen atoms are omitted for clarity.

TIPS-BP (Figure 2-6). The value of t_{HOMO} indicates the strength of electronic coupling of HOMOs and correlated with μ_{h} of OFET.[25–28] The calculated t_{HOMO}s in π-stack column of TMS-BP crystal are all higher than that of TIPS-BP. Especially, the highest t_{HOMO} of TMS-BP (84.5 meV) is higher than that of TIPS-BP (14.2 meV) by a factor of 6. These results indicate that the crystal structure of TMS-BP is better than that of TIPS-BP for charge-carrier transport. However, the highest t_{HOMO} in BP crystal (100.2 meV, Figure S2-7) is still higher than that of TMS-BP may be due to the shorter π-π stacking distance of BP (3.15 Å) than that of TMS-BP (3.21 Å).

2-4. Optical and Electronic Properties

The absorption spectra of TMS-BP, TIPS-BP and their metal complexes in solvents are shown in Figure 2-3 and summarized in Table 2-2. The absorption spectra of TMS-BPs and TIPS-BPs are red-shifted from TMS-CPs and TIPS-CPs because of the π-expansion from precursors to correspond BP compounds (Figure S2-8a,b). TMS-, TIPS-BPs and their metal complexes show peaks of the Soret- and Q-band at around 460 nm and 700 nm, respectively. The offset absorption edges of TMS- and TIPS-BPs are around 700–730 nm which are red-shifted about 30–60 nm from pristine BP solution (Figure S2-8b).

Table 2-2. Electronic properties of compounds

Coumpounds	λ_{onset} (solution) / nm	λ_{onset} (film) / nm	E_g[d] / eV	E_{HOMO}[e] / eV	E_{LUMO}[f] / eV
BP	670[a]	716	1.73	–4.89[18]	–3.15
TMS-BP	723[a]	782	1.59	–4.77	–3.18
TMS-ZnBP	698[b]	779	1.59	–4.72	–3.13
TMS-CuBP	708[b]	772	1.61	–4.72	–3.11
TMS-NiBP	710[b]	–	–	–	–
TIPS-BP	724[a]	782	1.59	–4.94	–3.35
TIPS-ZnBP	698[c]	770	1.61	–4.92	–3.31
TIPS-CuBP	711[a]	768	1.61	–4.89	–3.28
TIPS-NiBP	727[a]	–	–	–	–

[a]in CH_2Cl_2, [b]in DMF, [c]in THF, [d]Determined by optical gaps from the absorption onsets of thin films. [e]Determined by photoelectron spectroscopy in air. [f]$E_{\text{LUMO}} = E_{\text{HOMO}} + E_g$

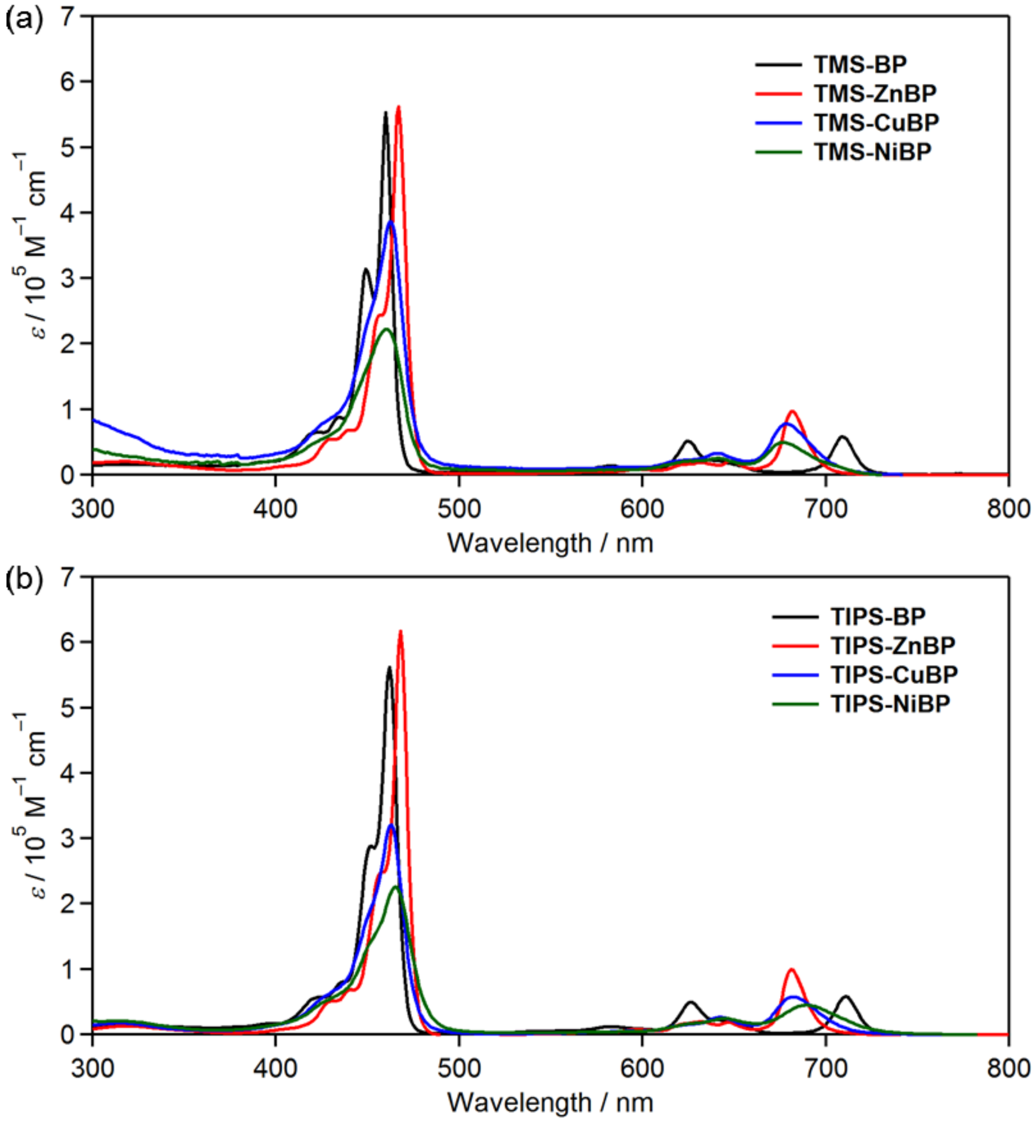

Figure 2-7. Absorption spectra of (a) TMS- and (b) TIPS-BPs in CH_2Cl_2 (TMS-BP, TIPS-BP, TIPS-CuBP and TIPS-NiBP), DMF (TMS-ZnBP, TMS-CuBP and TMS-NiBP), or THF (TIPS-ZnBP).

The absorption spectra of compounds in the film state are shown in Figure 2-7. Since the planarity of Ni complexes (TMS-NiBP and TIPS-NiBP) is low, it was assumed that the device performance of OFETs and OPVs would be poor because of low intermolecular interaction indicated by their crystal structures. Thus, the properties of Ni complexes in the solid state as well as device performances were not studied further. Thin films of BP derivatives except for Ni complexes were prepared by spin-coating of precursors on glass substrates followed by thermal annealing at 180 °C for 30 min. All absorption spectra are broader and red-shifted about 60–80 nm compared with those of absorption spectra in solutions. The offset absorption

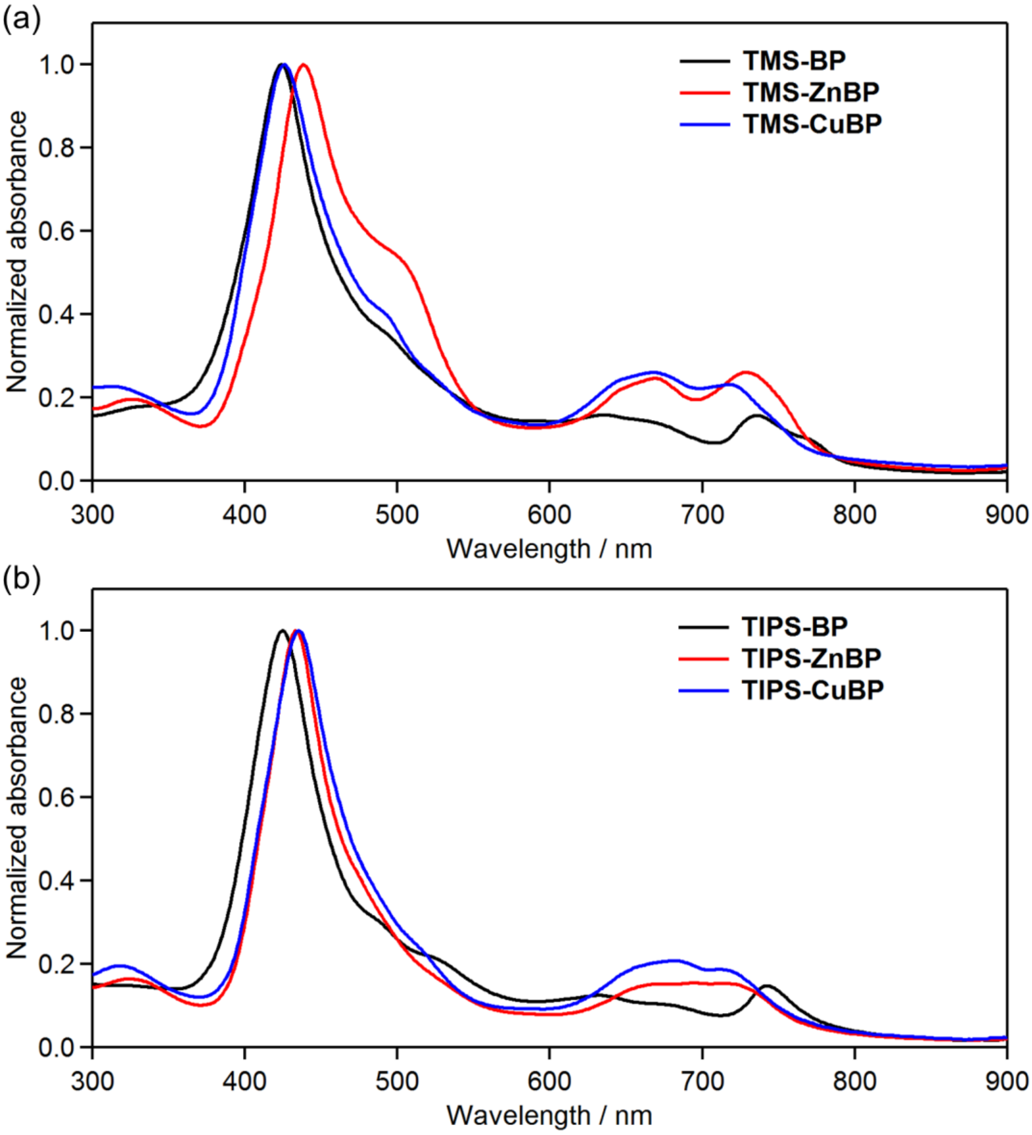

Figure 2-8. Absorption spectra of (a) TMS- and (b) TIPS-BPs as thin-films.

edges of TMS- and TIPS-BPs films are around 770–780 nm which are red-shifted about 50–60 nm from that of pristine BP (Figure S2-8b). This absorption red-shift phenomenon in both solution and film states indicates that the substitution of ethynyl groups at 5- and 15-position of a BP framework is effective for π-expansion.

In terms of organic electronic devices, determining the HOMO (E_{HOMO}) and LUMO (E_{LUMO}) levels of materials in the solid state are important. For OFETs, the positional relation between the energy levels of organic semiconductors (E_{HOMO} and E_{LUMO}) and work function of metal electrodes decides the type of OFET such as p-, n-type, or ambipolar OFETs.[29,30] If the E_{HOMO} or E_{LUMO} of organic semiconductors are much different from the work function of metal electrodes, the injection of holes or electrons is not available to work as OFETs.[31] In the case of OPVs, V_{OC} is proportional to the offset between E_{HOMO} of donors and E_{LUMO} of acceptors.[32]

To determine the E_{HOMO} of compounds, ionization energy of thin films was measured by photoelectron spectroscopy in air (Figure 2-9) and the results are summarized in Table 2-2. The E_{LUMO} were calculated by adding the optical energy gaps of thin films (E_{g}) to the E_{HOMO}. The E_{g} were determined from the absorption onset of the thin-films. E_{HOMO} of TMS-BPs are –4.72 to –4.77 eV which are 0.12–0.17 eV higher than that of BP (–4.89 eV), whereas E_{HOMO}s of TIPS-BPs are –4.89 to –4.94 eV which are similar to that of BP. E_{LUMO}s of TMS-BPs are

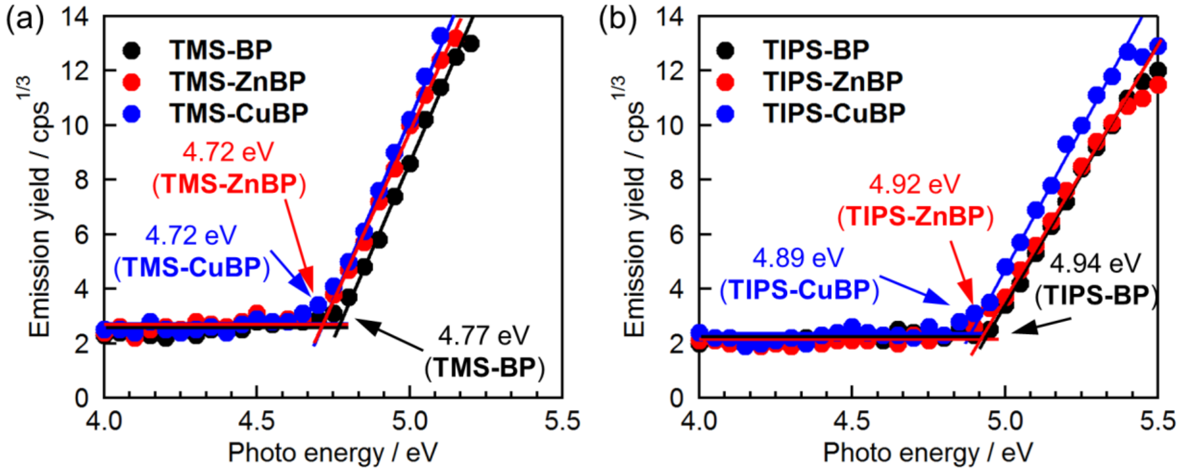

Figure 2-9. Photoelectron spectra of compounds.

similar with that of BP, while the E_{LUMO}s of TIPS-BPs are lower than that of BP (ca. 0.1 eV).

To understand the difference of E_{HOMO} between TMS-BPs and TIPS-BPs in the solid state, the author estimated the E_{HOMO}s for the packing motifs obtained from their single-crystal structures by density functional theory (DFT) calculation. The results of calculations are shown in Figure 2-10. The E_{HOMO}s of both TMS-BP and TIPS-BP are similar in single-molecular state. However, the E_{HOMO}s of TMS-BP are getting higher with increasing the neighboring π-stack columns, while the E_{HOMO}s of TIPS-BP are not changing. The π-stack columns in TMS-BP crystal have contacts with π-frameworks in neighboring π-stack columns to interact HOMO making its E_{HOMO} is higher, while the π-stack columns in the TIPS-BP crystal do not have contacts each other. Since the each π-stack column in the TIPS-BP crystal is separated by insulating TIPS-groups (Figure 2-5). Thus, the author presumes that this E_{HOMO} difference caused by the difference of packing motifs. Thus, the difference of crystal structure induces the different E_{HOMO}s in the solid state.

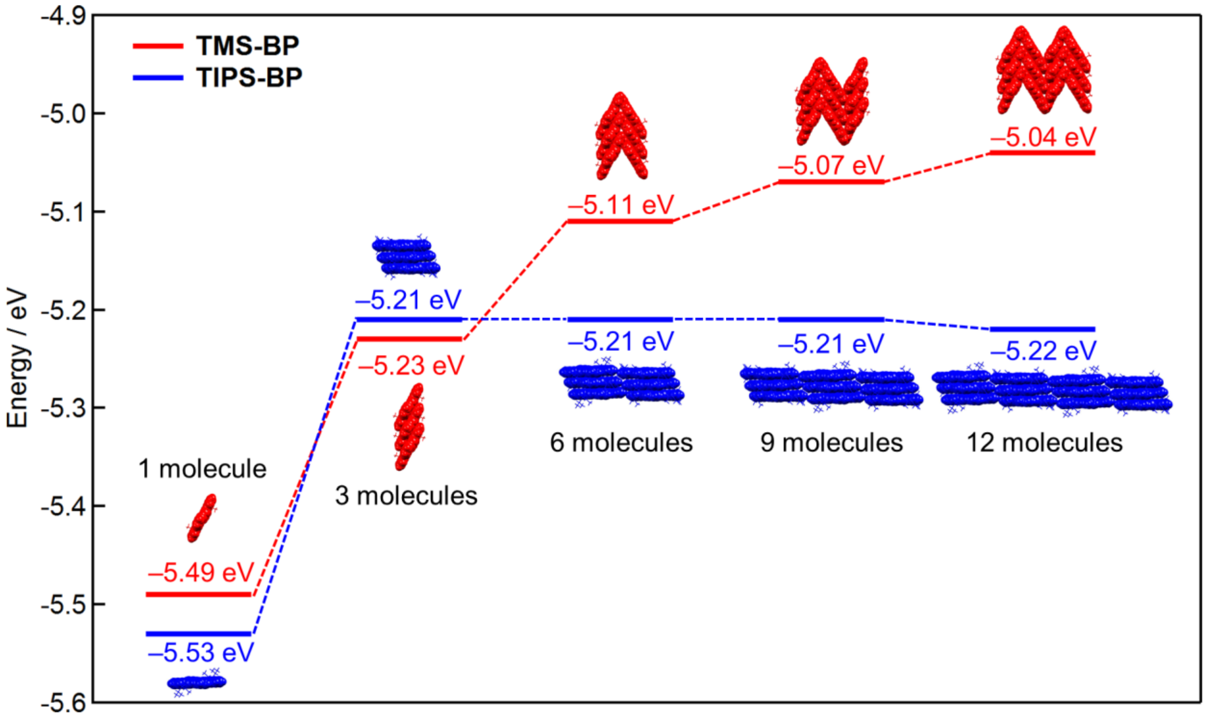

Figure 2-10. Energy diagram of E_{HOMO}s obtained from DFT calculation (CAM-B3LYP/6-31G(d)) for packing motifs of TMS-BP and TIPS-BP. Red and blue molecules indicate TMS-BP and TIPS-BP molecules, respectively.

2-5. Fabrication and Evaluation of OFETs

OFET devices comprising the free-base, the corresponding zinc(II), and copper(II) complexes of TMS-BP and TIPS-BP have been fabricated to investigate the effect of the substituents and metalation on the charge-carrier transport property. Fabrication and evaluation of OFET devices of this chapter was conducted by Mr. Naoya Yamada of Prof. Nakayama's group in Yamagata University. TIPS-substituted compounds (TIPS-BP, TIPS-ZnBP and TIPS-CuBP) are soluble in organic solvents, while the solubility of TMS-substituted compounds (TMS-BP, TMS-ZnBP and TMS-CuBP) are too low to deposit the active layer by solution processes. Thus, the active layers were deposited by precursor approach to compare the OFET performance between TMS- and TIPS-BPs in the same deposition process. The active layers of OFET were prepared by heating thin-films which were fabricated by spin-coating of the corresponding precursors on 300 nm-thick SiO_2 dielectric layers above the n-doped Si substrates. Source–drain electrodes of gold were deposited on organic active layers by vacuum deposition to fabricate bottom-gate-top-contact OFETs (Figure 2-11).

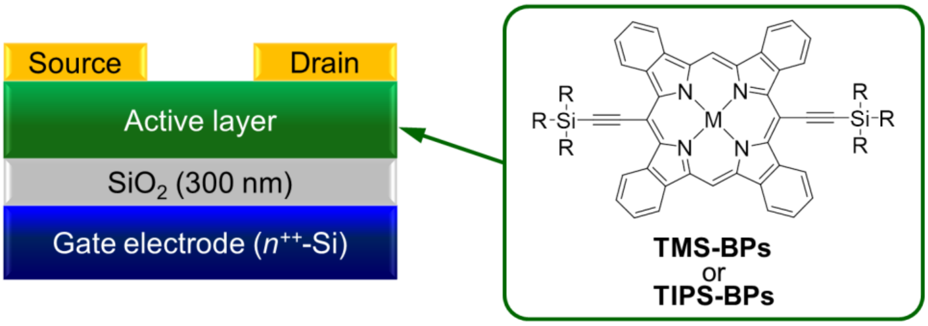

Figure 2-11. Device structure of OFET.

Performance and parameters of each OFET device are summarized in Table 2-3. The best μ_h of 0.12 $cm^2\ V^{-1}\ s^{-1}$ was obtained in an OFET based on TMS-BP, which is higher than the previously reported bottom-gate-bottom-contact OFET of BP by a factor of 2.[4] The transfer and output curves of this OFET device are shown in Figure 2-12 and others are shown in

Table 2-3. Summary of OFET parameters of TMS- and TIPS-BPs.

Compounds	μ_h / cm^2 V^{-1} s^{-1}	I_{on} / I_{off}	V_{th} / V
TMS-BP	0.12	2.4×10^6	–13.0
TMS-ZnBP	9.2×10^{-5}	2.8×10^1	27.5
TMS-CuBP	5.0×10^{-4}	9.4×10^4	–12.5
TIPS-BP	4.8×10^{-5}	4.3×10^4	–18.4
TIPS-ZnBP	1.3×10^{-5}	6.6×10^3	–1.5
TIPS-CuBP	5.7×10^{-3}	8.9×10^6	–8.2

Figure S2-9 and S2-10. The μ_h of TMS-ZnBP and TMS-CuBP are much lower than that of TMS-BP even though their crystal structures are similar. On the other hand, the μ_h of all TIPS-BPs (10^{-3} to 10^{-5} cm^2 V^{-1} s^{-1}) are much lower than that of TMS-BP. The μ_h of TIPS-CuBP is higher than those of TIPS-BP and TIPS-ZnBP by two orders.

To understand what kind of factors affect the μ_h of OFET among this system, the X-ray diffraction (XRD) patterns of the films were measured (Figure 2-13, Table 2-4) by Mr. Naoya Yamada in Prof. Nakayama’s group in Yamagata University.

The XRD patterns of TMS-BP, TMS-ZnBP, and TMS-CuBP neat films are similar each other indicating that their crystal stuctures and molecular orientations are similar as observed in single-crystal structures (Figure 2-4). However, these peaks are not overlaped with the simulated poweder patterns from their single-crystal structures, indicating that their thin-film

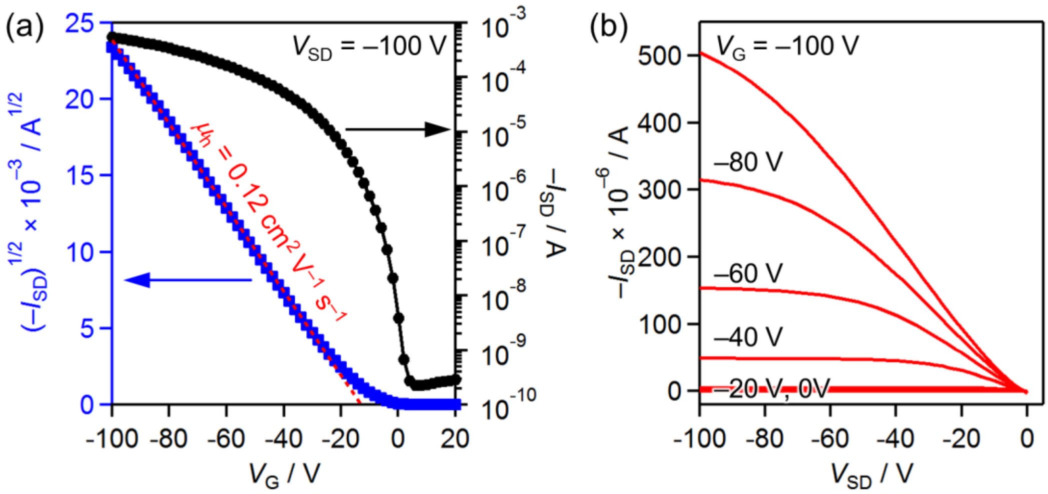

Figure 2-12. (a) Transfer and (b) output curves of an OFET of TMS-BP.

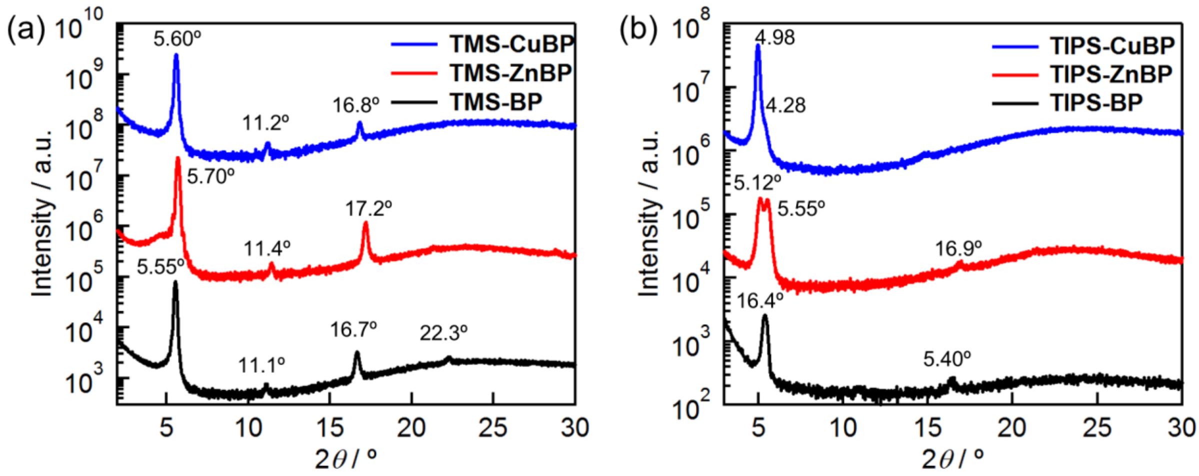

Figure 2-13. Out-of-plane XRD patterns of (a) TMS-BPs and (b) TIPS-BPs neat film prepared by the same conditions with OFET.

crystal structures are different from bulk single crystal structures (Figure S2-11). In the case of TIPS-BPs, the intensities of their primary peaks were smaller than those of TMS-BPs (Figure S2-12) indicating that the crystallinity of TIPS-BPs is lower than that of TMS-BPs. In contrast to the case of TMS-BPs, XRD patterns of TIPS-BPs are similar with their simulated powder patterns of bulk single-crystal sturctures (Figure S2-13), indicating the thin-film crystal stuctures and bulk single-crystal structures of TIPS-BPs are similar or same. The errors of the degrees between observed primary peaks and simulated 001 planes are 0.17° (TIPS-BP), 0.06° (TIPS-ZnBP), and 0.08° (TIPS-CuBP), respectively. Such minor differences between single-crystal and thin-film packings are sometimes observed for ornigac molecular crystals.[33,34] Observation of the peaks from 001 planes in out-of-plane XRD measurement

Table 2-4. Summary of XRD parameters of TMS- and TIPS-BPs.

Compounds	$2\theta^a$ / °	d / Å	Normalized peak area	D / nm
TMS-BP	5.55	15.9	0.604	86.5
TMS-ZnBP	5.70	15.5	1.00	78.5
TMS-CuBP	5.60	15.8	0.388	79.5
TIPS-BP	5.40	16.4	0.029	51.1
TIPS-ZnBP	5.12	17.3	0.165	47.2
TIPS-CuBP	4.98	17.7	0.380	74.2

[a] Angles of primary peaks. Active layers were prepared by spin-coating (1000 rpm, 40 s) a chloroform solution of CP (7.0 mg mL^{-1}) followed by thermal annealing at 180 °C for 30 min.

indicates that 001 planes are excisted in parallel to substrates, namely, TIPS-BPs adopt end-on mode (Figure S2-14).

To extract deeper insights from XRD patterns, the peak area and size of TMS-BPs and TIPS-BPs crystallites (D) were extracted. The peak area indicates a relative measure of the crsytallite volume within the film.[35] D can be estimated from the full-width at half-maximum (FWHM) of the respective XRD peaks using Scherrer's equation[36] $D = (K\lambda)/(\beta \cos\theta)$, where K is the shape factor (normally assumed to be 0.89), λ is the incidnt X-ray wavelength, β is the FWHM in radians of the XRD peak, and θ is the diffaction agnle. The peak area and FWHM were observed from gaussian fitting of XRD patterns. The plot of the μ_hs, peak areas, and Ds is shown in Figure 2-14. The μ_hs are correlated with both the peak areas and Ds and, namely, the crystallite volumes and sizes of compounds. Ds are more correlated with the μ_hs than peak areas (Figure 2-14). Noguchi et al. reported the crytallite sizes of pristine BP are correlated with the μ_hs of OFET.[4]

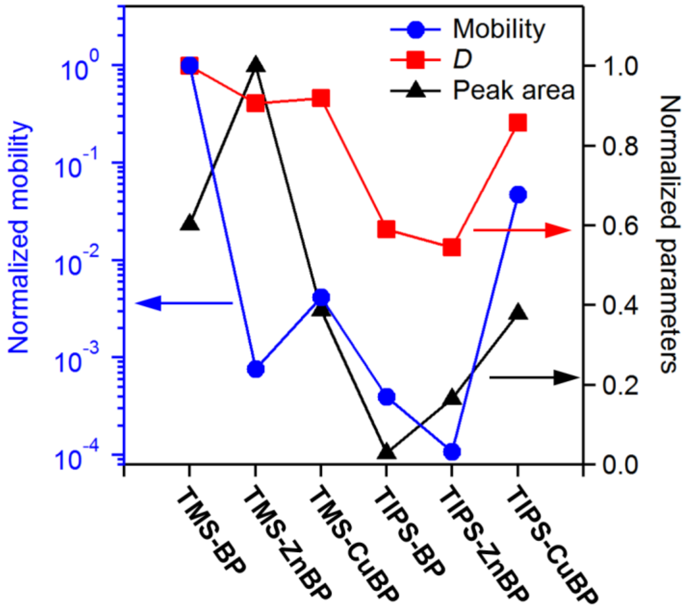

Figure 2-14. Plot of μ_hs, normalized peak areas, and Ds of XRD peaks.

2-6. Fabrication and Evaluation of OPVs

To investigate substituents and metalation effect of BP derivatives on the photovoltaic performance, solution-processed BHJ OPVs have been fabricated and evaluated comprising TMS-BPs and TIPS-BPs as p-type materials with $PC_{71}BM$ as an n-type material (Figure 2-15). Fabrication and evaluation of OPV devices as well as their XRD patterns and AFM images were measured by Mr. Naoya Yamada of Prof. Nakayama's group in Yamagata University.

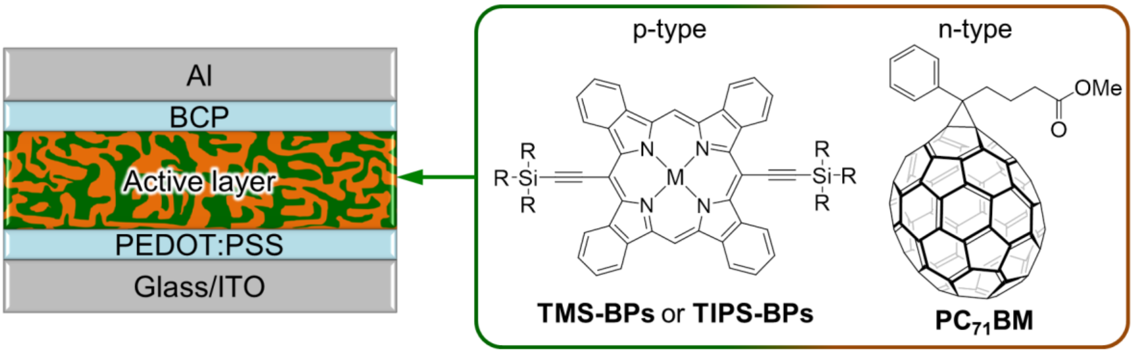

Figure 2-15. Device structure of BHJ OPV and active components.

The current density–voltage (J–V) curves, external quantum efficiency (EQE) spectra, and absorption spectra of OPV devices of TMS-BP:$PC_{71}BM$ and TIPS-BP:$PC_{71}BM$ are shown in Figure 2-16 and summarized in Table 2-5. When the TMS-BP:$PC_{71}BM$ film was annealed at 160 ºC, a PCE of 0.33% was obtained. By increasing the annealing temperature to 180 ºC, PCE was improved to 1.09% with J_{SC} = 5.07 mA cm^{-2}, V_{OC} = 0.48 V and fill factor (FF) = 0.40. However, further increase of the annealing temperature to 200 ºC resulted in a decreased PCE of 0.47%. The TIPS-BP:$PC_{71}BM$ system showed a similar tendency to TMS-BP:$PC_{71}BM$ and the highest PCE of 0.97% was obtained by annealing at 180 ºC. The other annealing temperatures (160 and 200 ºC) gave lower PCE values (0.57% and 0.19%). The TMS-BP:$PC_{71}BM$ and TIPS-BP:$PC_{71}BM$ devices are comparable in J_{SC} and FF values, while the V_{OC} values of TMS-BP:$PC_{71}BM$ (0.47–0.48 V) system are lower than those of TIPS-BP:$PC_{71}BM$ (0.53–0.66 V) reflecting the relationship of their E_{HOMO}s. The both EQE

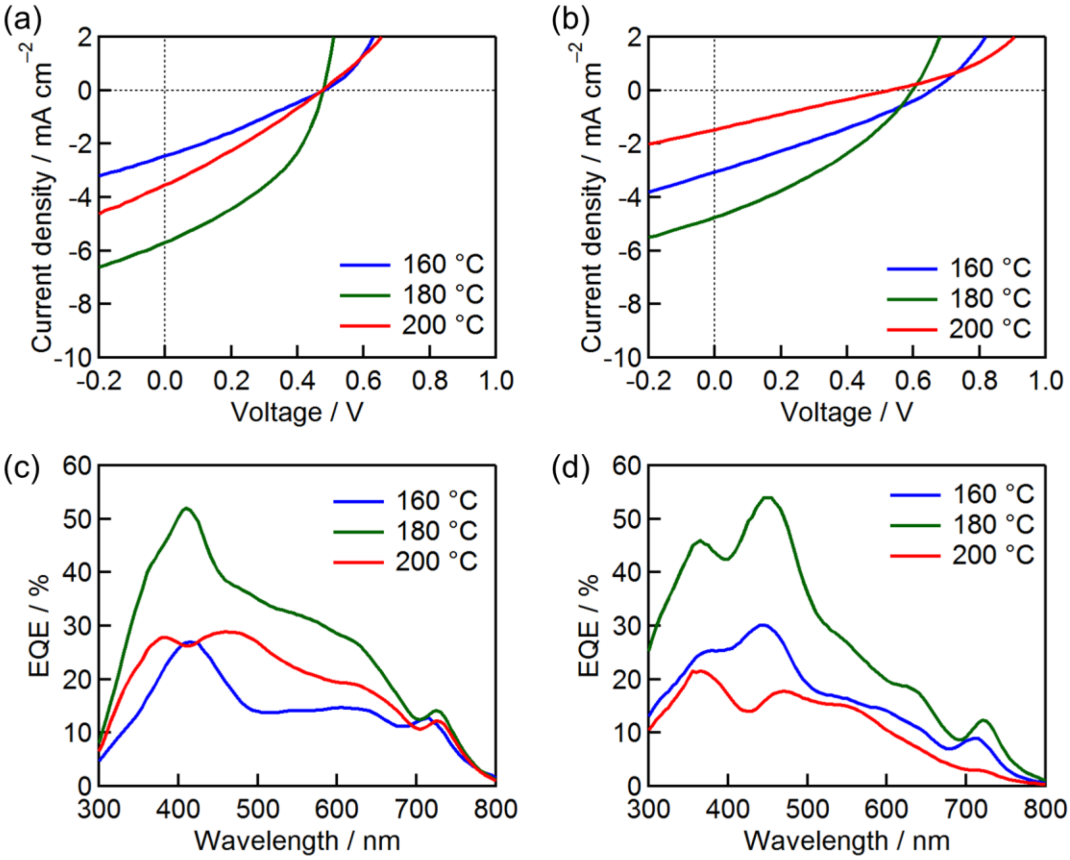

Figure 2-16. (a) *J*–*V* curves and (b) EQE spectra of OPVs based on TMS-BP:PC$_{71}$BM. (c) *J*–*V* curves and (d) EQE spectra of OPVs based on TIPS-BP:PC$_{71}$BM.

Table S2-5. Performance of OPVs with different annealing temperatures.

p-type materials	Annealing temperature / ºC	J_{SC} / mA cm^{-2}	V_{OC} / V	FF	PCE / %
TMS-BP	160	2.46	0.48	0.28	0.33
	180	5.70	0.48	0.40	1.09
	200	3.53	0.47	0.28	0.47
TIPS-BP	160	3.06	0.66	0.29	0.57
	180	4.75	0.60	0.34	0.97
	200	1.47	0.53	0.24	0.19

spectra of TMS-BP:PC$_{71}$BM and TIPS-BP:PC$_{71}$BM OPVs prepared by annealing at 180 ºC are higher than those of OPVs prepared by other annealing temperatures (160 and 200 ºC) (Figure 2-16b,e).

Surface morphology and molecular ordering of active-layers in these devices were investigated by out-of-plane XRD and tapping-mode AFM. Figure 2-17 shows the AFM images of TMS-BP:PC$_{71}$BM and TIPS-BP:PC$_{71}$BM blend films. The AFM images of

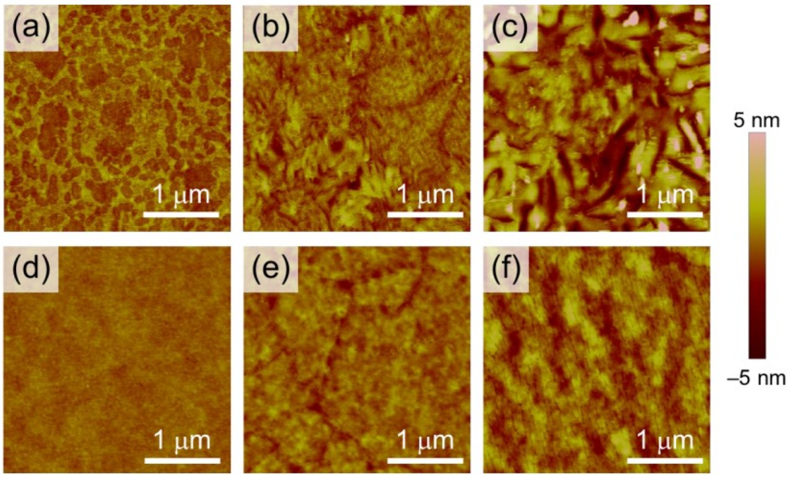

Figure 2-17. Tapping mode AFM images of TMS-BP:PC$_{71}$BM blend films annealing at (a) 160, (b) 180, and (c) 200 °C. Tapping mode AFM images of TIPS-BP:PC$_{71}$BM blend films annealing at (d) 160, (e) 180, and (f) 200 °C.

TMS-BP:PC$_{71}$BM blend films indicate that several hundred of nanometers to 1 µm-sized large domains were formed in all blend films deposited by all annealing temperatures.

In particular, domains as large as 1 µm and large valleys were observed for the TMS-BP:PC$_{71}$BM blend film annealed at 200 ºC. In contrast, the TIPS-BP:PC$_{71}$BM blend films annealed at 160 and 180 ºC show smooth surfaces. In the case of the blend film annealed at 200 ºC, cracks were notably observed on the surface of the blend film (Figure 2-17f). These cracks were also observed in the neat films of TIPS-BP indicating the thin-film of TIPS-BP prepared by a precursor approach tends to form cracks (Figure S2-15). Since these cracks were observed in the blend film which showed the worst PCE among TMS-BP and TIPS-BP systems, it is indicated that these cracks have a significant bad influence for the performance of OPV.

Figure 2-18 and Table 2-6 show XRD patterns and their parameters of the TMS-BP:PC$_{71}$BM and TIPS-BP:PC$_{71}$BM blend films. Diffracted primary peaks are observed at around 2θ = 5.42–5.55º for both TMS-BP:PC$_{71}$BM and TIPS-BP:PC$_{71}$BM blend films annealed at 180 and 200 ºC, while the blend films annealed at 160 °C showed no specific peaks. This observation indicates that TMS-BP and TIPS-BP crystallize over 180 ºC, while

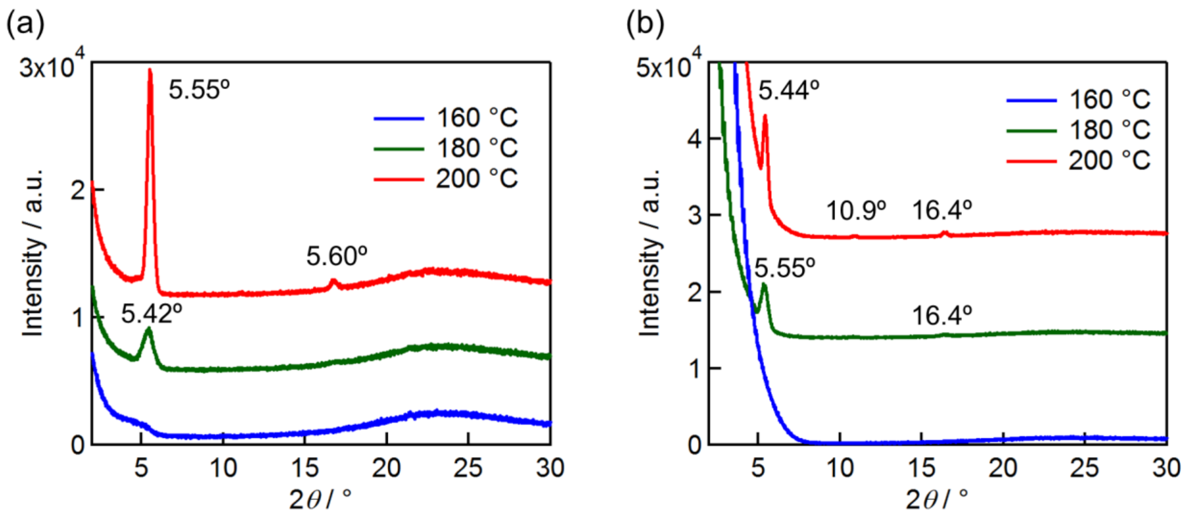

Figure 2-18. XRD patterns of (a) TMS-BP:PC$_{71}$BM blend films and (b) TIPS-BP:PC$_{71}$BM blend films annealing at different temperature.

Table 2-6. Summary of XRD parameters of TMS- and TIPS-BPs blend films.

p-type materials	Annealing temperature / °C	$2\theta^a$ / °	d / Å	D / nm
TMS-BP	160	–	–	–
	180	5.42	16.3	22
	200	5.55	15.9	38
TIPS-BP	160	–	–	–
	180	5.31	16.6	16
	200	5.30	16.7	49

[a] Angles of primary peaks.

they don't crystallize by annealing at 160 °C to afford amorphous films. By increasing annealing temperature 180 °C to 200 °C, the peak intensities of primary peaks are getting larger, indicating that higher annealing temperature promotes the crystallization of TMS-BP.[37]

In the case of TIPS-BP:PC$_{71}$BM films annealed at 180 and 200 °C, diffraction peaks are observed at 5.44° and 5.55°, respectively. These peaks correspond to the diffraction from a 001 plane of TIPS-BP as observed for the TIPS-BP neat film and its simulated powder XRD pattern (Figure S2-13a). This observation indicates that the dominant molecular orientation of TIPS-BP in active layer is edge-on which is not suitable for OPV.[38,39] The *D*s of TMS-BP and TIPS-BP were extracted from their primary peaks of blend films in XRD patterns. The extracted *D*s of TMS-BP and TIPS-BP annealed at 200 °C are 38.2 and 48.6 nm, respectively.

These *D*s are larger than those of TMS-BP (22 nm) and TIPS-BP (16 nm) annealing at 180 °C. Considering the L_D of BP is 15 nm,[16] the *D*s in the blend films annealed at 200 °C of both TMS-BP and TIPS-BP are too large for the efficient charge separation. Thus, the PCEs of OPVs annealing at 200 °C are lower than those of 180 °C.

The OPV using TMS-ZnBP or TIPS-ZnBP as a p-type material with $PC_{71}BM$ as an n-type material was also fabricated and evaluated. The results are shown in Figure 2-19 and summarized in Table 2-7.

The best PCE of 1.51% was attained with the highest J_{SC} (7.60 mA cm^{-2}) and FF (0.42) in a OPV based on TMS-ZnBP:$PC_{71}BM$ among the BP compounds in this chapter. The best annealing temperature for TMS-ZnBP:$PC_{71}BM$ and TIPS-ZnBP:$PC_{71}BM$ are 200 ºC and 180 °C, respectively. J_{SC} and FF values of both TMS-ZnBP and TIPS-ZnBP were the higher than those of free-base compounds. The V_{OC} values of TMS-ZnBP and TIPS-ZnBP were

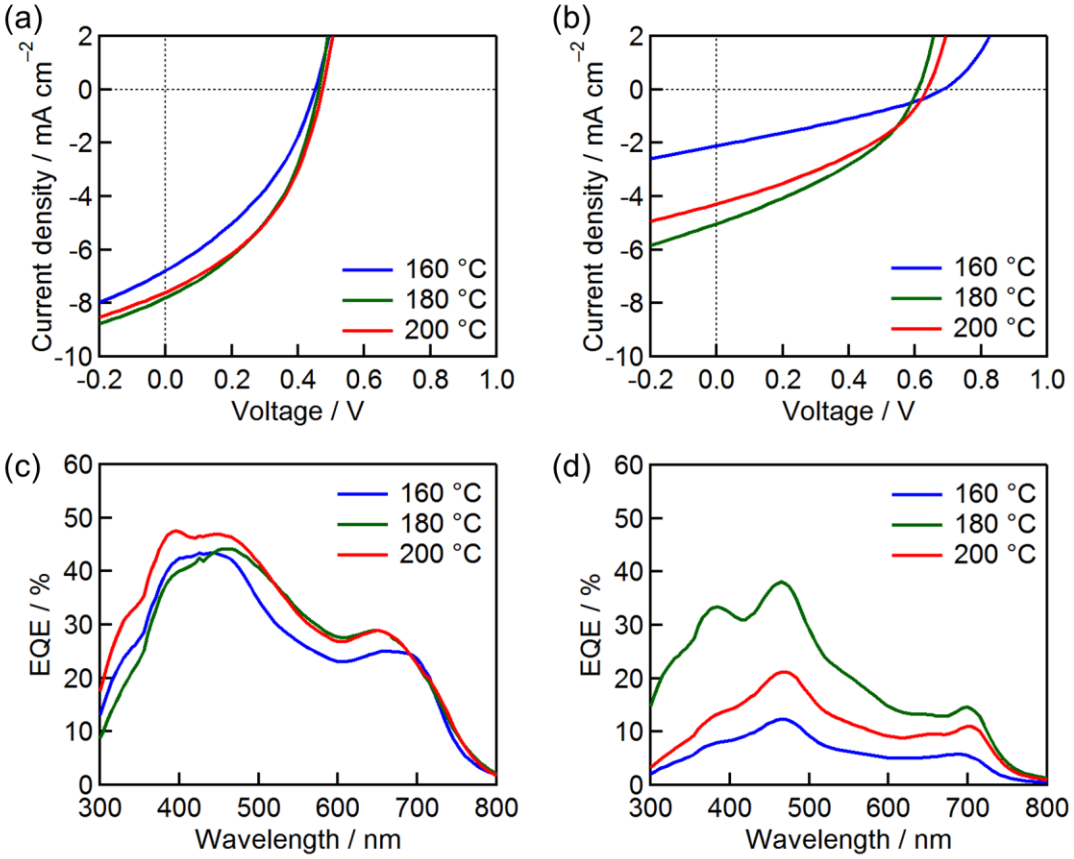

Figure 2-19. (a) *J*–*V* curves and (b) EQE spectra of OPVs based on TMS-ZnBP:$PC_{71}BM$. (c) *J*–*V* curves and (d) EQE spectra of OPVs based on TIPS-ZnBP:$PC_{71}BM$.

Table 2-7. Performance of OPVs based on TMS-ZnBP:PC$_{71}$BM and TIPS-BP:PC$_{71}$BM with different annealing temperatures.

p-type materials	Annealing temperature / °C	J_{SC} / mA cm^{-2}	V_{OC} / V	FF	PCE / %
TMS-ZnBP	160	6.79	0.45	0.37	1.13
	180	7.81	0.46	0.41	1.49
	200	7.60	0.47	0.42	1.51
TIPS-ZnBP	160	2.12	0.68	0.30	0.44
	180	5.03	0.61	0.37	1.13
	200	4.29	0.64	0.36	0.99

comparable to those of TMS-BP and TIPS-BP, reflecting the E_{HOMO}s of zinc complexes are similar to that of free-base compounds. TIPS-ZnBP also showed the PCE of 1.13% with the improvement of the PCE compared with that of TIPS-BP.

Figure 2-20 shows the AFM images of TMS-ZnBP:PC$_{71}$BM and TIPS-ZnBP:PC$_{71}$BM blend films. The surface of TMS-ZnBP:PC$_{71}$BM blend film prepared by annealing at 160 °C is very smooth. By increasing annealing temperature to 180 °C and 200 °C, relatively finer grains are observed without forming large aggregation and valleys as observed in a TMS-BP:PC$_{71}$BM system. In the case of TIPS-ZnBP, the surface of the blend film annealed at 160 °C is also smooth, while the blend films annealed at 180 °C shows sharp and clear shaped grains. By increasing annealing temperature from 180 °C to 200 °C, these grains grow larger to be a few hundred nanometers.

Molecular ordering in active-layers of these devices was investigated by out-of-plane XRD. Figure 2-21 and Table 2-8 show XRD patterns and their parameters of the TMS-ZnBP:PC$_{71}$BM and TIPS-ZnBP:PC$_{71}$BM blend films. Diffracted primary peaks are observed at around $2\theta = 5.03$–5.56° for both TMS-ZnBP:PC$_{71}$BM and TIPS-ZnBP:PC$_{71}$BM blend films annealed at 180 and 200 ºC, while the blend films annealed at 160 °C showed no specific peaks at around $2\theta = 5$–6°. However, there are diffracted peaks at round $2\theta = 9.1$–9.4° in all blend films which can be assigned as a peak from 110 plane of PC$_{71}$BM (Figure S2-16).[40] These peaks were not observed in free-base and copper complexes of blend films. This observation indicates that zinc complexes mixing with PC$_{71}$BM induce the

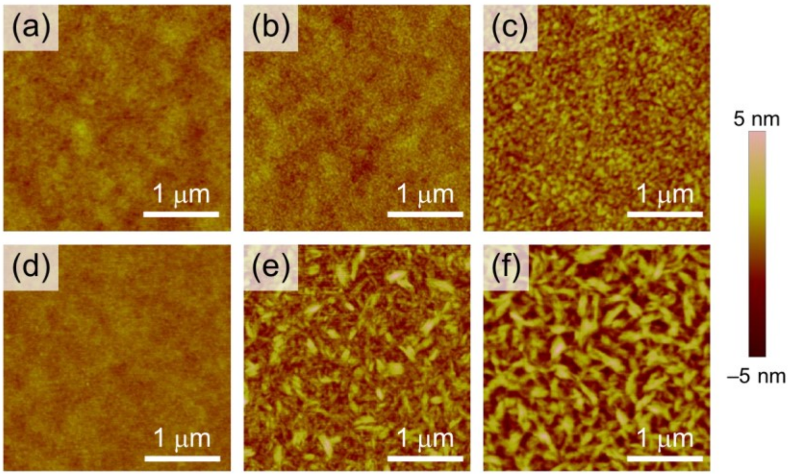

Figure 2-20. Tapping mode AFM images of TMS-ZnBP:$PC_{71}BM$ blend films annealing at (a) 160, (b) 180, and (c) 200 °C. Tapping mode AFM images of TIPS-ZnBP:$PC_{71}BM$ blend films annealing at (d) 160, (e) 180, and (f) 200 °C.

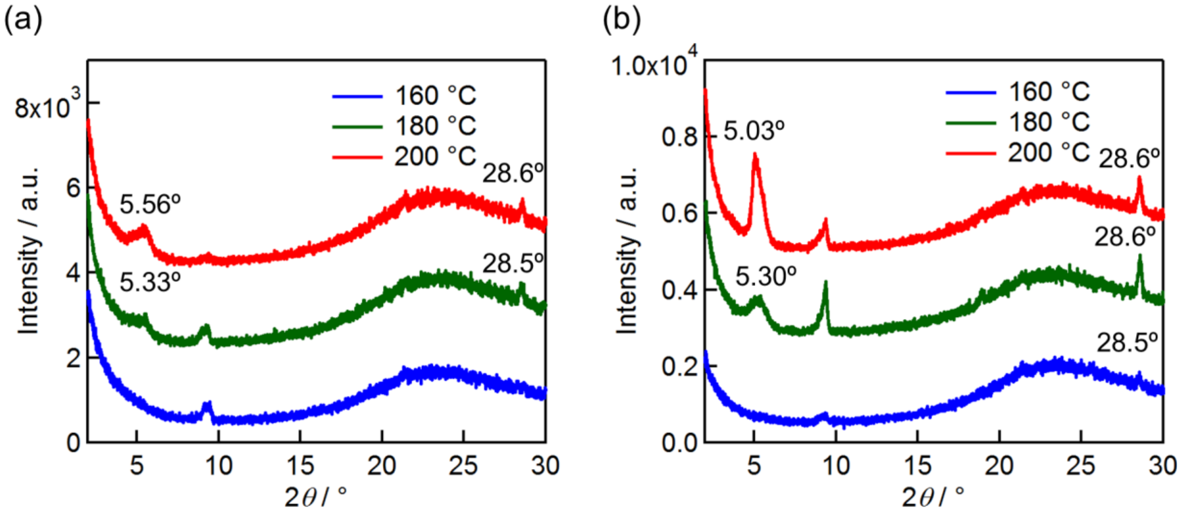

Figure 2-21. XRD patterns of (a) TMS-ZnBP:$PC_{71}BM$ blend films and (b) TIPS-ZnBP:$PC_{71}BM$ blend films annealing at different temperature.

Table 2-8. Summary of XRD parameters of TMS- and TIPS-ZnBPs blend films.

p-type materials	Annealing temperature / ºC	$2\theta^a$ / °	*d* / Å	*D* / nm
TMS-ZnBP	160	–	–	–
	180	5.33	16.6	14
	200	5.56	15.9	23
TIPS-ZnBP	160	–	–	–
	180	5.31	16.6	16
	200	5.03	17.6	49

[a] Angles of primary peaks.

crystallization of $PC_{71}BM$. In addition, the peaks correspond to the π–π stacking ($2\theta = 28.5$–28.6°, $d = 3.12$–3.13 Å) were observed in the blend films of both TMS-ZnBP:$PC_{71}BM$ and TIPS-ZnBP:$PC_{71}BM$ blend films prepared by annealing at 180 °C and 200 °C. The J_{SC} and FF improvement of zinc complexes from that of free-base compounds is probably due to form the π–π stacking crystallites of BP compounds and $PC_{71}BM$ crystallites in the out-on-plane direction. The Ds of TMS-ZnBP and TIPS-ZnBP were extracted from primary peaks in XRD patterns. The Ds of TMS-ZnBP:$PC_{71}BM$ blend films were getting larger with incresing annealing temperature, but the D in the blend film anneaeled at 200 °C (23 nm) is smaller than that of free-base compounds annealed at 200 °C (38 nm). On the other hand, Ds of TIPS-BP:$PC_{71}BM$ blend films annealed at 180 °C and 200 °C are 16 nm and 49 nm, respectively. Thus, the D of TIPS-ZnBP crystallite in the blend film annealed at 180 °C is more favorable than that of 200 °C. Thus, the best annealing temperture for TIPS-ZnBP:$PC_{71}BM$ system is 180 °C.

The OPVs comprising TMS-CuBP:$PC_{71}BM$ and TIPS-CuBP:$PC_{71}BM$ blends were also fabricated. The results are shown in Figure 2-22 and summarized in Table 2-9. The best PCE values of 0.72 and 0.86% were respectively obtained for TMS-CuBP and TIPS-CuBP devices annealed at 160 °C. The J_{SC} values of copper complexes are lower than those of free-base and zinc complexes. In the J–V curve of copper complexes, leakage currents are observed in the reverse bias region, indicating the bad film quality. In EQE spectra of TMS-CuBP, the quantum yields are lower with increasing annealing temperature.

AFM images of copper complexes are shown in Figure 2-23. On contrast to the blend films of free-base and zinc complexes, a few hundred nanometers to 1 μm-sized of domains are observed in all the blend film of TMS-CuBP:$PC_{71}BM$, indicating that TMS-CuBP tends to form large aggregation compared to those of free-base and zinc complexes. On the other hand, the blend films of TIPS-CuBP:$PC_{71}BM$ are much smoother than those of TMS-CuBP:$PC_{71}BM$ blend.

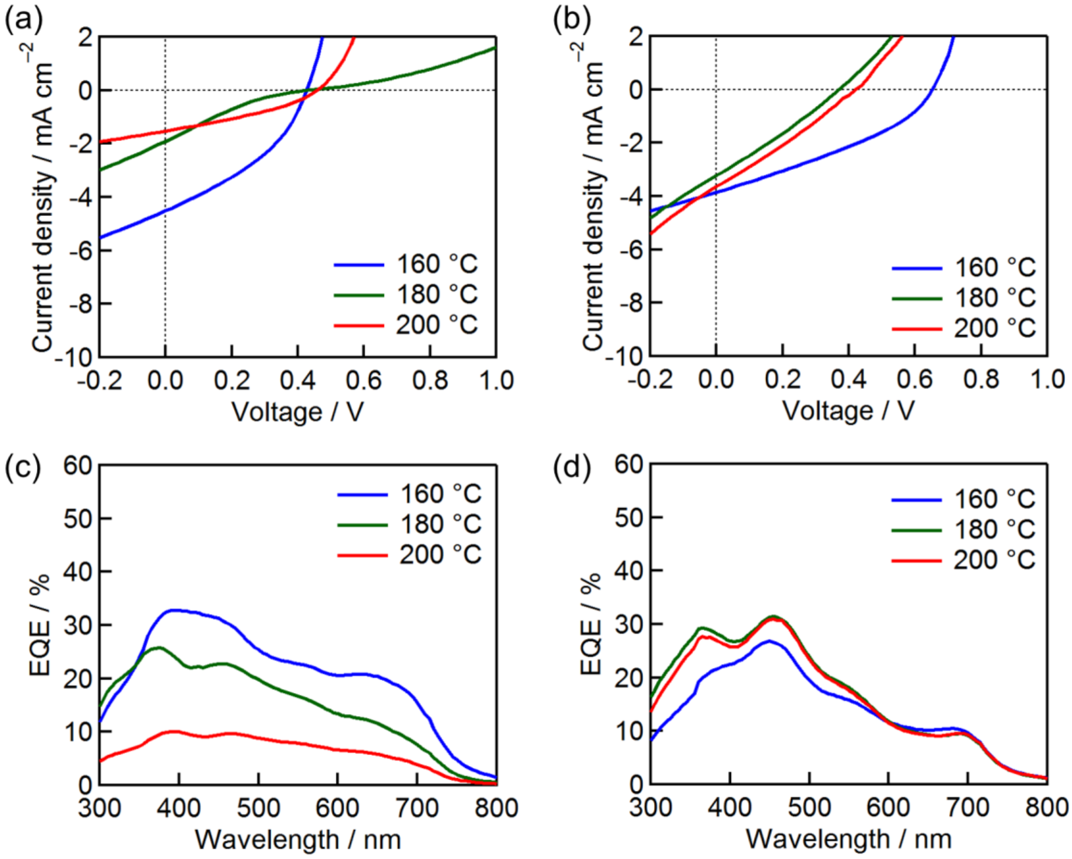

Figure 2-22. (a) *J*–*V* curves and (b) EQE spectra of OPVs based on TMS-CuBP:PC$_{71}$BM. (c) *J*–*V* curves and (d) EQE spectra of OPVs based on TIPS-CuBP:PC$_{71}$BM.

Table 2-9. Performance of OPVs based on TMS-CuBP:PC$_{71}$BM and TIPS-CuBP:PC$_{71}$BM with different annealing temperatures.

p-type materials	Annealing temperature / °C	J_{SC} / mA cm^{-2}	V_{OC} / V	FF	PCE / %
TMS-CuBP	160	4.51	0.43	0.38	0.72
	180	1.83	0.43	0.18	0.14
	200	1.49	0.42	0.30	0.19
TIPS-CuBP	160	3.85	0.65	0.34	0.86
	180	3.22	0.37	0.28	0.33
	200	3.64	0.42	0.28	0.42

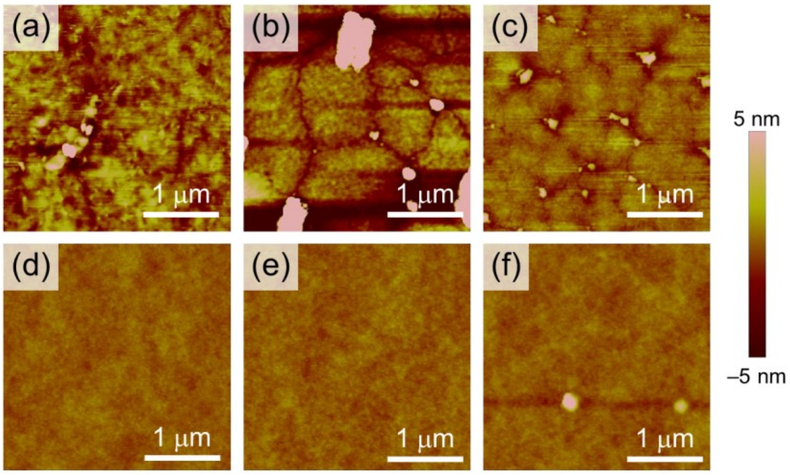

Figure 2-23. Tapping mode AFM images of TMS-CuBP:PC$_{71}$BM blend films annealing at (a) 160, (b) 180, and (c) 200 °C. Tapping mode AFM images of TIPS-CuBP:PC$_{71}$BM blend films annealing at (d) 160, (e) 180, and (f) 200 °C.

XRD patterns and their parameters of copper complexes are shown in Figure 2-24 and Table 2-10, respectively. In the XRD patterns of TMS-CuBP blend films annealed at 160 °C, a primary peak at $2\theta = 5.43°$. By increasing the annealing temperature to 180 °C, the intensity of the primary peak is weaker than that of the blend film annealed at 160 °C despite the larger grains are observed in an AFM image (Figure 2-23b). By increasing annealing temperature to 200 °C, there are no specific peaks in XRD patterns indicating the films are amorphous. In the XRD patterns of TIPS-CuBP blend films, only the blend film annealing at 160 °C shows a primary peak at $2\theta = 5.55$ but the intensity of this peak is weaker than that of TMS-CuBP. According to these results, the copper complexes tend to have lower crystallinity and form larger aggregations compared to those of free-base and zinc complexes resulting their J_{SC} and PCEs are lower than those of free-base and zinc complexes. It is also noteworthy that the L_D of a copper tetrabenzoporphyrin is shorter than that of the free-base BP.[22] This shorter L_D is also one of the reason for the lowest photovoltaic performance of copper complexes among this system.

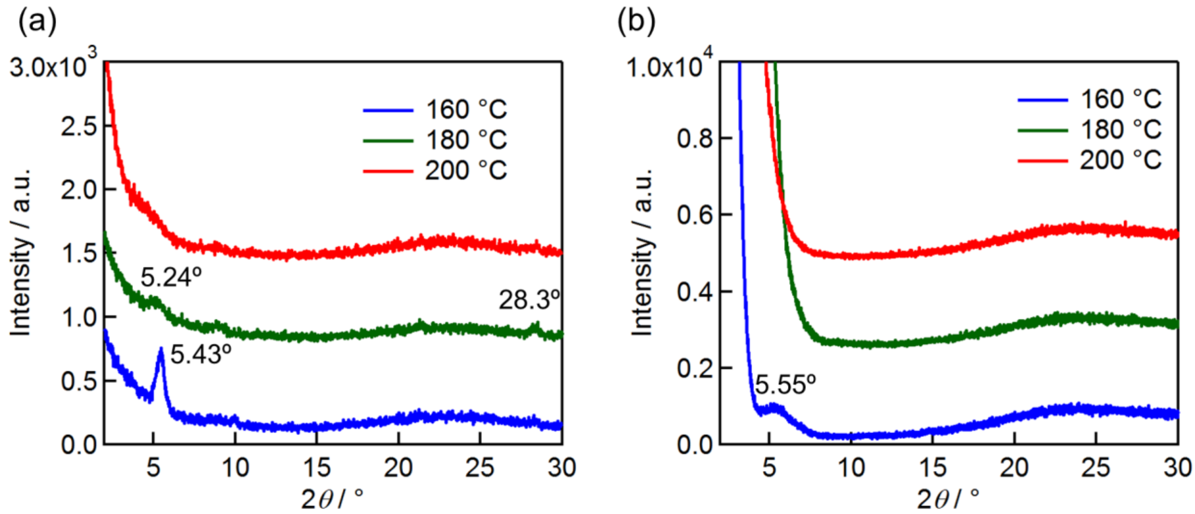

Figure 2-24. XRD patterns of (a) TMS-CuBP:$PC_{71}BM$ blend films and (b) TIPS-CuBP:$PC_{71}BM$ blend films annealing at different temperature.

Table 2-10. Summary of XRD parameters of TMS-BPs and TIPS-CuBPs blend films.

p-type materials	Annealing temperature / °C	$2\theta^a$ / °	*d* / Å	*D* / nm
TMS-CuBP	160	5.43	16.3	28
	180	5.33	16.6	14
	200	–	–	–
TIPS-CuBP	160	5.55	15.9	10
	180	–	–	–
	200	–	–	–

[a] Angles of primary peaks.

Summarizing the results of OPV, zinc complexes show the best OPV performance compared to those of free-base and copper complexes, because of forming π– π stacking and $PC_{71}BM$ crystallites, moderate crystal sizes, and good film morphology. Free-base compounds have the highest crystallinity to form large grains to afford moderate OPV performance. Copper complexes tend to form large aggregations and show low crystallinity showing the lowest OPV performance. It is indicated that the free-base and zinc complexes of BP derivatives are more suitable for the OPV materials than the copper complexes.

2-7. Summary

In summary, we have succeeded in the preparation of 5,15-bis(alkylsilylethynyl)tetrabenzoporphyrins (TMS-BP and TIPS-BP) and their metal complexes by retro Diels–Alder reaction. Single-crystal structures of TMS-BP and their metal complexes are herringbone packing motifs which are similar with that of pristine BP. On the other hand, TIPS-BP and their metal complexes form one dimensionally extended columnar π-stacking motifs. OFET devices of these compounds were fabricated by precursor approach and the best μ_h of 0.12 cm^2 V^{-1} s^{-1} was obtained for TMS-BP which is higher than that of BP by a factor of 2. The effect of substituents and metalation on the BP derivatives has impacts on the crystallite sizes as well as the μ of OFET. BHJ OPV devices of these compounds were also fabricated and the best PCE was obtained for TMS-ZnBP with a PCE of 1.51 % which is much higher than that of BP:PC$_{61}$BM-based BHJ OPV. The effect of substituents and metalation has impacts on the film morphology and crystallinity as well as OPV performances. Specifically, the compounds with TMS-groups tend to form larger grains while compounds with TIPS-groups form smooth surfaces. Free-base compounds have higher crystallinity than those of zinc and copper complexes, and zinc complexes tend to form π–π stacking and PC$_{71}$BM crystallites in the out-of-plane direction. Copper complexes tend to form large aggregations and show lower crystallinity to afford lowest OPV performance compared to those of free-base and zinc complexes.

2-8. Outlook

The OFET device based on TMS-BP achieved the μ_h of 0.12 cm^2 V^{-1} s^{-1} by a precursor approach. However, the μ_h over 1 cm^2 V^{-1} s^{-1} should be achieved for the practical application indicating the further improvement of μ_h is desired. To improve the μ_h, direct solution processes such as drop casting[41–43] and dip coating[44–48] methods could be applied to this system to control the anisotropy of crystal growth. Since the TIPS-BP has enough solubility for the deposition of active layer of OFET by solution processes, further improvement of μ_h can be expected. Thus the author further investigated OFET performance of TIPS-BP in the next chapter.

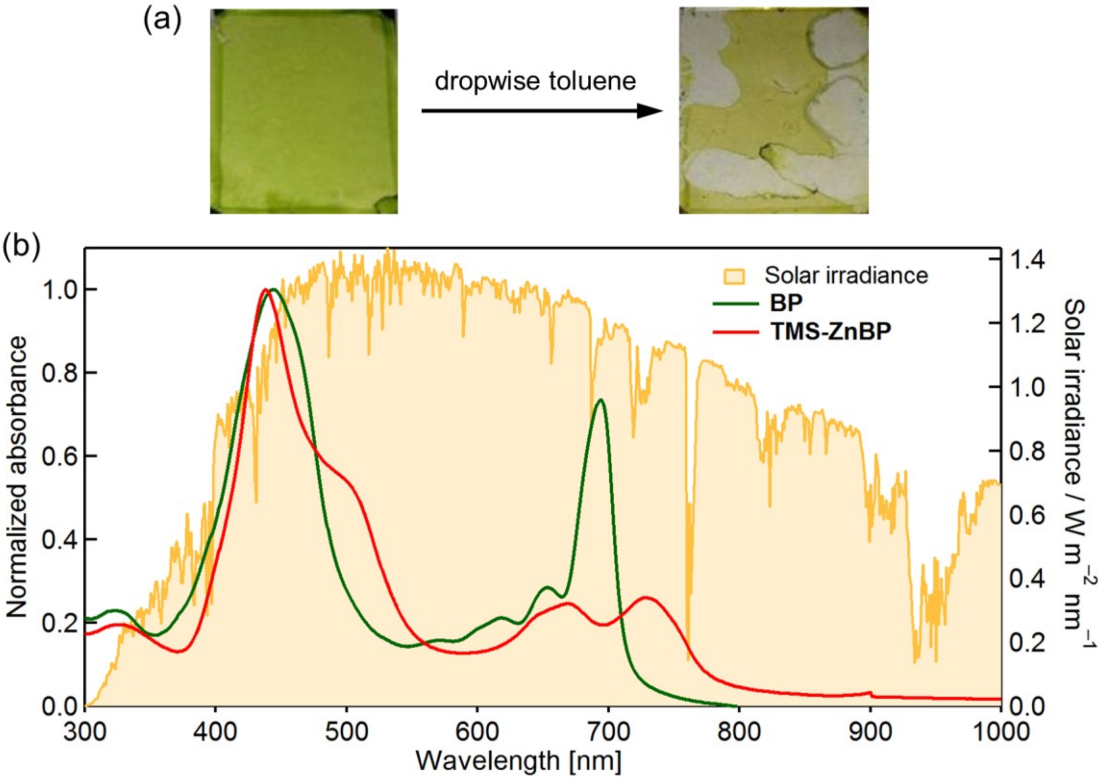

Figure 2-25. (a) Photographs of a TIPS-BP:PC$_{61}$BM blend film before (left) and after (right) dropwise toluene droplet followed by spin-coating. (b) Solar spectrum and absorption spectra of BP and TMS-ZnBP films.

The BHJ OPV of TMS-BPs and TIPS-BPs were achieved the PCE of about 1% which are much higher than the BHJ OPV based on BP:PC$_{61}$BM blend. This improvement caused by the introduction of substituents into a BP framework to have better miscibility, film morphology and moderate crystallinity in the blend film. However, the PCE of p–i–n-type OPV of BP:$PC_{61}BM$ system (2.0%) is still higher than those of TMS-BPs and TIPS-BPs systems.[4] This is because of the p–i–n-type OPV have three active layers to generate larger amount of excitons and have better electronic property compared with that of BHJ OPV (PCE = 0.02%).[18] Thus, the fabrication of p–i–n-type OPVs comprising TMS-BP:$PC_{71}BM$ and TIPS-BP:$PC_{71}BM$ blend were tried to improve the PCE of OPVs. Unfortunately, TMS-BP and TIPS-BP blend films were washed away when the deposition of another active layer onto the TMS-BP and TIPS-BP films, indicating the fabrication of p–i–n-type OPVs based on these compounds by solution-processes are essentially impossible (Figure 2-25a). Thus, the further PCE improvement by using TMS-BPs and TIPS-BPs is mostly impossible. Moreover, the absorption of TMS-BPs and TIPS-BPs are still weak at 500–600 and over 800 nm even though their absorptions are red-shifted from that of BP. In addition, the V_{OC}s of TMS-BPs and TIPS-BPs (0.4–0.7 V) are much lower than the state-of-the-art OPV materials which show the PCEs over 10% reflecting the high lying E_{HOMO}s of TMS-BPs and TIPS-BPs (Table 2-11). These problems of TMS-BPs and TIPS-BPs should be overcome by developing new BP derivatives.

Table 2-11. OPV performance of TMS-ZnBP and DRCN5T.

p-type materials	E_{HOMO}	J_{SC} / mA cm^{-2}	V_{OC} / V	FF	PCE / %
TMS-ZnBP	–4.8	7.6	0.47	0.42	1.5
DRCN5T[19]	–5.2	15.7	0.92	0.68	10.0
BTID-2F[20]	–5.1	15.7	0.95	0.76	11.3

2-9. Supporting Figures

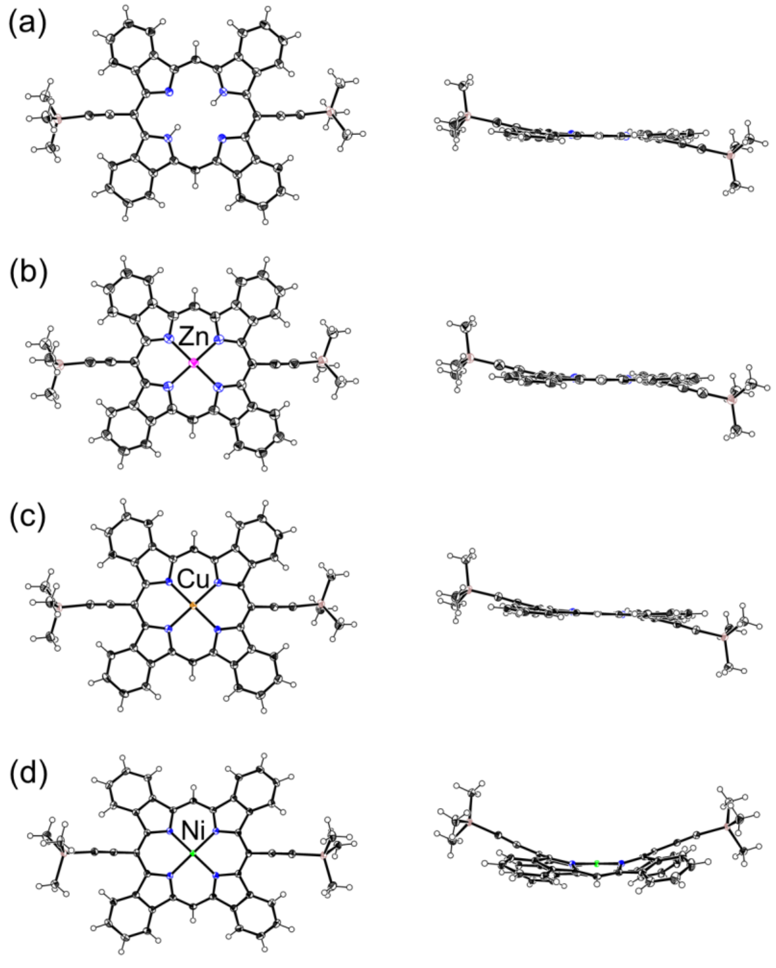

Figure S2-1. Crystal structures of top view (left) and side view of (a) TMS-BP, (b) TMS-ZnBP, (c) TMS-CuBP, and (d) TMS-NiBP. Thermal ellipsoids represent the 50% probability.

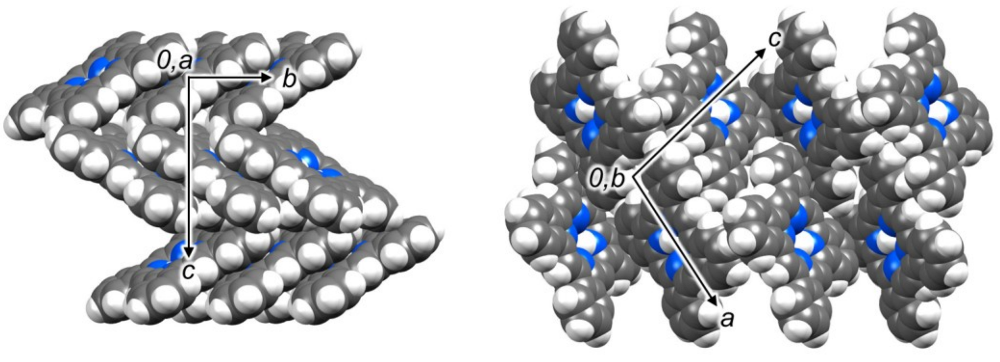

Figure S2-2. Crystal structure of **BP** (CCDC No. 2202816).[24]

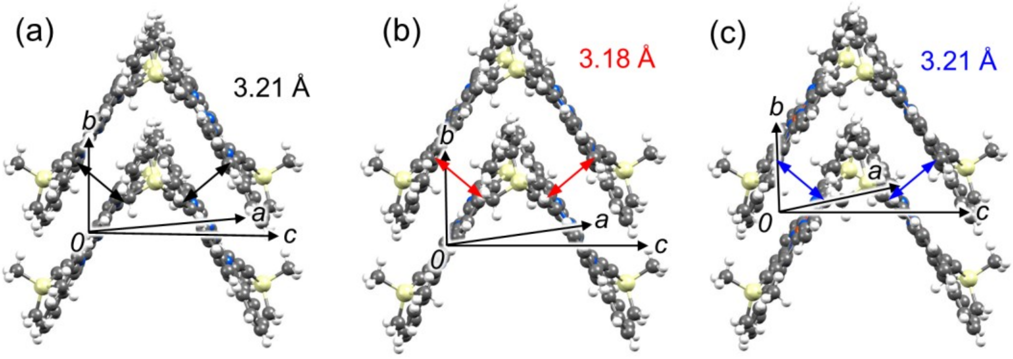

Figure S2-3. Crystal structures of (a) TMS-BP, (b) TMS-ZnBP, and (c) TMS-CuBP with π–π stacking distances.

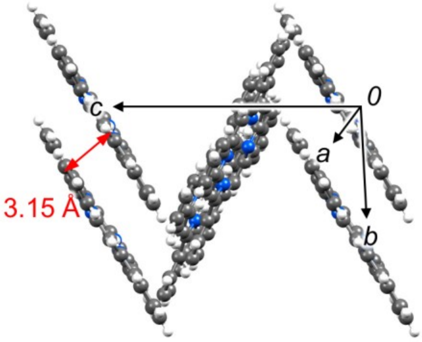

Figure S2-4. Crystal structures of BP[24] with π–π stacking distances.

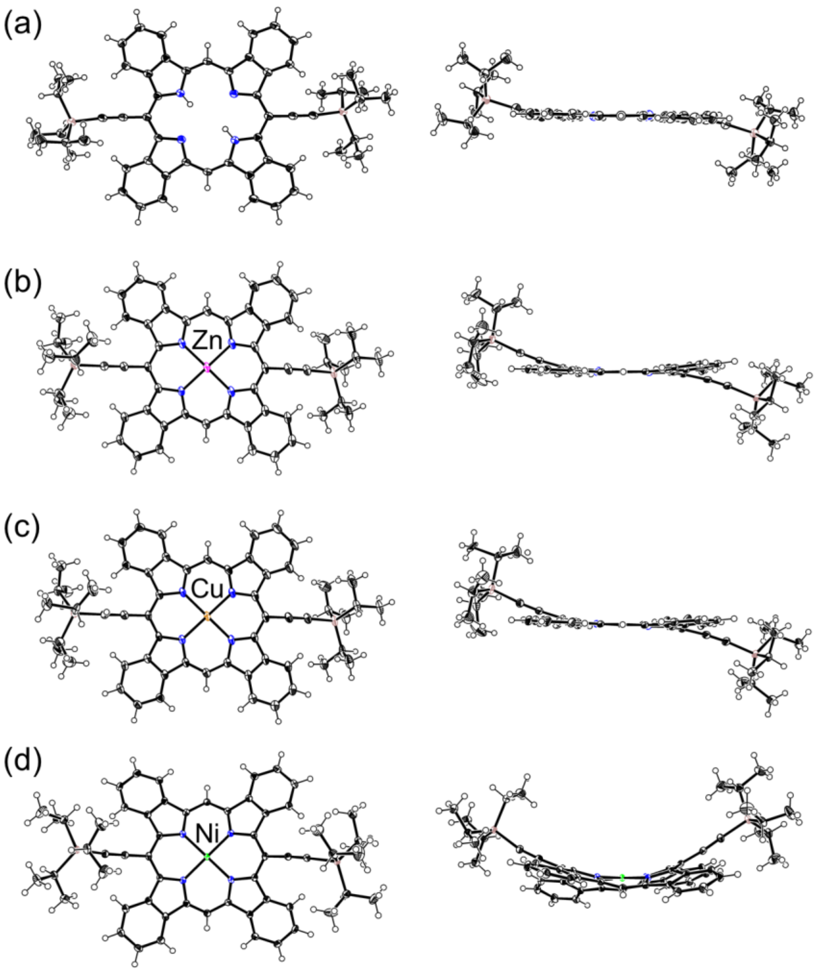

Figure S2-5. Crystal structures of top view (left) and side view of (a) TIPS-BP, (b) TIPS-ZnBP, (c) TIPS-CuBP, and (d) TIPS-NiBP. Thermal ellipsoids represent the 50% probability.

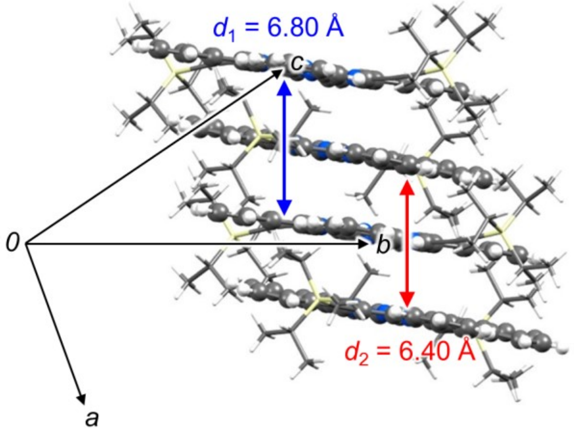

Figure S2-6. The average of interplane spacing of a TIPS-BP crystal structure was calculated as: $(d_1 + d_2)/4 = 3.30$ Å.

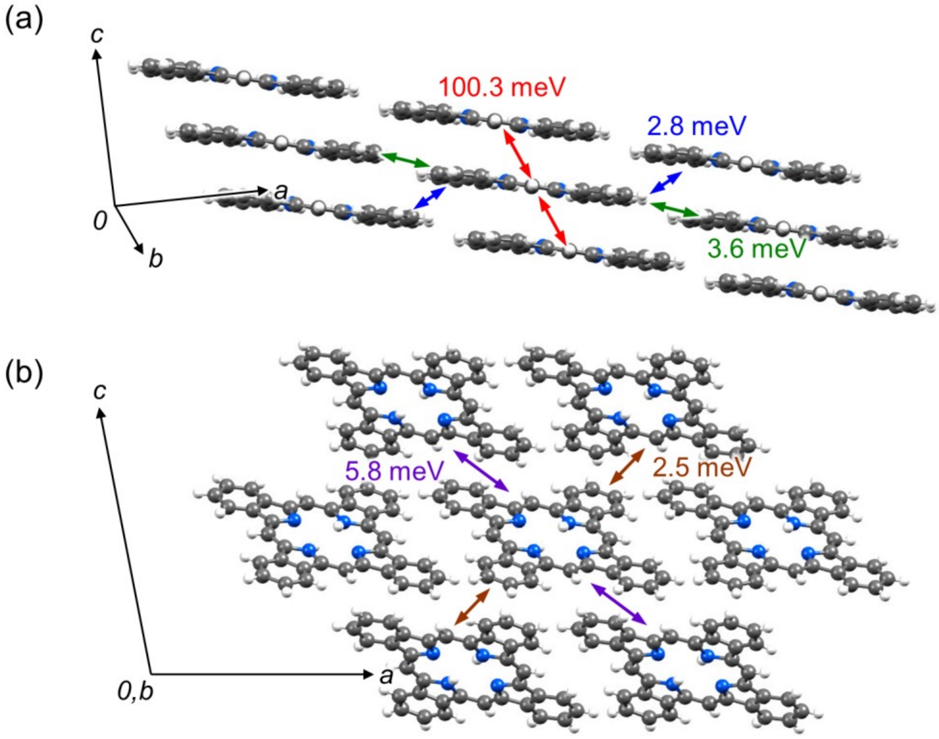

Figure S2-7. Charge-transfer integrals in BP single-crystal[24]: Views from (a) the side and (b) top of π-stack columns.

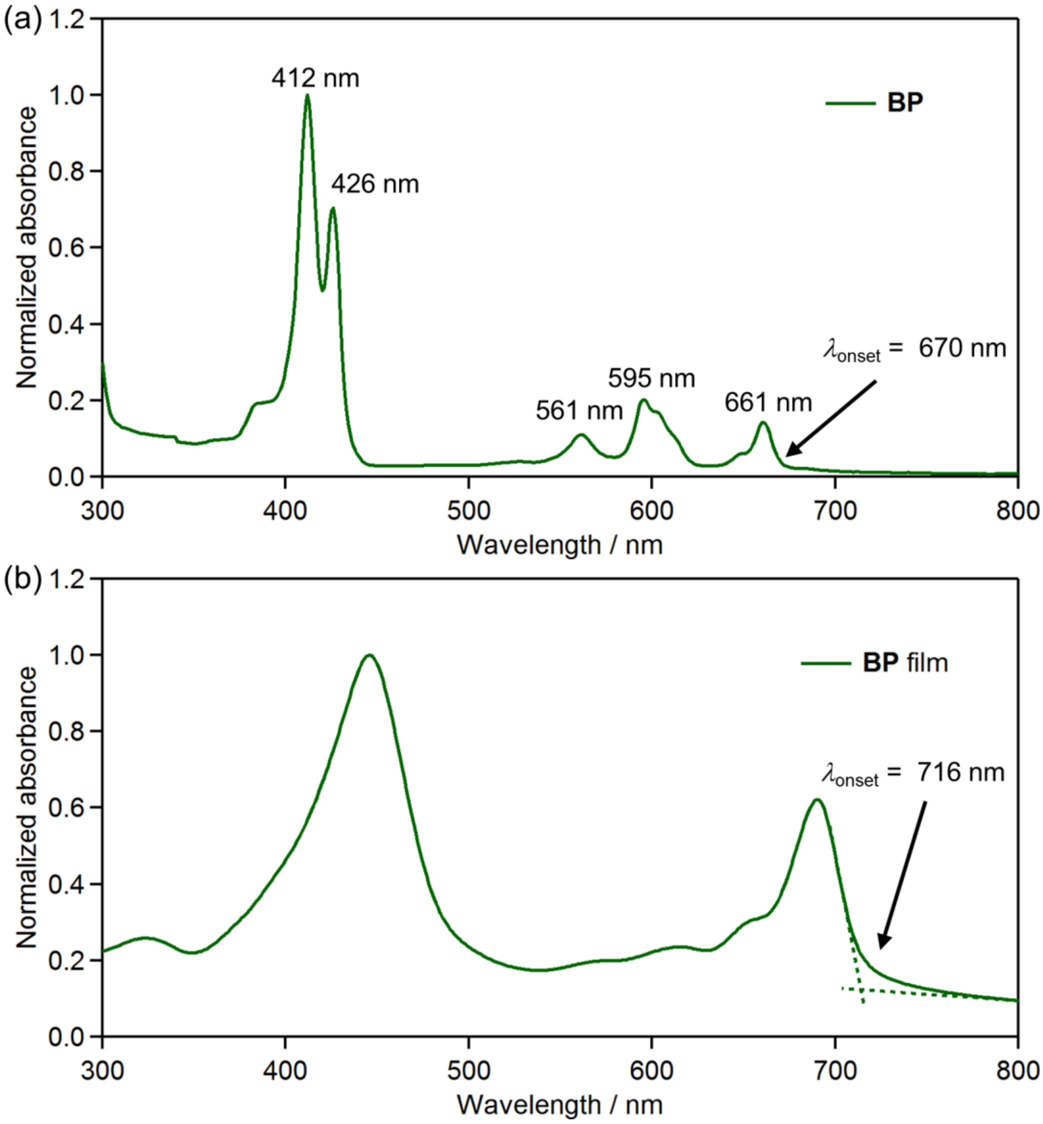

Figure S2-8. Absorption spectra of (a) BP in THF (5% v/v pyridine) and (b) as a thin film.

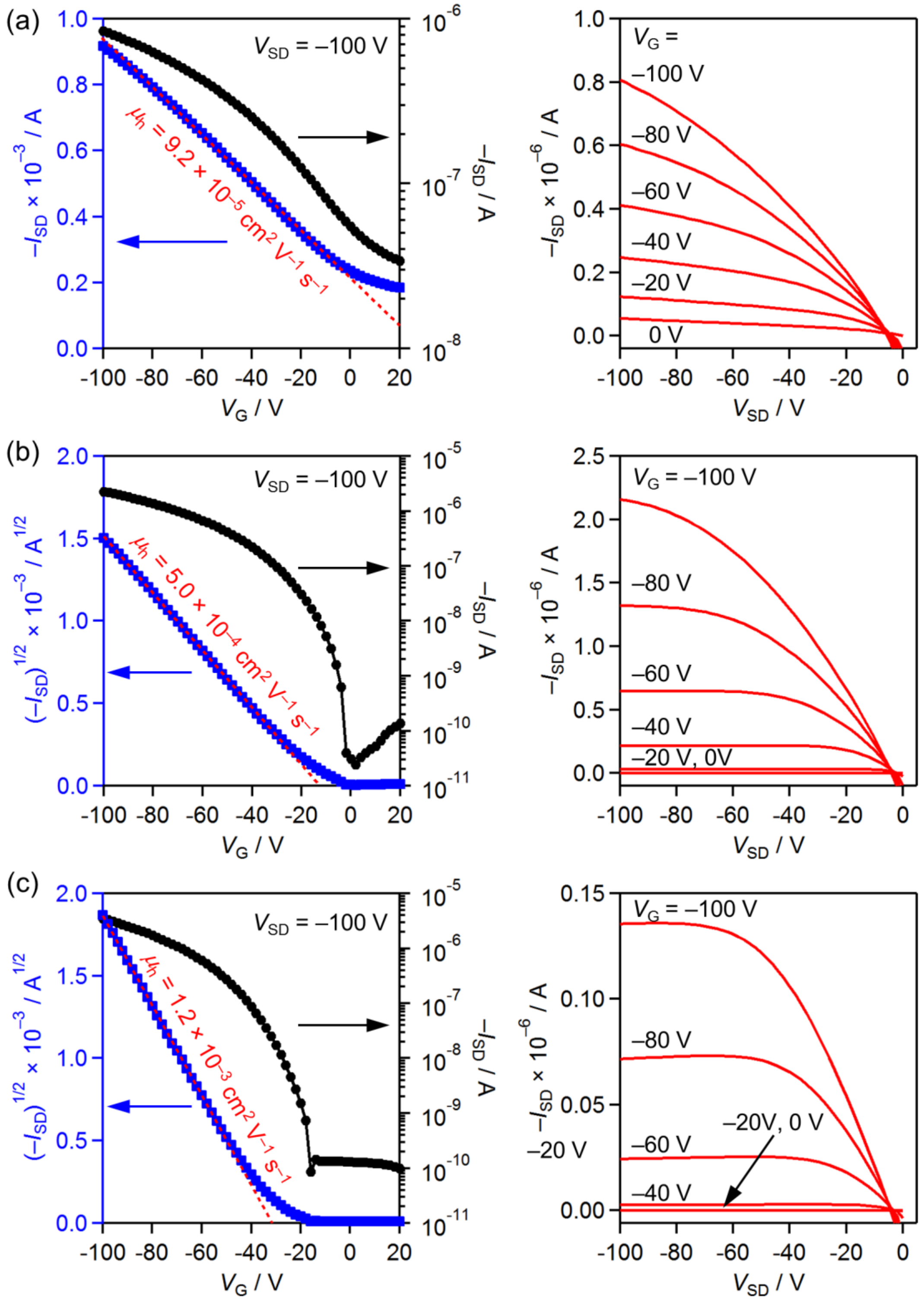

Figure S2-9. Transfer curve (left) and output curves (right) of OFETs based on (a) TMS-ZnBP, (b) TMS-CuBP, and (c) BP.

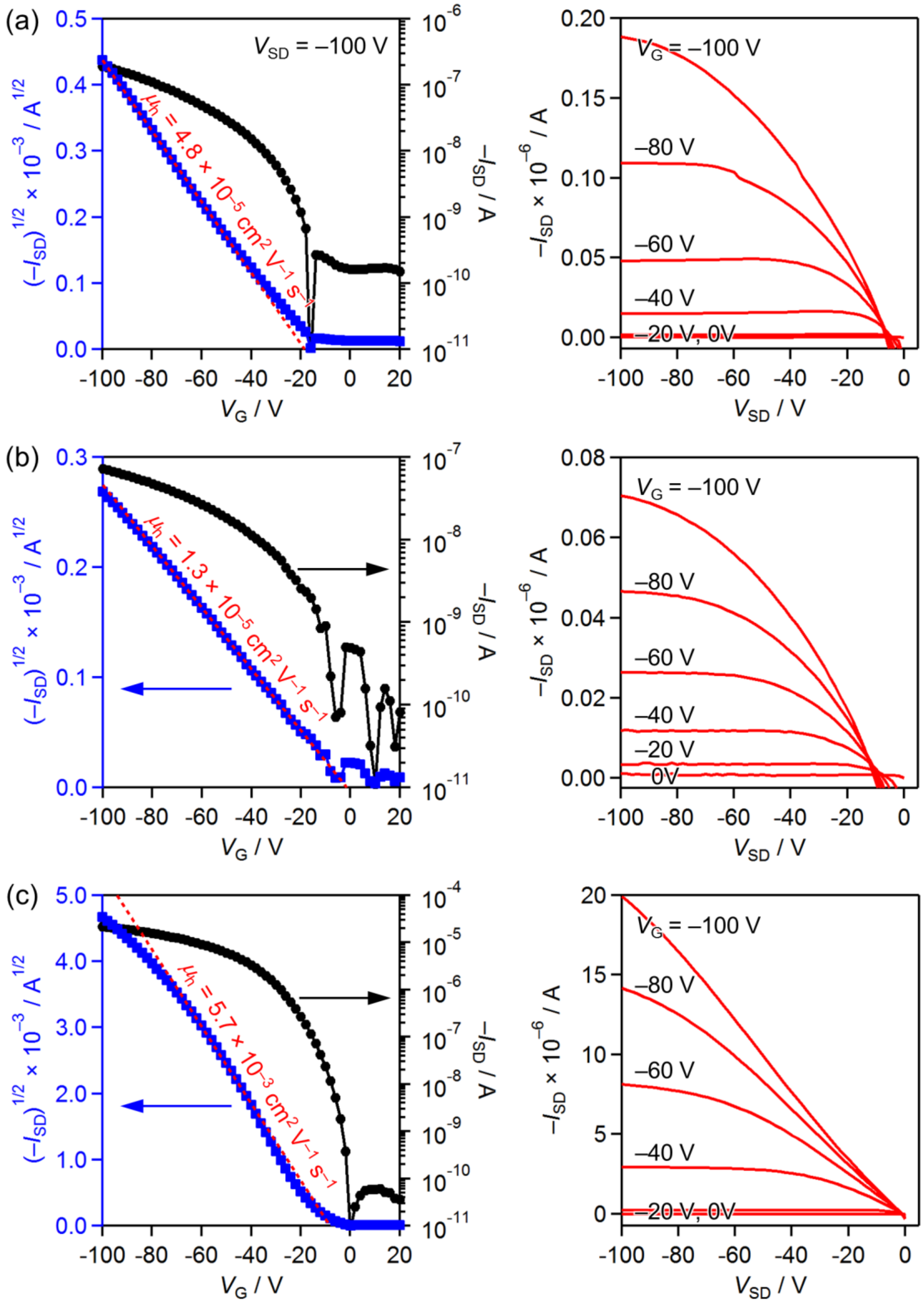

Figure S2-10. Transfer curve (left) and output curves (right) of OFETs based on (a) TIPS-BP, (b) TMS-ZnBP, and (c) TIPS-CuBP.

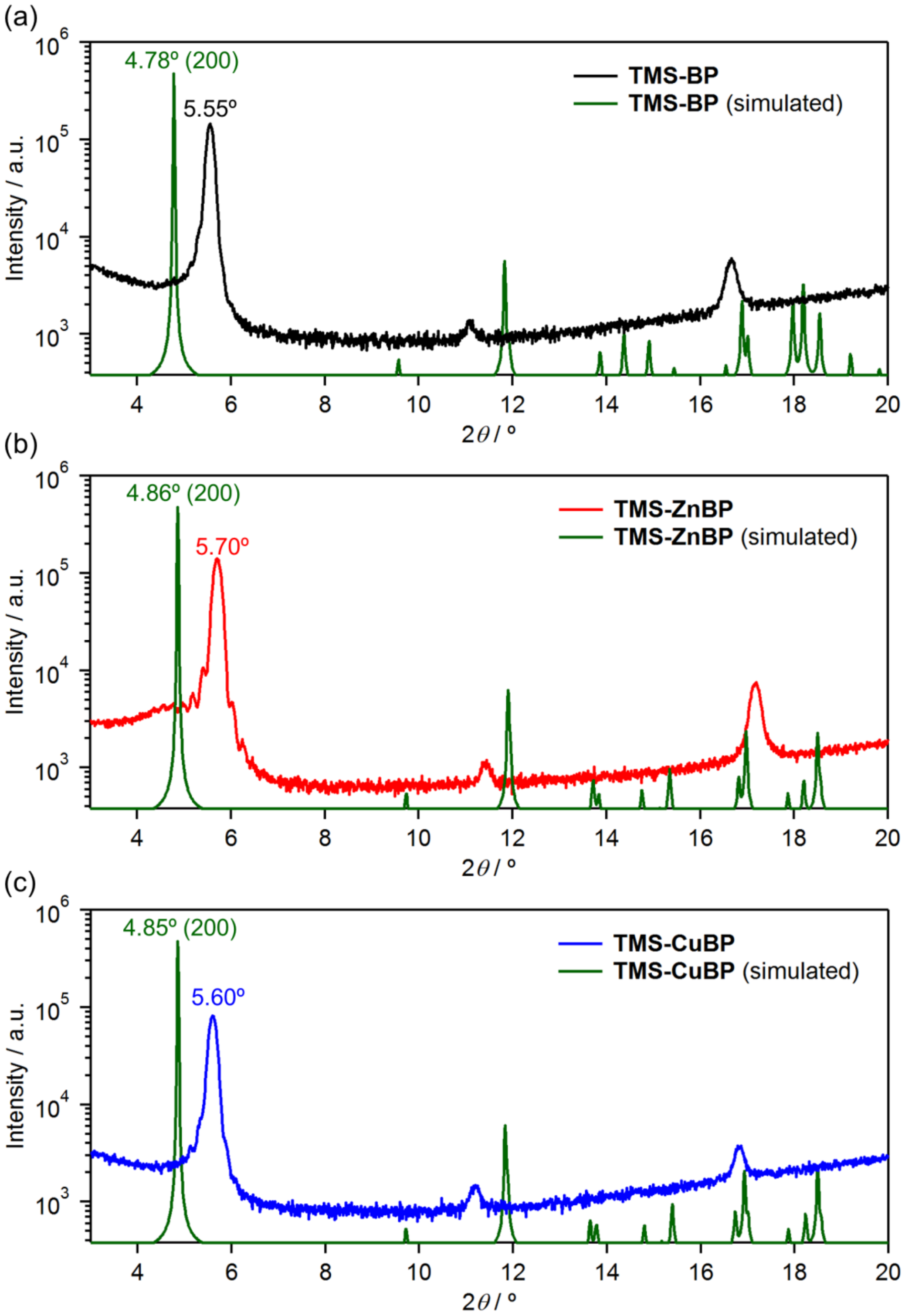

Figure S2-11. XRD and simulated powder patterns of (a) TMS-BP, (b) TMS-ZnBP, and (c) TMS-CuBP.

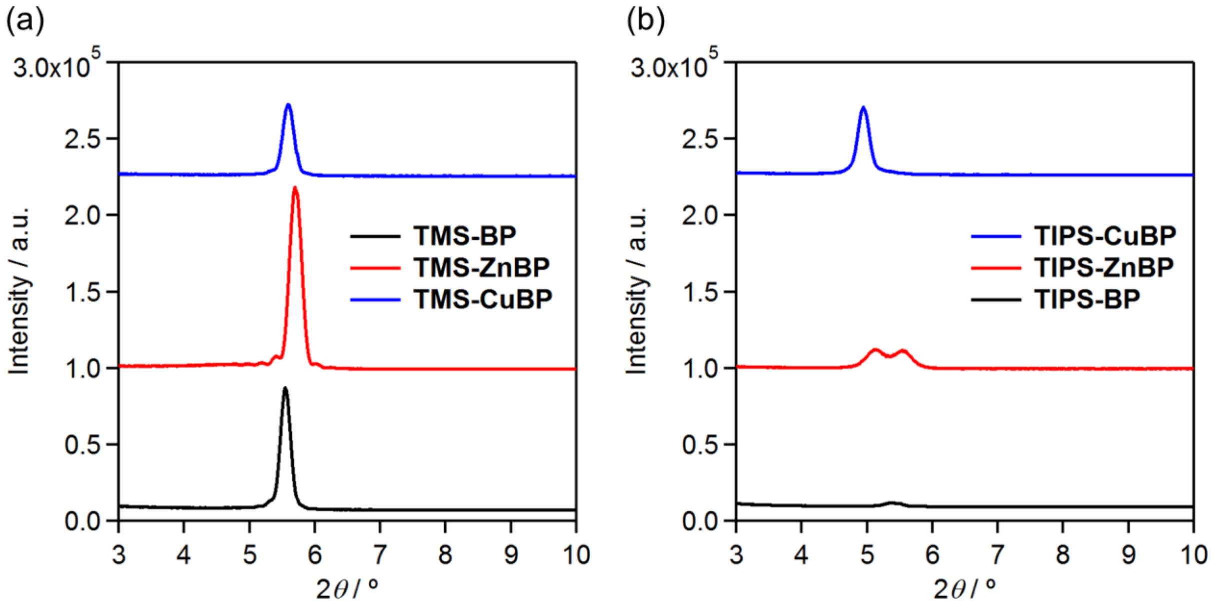

Figure S2-12. Intensity comparison of the primary XRD peaks of (a) TMS- and (b) TIPS-BP and their metal complexes.

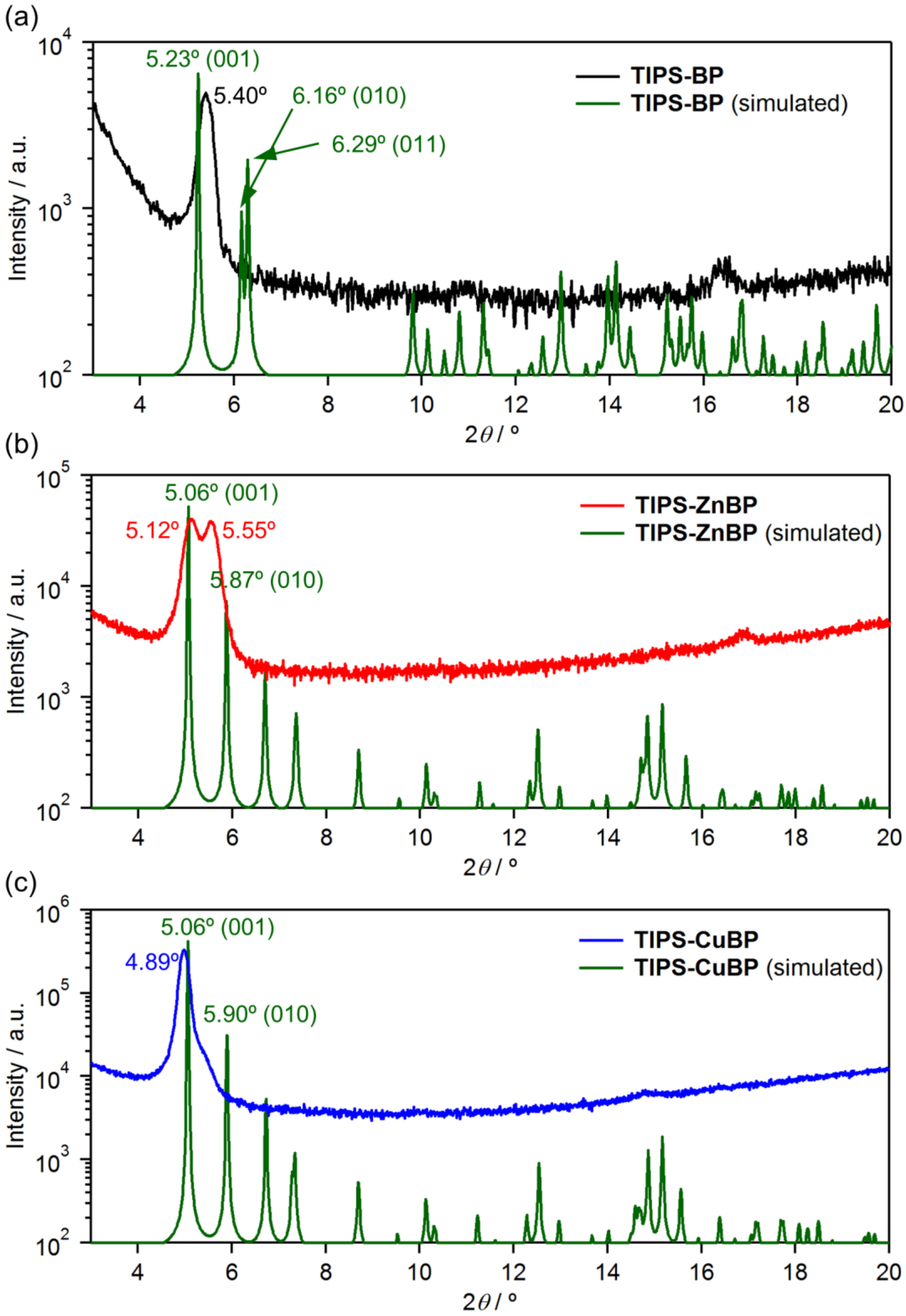

Figure S2-13. XRD and simulated powder patterns of (a) TIPS-BP, (b) TIPS-ZnBP, and (c) TIPS-CuBP.

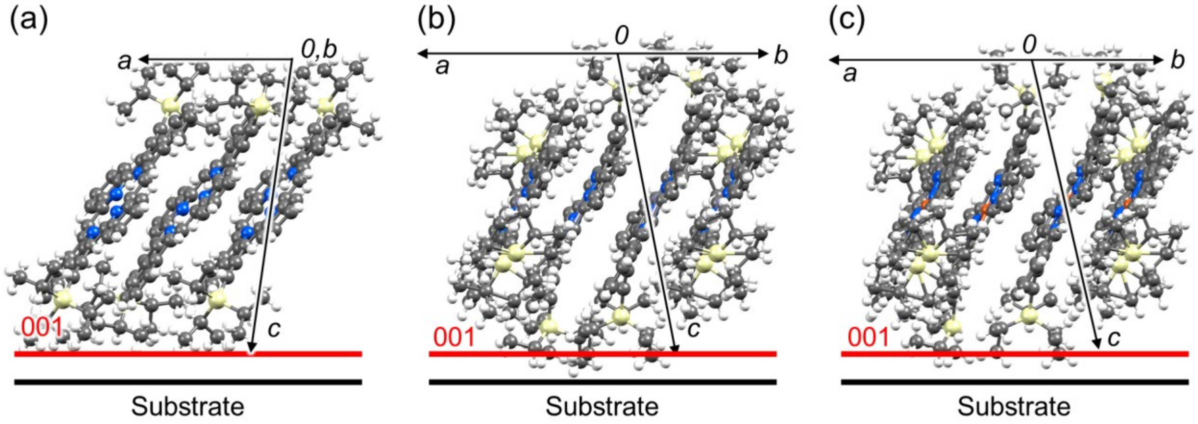

Figure S2-14. Relation between 001 planes and substrates of (a) TIPS-BP, (b) TIPS-ZnBP, and (c) TIPS-CuBP.

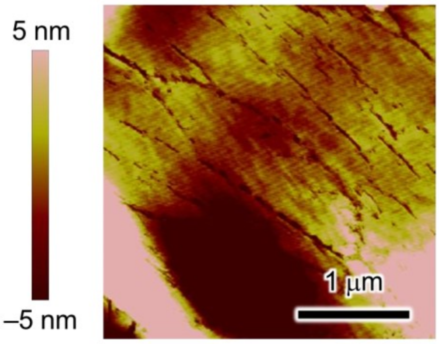

Figure S2-15. AMF image of a TIPS-BP neat film prepared by annealing at 180 °C.

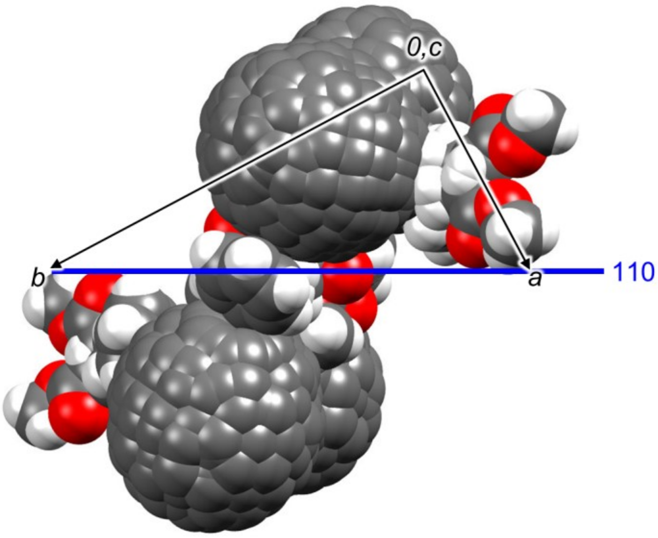

Figure S2-16. 110 plane of a single-crystal structure of $PC_{71}BM$[40] (CCDC No. 1420203).

2-10. Experimental Section

2-10-1. General

Materials for Synthesis

Solvents and chemical reagents were reagent grade quality, obtained from commercial sources and used without further purification. 3-(Triisopropylsilyl)propiolaldehyde[49] and bis(4,7-dihydro-2*H*-4,7-ethanoisoindol-1-yl)methane (**1**)[21] were prepared as described in literatures.

Materials for Device Fabrication

CP was prepared as described in literatures.[50] Semico Clean 53 was purchased from Furuuchi Chemical. PC$_{71}$BM was purchased from Luminescence Technology Crop. and used as received. For OPV device fabrication, solvents were purchased from Sigma-Aldrich and used as received.

Purification and Characterization of Materials

Material purification by flash column chromatography was conducted on silica gel purchased from Kanto Chemical (Silica Gel 60N, 60 Å, 40–50 μm). Analytical thin-layer chromatography (TLC) was conducted on Merck 200-μm thickness silica gel plates with a fluorescent indicator. Visualization was accomplished with UV light at 254 nm and 365 nm. ^{1}H NMR and ^{13}C NMR spectra were recorded on a JEOL AL–300 (300 MHz), ECX–400P (400 MHz), or ECA–600 (600 MHz) spectrometer at 294 K using tetramethylsilane as an internal standard. High resolution ESI mass spectra were measured on a JEOL AccuTOF/JMS-T100LC mass spectrometer. High resolution MALDI mass spectrum was measured on a JEOL SpiralTOF$^{\mathrm{TM}}$/JMS-S3000 mass spectrometer. UV−vis–NIR absorption spectra in solutions and thin films were measured on a JASCO V-670 and V-650 spectrophotometer, respectively. For spectral measurements, spectral grade solvents were purchased from Nacalai Tesque Inc. The TGA were carried out on a Seiko Exstar 6000 TG/DTA 6200 instrument under nitrogen gas flow with a heating rate of 10 °C min^{-1}.

DFT Calculation

DFT calculation was carried out using a Gaussian 09 package based on CAM-B3LYP/6-31G(d) level of theory.

Charge Transfer Integral Calculation

Charge transfer integrals are calculated by fragment orbital method with the GGA:BP/DZP level of theory using Amsterdam Density Functional (ADF) program.[51]

Film Characterization

Ionization energies of the thin films were determined from the onset of photoelectron spectra measured by a photoelectron spectrometer in air (AC-3, Riken Keiki). Thin films for photoelectron spectroscopy were deposited as follows: ITO-coated glass substrates (18 × 20 mm, 15 Ω per square) were cleaned by sonication in Semico Clean 53, deionized water, and isopropanol for 10 min each. The washed substrates were further treated in a UV–O_3 cleaner (UV253V8, Filgen) for 20 min. The substrates were then transferred to a N_2-filled glove box (<0.5 ppm O_2 and H_2O). Active layers were deposited by spin-coating (800 rpm, 30 s) of a solution containing a precursor (TMS-CP, TMS-ZnCP, TMS-CuCP, TIPS-CP, TIPS-ZnCP, or TIPS-CuCP) in a chloroform solution (5 mg mL^{-1}) followed by heating at 180 °C for 30 min to convert the corresponding BP compound. Thin-films for absorption spectroscopy were deposited as follows: glass substrates (18 × 18 mm) were cleaned by sonication in Semico Clean 53, deionized water, and isopropanol for 10 min each. The washed substrates were further treated in a UV–O_3 cleaner (UV253V8, Filgen) for 20 min. The substrates were then transferred to a N_2-filled glove box (<0.5 ppm O_2 and H_2O). Active layers were deposited by spin-coating (800 rpm, 30 s) of a solution containing a precursor (TMS-CP, TMS-ZnCP, TMS-CuCP, TIPS-CP, TIPS-ZnCP, or TIPS-CuCP) in a chloroform solution (5 mg mL^{-1}) followed by heating at 180 °C for 30 min to convert the corresponding BP compound. AFM images awere recorded on a Buruker Dimension Icon. Thin film XRD patterns were recorded on a Rigaku SmartLab system.

Fabrication and Evaluation of OFET

The heavily doped n-doped Si substrates with 300 nm-thick thermally grown SiO_2 layer as the gate dielectric layer Si substrates were cleaned sequentially with H_2O, acetone and 2-propanol in an ultrasonic bath, and treated with UV–ozone (UV253V8, Filgen) for 20 min. Chloroform solutions of precursors (7.0 mg mL^{-1}) were spin coated at 1000 rpm for 40 s on Si substrates in a nitrogen glove box, where H_2O and O_2 concentrations were <0.5 ppm. TMS-CPs or TIPS-CPs films were annealed at 180 ºC for 30 min to convert precusors to corresponding BP compounds. Au source and drain electrodes (70 nm) were vacuum deposited through a metal shadow mask. The channel length (L) and width (W) were 50 µm and 5.5 mm, respectively. Transfer (I_{SD}–V_G) and output (I_{SD}–V_{SD}) curves were measured using an Agilent HP4155C semiconductor parameter analyzer in a glove box at room temperature. Field-effect μ_h was estimated from the saturation regime at drain voltage $V_{SD} = -100$ V, using the equation:

$$I_{SD} = (\mu W C_i/2L)(V_G - V_{th})^2 \qquad (1)$$

where I_{SD} is the drain-source current, μ the field-effect mobility, W the channel width, L the channel length, C_i the capacitance per unit area of the gate dielectric layer, and V_{th} the threshold voltage.

Fabrication and Evaluation of OPV

The BHJ OPV devices of donors and $PC_{71}BM$ were fabricated as follows: ITO-coated glass substrates (20 × 25 mm, 15 Ω per square) were cleaned by gentle rubbing with an acetone-soaked wipe for ca. 5s, sonication in acetone and isopropanol for 10 min each, and exposure to boiling isopropanol for 10 min. The washed substrates were further treated in a UV–O_3 cleaner (UV253V8, Filgen) for 20 min, and the PEDOT:PSS (Clevios PVP Al4083) was spin-coated at 5000 rpm for 40 s in air followed by a thermal annealing treatment at 120 °C for 20 min in air. The thickness of the resulting PEDOT:PSS layer was about 30 nm. The substrates were then transferred to a N_2-filled glove box (< 0.5 ppm O_2 and H_2O). Active layers were deposited by spin-coating (2500 rpm for TMS-CPs or 800 rpm for TIPS-CPs) of a solution containing a precursor (TMS-CPs or TIPS-CPs) and $PC_{71}BM$ (D:A w/w = 1:1 for TMS-BP, TMS-ZnBP, TIPS-BP, and TIPS-ZnBP; 2:1 for TMS-CuBP; 1:2 for TIPS-CuBP) in a chloroform solution for TMS-CPs (20 mg mL^{-1}) or a mixture of $CHCl_3$:chlorobenzene (1:1 v/v) solution for TIPS-CPs (10 mg mL^{-1}) followed by heating at 160, 180 or 200 °C for 30 min to convert the corresponding benzoporphyrin *in situ*. Finally, BCP (7 nm) and Al (100 nm) were vapor deposited at high vacuum (~10^{-5} Pa) through a shadow mask that defined an active area of 4.0 mm^2. The device was then tested in air after the encapsulation in the glove box. *J–V* curves were measured using a Keithley 2400 source measure unit under AM 1.5G illumination at an intensity of 100 mW cm^{-2} using a solar simulator (CEP-2000TF, Bunko-keiki). The EQE spectra were obtained under illumination of monochromatic light using the same system.

Single-Crystal X-ray Crystallography

Single-crystal X-ray diffraction data were collected at 103 K on a Rigaku VariMax RAPID using Mo-Kα radiation. The structures were solved by direct methods and refined on F^2 by full-matrix least-squares using the CrystalClear and SHELXS-2000 program. CCDC No. 930877 (TIPS-CP), 930879 (TIPS-ZnCP), 1031711 (TMS-BP), 1039260 (TMS-ZnBP), 1031710 (TMS-CuBP), 1031712 (TMS-NiBP), 930876 (TIPS-BP, 1D π-stack), 1441675 (TIPS-BP, 2D π-stack), 930878 (TIPS-ZnBP, with *i*-PrOH), 1040808 (TIPS-ZnBP), 1031708 (TIPS-CuBP), and 1031709 (TIPS-NiBP) contain the crystallographic data for this chapter. This data can be obtained free of charge from The Cambridge Crystallographic Data Centre (CCDC) via https://summary.ccdc.cam.ac.uk/structure-summary-form.

2-10-2. Synthesis

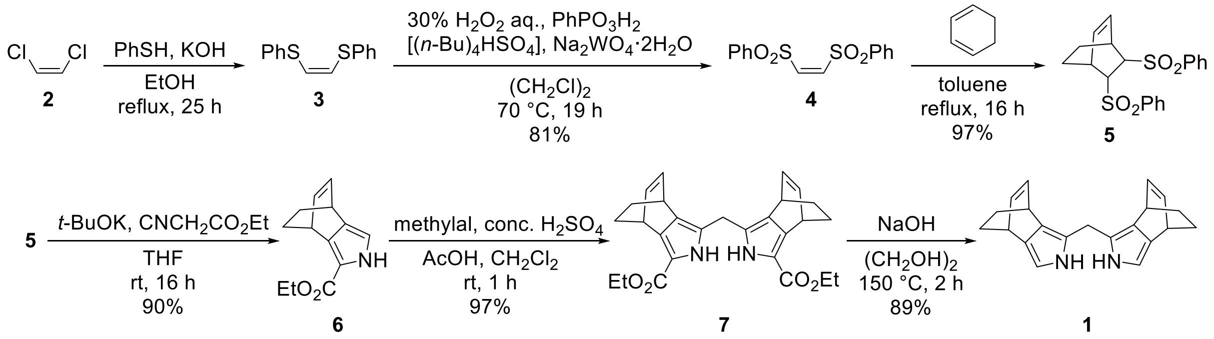

Scheme S2-1. Synthesis of **1**.[21]

(Z)-1,2-Bis(phenylthio)ethene (3)

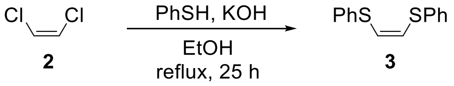

KOH (92.7 g, 1.65 mol) was dissolved in ethanol (1000 mL) by stirring at room temperature. Thiophenol (82.2 mL, 0.799 mol) and *cis*-1,2-dichloroethylene (**2**) (30.2 mL, 0.399 mol) were then added to the solution. After the reaction mixture was refluxed with stirring for 25 h, the mixture was cooled to room temperature. After the obtained KCl salt was removed by filtration, ethanol was removed under reduced pressure. After the residue was quenched by adding water, the mixture was extracted with $CHCl_3$ for three times and the organic layer was washed with water and brine. The mixture was then dried over Na_2SO_4 and the solvent was removed under reduced pressure to give a target compound **3** as orange oil. This product was directly used for the next reaction as this reaction was quantitatively proceeded. ^1H NMR (400 MHz, $CDCl_3$, δ): 7.21–7.44 (m, 10H), 6.52 (s, 2H).
(Experimental note-4, page 46–47, reaction No. 4-23)

(Z)-1,2-Bis(phenylsulfonyl)ethene (4)

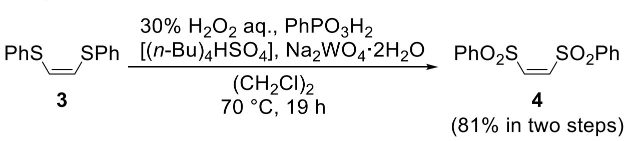

A solution of compound **3** (399 mmol) in $(CH_2Cl)_2$ (200 mL) was added dropwise into a solution of $PhPO_3H_2$ (1.90 g, 12.0 mmol), $[(n\text{-Bu})_4N]HSO_4$ (2.53 g, 12.0 mmol), and $Na_2WO_4 \cdot 2H_2O$ (3.96 g, 12.0 mmol) in a 30% hydrogen peroxide water (300 mL) at 0 °C. After finishing dropping, the reaction mixture was vigorously stirred (>1000 rpm) at 70 °C for 19 h. After cooling the mixture to room temperature, the mixture was extracted with $CHCl_3$. The organic layer was washed with saturated $NaHCO_3$ aqueous solution, water, and brine. The washed organic layer was dried over Na_2SO_4 and the solvent was removed under reduced pressure. The obtained white solid was washed with MeOH to give a target compound **4** as a

white solid in 81% yield (99.7 g, 323 mmol). ^{1}H NMR (400 MHz, $CDCl_3$, δ): 8.08–8.06 (m, 4H), 7.73–7.69 (m, 2H), 7.62–7.58 (m, 4H), 6.82 (s, 2H).
(Experimental note-4, page 50–51, reaction No. 4-25)

5,6-Bis(phenylsulfonyl)bicyclo[2.2.2]oct-2-ene (5)

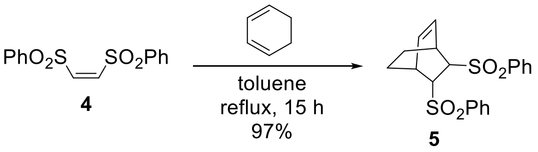

The reaction mixture of compound **4** (57.4 g, 186 mmol) and 1,3-cyclohexadiene (19.5 mL, 205 mmol) in toluene (230 mL) was refluxed with stirring for 15 h. After cooling the mixture to room temperature, the solvent was removed under reduced pressure. The obtained white solid was washed with Et_2O to give a target compound **5** as a white solid in 97% yield (70.3 g, 181 mmol). ^{1}H NMR (300 MHz, $CDCl_3$, δ): 7.95–7.52 (m, 10H), 6.37–6.22 (m, 2H), 3.95–3.92 (m, 1H), 3.77–3.74 (m, 1H), 3.18–3.15 (m, 1H), 3.07–3.05 (m, 1 H), 2.40–2.31 (m, 1H), 1.73–1.63 (m, 1H), 1.45–1.35 (m, 1H), 1.17–1.06 (m, 1H).
(Experimental note-6, page 134–135, reaction No. 6-64)

Ethyl 4,7-dihydro-4,7-ethano-2*H*-isoindole-1-carboxylate (6)

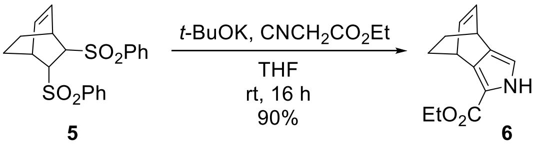

To a stirred solution of compound **5** (53.6 g, 138 mmol) and ethyl isocyanoacetate (19.6 mL, 180 mmol) in dehydrated THF (586 mL) was added dropwise a solution of potassium *tert*-butoxide (46.4 g, 414 mmol) in dehydrated THF (414 mL) at 0 °C under Ar atmosphere. The resulting mixture was stirred for 16 h at room temperature. After neutralizing the reaction mixture with 1 M HCl aqueous solution, THF was removed under reduced pressure. The residue was added water and extracted with $CHCl_3$. The organic layer was washed with saturated $NaHCO_3$ aqueous solution and dried over Na_2SO_4. The solvent was removed under reduced pressure. The residue was purified by column chromatography on silica gel (CH_2Cl_2) followed by recrystallization ($CHCl_3$/hexane) to give a target compound **6** as a white solid in 90% yield (27.0 g. 124 mmol). ^{1}H NMR (300 MHz, $CDCl_3$, δ): 8.37 (brs, 1H), 6.57 (m, 1H), 6.52–6.49 (m, 2H), 4.39–4.35 (m, 1H), 4.31 (q, J = 7.1 Hz, 2H), 3.89–3.86 (m, 1H), 1.61–1.42 (m, 4H), 1.37 (t, J = 7.1 Hz, 3H).
(Experimental note-1, page 96–97, reaction No. 1-53)

Diethyl 5,5’-methylenebis(4,7-dihydro-2*H*-4,7-ethanoisoindole-1-carboxylate) (7)[21]

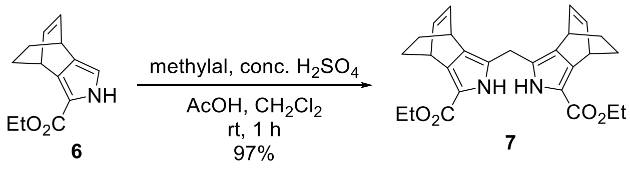

To a stirred solution of compound **6** (10.9 g, 50.2 mmol) and methylal (2.70 mL, 30.6 mmol) in a mixture solution of CH_2Cl_2 (50 mL) and acetic acid (100 mL) was added dropwise a concentrated H_2SO_4 (0.55 mL) at room temperature. The resulting mixture was stirred for 1 h at room temperature. The reaction mixture was poured into water and extracted with CH_2Cl_2. The organic layer was neutralized with saturated $NaHCO_3$ aqueous solution and washed with water and brine, then dried over Na_2SO_4. The solvent was removed under reduced pressure. After the residue was washed with hexane by ultrasonication, the white precipitation was obtained and collected by filtration (hexane) to give a target compound **7** as a white solid in 97% yield (10.8 g. 24.2 mmol). ^{1}H NMR (300 MHz, $CDCl_3$, δ): 8.67–8.62 (m, 2H), 6.51–6.43 (m, 4H), 4.34–4.24 (m, 6H), 3.99–3.84 (m, 2H), 3.69–3.61 (m, 2H), 1.58–1.31 (m, 14H).
(Experimental note-2, page 100–101, reaction No. 2-43)

Bis(4,7-dihydro-2*H*-4,7-ethanoisoindol-1-yl)methane (1)[21]

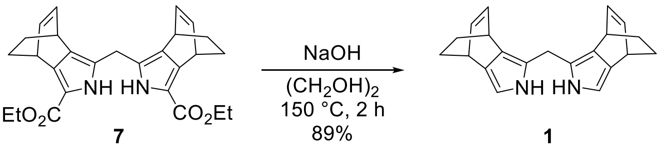

A solution of **7** (24.4 g, 54.6 mmol), NaOH (11.7 g, 293 mmol) in $(CH_2OH)_2$ (250 mL) was heated at 150 °C for 2 h under Ar atmosphere. The reaction mixture was cooled to room temperature by using ice bath, added water, and extracted with EtOAc. The organic layer was washed with water and brine, dried over Na_2SO_4, and concentrated under reduced pressure. The residue was purified by column chromatography on silica gel (CH_2Cl_2) to give a target compound **1** as a brown solid in 89% yield (6.58 g, 21.8 mmol). ^{1}H NMR (300 MHz, $CDCl_3$, δ): 7.15 (brs, 2H), 6.52–6.4w (m, 4H), 6.31–6.29 (m, 2H), 3.90–3.89 (m, 2H), 3.80–3.79 (m, 2H), 3.61–3.55 (m, 2H), 1.60–1.44 (m, 8H).
(Experimental note-6, page 142–143, reaction No. 6-68)

5,15-Bis(trimethylsilylethynyl)tetrakis(bicycle[2,2,2]octadieno)porphyrin (TMS-CP)[21]

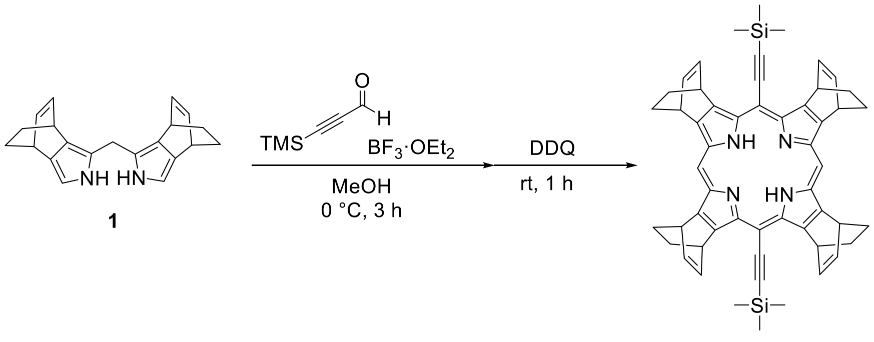

TMS-CP (57%)

A solution of compound **1** (455 mg, 1.50 mmol) in methanol (150 mL) was deoxygenated by bubbling of argon gas for 20 min. 3-(Trimethylsilyl)propiolaldehyde (0.22 ml, 149 mmol) was added to a solution of compound **7** and then the reaction system was covered with aluminum foil. Boron trifluoride etherate ($BF_3 \cdot OEt_2$) (26.0 μl, 0.207 mmol) was added dropwise to the solution and the resulting mixture was stirred for 3 h at 0 °C. DDQ (681 mg, 3.00 mmol) was added to the solution and stirred for 1 h at room temperature. Then, the solvent was removed under reduced pressure. The residue was purified by alumina column chromatography (CH_2Cl_2) to give **TMS-CP** as a purple solid in 57% yield (347 mg, 0.426 mmol). ^1H NMR (400 MHz, $CDCl_3$, δ): 10.22–10.21 (m, 2H), 7.11–7.07 (m, 8H), 6.53 (m, 4H), 5.69 (m, 4H), 2.21–1.86 (m, 16H), 0.70–0.68 (m, 18H), –3.08 (s, 2H).
(Experimental note-3, page 106–107, reaction No. 3-52)

5,15-Bis(triisopropylsilylethynyl)tetrakis(bicycle[2,2,2]octadieno)porphyrin (TIPS-CP)

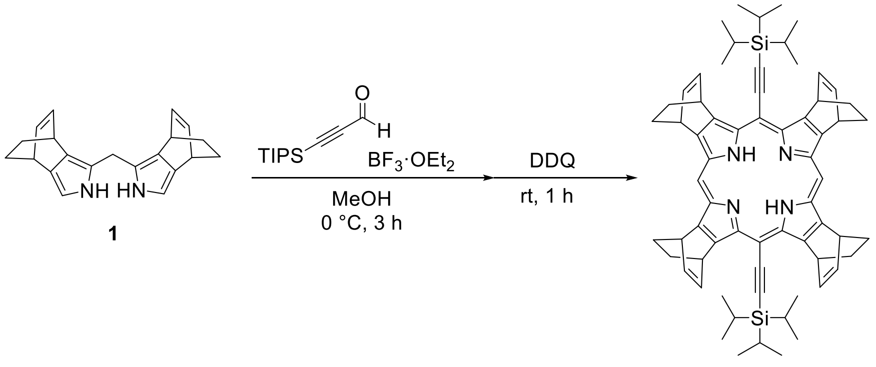

TIPS-CP (57%)

A solution of compound **1** (889 mg, 2.94 mmol) in methanol (300 mL) was deoxygenated by bubbling of argon gas for 20 min. 3-(Triisopropylsilyl)propiolaldehyde (0.80 ml, 3.27 mmol) was added to a solution of compound **7** and then the reaction system was covered with aluminum foil. Boron trifluoride etherate ($BF_3 \cdot OEt_2$) (0.10 ml, 0.796 mmol) was added dropwise to the solution and the resulting mixture was stirred for 3 h at 0 °C. DDQ (1.33 g, 5.86 mmol) was added to the solution and stirred for 1 h at room temperature. Then, the solvent was removed under reduced pressure. The residue was purified by alumina column chromatography (CH_2Cl_2) followed by recrystallization ($CHCl_3$/MeOH) to give **TIPS-CP** as a purple solid in 57% yield (347 mg, 0.426 mmol). ^{1}H NMR (400 MHz, CDCl$_3$, δ): 10.24 (m, 2H), 7.06 (m, 8H), 6.63 (m, 4H), 5.71 (m, 4H), 2.27–1.81 (m, 16H), 1.66 (m, 6H), 1.57–1.46 (m, 36H). ^{13}C NMR (75 MHz, CDCl$_3$, δ): 151.39, 148.00, 142.06, 137.23, 136.20, 136.02, 109.00, 100.67, 98.75, 97.45, 38.39, 36.25, 27.36, 19.05, 12.13. HRMS (ESI): *m*/*z* $[M + H]^+$ calcd for $C_{66}H_{79}N_4Si_2$, 983.5843; found, 983.5445. UV–vis (CH_2Cl_2) λ_{max}, nm ($\varepsilon \times 10^4$): 661 (1.58), 603 (0.759), 576 (4.27), 535 (1.09), 506 (0.564), 423 (21.5).

(Experimental note-1, page 49–51, reaction No. 1-25)

[5,15-Bis(trimethylsilylethynyl)tetrakis(bicycle[2,2,2]octadieno)porphyrinato]zinc(II) (TMS-ZnCP)[21]

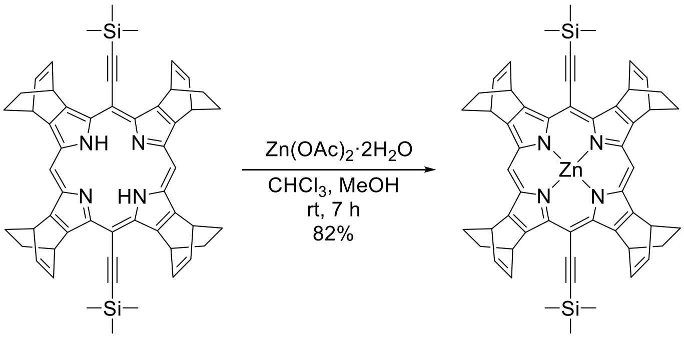

TMS-CP **TMS-ZnCP**

A solution of $Zn(OAc)_2 \cdot 2H_2O$ (305 mg, 1.39 mmol) in methanol (3.0 mL) was added to a solution of **TMS-CP** (227 mg, 0.278 mmol) in CHCl$_3$ (30 mL). After stirring for 7 h at room temperature, the reaction mixture was poured into water and extracted with CHCl$_3$. The organic layer was washed with saturated $NaHCO_3$ aqueous solution, dried over Na_2SO_4, and the solvent was removed under reduced pressure. The residue was purified by column chromatography (CH_2Cl_2) on silica gel followed by reprecipitation (CH_2Cl_2/hexane) to give a target compound **TMS-ZnCP** as purple crystals in 82% yield (200 mg, 0.228 mmol). ^{1}H NMR (400 MHz, CDCl$_3$, δ): 10.24 (m, 2H), 7.11–7.08 (m, 8H), 6.63 (m, 4H), 5.69 (m, 4H), 2.23–1.92 (m, 16H), 0.71–0.68 (m, 18H).

(Experimental note-5, page 49–51, reaction No. 5-66)

[5,15-Bis(trimethylsilylethynyl)tetrakis(bicycle[2,2,2]octadieno)porphyrinato]copper(II) (TMS-CuCP)

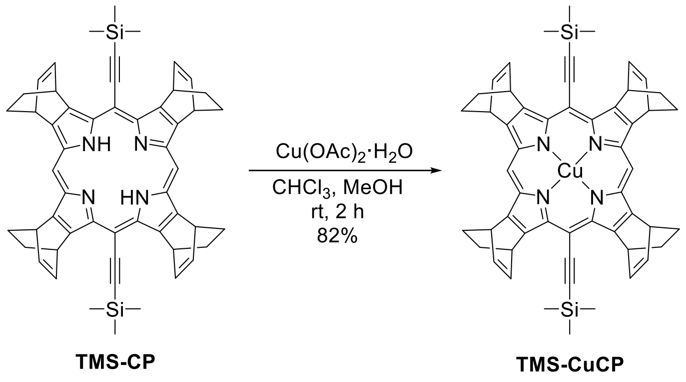

A saturated solution of Cu(OAc)$_2$·H$_2$O (344 mg, 1.72 mmol) in methanol (30 mL) was added to a solution of **TMS-CP** (250 mg, 0.307 mmol) in CHCl$_3$ (50 mL). After stirring for 4 h at room temperature, the reaction mixture was poured into water and extracted with CHCl$_3$. The organic layer was washed with water and brine, then dried over Na$_2$SO$_4$, and the solvent was removed under reduced pressure. The residue was purified by recrystallization (CHCl$_3$/MeOH) to give **TMS-CuCP** as purple crystals in 82% yield (221 mg, 0.252 mmol). HRMS (ESI): *m*/*z* [M + H]$^+$ calcd for C$_{54}$H$_{53}$CuN$_4$Si$_2$, 876.3105; found, 876.3119. Elemental analysis: calcd for C$_{54}$H$_{52}$CuN$_4$Si$_2$: C, 73.98; H, 5.98; N, 6.39. found: C, 73.92; H, 5.97; N, 6.41. UV–vis (CH$_2$Cl$_2$) $\lambda_{\max}$, nm ($\varepsilon \times 10^4$): 431 (39.9), 563 (1.47), 591 (2.23), 605 (2.31). (Experimental note-4, page 28–29, reaction No. 4-14)

[5,15-Bis(trimethylsilylethynyl)tetrakis(bicycle[2,2,2]octadieno)porphyrinato]nickel(II) (TMS-NiCP)

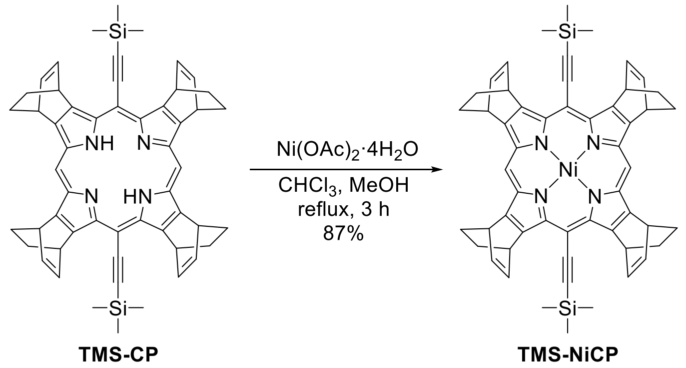

A solution of Ni(OAc)$_2$·4H$_2$O (153 mg, 0.615 mmol) in methanol (10 mL) was added to a solution of **TMS-CP** (50 mg, 0.0613 mmol) in CHCl$_3$ (25 mL) at room temperature. The mixture was refluxed for 7 h. After being cooled to room temperature, the reaction mixture was poured into water and extracted with CHCl$_3$. The organic layer was washed with saturated NaHCO$_3$ aqueous solution and water, then dried over Na$_2$SO$_4$, and the solvent was removed under reduced pressure. The residue was purified by recrystallization (CHCl$_3$/MeOH) to give **TMS-NiCP** as purple crystals in 80% yield (42.9 mg, 0.0492 mmol).

^{1}H NMR (400 MHz, $CDCl_3$, δ): 9.55 (m, 2H), 6.97 (m, 8H), 6.35 (m, 4H), 5.39 (m, 4H), 2.04–1.83 (m, 16H), 0.57 (m, 18 H). HRMS (ESI): *m*/*z* $[M + H]^+$ calcd for $C_{54}H_{53}N_4NiSi_2$, 871.3162; found, 871.3168. UV–vis (CH_2Cl_2) λ_{max}, nm ($\varepsilon \times 10^4$): 430 (29.6), 603 (1.95).
(Experimental note-5, page 66–67, reaction No. 5-33)

[5,15-Bis(triisopropylsilylethynyl)tetrakis(bicycle[2,2,2]octadieno)porphyrinato]zinc(II) (TIPS-ZnCP)

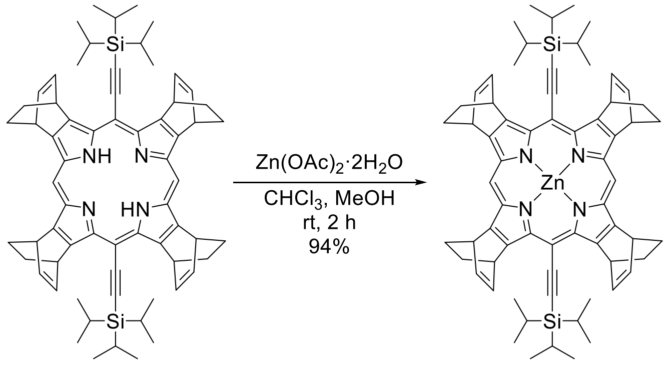

TIPS-CP **TIPS-ZnCP**

A solution of $Zn(OAc)_2 \cdot 2H_2O$ (226 mg, 1.03 mmol) in methanol (5.0 mL) was added to a solution of **TIPS-CP** (202 mg, 0.205 mmol) in $CHCl_3$ (25 mL). After stirring for 2 h at room temperature, the reaction mixture was poured into water and extracted with $CHCl_3$. The organic layer was washed with saturated $NaHCO_3$ aqueous solution and water, dried over Na_2SO_4, and the solvent was removed under a reduced pressure. The residue was purified by recrystallization ($CHCl_3$/MeOH) to give a target compound **TIPS-ZnCP** as purple crystals in 82% (202 mg, 0.193 mmol). ^{1}H NMR (400 MHz, $CDCl_3$, δ): 10.25 (s, 2H), 7.12–7.09 (m, 8H), 6.79–6.78 (m, 4H), 5.71–5.70 (m, 4H), 2.22–1.90 (m, 16H), 1.74–1.63 (m, 6H), 1.53–1.48 (m, 36H). ^{13}C NMR (100 MHz, $CDCl_3$, δ): 151.93, 151.89, 149.95, 149.90, 144.79, 144.77, 140.74, 140.72, 140.70, 137.66, 137.63, 137.61, 137.58, 136.26, 136.20, 110.12, 100.51, 100.48, 99.57, 99.55, 99.52, 98.62, 98.58, 39.21, 39.19, 36.18, 27.35, 27.29, 18.99, 18.97, 12.15. HRMS (ESI): *m*/*z* $[M + H]^+$ calcd for $C_{66}H_{77}N_4Si_2Zn$, 1045.4978; found, 1045.4977. UV–vis (CH_2Cl_2) λ_{max}, nm ($\varepsilon \times 10^4$): 433 (4.64), 563 (1.47), 569 (1.45), 599 (3.28), 609 (2.59).

(Experimental note-2, page 54–55, reaction No. 2-26)

[5,15-Bis(triisopropylsilylethynyl)tetrakis(bicycle[2,2,2]octadieno)porphyrinato]copper(II) (TIPS-CuCP)

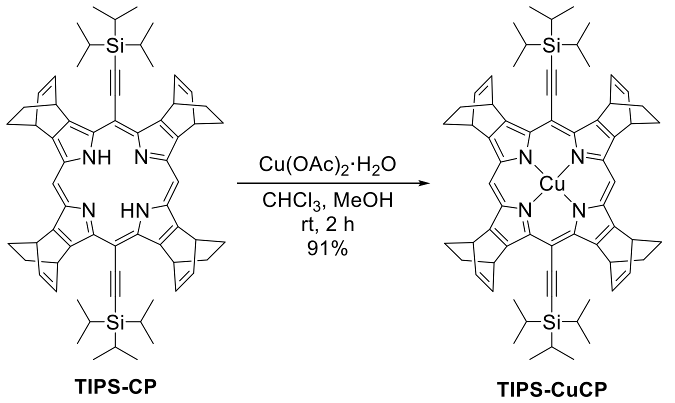

A solution of $Cu(OAc)_2 \cdot H_2O$ (407 mg, 2.04 mmol) in methanol (15 mL) was added to a solution of **TIPS-CP** (101 mg, 0.103 mmol) in $CHCl_3$ (50 mL). After stirring for 2 h at room temperature, the reaction mixture was washed with saturated $NaHCO_3$ aqueous solution, and water. The mixture was then dried over Na_2SO_4, and the solvent was removed under reduced pressure. The residue was purified by recrystallization ($CHCl_3$/MeOH) to give **TIPS-CuCP** as purple crystals in 91% yield (97.7 mg, 0.0935 mmol). HRMS (ESI): m/z $[M + H]^+$ calcd for $C_{66}H_{77}CuN_4Si_2$, 1044.4983; found, 1044.4984. UV–vis (CH_2Cl_2) λ_{max}, nm ($\varepsilon \times 10^4$): 431 (41.1), 562 (1.74), 592 (2.64), 604 (2.47).
(Experimental note-2, page 40–41, reaction No. 2-20)

[5,15-Bis(triisopropylsilylethynyl)tetrakis(bicycle[2,2,2]octadieno)porphyrinato]nickel(II) (TIPS-NiCP)

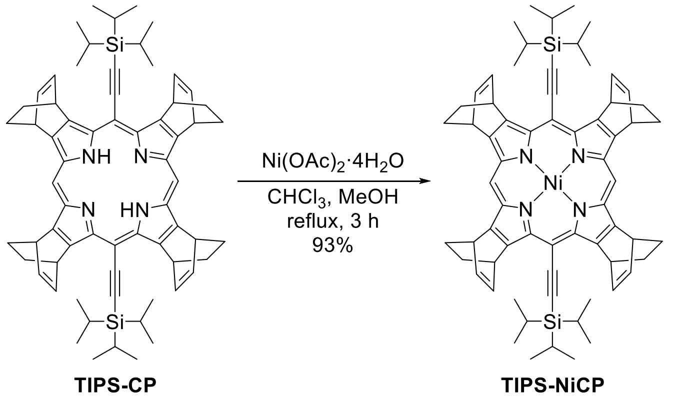

A solution of $Ni(OAc)_2 \cdot 4H_2O$ (507 mg, 2.04 mmol) in methanol (15 mL) was added to a solution of **TIPS-CP** (101 mg, 0.103 mmol) in $CHCl_3$ (50 mL) at room temperature. The mixture was refluxed for 3 h. After being cooled to room temperature, the reaction mixture was washed with saturated $NaHCO_3$ aqueous solution, and water. The mixture was then dried over Na_2SO_4, and the solvent was removed under reduced pressure. The residue was purified by recrystallization ($CHCl_3$/MeOH) to give **TIPS-NiCP** as purple crystals in 93% yield (98.6

mg, 0.0948 mmol). ^{1}H NMR (400 MHz, CDCl$_3$, δ): 9.51 (s, 2H), 6.96–6.93 (m, 8H), 6.42–6.40 (m, 4H), 5.38–5.37 (m, 4H), 2.07–1.78 (m, 16H), 1.52–1.43 (m, 6H), 1.36–1.33 (m, 36H). ^{13}C NMR (100 MHz, CDCl$_3$, δ): 151.91, 151.87, 151.83, 151.80, 151.77, 150.55, 150.52, 150.50, 137.19, 137.15, 136.40, 136.38, 136.36, 135.90, 135.86, 135.82, 135.78, 133.06, 133.03, 107.28, 104.73, 104.66, 98.14, 95.30, 95.26, 38.66, 38.63, 35.90, 35.88, 27.23, 27.20, 27.15, 18.86, 11.78. HRMS (ESI): *m/z* [M + H]$^+$ calcd for $C_{66}H_{77}N_4NiSi_2$, 1039.5040; found, 1039.5042. UV–vis (CH_2Cl_2) λ_{max}, nm ($\varepsilon \times 10^4$): 432 (23.8), 594 (1.65), 601 (1.62).
(Experimental note-2, page 40–41, reaction No. 2-19)

5,15-Bis(trimethylsilylethynyl)tetrabenzoporphyrin (TMS-BP)[20]

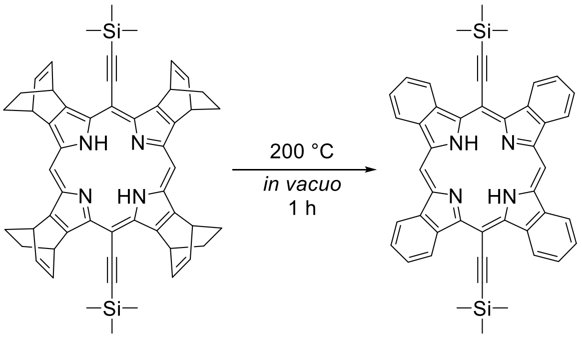

TMS-CP **TMS-BP**

TMS-CP was heated at 200 °C for 1 h in a sample tube under reduced pressure to give a target compound **TMS-BP** quantitatively as a deep blue solid. ^{1}H and ^{13}C NMR spectra were not available due to poor solubility.
(Experimental note-4, page 56–57, reaction No. 4-28)

[5,15-Bis(trimethylsilylethynyl)tetrabenzoporphyrinato]zinc(II) (TMS-ZnBP)[20]

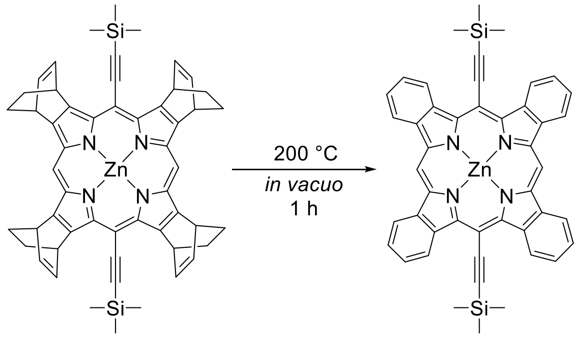

TMS-ZnCP **TMS-ZnBP**

TMS-ZnCP was heated at 200 °C for 1 h in a sample tube under reduced pressure to give a target compound **TMS-ZnBP** quantitatively as a deep blue solid. ^{1}H and ^{13}C NMR spectra were not available due to poor solubility.

[5,15-Bis(trimethylsilylethynyl)tetrabenzoporphyrinato]copper(II) (TMS-CuBP)

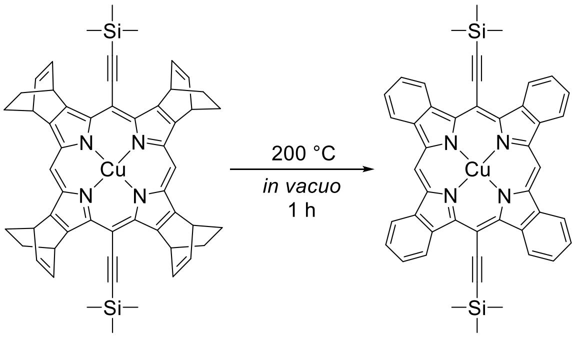

TMS-CuCP **TMS-CuBP**

TMS-CuCP was heated at 200 °C for 1 h in a sample tube under reduced pressure to give **TMS-CuBP** quantitatively as a deep blue solid. HRMS (MALDI): *m*/*z* [M]$^+$ calcd for $C_{46}H_{36}CuN_4Si_2$, 763.1789; found, 763.1769. UV–vis (DMF) λ_{max}, nm (ε × 10^4): 462 (38.6), 641 (3.27), 678 (7.81).
(Experimental note-4, page 58–59, reaction No. 4-29)

[5,15-Bis(trimethylsilylethynyl)tetrabenzoporphyrinato]nickel(II) (TMS-NiBP)

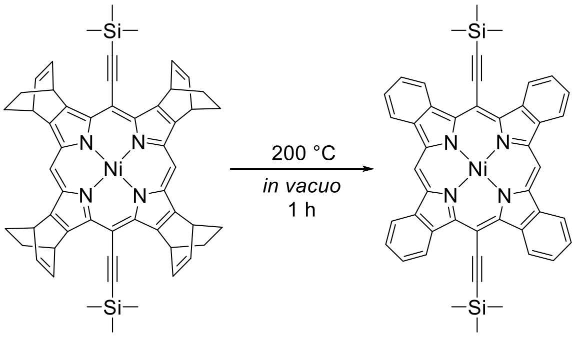

TMS-NiCP **TMS-NiBP**

TMS-NiCP was heated at 200 °C for 1 h in a sample tube under reduced pressure to give **TMS-NiBP** quantitatively as a deep blue solid. ^{1}H and ^{13}C NMR spectra were not available due to poor solubility. HRMS (MALDI): *m*/*z* [M]$^+$ calcd for $C_{46}H_{36}N_4Si_2Ni$, 758.1837; found, 758.1827. UV–vis (DMF) λ_{max}, nm (ε × 10^4): 462 (30.0), 642 (2.53), 677 (4.94).

5,15-Bis(triisopropylsilylethynyl)tetrabenzoporphyrin (TIPS-BP)

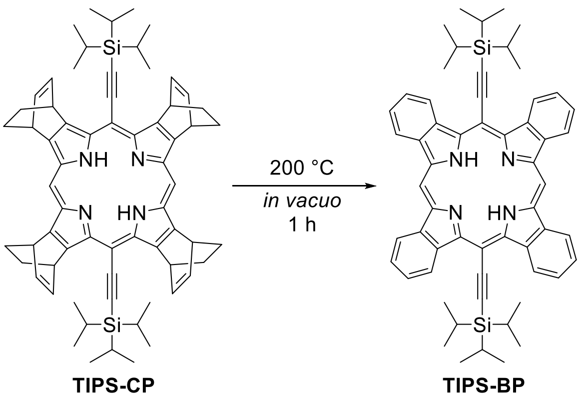

TIPS-CP was heated at 200 °C for 1 h in a sample tube under reduced pressure to give a target compound quantitatively **TIPS-BP** as a black solid. ^{1}H NMR (400 MHz, $CDCl_3$, δ): 10.19 (d, J = 7.8 Hz, 4H), 10.00 (s, 2H), 9.17 (d, J = 7.8 Hz, 4H), 8.02 (t, J = 7.8 Hz, 4H), 7.90 (d, J = 7.8 Hz, 4H), 1.83–1.74 (m, 6H), 1.65–1.63 (m, 36H), –3.19 (s, 2H). ^{13}C NMR (100 MHz, $CDCl_3$, δ): 142.30, 137.79, 136.17, 134.82, 126.91, 126.80, 125.50, 120.25, 108.55, 104.06, 94.51, 92.80, 19.30, 12.06. HRMS (ESI): m/z $[M + H]^+$ calcd for $C_{58}H_{63}N_4Si_2$, 871.4591; found, 871.4592. UV–vis (CH_2Cl_2) λ_{max}, nm ($\varepsilon \times 10^4$): 711 (5.79), 626 (4.93), 583 (1.20), 462 (56.2), 452 (28.8), 437 (8.05), 424 (5.72).

(Experimental note-2, page 56–57, reaction No. 2-35)

[5,15-Bis(triisopropylsilylethynyl)tetrabenzoporphyrinato]zinc(II) (TIPS-ZnBP)

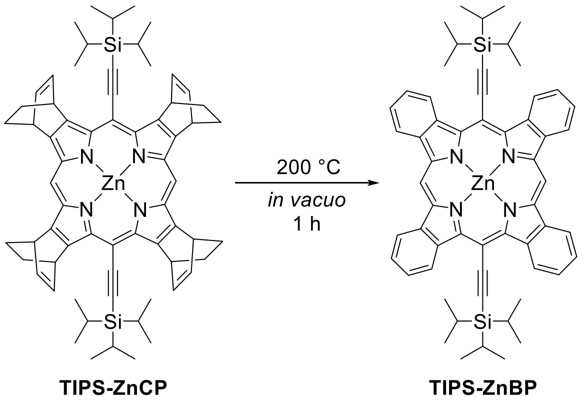

TIPS-ZnCP was heated at 200 °C for 1 h in a sample tube under reduced pressure to give a target compound quantitatively **TIPS-ZnBP** as a black solid. ^{1}H NMR (400 MHz, pyridine-d_5, δ): 11.34 (s, 2H), 11.11–11.07 (m, 4H), 9.86–9.84 (m, 4H), 8.30–8.25 (m, 8H), 1.78–1.67 (m, 6H), 1.53–1.51 (m, 36H). ^{13}C NMR (100 MHz, pyridine-d_5, δ): 146.54, 143.39, 140.49, 138.79, 127.68, 127.39, 127.14, 121.62, 111.75, 105.36, 96.60, 19.30, 12.16. HRMS (ESI): m/z $[M + Na]^+$ calcd for $C_{58}H_{60}N_4NaSi_2Zn$, 955.3546; found, 955.3544. UV–vis (THF) λ_{max}, nm ($\varepsilon \times 10^4$): 468 (61.7), 632 (1.96), 647 (1.87), 681 (9.96).

(Experimental note-2, page 56–57, reaction No. 2-41)

[5,15-Bis(triisopropylsilylethynyl)tetrabenzoporphyrinato]copper(II) (TIPS-CuBP)

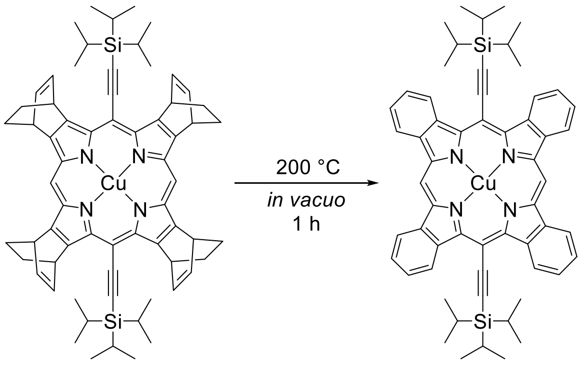

TIPS-CuCP **TIPS-CuBP**

TIPS-CuCP was heated at 200 °C for 1 h in a sample tube under reduced pressure to give **TIPS-CuBP** quantitatively. HRMS (ESI): *m*/*z* [M + Na]$^+$ calcd for $C_{58}H_{60}CuN_4NaSi_2$, 954.3550; found, 954.3551. UV–vis (CH_2Cl_2) λ_{max}, nm ($\varepsilon \times 10^4$): 682 (5.75), 642 (2.64), 463 (32.0), 314 (1.75).
(Experimental note-2, page 56–57, reaction No. 2-41)

[5,15-Bis(triisopropylsilylethynyl)tetrabenzoporphyrinato]nickel(II) (TIPS-NiBP)

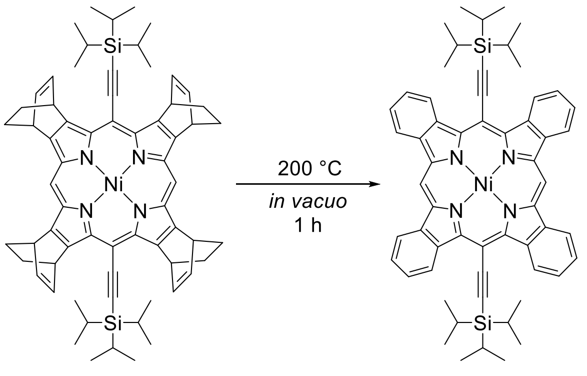

TIPS-NiCP **TIPS-NiBP**

TIPS-NiCP was heated at 200 °C for 1 h in a sample tube under reduced pressure to give **TIPS-NiBP** quantitatively as a dark green solid. ^{1}H NMR (400 MHz, $CDCl_3$, δ): 9.97 (d, *J* = 7.6 Hz, 4H), 8.92 (s, 2H), 8.70 (d, *J* = 7.6 Hz, 4H), 7.91 (t, *J* = 7.6 Hz, 4H), 7.81 (t, *J* = 7.6 Hz, 4H), 1.53–1.44 (m, 6H), 1.36–1.35 (m, 36H). ^{13}H NMR (100 MHz, $CDCl_3$, δ): 138.25, 137.34, 136.58, 133.58, 126.19, 125.95, 124.66, 119.69, 108.51, 106.41, 94.18, 92.37, 18.96, 11.71. HRMS (ESI): *m*/*z* [M + H]$^+$ calcd for $C_{58}H_{61}N_4NiSi_2$, 927.3788; found, 927.3787. UV–vis (CH_2Cl_2): λ_{max}, nm ($\varepsilon \times 10^4$): 689 (4.51), 645 (2.48), 465 (22.6), 314 (2.08).
(Experimental note-2, page 90, reaction No. 2-37)

2-10-3. Photoabsorption Spectra

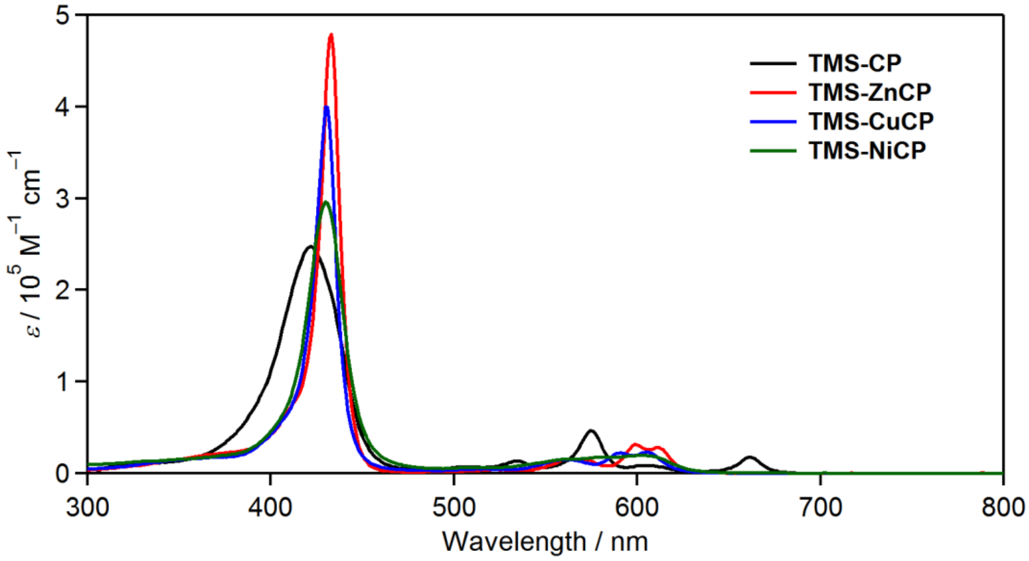

Figure S2-17. Absorption spectra of TMS-CPs in CH_2Cl_2.

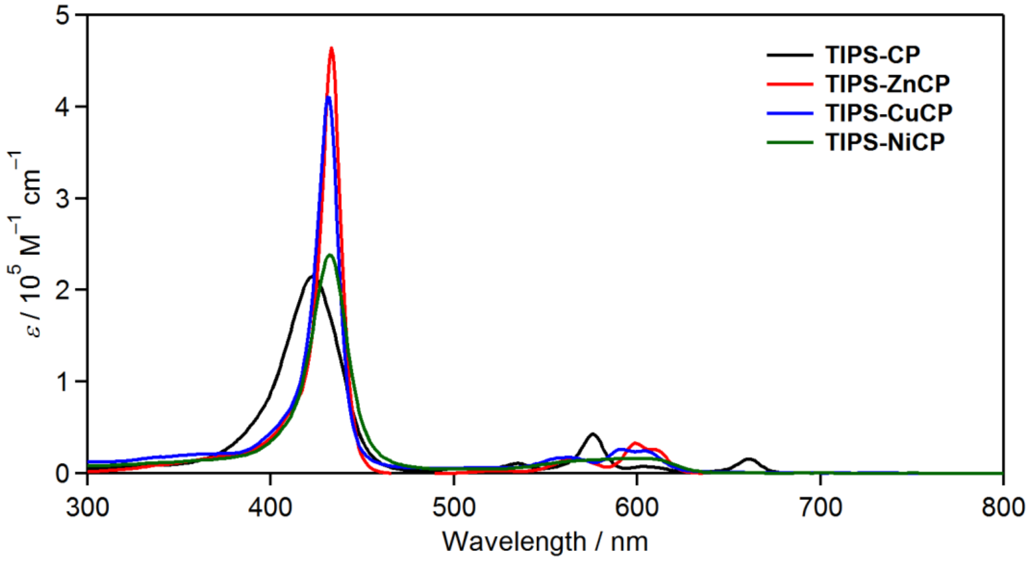

Figure S2-18. Absorption spectra of TIPS-CPs in CH_2Cl_2.

2-10-4. NMR Spectra

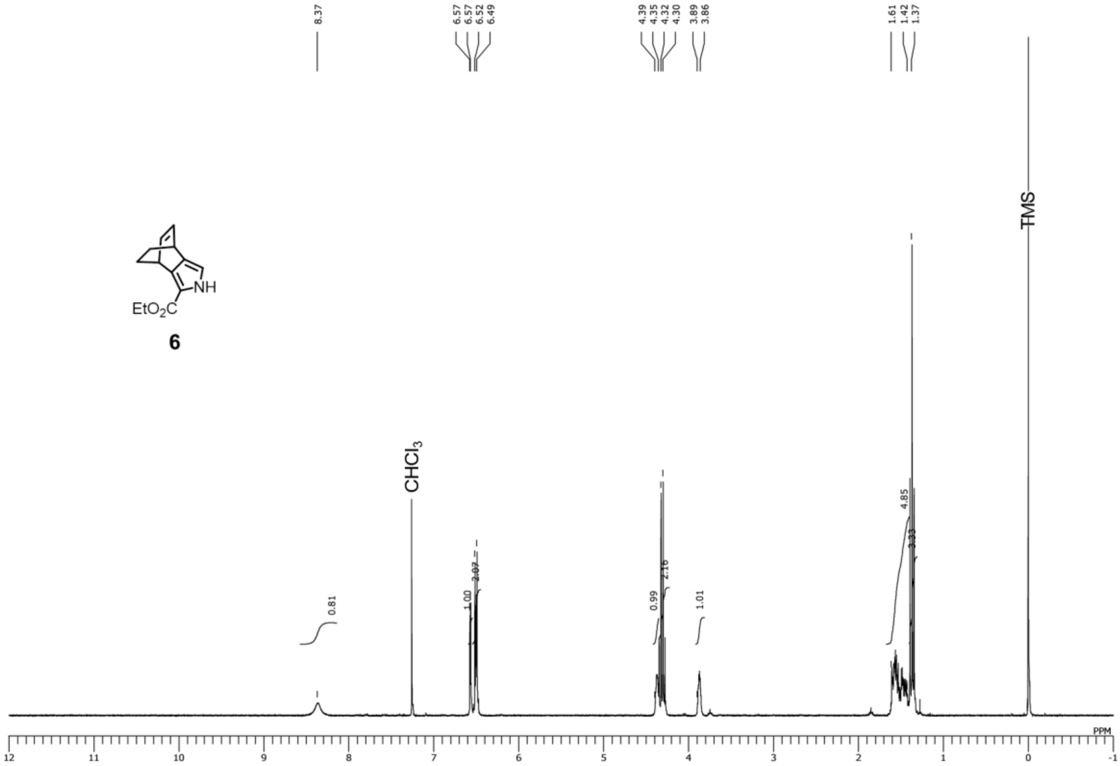

Figure S2-19. ^{1}H NMR spectrum of **6** in $CDCl_3$.

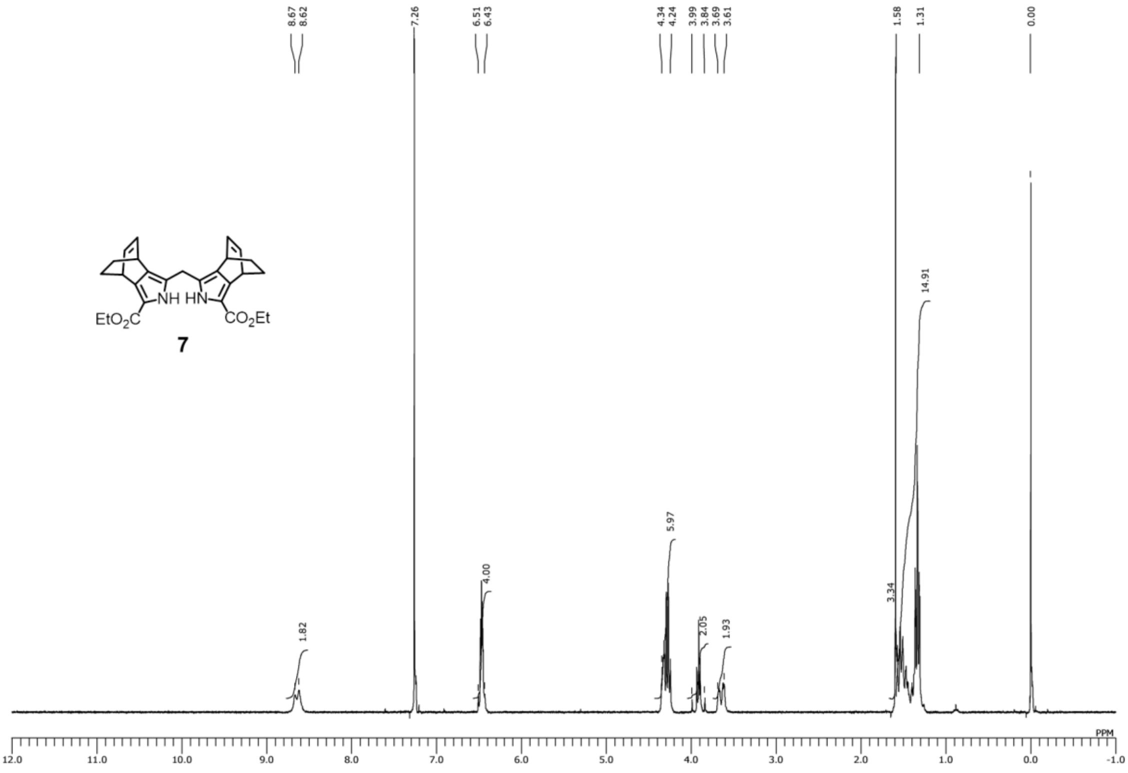

Figure S2-20. ^{1}H NMR spectrum of **7** in $CDCl_3$.

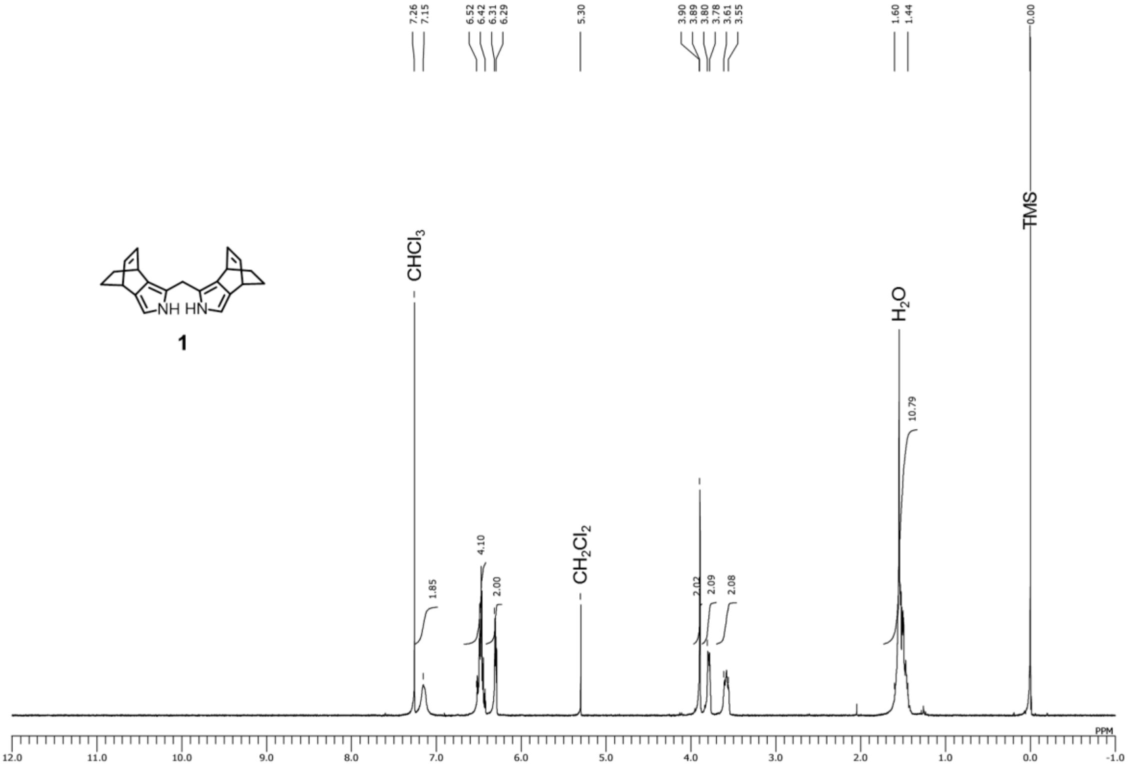

Figure S2-21. ^{1}H NMR spectrum of **1** in CDCl$_3$.

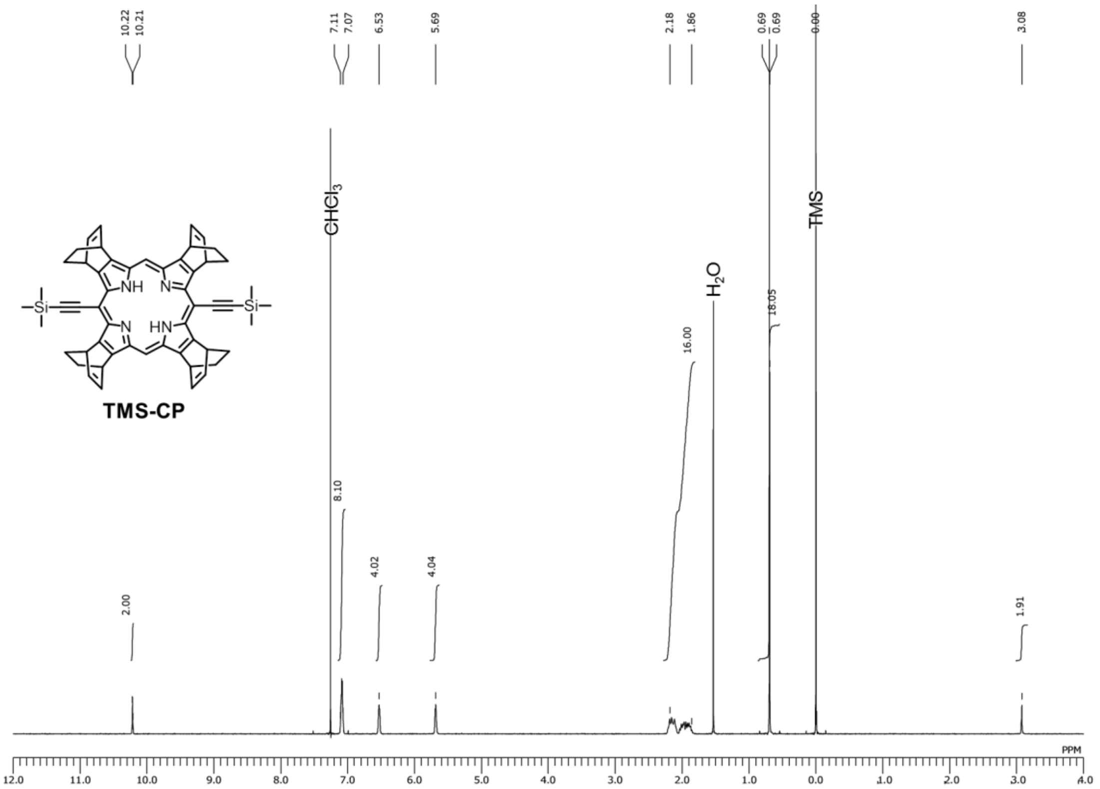

Figure S2-22. ^{1}H NMR spectrum of **TMS-CP** in CDCl$_3$.

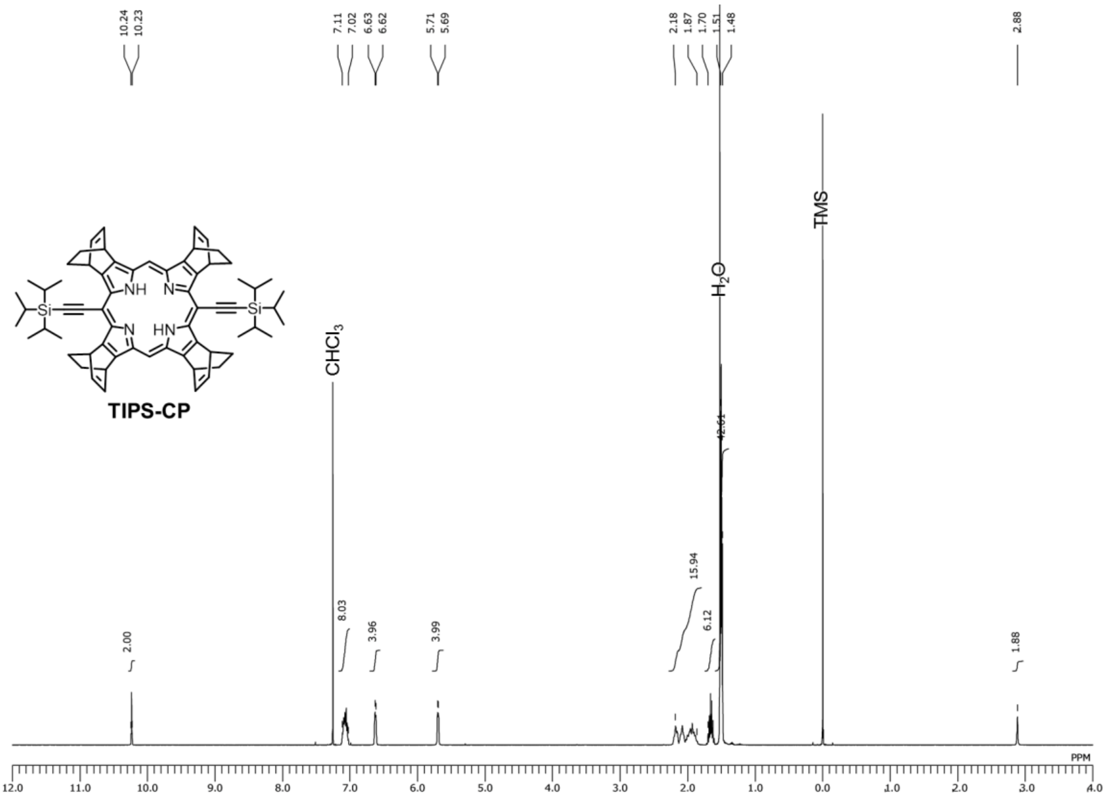

Figure S2-23. ^{1}H NMR spectrum of **TIPS-CP** in CDCl$_3$.

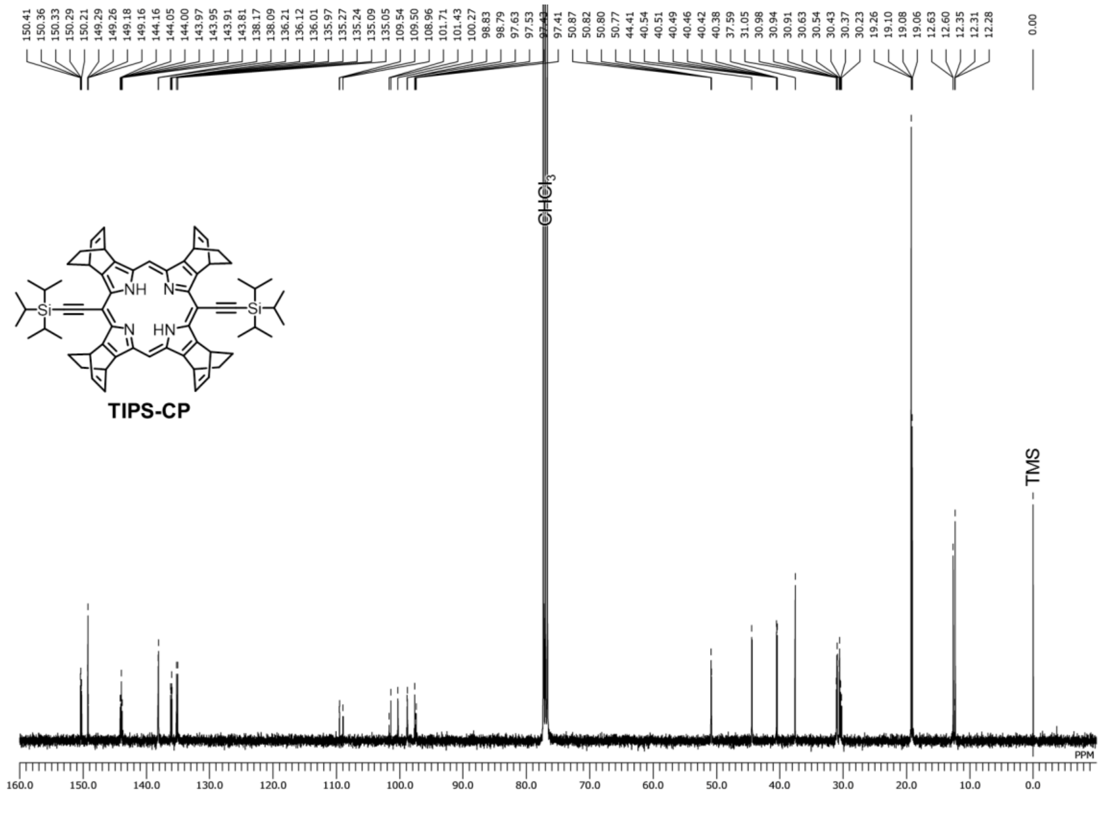

Figure S2-24. ^{13}C NMR spectrum of **TIPS-CP** in CDCl$_3$.

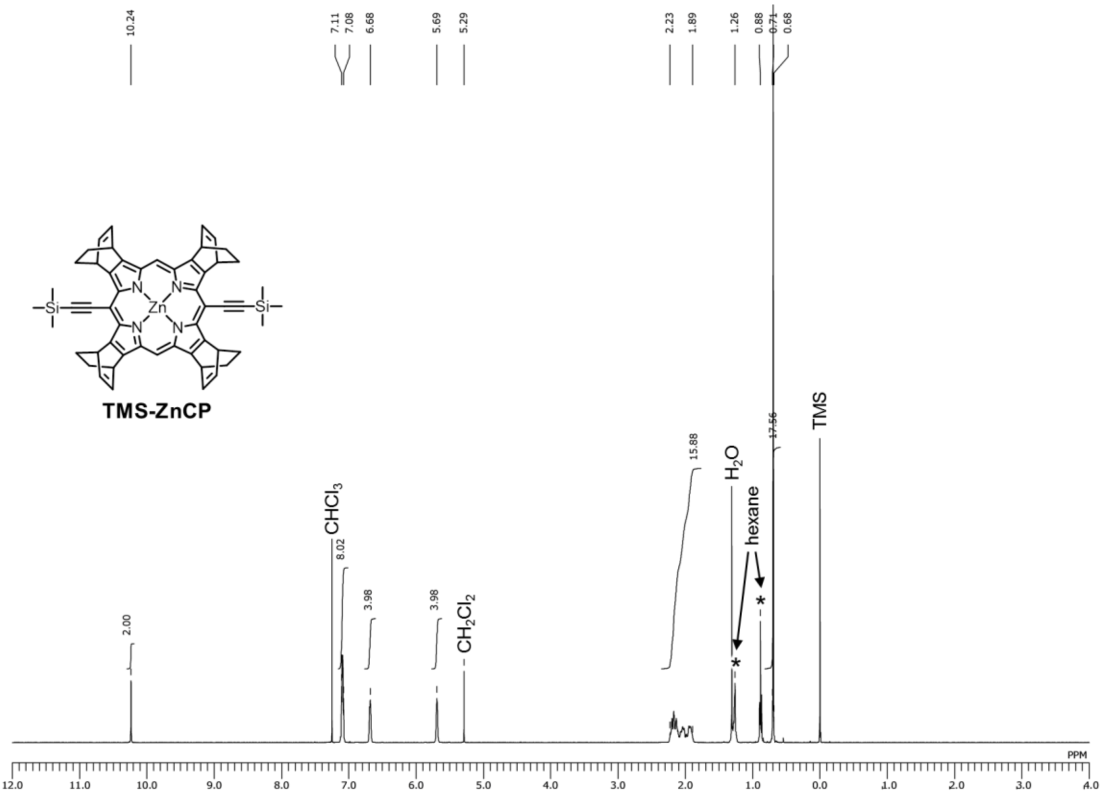

Figure S2-25. ^{1}H NMR spectrum of **TMS-ZnCP** in $CDCl_3$.

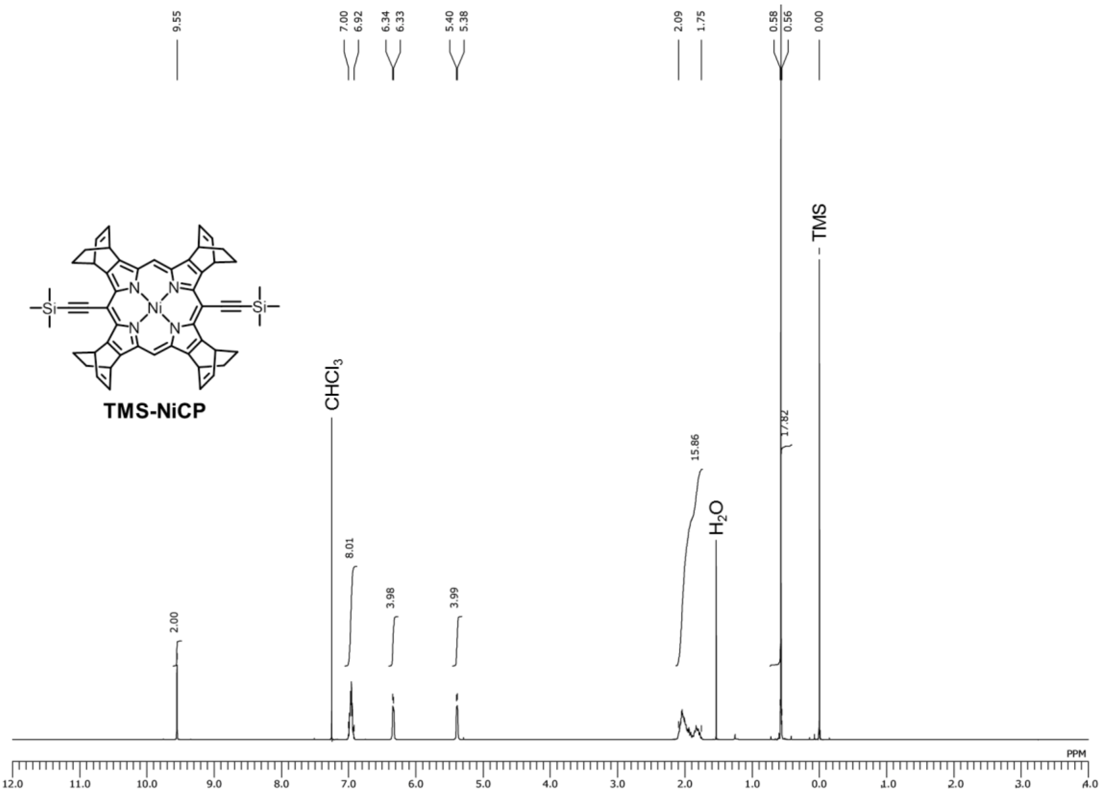

Figure S2-26. ^{1}H NMR spectrum of **TMS-NiCP** in $CDCl_3$.

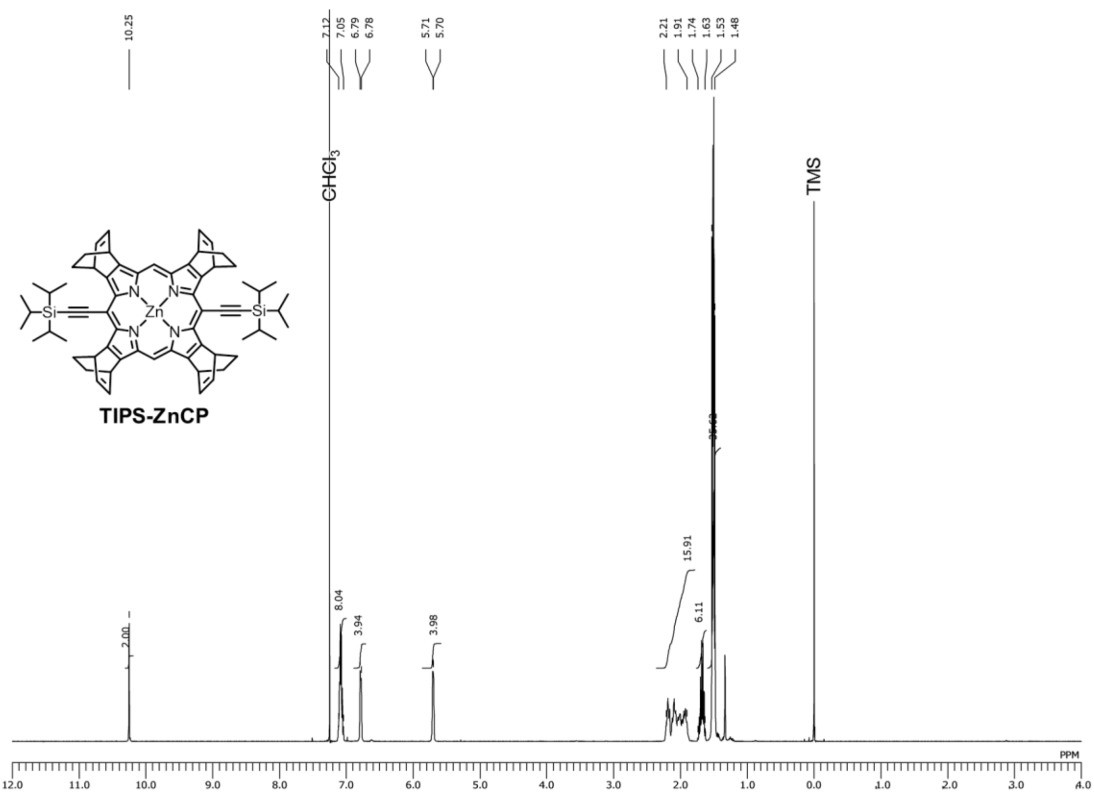

Figure S2-27. ^{1}H NMR spectrum of **TIPS-ZnCP** in CDCl$_3$.

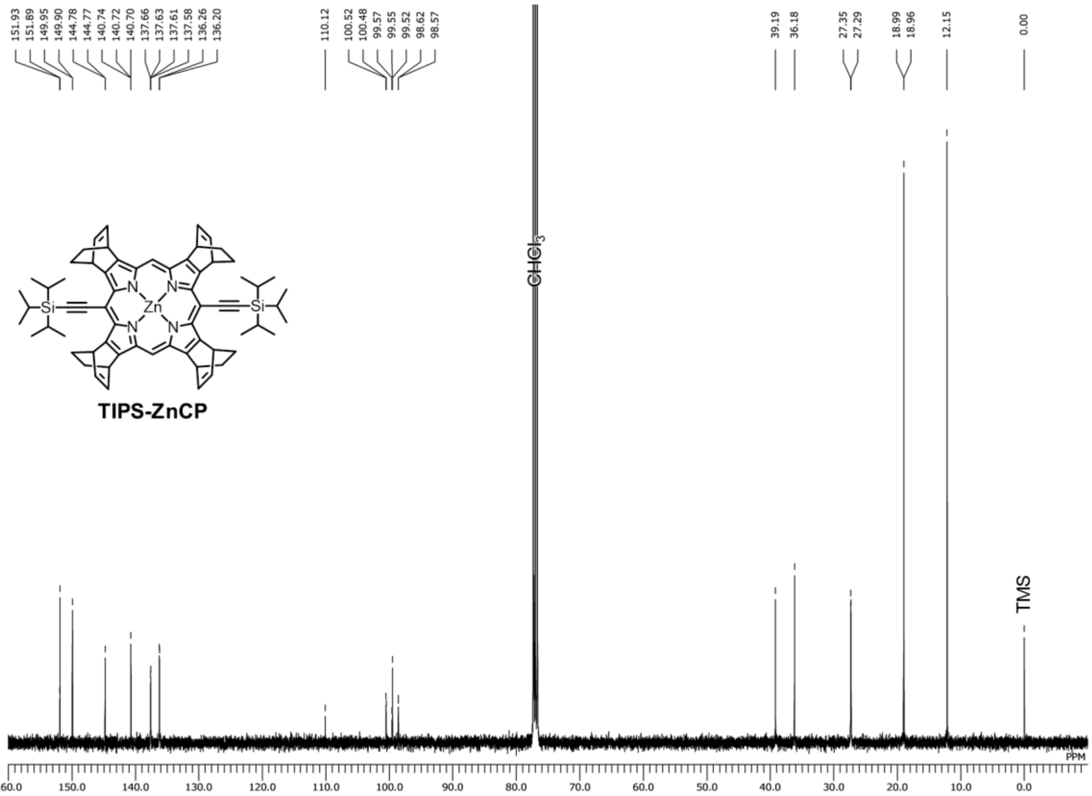

Figure S2-28. ^{13}C NMR spectrum of **TIPS-ZnCP** in CDCl$_3$.

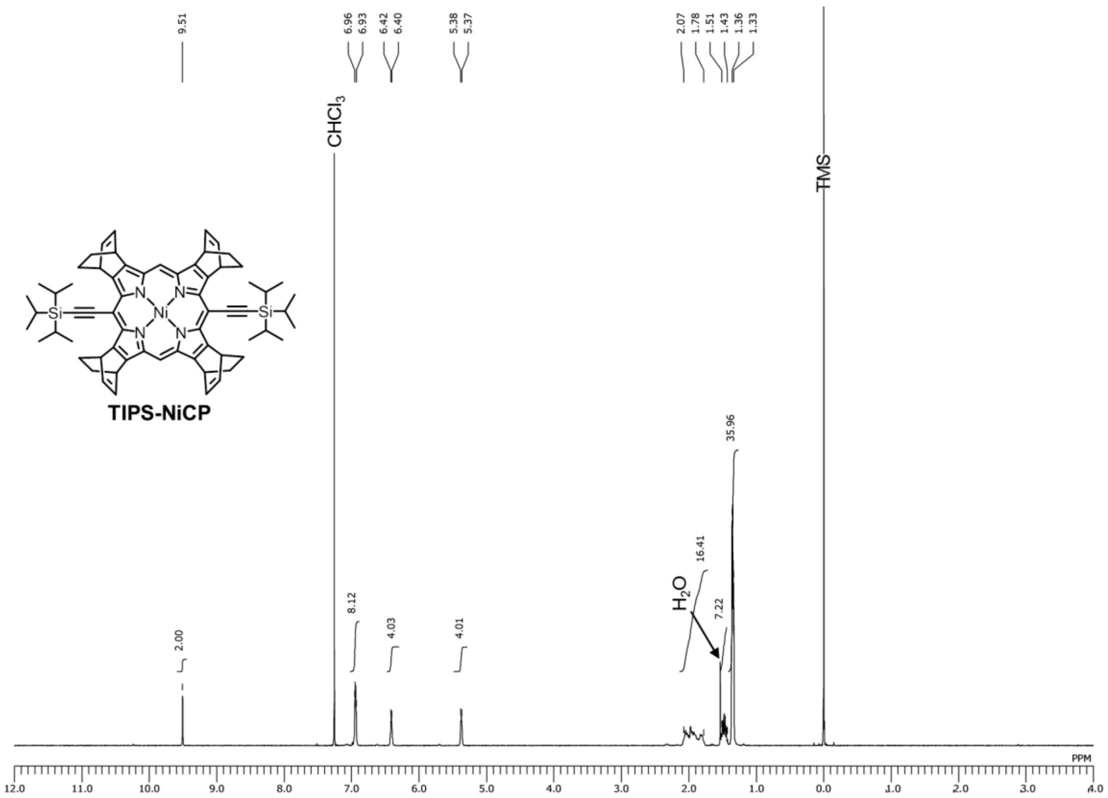

Figure S2-29. ^{1}H NMR spectrum of **TIPS-NiCP** in CDCl$_3$.

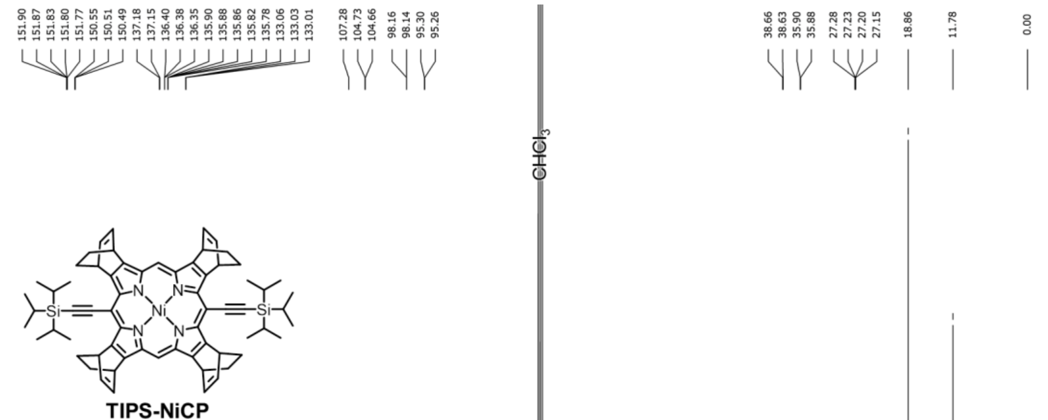

Figure S2-30. ^{13}C NMR spectrum of **TIPS-NiCP** in CDCl$_3$.

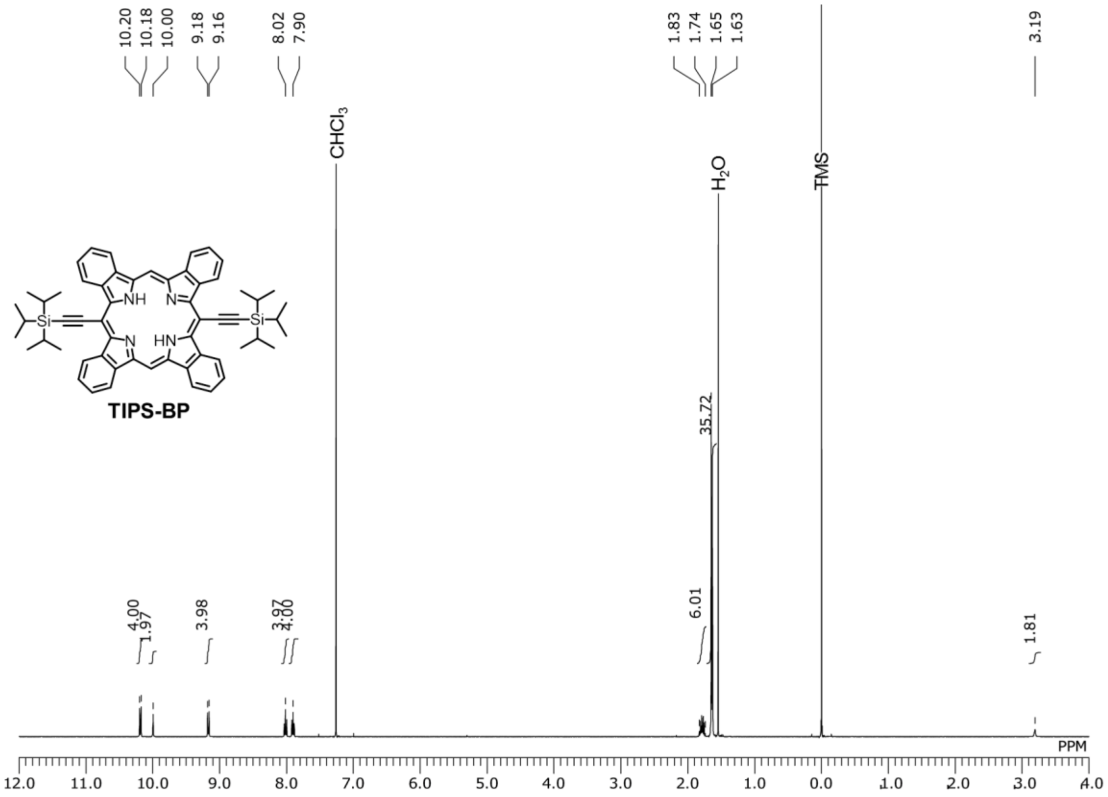

Figure S2-30. ^{1}H NMR spectrum of **TIPS-BP** in CDCl$_3$.

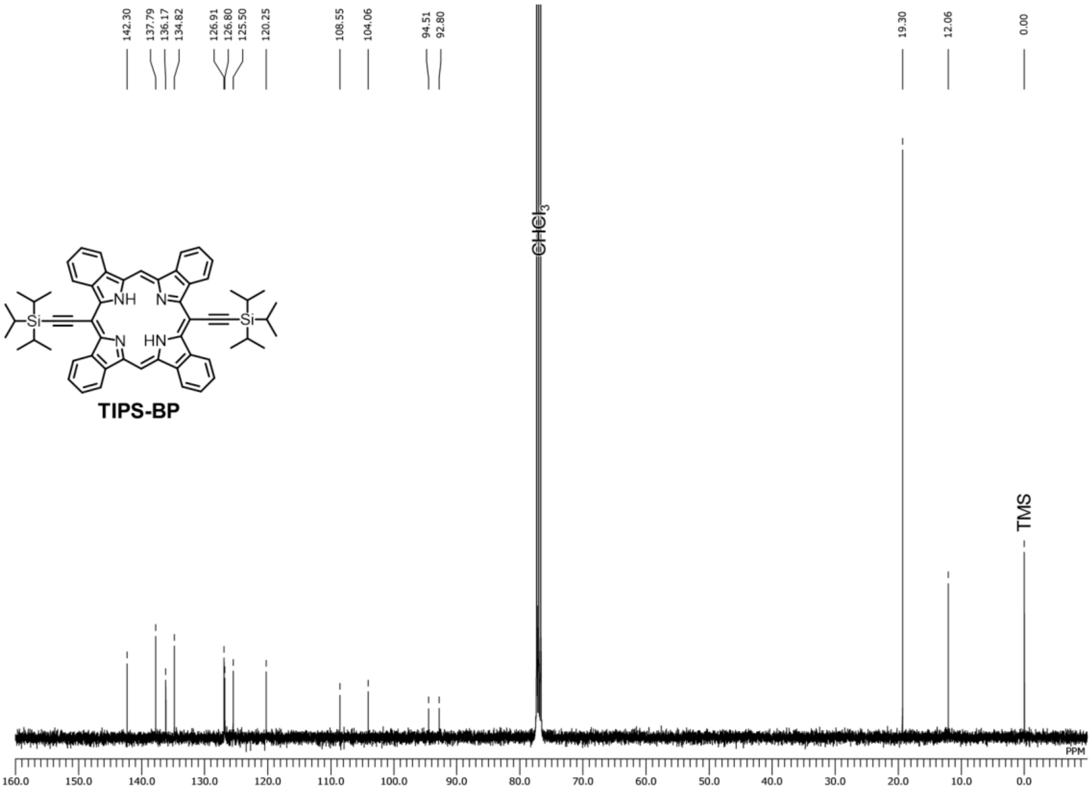

Figure S2-32. ^{13}C NMR spectrum of **TIPS-BP** in CDCl$_3$.

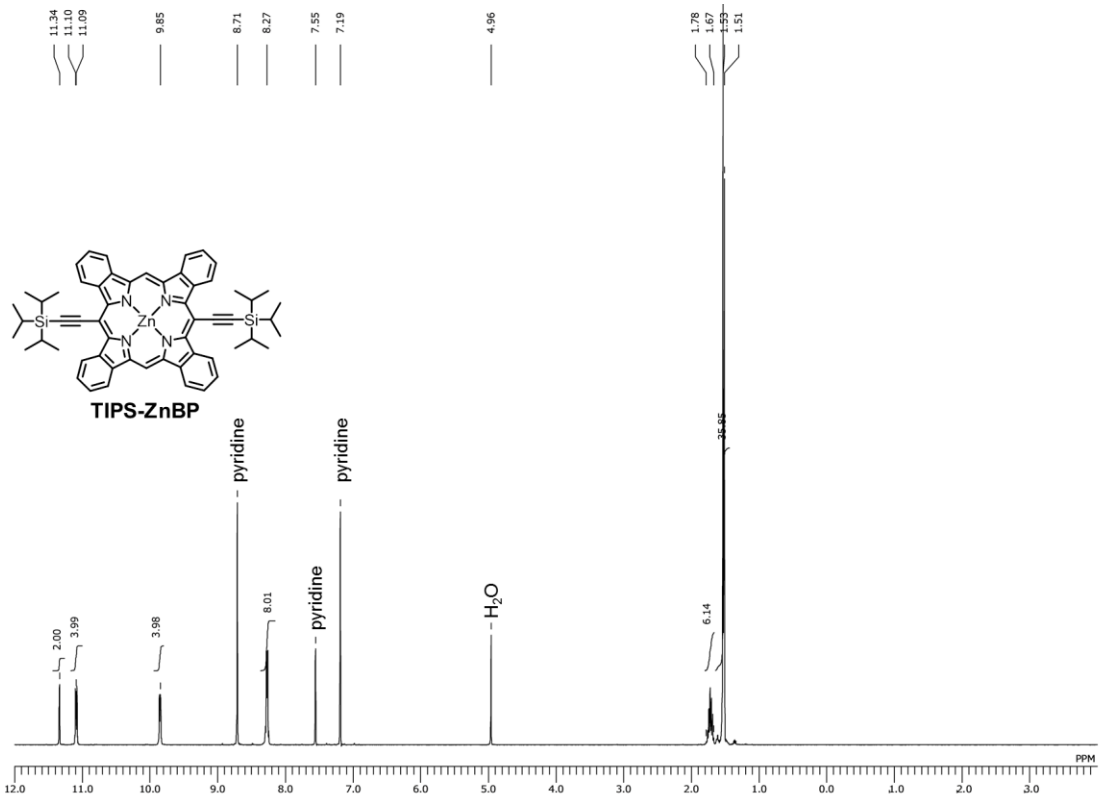

Figure S2-33. ^{1}H NMR spectrum of **TIPS-ZnBP** in pyridine-d_5.

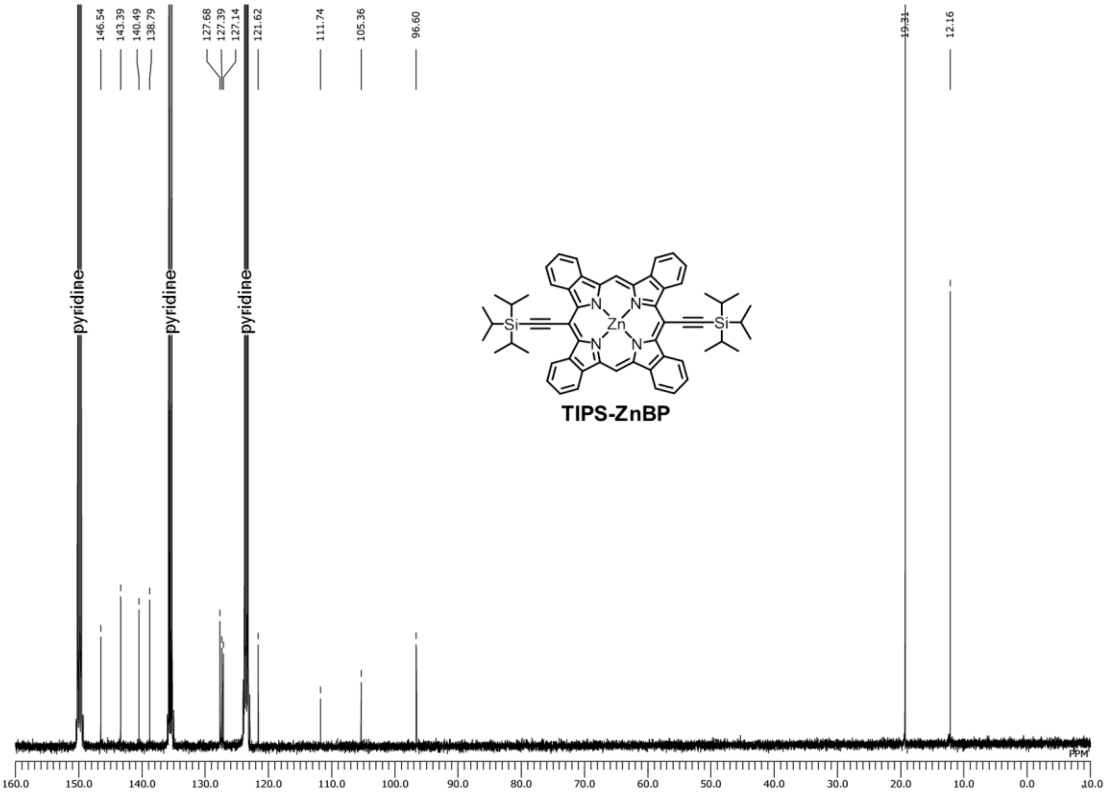

Figure S2-34. ^{13}C NMR spectrum of **TIPS-CP** in pyridine-d_5.

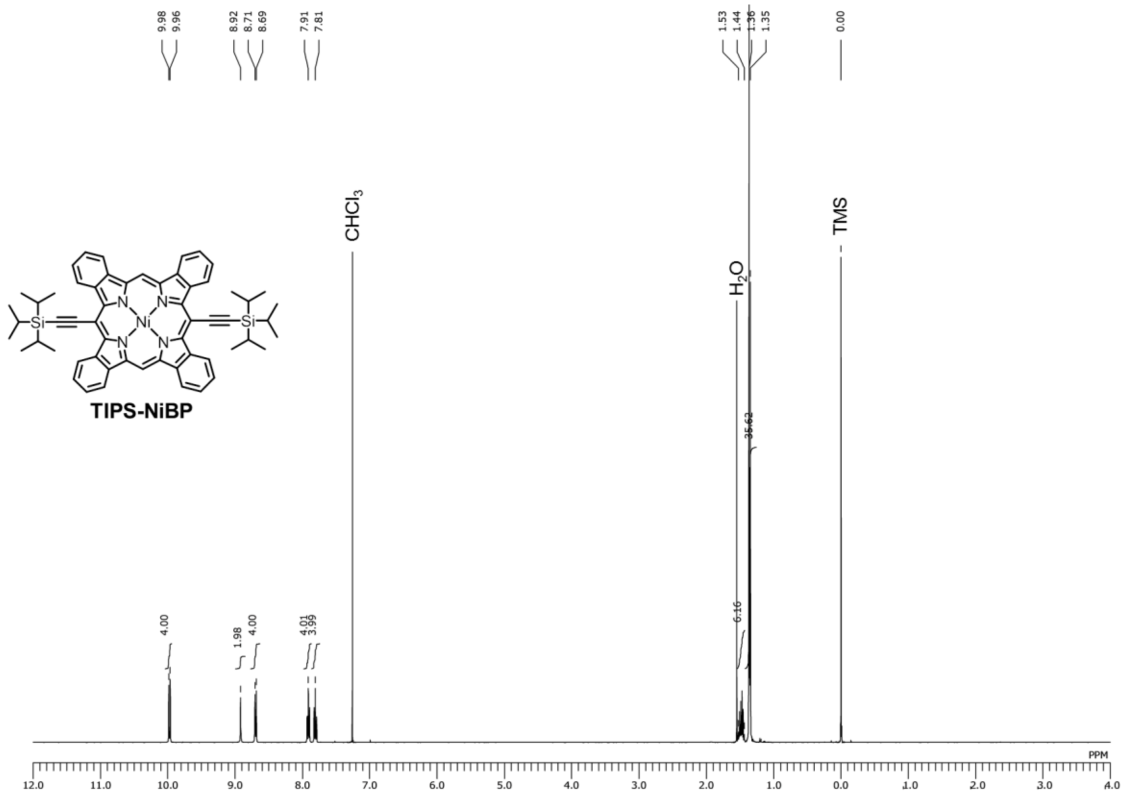

Figure S2-35. ^{1}H NMR spectrum of **TIPS-NiBP** in CDCl$_3$.

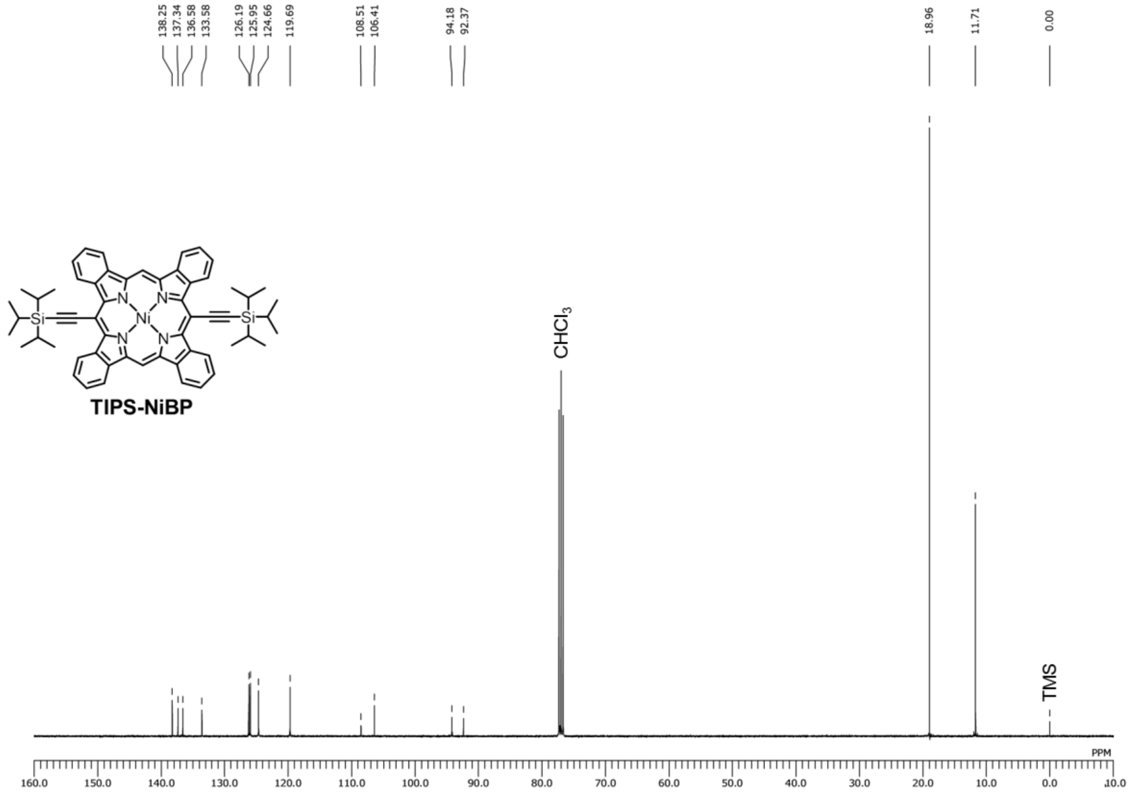

Figure S2-36. ^{13}C NMR spectrum of **TIPS-NiBP** in CDCl$_3$.

2-11. References

(1) Shea, P. B.; Kanicki, J.; Pattison, L. R.; Petroff, P.; Kawano, M.; Yamada, H.; Ono, N. Solution-Processed Nickel Tetrabenzoporphyrin Thin-Film Transistors. *J. Appl. Phys.* **2006**, *100*, 34502.

(2) Shea, P. B.; Yamada, H.; Ono, N.; Kanicki, J. Solution-Processed Zinc Tetrabenzoporphyrin Thin-Films and Transistors. *Thin Solid Films* **2012**, *520*, 4031–4035.

(3) Shea, P. B.; Pattison, L. R.; Kawano, M.; Chen, C.; Chen, J.; Petroff, P.; Martin, D. C.; Yamada, H.; Ono, N.; Kanicki, J. Solution-Processed Polycrystalline Copper Tetrabenzoporphyrin Thin-Film Transistors. *Synth. Met.* **2007**, *157*, 190–197.

(4) Noguchi, N.; Junwei, S.; Asatani, H.; Matsuoka, M. Control of Morphology and Orientation of a Thin Film Tetrabenzoporphyrin (TBP) Organic Semiconductor by Solid-State Crystallization. *Cryst. Growth Des.* **2010**, *10*, 1848–1853.

(5) Minemawari, H.; Yamada, T.; Matsui, H.; Tsutsumi, J.; Haas, S.; Chiba, R.; Kumai, R.; Hasegawa, T. Inkjet Printing of Single-Crystal Films. *Nature* **2011**, *475*, 364–367.

(6) Yuan, Y.; Giri, G.; Ayzner, A. L.; Zoombelt, A. P.; Mannsfeld, S. C. B.; Chen, J.; Nordlund, D.; Toney, M. F.; Huang, J.; Bao, Z. Ultra-High Mobility Transparent Organic Thin Film Transistors Grown by an Off-Centre Spin-Coating Method. *Nat. Commun.* **2014**, *5*, 3005.

(7) Iino, H.; Usui, T.; Hanna, J. Liquid Crystals for Organic Thin-Film Transistors. *Nat. Commun.* **2015**, *6*, 6828.

(8) Xu, X.; Yao, Y.; Shan, B.; Gu, X.; Liu, D.; Liu, J.; Xu, J.; Zhao, N.; Hu, W.; Miao, Q. Electron Mobility Exceeding 10 $cm^2 V^{-1} s^{-1}$ and Band-Like Charge Transport in Solution-Processed n-Channel Organic Thin-Film Transistors. *Adv. Mater.* **2016**, *28*, 5276–5283.

(9) Paterson, A. F.; Treat, N. D.; Zhang, W.; Fei, Z.; Wyatt-Moon, G.; Faber, H.; Vourlias,

G.; Patsalas, P. A.; Solomeshch, O.; Tessler, N.; Heeney, M.; Anthopoulos, T. D. Small Molecule/Polymer Blend Organic Transistors with Hole Mobility Exceeding 13 cm^2 V^{-1} s^{-1}. *Adv. Mater.* **2016**, *28*, 7791–7798.

(10) Anthony, J. E.; Brooks, J. S.; Eaton, D. L.; Parkin, S. R. Functionalized Pentacene: Improved Electronic Properties from Control of Solid-State Order. *J. Am. Chem. Soc.* **2001**, *123*, 9482–9483.

(11) Maliakal, A.; Raghavachari, K.; Katz, H.; Chandross, E.; Siegrist, T. Photochemical Stability of Pentacene and a Substituted Pentacene in Solution and in Thin Films. *Chem. Mater.* **2004**, *16*, 4980–4986.

(12) Anthony, J. E.; Eaton, D. L.; Parkin, S. R. A Road Map to Stable, Soluble, Easily Crystallized Pentacene Derivatives. *Org. Lett.* **2002**, *4*, 15–18.

(13) Anthony, J. E. Functionalized Acenes and Heteroacenes for Organic Electronics. *Chem. Rev.* **2006**, *106*, 5028–5048.

(14) Diao, Y.; Tee, B. C.-K.; Giri, G.; Xu, J.; Kim, D. H.; Becerril, H. A.; Stoltenberg, R. M.; Lee, T. H.; Xue, G.; Mannsfeld, S. C. B.; Bao, Z. Solution Coating of Large-Area Organic Semiconductor Thin Films with Aligned Single-Crystalline Domains. *Nat. Mater.* **2013**, *12*, 665–671.

(15) Matsuo, Y.; Sato, Y.; Niinomi, T.; Soga, I.; Tanaka, H.; Nakamura, E. Columnar Structure in Bulk Heterojunction in Solution-Processable Three-Layered p-i-n Organic Photovoltaic Devices Using Tetrabenzoporphyrin Precursor and Silylmethyl[60]fullerene. *J. Am. Chem. Soc.* **2009**, *131*, 16048–16050.

(16) Mikhnenko, O. V.; Blom, P. W. M.; Nguyen, T.-Q. Exciton Diffusion in Organic Semiconductors. *Energy Environ. Sci.* **2015**, *8*, 1867–1888.

(17) Guide, M.; Dang, X.-D.; Nguyen, T.-Q. Nanoscale Characterization of Tetrabenzoporphyrin and Fullerene-Based Solar Cells by Photoconductive Atomic Force Microscopy. *Adv. Mater.* **2011**, *23*, 2313–2319.

(18) Tamura, Y.; Saeki, H.; Hashizume, J.; Okazaki, Y.; Kuzuhara, D.; Suzuki, M.; Aratani, N.; Yamada, H. Direct Comparison of a Covalently-Linked Dyad and a 1:1 Mixture of Tetrabenzoporphyrin and Fullerene as Organic Photovoltaic Materials. *Chem. Commun.* **2014**, *50*, 10379–10381.

(19) Kan, B.; Li, M.; Zhang, Q.; Liu, F.; Wan, X.; Wang, Y.; Ni, W.; Long, G.; Yang, X.; Feng, H.; Zuo, Y.; Zhang, M.; Huang, F.; Cao, Y.; Russell, T. P.; Chen, Y. A Series of Simple Oligomer-like Small Molecules Based on Oligothiophenes for Solution-Processed Solar Cells with High Efficiency. *J. Am. Chem. Soc.* **2015**, *137*, 3886–3893.

(20) Deng, D.; Zhang, Y.; Zhang, J.; Wang, Z.; Zhu, L.; Fang, J.; Xia, B.; Wang, Z.; Lu, K.; Ma, W.; Wei, Z. Fluorination-Enabled Optimal Morphology Leads to over 11% Efficiency for Inverted Small-Molecule Organic Solar Cells. *Nat. Commun.* **2016**, *7*, 13740.

(21) Yamada, H.; Kushibe, K.; Okujima, T.; Uno, H.; Ono, N. Novel One-Pot Synthesis of 5-Alkenyl-15-Alkynylporphyrins and Their Derivatisation to a Butadiyne-Linked Benzoporphyrin Dimer. *Chem. Commun.* **2006**, *4*, 383–385.

(22) Guide, M.; Lin, J. D. A.; Proctor, C. M.; Chen, J.; García-Cervera, C.; Nguyen, T.-Q. Effect of Copper Metalation of Tetrabenzoporphyrin Donor Material on Organic Solar Cell Performance. *J. Mater. Chem. A* **2014**, *2*, 7890–7896.

(23) Takahashi, K.; Kuzuhara, D.; Aratani, N.; Yamada, H. Synthesis and Crystal Structures of 5,15-Bis(triisopropylsilylethynyl)-tetrabenzoporphyrins. *J. Photopolym. Sci. Technol.* **2013**, *26*, 213–216.

(24) Aramaki, S.; Mizuguchi, J. 29*H*,31*H*-Tetrabenzo[*b*,*g*,*l*,*q*]porphin. *Acta Crystallogr. Sect. E: Crystallogr. Commun.* **2003**, *E59*, o1556–o1558.

(25) Brédas, J. L.; Calbert, J. P.; da Silva Filho, D. A.; Cornil, J. Organic Semiconductors: A Theoretical Characterization of the Basic Parameters Governing Charge Transport.

Proc. Natl. Acad. Sci. U. S. A. **2002**, *99*, 5804–5809.

(26) Senthilkumar, K.; Grozema, F. C.; Bickelhaupt, F. M.; Siebbeles, L. D. A. Charge Transport in Columnar Stacked Triphenylenes: Effects of Conformational Fluctuations on Charge Transfer Integrals and Site Energies. *J. Chem. Phys.* **2003**, *119*, 9809–9817.

(27) Deng, W.-Q.; Goddard, W. A. Predictions of Hole Mobilities in Oligoacene Organic Semiconductors from Quantum Mechanical Calculations. *J. Phys. Chem. B* **2004**, *108*, 8614–8621.

(28) Niimi, K.; Shinamura, S.; Osaka, I.; Miyazaki, E.; Takimiya, K. Dianthra[2,3-*b*:2′,3′-*f*]thieno[3,2-*b*]thiophene (DATT): Synthesis, Characterization, and FET Characteristics of New π-Extended Heteroarene with Eight Fused Aromatic Rings. *J. Am. Chem. Soc.* **2011**, *133*, 8732–8739.

(29) Murphy, A. R.; Fréchet, J. M. J. Organic Semiconducting Oligomers for Use in Thin Film Transistors. *Chem. Rev.* **2007**, *107*, 1066–1096.

(30) Tang, M. L.; Reichardt, A. D.; Wei, P.; Bao, Z. Correlating Carrier Type with Frontier Molecular Orbital Energy Levels in Organic Thin Film Transistors of Functionalized Acene Derivatives. *J. Am. Chem. Soc.* **2009**, *131*, 5264–5273.

(31) Dimitrakopoulos, C. D.; Malenfant, P. R. L. Organic Thin Film Transistors for Large Area Electronics. *Adv. Mater.* **2002**, *14*, 99–117.

(32) Scharber, M. C.; Mühlbacher, D.; Koppe, M.; Denk, P.; Waldauf, C.; Heeger, A. J.; Brabec, C. J. Design Rules for Donors in Bulk-Heterojunction Solar Cells—Towards 10 % Energy-Conversion Efficiency. *Adv. Mater.* **2006**, *18*, 789–794.

(33) Liman, C. D.; Choi, S.; Breiby, D. W.; Cochran, J. E.; Toney, M. F.; Kramer, E. J.; Chabinyc, M. L. Two-Dimensional GIWAXS Reveals a Transient Crystal Phase in Solution-Processed Thermally Converted Tetrabenzoporphyrin. *J. Phys. Chem. B* **2013**, *117*, 14557–14567.

(34) Youn, J.; Kewalramani, S.; Emery, J. D.; Shi, Y.; Zhang, S.; Chang, H.-C.; Liang, Y.;

Yeh, C.-M.; Feng, C.-Y.; Huang, H.; Stern, C.; Chen, L.-H.; Ho, J.-C.; Chen, M.-C.; Bedzyk, M. J.; Facchetti, A.; Marks, T. J. Fused Thiophene Semiconductors: Crystal Structure–Film Microstructure Transistor Performance Correlations. *Adv. Funct. Mater.* **2013**, *23*, 3850–3865.

(35) Sharenko, A.; Kuik, M.; Toney, M. F.; Nguyen, T.-Q. Crystallization-Induced Phase Separation in Solution-Processed Small Molecule Bulk Heterojunction Organic Solar Cells. *Adv. Funct. Mater.* **2014**, *24*, 3543–3550.

(36) Shin, W.; Yasuda, T.; Watanabe, G.; Yang, Y. S.; Adachi, C. Self-Organizing Mesomorphic Diketopyrrolopyrrole Derivatives for Efficient Solution-Processed Organic Solar Cells. *Chem. Mater.* **2013**, *25*, 2549–2556.

(37) Saeki, H.; Kurimoto, O.; Nakaoka, H.; Misaki, M.; Kuzuhara, D.; Yamada, H.; Ishida, K.; Ueda, Y. Effect of Crystallinity in Small Molecular Weight Organic Heterojunction Solar Cells. *J. Mater. Chem. C* **2014**, *2*, 5357–5364.

(38) Osaka, I.; Kakara, T.; Takemura, N.; Koganezawa, T.; Takimiya, K. Naphthodithiophene–Naphthobisthiadiazole Copolymers for Solar Cells: Alkylation Drives the Polymer Backbone Flat and Promotes Efficiency. *J. Am. Chem. Soc.* **2013**, *135*, 8834–8837.

(39) Vohra, V.; Kawashima, K.; Kakara, T.; Koganezawa, T.; Osaka, I.; Takimiya, K.; Murata, H. Efficient Inverted Polymer Solar Cells Employing Favourable Molecular Orientation. *Nat. Photonics* **2015**, *9*, 403–408.

(40) Umeyama, T.; Miyata, T.; Jakowetz, A. C.; Shibata, S.; Kurotobi, K.; Higashino, T.; Koganezawa, T.; Tsujimoto, M.; Gélinas, S.; Matsuda, W.; Seki, S.; Friend, R. H.; Imahori, H. Regioisomer Effects of [70]fullerene Mono-Adduct Acceptors in Bulk Heterojunction Polymer Solar Cells. *Chem. Sci.* **2017**, *8*, 181–188.

(41) Li, H.; Tee, B. C.-K.; Cha, J. J.; Cui, Y.; Chung, J. W.; Lee, S. Y.; Bao, Z. High-Mobility Field-Effect Transistors from Large-Area Solution-Grown Aligned C60

Single Crystals. *J. Am. Chem. Soc.* **2012**, *134*, 2760–2765.

(42) Liu, D.; Xu, X.; Su, Y.; He, Z.; Xu, J.; Miao, Q. Self-Assembled Monolayers of Phosphonic Acids with Enhanced Surface Energy for High-Performance Solution-Processed n-Channel Organic Thin-Film Transistors. *Angew. Chem. Int. Ed.* **2013**, *52*, 6222–6227.

(43) Liu, D.; He, Z.; Su, Y.; Diao, Y.; Mannsfeld, S. C. B.; Bao, Z.; Xu, J.; Miao, Q. Self-Assembled Monolayers of Cyclohexyl-Terminated Phosphonic Acids as a General Dielectric Surface for High-Performance Organic Thin-Film Transistors. *Adv. Mater.* **2014**, *26*, 7190–7196.

(44) Sele, C. W.; Kjellander, B. K. C.; Niesen, B.; Thornton, M. J.; van der Putten, J. B. P. H.; Myny, K.; Wondergem, H. J.; Moser, A.; Resel, R.; van Breemen, A. J. J. M.; van Aerle, N.; Heremans, P.; Anthony, J. E.; Gelinck, G. H. Controlled Deposition of Highly Ordered Soluble Acene Thin Films: Effect of Morphology and Crystal Orientation on Transistor Performance. *Adv. Mater.* **2009**, *21*, 4926–4931.

(45) Rogowski, R. Z.; Dzwilewski, A.; Kemerink, M.; Darhuber, A. A. Solution Processing of Semiconducting Organic Molecules for Tailored Charge Transport Properties. *J. Phys. Chem. C* **2011**, *115*, 11758–11762.

(46) Jang, J.; Nam, S.; Im, K.; Hur, J.; Cha, S. N.; Kim, J.; Son, H. B.; Suh, H.; Loth, M. A.; Anthony, J. E.; Park, J.-J.; Park, C. E.; Kim, J. M.; Kim, K. Highly Crystalline Soluble Acene Crystal Arrays for Organic Transistors: Mechanism of Crystal Growth During Dip-Coating. *Adv. Funct. Mater.* **2012**, *22*, 1005–1014.

(47) Nam, S.; Jang, J.; Anthony, J. E.; Park, J.-J.; Park, C. E.; Kim, K. High-Performance Triethylsilylethynyl Anthradithiophene Transistors Prepared without Solvent Vapor Annealing: The Effects of Self-Assembly during Dip-Coating. *ACS Appl. Mater. Interfaces* **2013**, *5*, 2146–2154.

(48) Jeong, H.; Han, S.; Baek, S.; Kim, S. H.; Lee, H. S. Dense Assembly of Soluble Acene

Crystal Ribbons and Its Application to Organic Transistors. *ACS Appl. Mater. Interfaces* **2016**, *8*, 24753–24760.

(49) Robles, O.; McDonald, F. E. Modular Synthesis of the C9−C27 Degradation Product of Aflastatin A via Alkyne−Epoxide Cross-Couplings. *Org. Lett.* **2008**, *10*, 1811–1814.

(50) Ito, S.; Murashima, T.; Uno, H.; Ono, N. A New Synthesis of Benzoporphyrins Using 4,7-Dihydro-4,7-Ethano-2*H*-Isoindole as a Synthon of Isoindole. *Chem. Commun.* **1998**, 1661–1662.

(51) te Velde, G.; Bickelhaupt, F. M.; Baerends, E. J.; Fonseca Guerra, C.; van Gisbergen, S. J. A.; Snijders, J. G.; Ziegler, T. Chemistry with ADF. *J. Comput. Chem.* **2001**, *22*, 931–967.

Chapter 3

Engineering Thin Films of a Tetrabenzoporphyrin toward Efficient Charge-Carrier Transport: Selective Formation of a Brickwork Motif

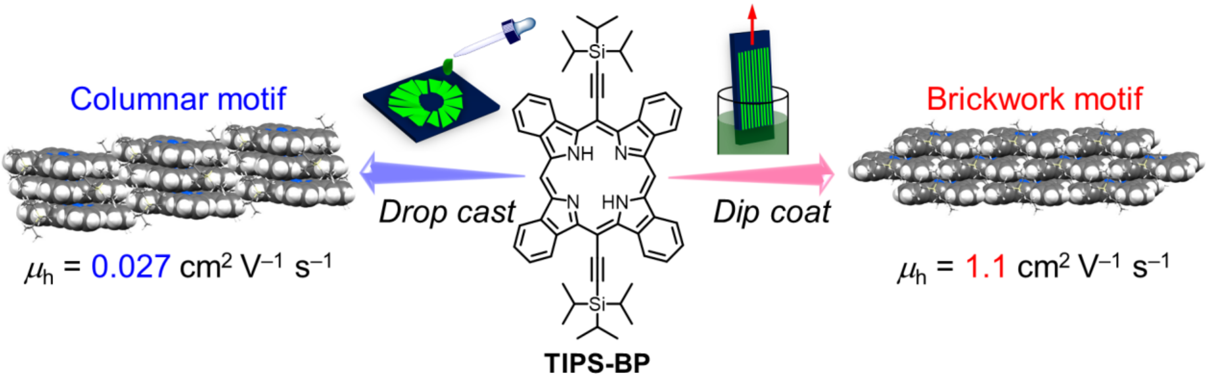

This chapter concentrates on engineering the solid-state packing of a TIPS-BP toward achieving efficient charge-carrier transport in its solution-processed thin films. The effort leads to the selective formation of a brickwork packing that has two-dimensionally extended π-staking. The maximum field-effect hole mobility in the resulting films reaches 1.1 $cm^2 V^{-1} s^{-1}$, which is approximately 14 times higher than the record value for pristine free-base BP (0.070 $cm^2 V^{-1} s^{-1}$). This achievement is enabled mainly through the optimization of three factors; namely, deposition process, cast solvent, and self-assembled monolayer that constitutes the dielectric surface. These results will provide a useful basis for the polymorph engineering and morphology optimization in solution-processed organic molecular semiconductors.

3-1. Introduction

The μ in organic semiconducting thin films is largely influenced by molecular packing[1–4] and film morphology.[5–9] Accordingly, much effort has been devoted toward efficient preparation of semiconducting thin films having optimal molecular arrangement and minimal domain boundary. Several successful examples have already been reported in which excellent field-effect charge-carrier mobilities were observed in organic molecular thin films deposited via fine-tuned solution processes. For instance, Bao and co-workers achieved the highest and average hole mobilities of 43 and 25 cm^2 V^{-1} s^{-1}, respectively, in 2,7-dioctyl[1]benzothieno[3,2-*b*][1]benzothiophene (C8-BTBT) deposited by off-center spin coating.[10] The same group also obtained hole mobilities of up to 11 cm^2 V^{-1} s^{-1} in 6,13-bis(triisopropylsilylethynyl)pentacene (TIPS-PEN) deposited by solution shearing with a micropillar-patterned blade (Figure 3-1).[11] These deposition methods were carefully optimized to obtain homogeneous, large-area thin films of specific polymorphs that are suitable for efficient charge-carrier transport across the device area.

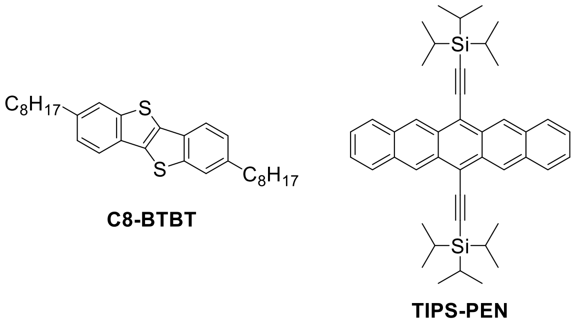

Figure 3-1. Chemical structure of C8-BTBT and TIPS-PEN.

In the previous chapter, the OFET device based on TMS-BP achieved the μ_h of 0.12 cm^2 V^{-1} s^{-1} by precursor approach. However, the μ_h over 1 cm^2 V^{-1} s^{-1} should be achieved for the practical application indicating the further improvement of μ_h is desired. To improve the μ_h, direct solution processes such as drop casting[40–42] and dip coating[43–47] method would be applied to this system in order to control the anisotropy of crystal growth. Unfortunately, the solubility of TMS-BP is too poor to deposit the active layer of OFET by solution-processes, indicating the further improvement of μ_h TMS-BP-based OFET is almost impossible. On the other hand, since TIPS-BP has enough solubility for the deposition of active layer of OFET by solution processes, further improvement of μ_h can be expected.

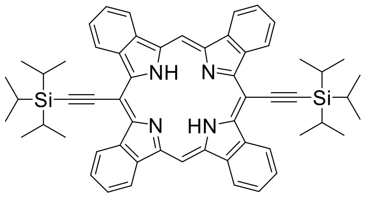

TIPS-BP

Figure 3-2. Chemical structure of TIPS-BP.

This chapter shows that TIPS-BP (Figure 3-2) can be crystallized in a brickwork arrangement in solution-processed thin films. The maximum field-effect hole mobility in resulting films reaches 1.1 $cm^2 V^{-1} s^{-1}$, which is higher by orders of magnitude as compared to the mobilities obtained in the previous chapter (4.4×10^{-5} $cm^2 V^{-1} s^{-1}$).[17] This achievement is enabled by careful optimization of deposition conditions and proper selection of a SAM that constitute the dielectric surface.

3-2. Single-Crystal X-ray Structures

This study was initially motivated by the finding of two different packing structures of TIPS-BP in the single-crystalline state. The first polymorph, which was previously described in Chapter 2,[16] was obtained by slow diffusion of either methanol into a chloroform solution or *n*-hexane into a chlorobenzene solution. XRD analysis has revealed that this polymorph consists of a one-dimensionally extended columnar π-stacking motif (Figure 3-3a,b).[16]

The second polymorph was found to form, after several try-and-error cycles, when TIPS-BP was crystallized by slow evaporation of a chloroform or chlorobenzene solution. In this case, BP frameworks are arranged in a brickwork motif where π-stacking extends two dimensionally (Figures 3-3d,e). This structure is reminiscent of the brickwork arrangement of

TIPS-PEN[18] which is one of the benchmark high-performance organic semiconductors. The first and second polymorphs of TIPS-BP are referred to as "1D π-stack" and "2D π-stack", respectively, in the following discussion.

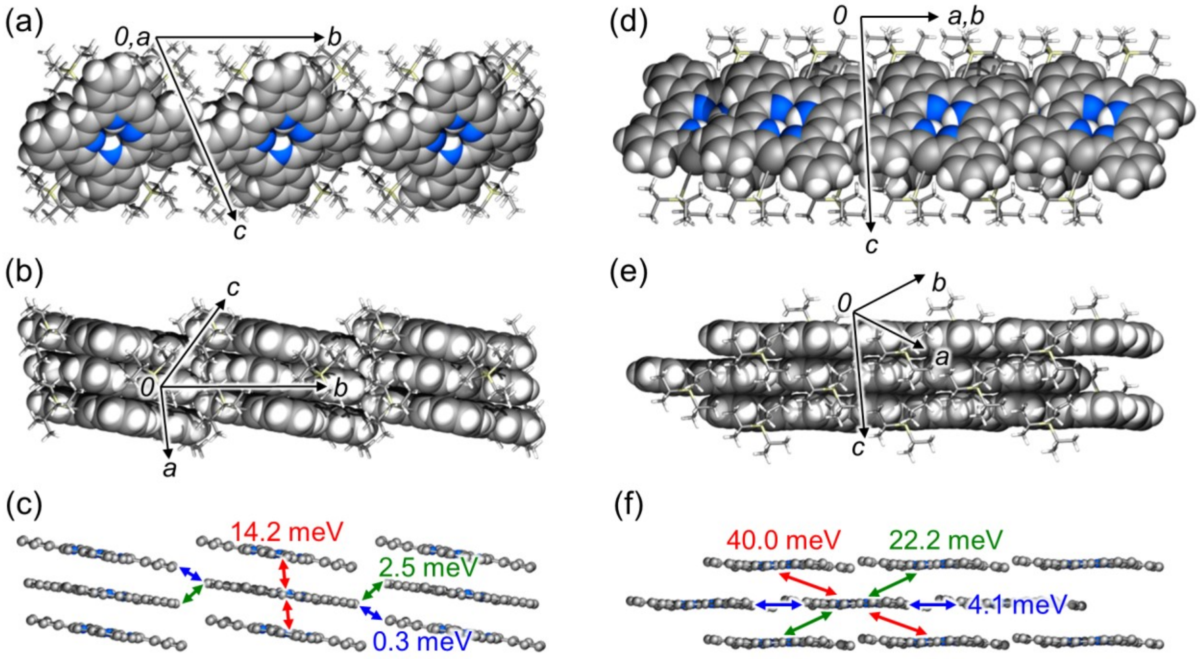

Figure 3-3. Comparison of the two polymorphs of TIPS-BP obtained as bulk single crystals: (a,b) 1D π-stack viewed along and perpendicular to the π-stacking axis; (c) transfer integrals in 1D π-stack; (d,e) 2D π-stack viewed along and perpendicular to the π-stacking axis; (f) transfer integrals in 2D π-stack. Substituents are omitted for clarity in c and f.

BP frameworks in 1D π-stack are piled up in such a way that the four edges of each columnar stack are sterically blocked with densely packed TIPS groups (Figure 3-3a,b). As a result, π–π contacts between BP frameworks are essentially limited to within each 1D columnar structure. The interplane spacing between stacked BP frameworks is 3.30 Å on average (Figure S3-1a), and the corresponding transfer integral between HOMOs is calculated to be only 14.2 meV (Figure 3-3c). In 2D π-stack, on the other hand, all the substituents orient parallel such that TIPS groups cover the surface of the two dimensionally extended brickwork (Figure 3-3d,e). Relatively short interplane distances of 3.24 and 3.45 Å (Figure S3-1b) associated with calculated transfer integrals of 40.0 and 22.2 meV, respectively, were observed within the brickwork motif. These values are similar to or higher than the maximum transfer integral calculated for TIPS-PEN in the bulk single-crystalline state[18] (23.5 meV, Figure S3-2a,b) and even comparable to that calculated for the thin-film strained state[19] (40.6 meV, Figure S3-2c,d). TIPS-PEN can generally afford good field-effect μ_hs of over 1 cm^2 V^{-1} s^{-1} both in single-crystal and thin-film transistors.[11,19–21] In addition, it has been postulated that charge-carrier transport in organic molecular semiconductors greatly benefits from the formation of two dimensionally extended π–π contacts.[22] Therefore, TIPS-BP is expected to afford high μ_hs upon the selective formation of 2D π-stack in high-quality thin films. This aspect is examined in the next section.

3-3. Charge-Carrier Mobilities in Solution-Processed Thin Films

Carrier-transport characteristics in TIPS-BP thin films were evaluated in bottom-gate-top-contact OFETs prepared on SiO_2/Al_2O_3 dielectric layers (Figure S3-3).[23] Fabrication and evaluation of OFETs as well as their polarized micrographs were measured by the author in the Prof. Miao's group of The Chinese University of Hong Kong (CUHK) during the internship. XRD patterns were measured by Dr. Shuaijun Yang of Prof. Miao's group in CUHK. The substrate surface was pretreated with a SAM of 12-methoxydodecylphosphonic acid (MODPA)[24] or 12-cyclohexyldodecylphosphonic acid (CDPA) (Figure 3-4).[11] In multiple cases of solution-processed OFETs, MODPA and CDPA were reported to afford higher μs as compared to more traditional SAM materials such as hexamethyldisilazane (HMDS) and octadecyltrimethoxysilane (OTMS).[24,25] For the contact electrodes, Au is the material of choice, as its work function (ca. 5 eV)[26,27] matches with the ionization energy of TIPS-BP (Figure S3-4 in SI). The observed OFET characteristics are summarized in Table 3-1.

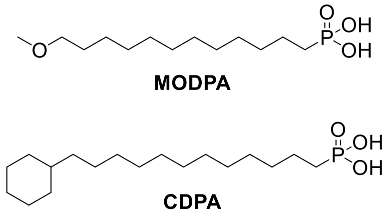

Figure 3-4. Chemical structures of the SAM materials employed in this chapter.

Table 3-1. Characteristics of TIPS-BP thin films.

entry	method	solvent	SAM	packing motif	$\mu_h{}^a$ / cm^2 V^{-1} s^{-1}	$V_{th}{}^b$ / V	$I_{on}/I_{off}{}^b$
1	drop casting	C_6H_5Cl	MODPA	unknown + 1D (minor)	0.027 (0.018)	2.5	1.2×10^4
2		$C_6H_5CH_3$	MODPA	1D + unknown (trace)	0.029 (0.018)	0.9	4.9×10^2
3	dip coating	$CHCl_3$	MODPA	1D + 2D (minor) + unknown (minor)	0.078 (0.028)	3.8	1.5×10^3
4		CH_2Cl_2	MODPA	2D + 1D (minor)	0.47 (0.29)	–15.2	1.9×10^5
5		CH_2Cl_2 + 10% $CHCl_3$	MODPA	2D + 1D (trace)	0.38 (0.27)	–11.3	1.7×10^5
6		CH_2Cl_2 + 10% $CHCl_3$	CDPA	2D + 1D (trace)	1.1 (0.90)	1.6	7.2×10^4

[a] Data of the best performing devices followed by the average of at least 6 devices in parentheses. [b] Data of the best performing devices.

The author first examined drop-cast films prepared with several different solvents. When chlorobenzene was used as cast solvent, the maximum and average μ_hs of 0.027 and 0.018 cm^2 V^{-1} s^{-1}, respectively, were obtained (entry 1 in Table 3-1 and Figure 3-5a). These μs are significantly improved from those obtained in spin-coated thin films on bare SiO_2 surface in the previous chapter (up to 4.4×10^{-5} cm^2 V^{-1} s^{-1})[17] and close to the highest value reported for free-base BP (0.070 cm^2 V^{-1} s^{-1}).[14] This improvement may be due to the change in film morphology induced by the difference in surface treatment (with vs without a SAM or deposition process (drop casting vs spin coating).

The out-of-plane thin-film XRD analysis showed that the main crystalline component in the TIPS-BP film cast from a chlorobenzene solution was neither the targeted 2D nor 1D π-stack, and had an unknown structure (Figure 3-5b). Specifically, the primary diffraction peak was observed at $2\theta = 5.03°$ (d = 17.6 Å), while the 001 diffractions of 2D and 1D π-stacks are expected at $2\theta = 4.66°$ (18.9 Å) and 5.23° (16.9 Å), respectively. A minor component was additionally detected which diffracted at $2\theta = 5.17°$ (17.1 Å). This peak is very close to the simulated 001 diffraction of 1D π-stack, and the small deviation may be attributed to thermal expansion of the unit cell because of the higher measurement temperature for the thin film (ambient temperature, 290–295 K) as compared to the case of single crystal (103 K). Such minor differences between single-crystal and thin-film packings are sometimes observed for organic molecular crystals.[28,29] Although it is not possible to fully determine the exact structure of this minor component at this moment, we have tentatively assigned it to 1D π-stack and describe accordingly in this report. It would also be worth pointing out here that the 010 ($2\theta = 6.16°$) and 011 ($2\theta = 6.29°$) diffractions of 1D π-stack were not observed in this case (Figure 3-5b), indicating that TIPS-BP molecules in 1D π-stack crystallites stand in an end-on mode with the *ab* plane parallel to the substrate (Figure S3-5). Note that the primary diffraction peak observed for a TIPS-BP film deposited by the precursor approach[17] was at $2\theta \approx 5.4°$, being different from those of 1D π-stack and the unknown structure obtained here. The formation of 2D π-stack was not detected in this case of drop casting from chlorobenzene.

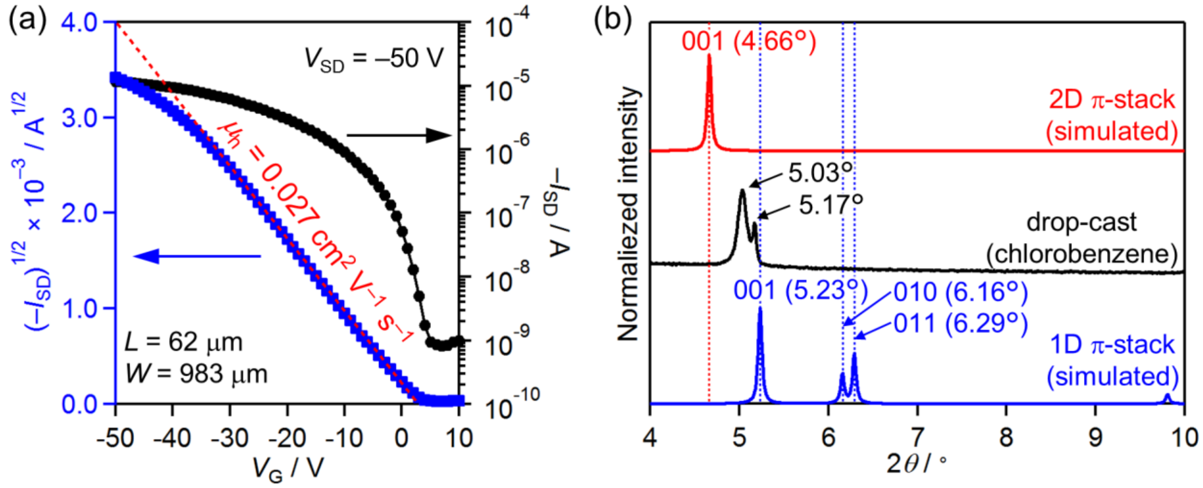

Figure 3-5. Characteristics of TIPS-BP thin films prepared by drop casting using chlorobenzene as cast solvent: (a) Transfer characteristics of the best-performing OFET device fabricated on a MODPA-modified substrate; (b) Comparison of experimental out-of-plane XRD and simulated powder XRD patterns.

Besides chlorobenzene, toluene afforded crystalline films of TIPS-BP in drop casting. Formation of the unknown structure was largely attenuated in the latter case, and instead 1D π-stack became a dominant crystalline phase (Figure S3-6). Unfortunately, however, any sign of the targeted 2D π-stack was not observed again, and the μ_h remained at the same level as the case of chlorobenzene (0.029 cm^2 V^{-1} s^{-1}, entry 2 in Table 3-1). Use of other solvents and application of postdeposition annealing did not lead to the formation of crystalline thin films adequate for OFET fabrication.

We then examined dip coating which has been demonstrated to be highly effective in gaining control over the film morphology of TIPS-PEN[30–32] and other organic semiconductors.[33–36] It turned out that dip coating from a chloroform solution at a pull rate of 0.10 mm min^{-1} could afford crystalline films of TIPS-BP on MODPA-modified substrates. (The pull rate was kept at 0.10 mm min^{-1} in the following experiments.) XRD analysis showed that 1D π-stack was formed as a primary crystalline component, along with 2D π-stack and an unknown structure as minor components (Table 3-1 and Figure 3-6a). Specifically, the primary peak in this case is observed at $2\theta = 5.19°$ (d = 17.0 Å) which can be assigned to the 001 diffraction of 1D π-stack. In addition, relatively small peaks are observed at $2\theta = 4.68$ and 5.03° (d = 18.9 and 17.6 Å) which are well consistent with the simulated 001 diffraction of 2D π-stack and the unknown structure observed in the case of drop casting with chlorobenzene, respectively. The resulting films showed field-effect μ_hs of up to 0.078 cm^2 V^{-1} s^{-1} (entry 3 in Table 3-1 and Figure S3-9a) which is approximately 3 times higher than the best value obtained in drop-cast films (0.029 cm^2 V^{-1} s^{-1}). This improvement may be attributed, at least partially, to the emergence of 2D π-stack. It should be noted here that 2D π-stack was also formed as a minor component when a TIPS-BP film drop-cast with chlorobenzene was annealed with chloroform vapor (Figure S3-7), indicating that the 1D π-stack motif is metastable. Unfortunately, field-effect μ could not be measured in the postannealing sample because of the extremely poor film quality. In addition, a film drop-cast from a chloroform solution was not crystalline. These observations indicate the superiority of dip coating over drop casting in forming crystalline thin films of TIPS-BP.

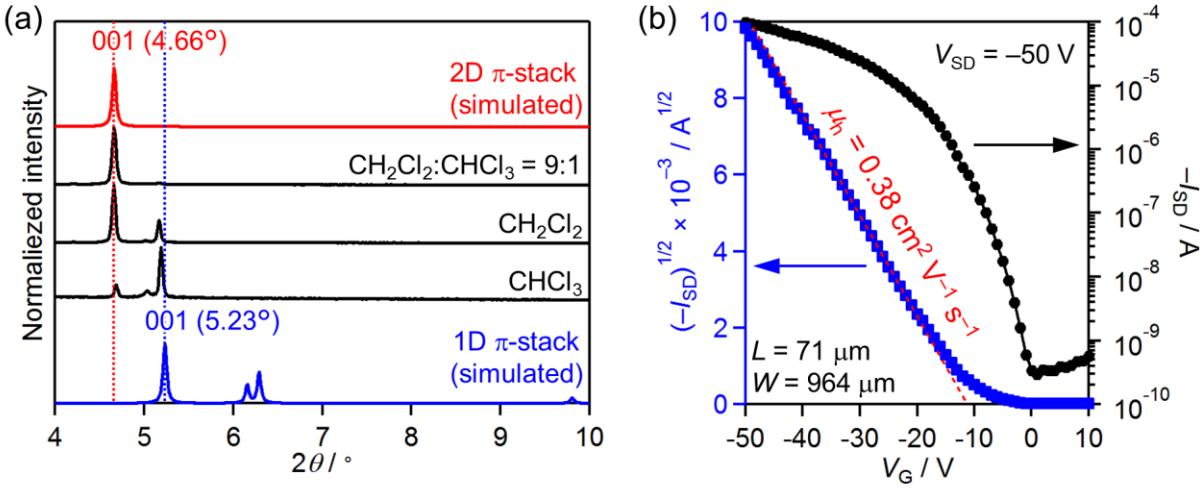

Figure 3-6. Characteristics of TIPS-BP thin films prepared by dip coating on MODPA-modified substrates: (a) Comparison of experimental out-of-plane XRD patterns of thin films prepared from different solvents and simulated powder XRD patterns; (b) Transfer characteristics of the best-performing OFET device fabricated using dichloromethane/chloroform (9:1 vol) as cast solvent.

It was found in further examination that 2D π-stack became a main component when dichloromethane was used as cast solvent instead of chloroform (Figure 3-6a). The highest μ_h in resulting films reached 0.47 cm^2 V^{-1} s^{-1} (entry 5 in Table 3-1 and Figure S3-9b). However, the overall film quality was not high, and the sample-to-sample reproducibility was low in terms of both the film morphology and carrier mobility. There were even cases, at relatively high probability, in which no or little organic films were formed on the MODPA-modified substrate. Furthermore, TIPS-BP precipitated on the surface of dip-coat solution during deposition because of the low solubility of TIPS-BP in dichloromethane, resulting in the formation of highly inhomogeneous, rough films.

These problems were significantly alleviated by adding chloroform, a better solvent than dichloromethane for TIPS-BP, as a cosolvent: that is, relatively homogeneous films were consistently obtained when TIPS-BP was dip-coated from a solution in dichloromethane/chloroform (9:1 vol). Gratifyingly, XRD analysis showed that the resulting films contained 2D π-stack as an essentially solo crystalline component (Figure 3-6a). Nonetheless, the best and average field-effect μ_hs observed in these films were 0.38 and 0.27 $cm^2 V^{-1} s^{-1}$, respectively, staying at the same level as the case where only dichloromethane was used as dip-coat solvent (entry 5 in Table 3-1 and Figure 3-6b).

Further improvement in μ_h was achieved when the molecule for SAM was changed from MODPA to CDPA. While CDPA has been reported to afford higher μs (1.64 ± 0.55 $cm^2 V^{-1} s^{-1}$)[25] than MODPA (1.1 ± 0.22 $cm^2 V^{-1} s^{-1}$)[24] for drop-cast films of TIPS-PEN, CDPA is also known to give surfaces with lower surface energies as compared to MODPA, making solution deposition of organic molecular materials more challenging. In fact, TIPS-BP could not be deposited on the CDPA-treated substrate when we tried dip coating from a chloroform solution. This led us to employ MODPA as the SAM material of choice in the earlier experiments described above. After careful examination, it was eventually found that TIPS-BP could be dip-coated on the CDPA-modified surface when dichloromethane/chloroform (9:1) mixed solvent was used. The XRD analysis showed that 2D π-stack was essentially a solo crystalline component in this case again (Figure 3-7a), and the resulting films afforded the best and average μ_hs of 1.1 and 0.90 $cm^2 V^{-1} s^{-1}$, respectively (entry 6 in Table 3-1 and Figure 3-7b). The improvement can be attributed, at least partly, to larger domain/crystallite sizes as compared to the case of MODPA (Figure S3-10–12). This result serves as yet another example that highlights the non-straightforward nature of achieving high-quality solution-processed thin films having specific target packing motifs. In addition, note also that the field-effect μ calculated from the saturation regime can be overestimated, and the μ from the linear regime is often considerably lower than the saturation mobility. In the present case of TIPS-BP, a film deposited under the optimized conditions gave saturation and linear mobilities of 0.70 and 0.31 $cm^2 V^{-1} s^{-1}$, respectively (Figure S3-13).

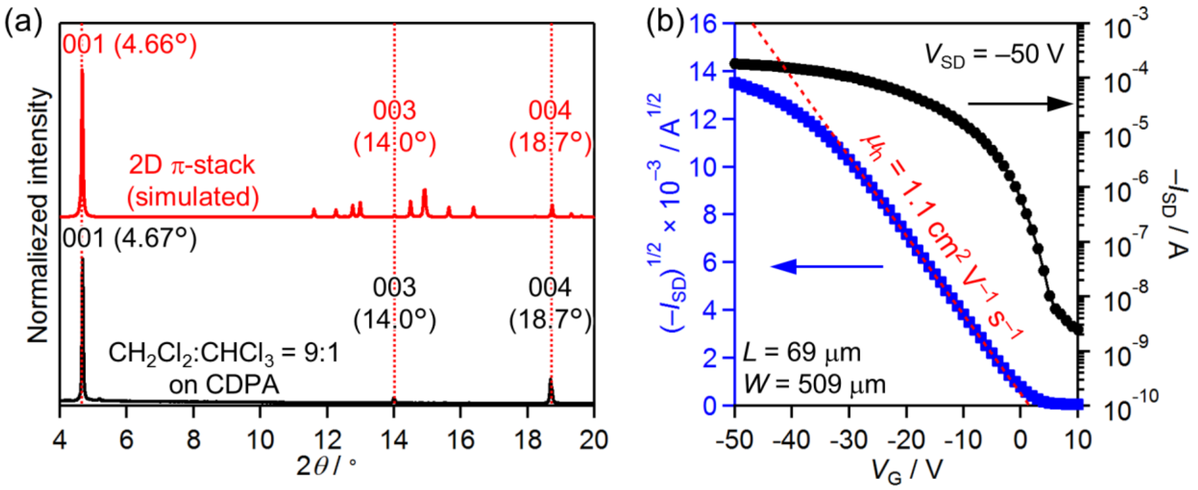

Figure 3-7. Characteristics of TIPS-BP thin films prepared by dip coating from a dichloromethane/chloroform (9:1 vol) solution on CDPA-modified substrates: (a) Assignment of the peaks in an experimental out-of-plane XRD pattern of a thin film. (b) Transfer characteristics of the best-performing OFET device.

3-4. Molecular Orientation in 2D π-Stack Films

The out-of-plane XRD data of a dip-coated thin film on CDPA shows diffraction peaks at $2\theta = 4.67, 14.0, 18.7°$ (d = 18.9, 6.32, 4.74 Å) which can be assigned to the 001, 003, 004 diffractions of 2D π-stack, respectively (Figure 3-7a). This observation indicates that the *ab* plane of 2D π-stack crystallites is parallel to the substrate, and TIPS-BP molecules stand in an end-on mode (Figure S3-14). We also studied the in-plane packing anisotropy by azimuthal (ϕ) diffraction scan using synchrotron radiation.[11,37] The scan was performed on the 110 diffraction [(q_{xy}, q_z) = (0.92 Å^{-1}, 0.03 Å^{-1}), see Figure S3-15 for the 2D-GIWAXD data], with the start point parallel to the pull axis of dip coating. The (110) planes are almost perpendicular to the (001) planes as well as the substrate. The scan showed two distinct peaks around ϕ = 99 and 177° along the in-plane rotation with rather wide distributions of ca. ±7°, suggesting that the crystallites populate in two main orientations (Figure 3-8a). From Bragg's law, the 110 diffraction is expected to appear when their angle against the incident X-ray is 4°. Thus the (110) planes are mainly oriented at angles of 103° (from 99 + 4°) and 181° (or 1°, from 177 + 4°) with distributions of ca. ±7° with respect to the pull axis (Figure 3-8b). The population of two main orientations are calculated to be 33% and 37% for $\phi = 99 \pm 7°$ and $177 \pm 7°$, respectively, by integrating peak intensities.

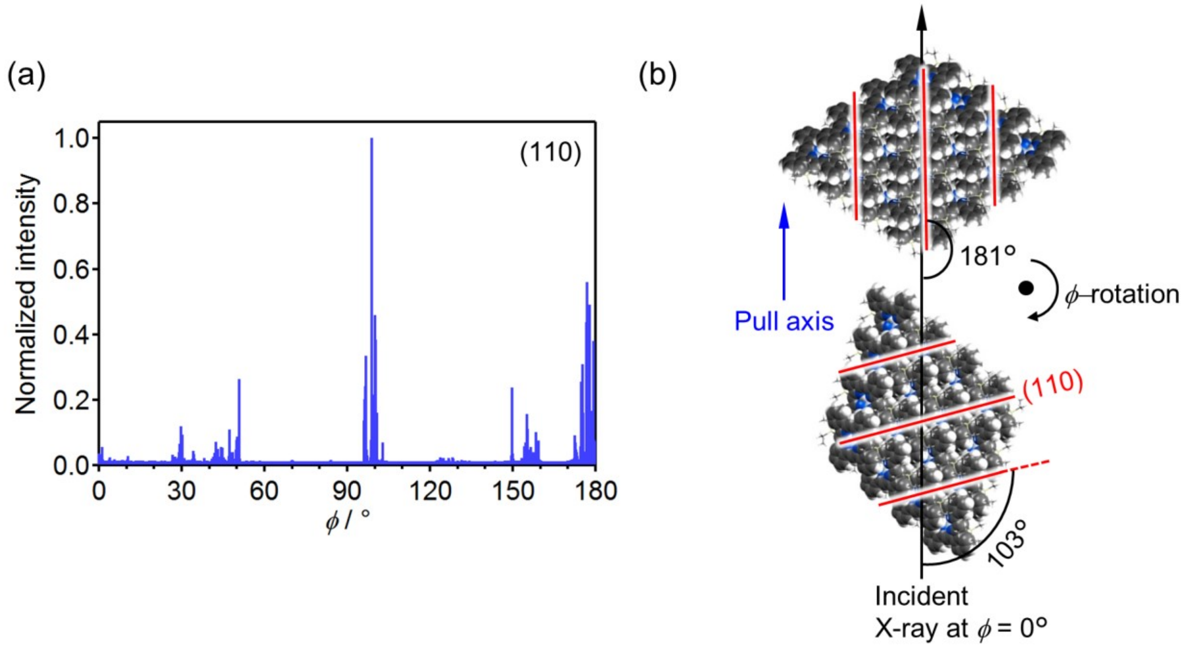

Figure 3-8. (a) X-ray ϕ diffraction scan of a 2D π-stack film prepared by dip coating on a CDPA-modified substrate. The start point of scan ($\phi = 0°$) is set to be parallel to the pull axis of the substrate in dip coating. (b) Relation between the pull axis and dominant molecular orientations.

Furthermore, polarized optical micrographs of 2D π-stack grown on a CDPA monolayer did not show strong contrast in brightness when the sample was rotated in-plane against polarizers (Figure S3-16). Thus, the in-plane anisotropy of molecular alignment would not be very high in the 2D π-stack obtained in this work. Considering the strong impact of packing misalignment on charge-carrier mobility in brickwork arrangement,[11] it can be assumed that there still remains much room for improvement in morphology and thus μ in TIPS-BP films.

3-5. Summary

This work has demonstrated that BP frameworks can be stacked in a brickwork motif having two-dimensionally extended intermolecular π–π contacts in solution-processed thin films. Those films with the 2D π-stack motif afforded the maximum field-effect μ_h of 1.1 cm^2 V^{-1} s^{-1}, which is higher by orders of magnitude than that obtained in TIPS-BP in the previous chapter (4.4×10^{-5} cm^2 V^{-1} s^{-1})[17] and even the record μ for pristine free-base BP (0.070 cm^2 V^{-1} s^{-1}).[14] The key to this achievement is threefold: employment of a suitable deposition method (dip coating), use of a proper solvent (dichloromethane/chloroform, 9:1), and choice of an appropriate SAM material (CDPA). With these three factors combined, TIPS-BP molecules can be arranged to form 2D π-stack selectively and reproducibly.

On the other hand, the thin-film XRD data and polarized-light micrographs have suggested that the 2D π-stack films obtained in this work are relatively inhomogeneous in terms of in-plane molecular orientation. Therefore, further improvement in charge-carrier mobility may be expected by reducing grain boundaries or, more preferably, forming large single-crystalline thin films. State-of-the-art solution-processing techniques[38] such as the use of a patterned surface[7,39,40] or a patterned shirring blade,[11,41] as well as the modification of molecular structure, may enable the formation of high-quality thin films of BP-based molecular semiconductors. The present work of "polymorph engineering"[19,42–44] will help pave the way toward realizing this goal.

3-6. Supporting Figures

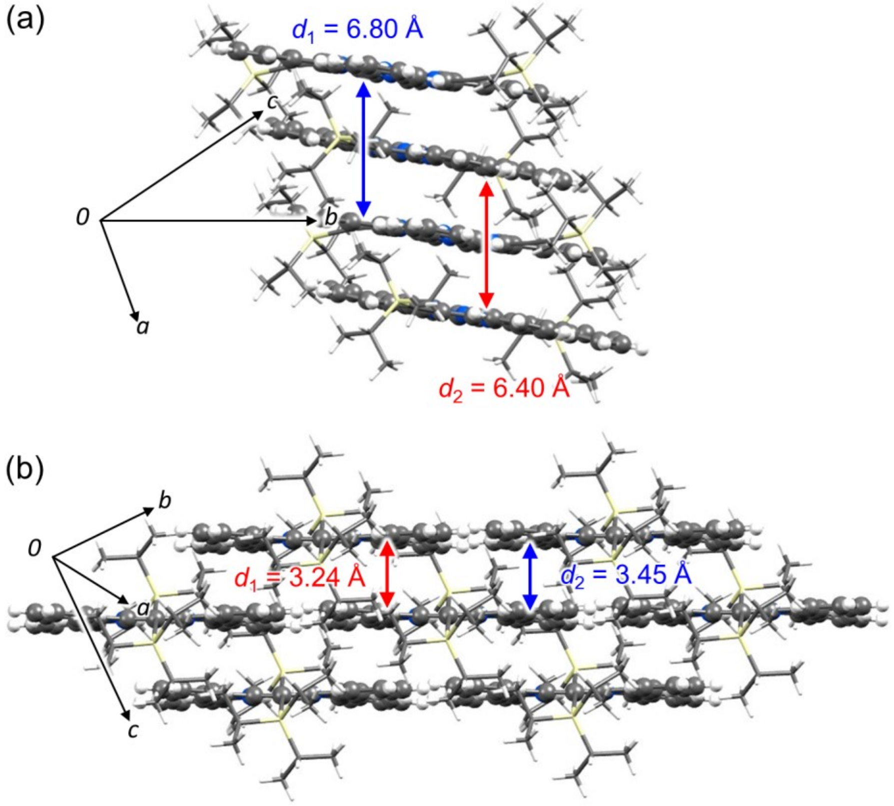

Figure S3-1. (a) 1D π-stack packing and (b) 2D π-stack packing motifs of TIPS-BP. The average of interplane spacing in the 1D π-stack packing motif was calculated as: $(d_1 + d_2)/4 = 3.30$ Å.

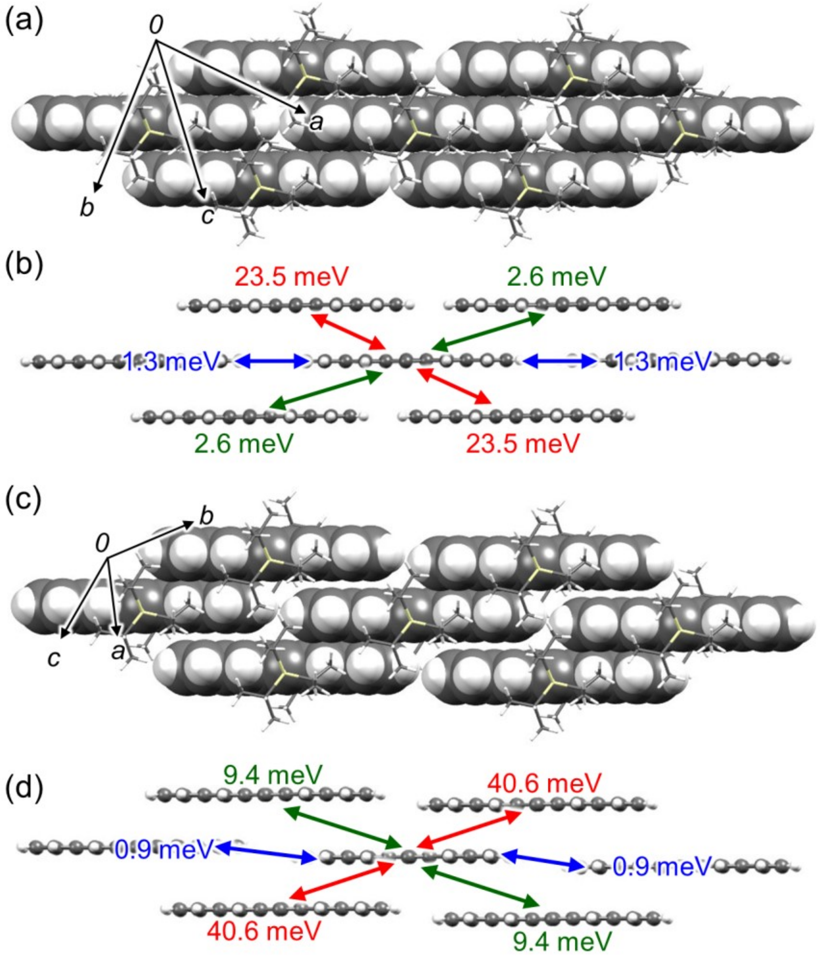

Figure S3-2. (a) Single-crystal structure of TIPS-PEN[18] (b) with the calculated charge-transfer integrals. (c) Packing structure of thin film strained TIPS-PEN[19] (d) with the calculated charge-transfer integrals. TIPS-ethynyl groups are omitted for clarity in (b) and (d).

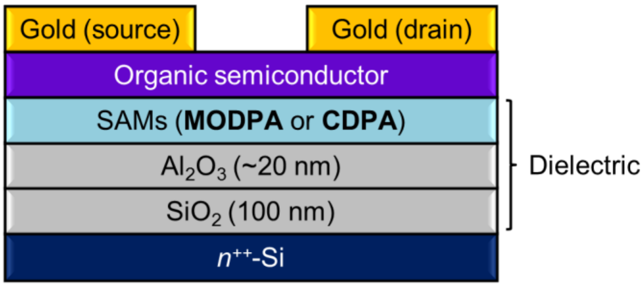

Figure S3-3. Schematic drawing of OFETs fabricated in this chapter.

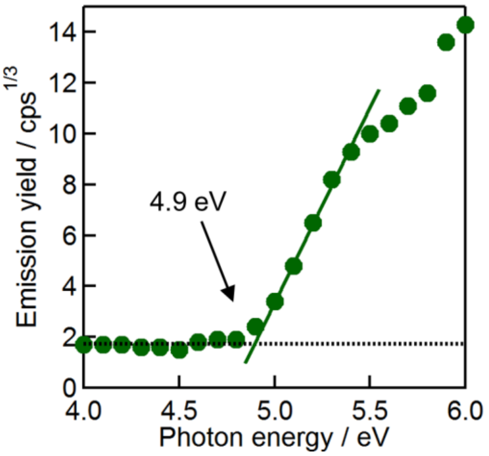

Figure S3-4. Photoelectron spectrum in air of a thin film of TIPS-BP on an ITO-coated glass substrate. The deposition conditions of the film are: concentration of solution: 2 mg mL^{-1}, solvent: $CHCl_3$, spin rate and time: 800 rpm, 30 s in air. The data was obtained on a RIKEN KEIKI AC-3 surface analyzer.

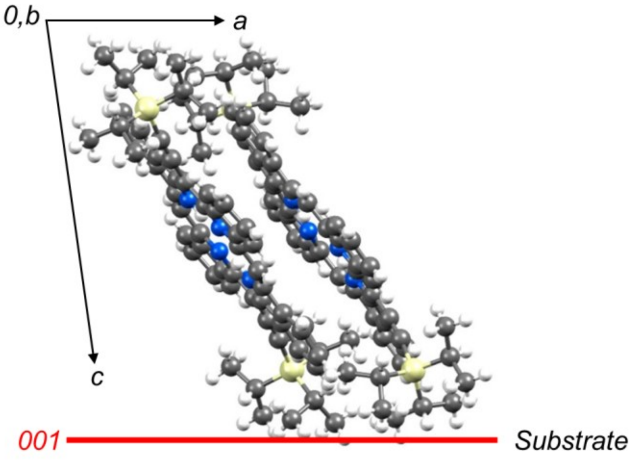

Figure S3-5. Relation between 1D π-stack crystallites and substrate.

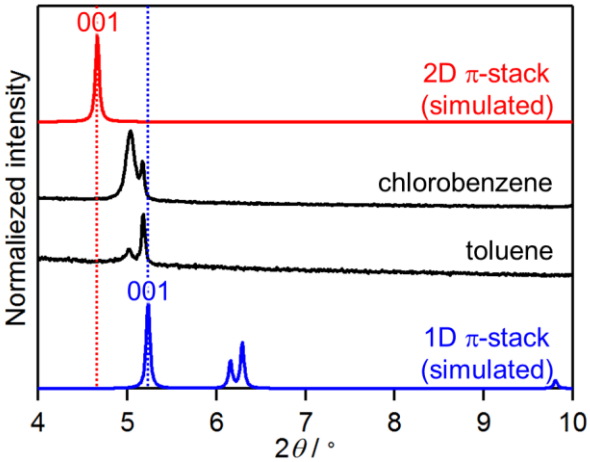

Figure S3-6. XRD patterns of TIPS-BP thin films prepared by drop casting from chlorobenzene and toluene solutions with simulated powder patters of 2D and 1D π-stack motif.

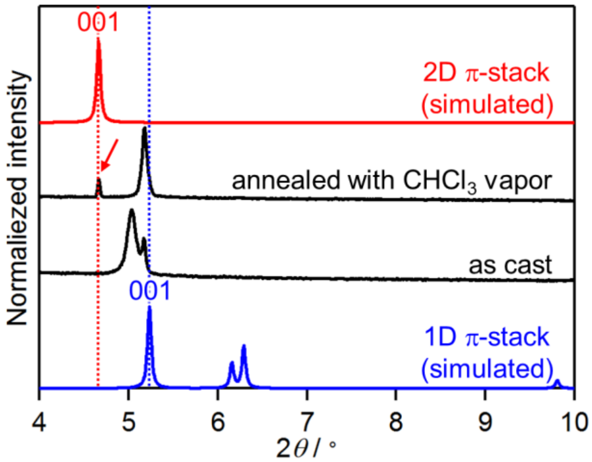

Figure S3-7. XRD patterns of TIPS-BP thin films prepared by drop casting from chlorobenzene followed by annealing with chloroform vapor with simulated powder patters of the 2D and 1D π-stack motifs. The red arrow indicates a peak from the 2D π-stack motif of TIPS-BP.

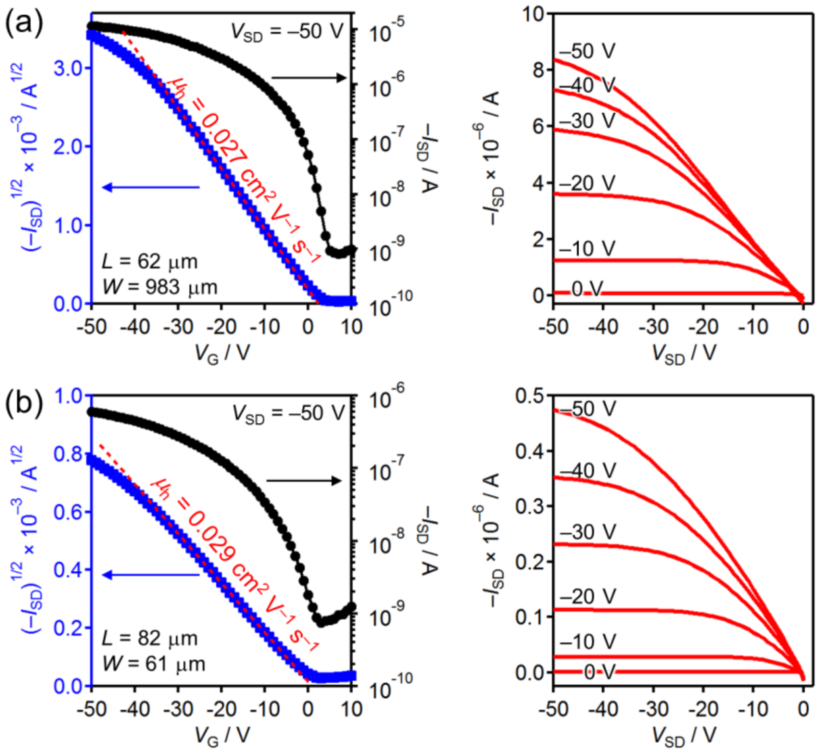

Figure S3-8. Transfer curve (left) and output curves (right) of OFETs fabricated by drop casting from (a) chlorobenzene and (b) toluene solution on MODPA-modified substrates.

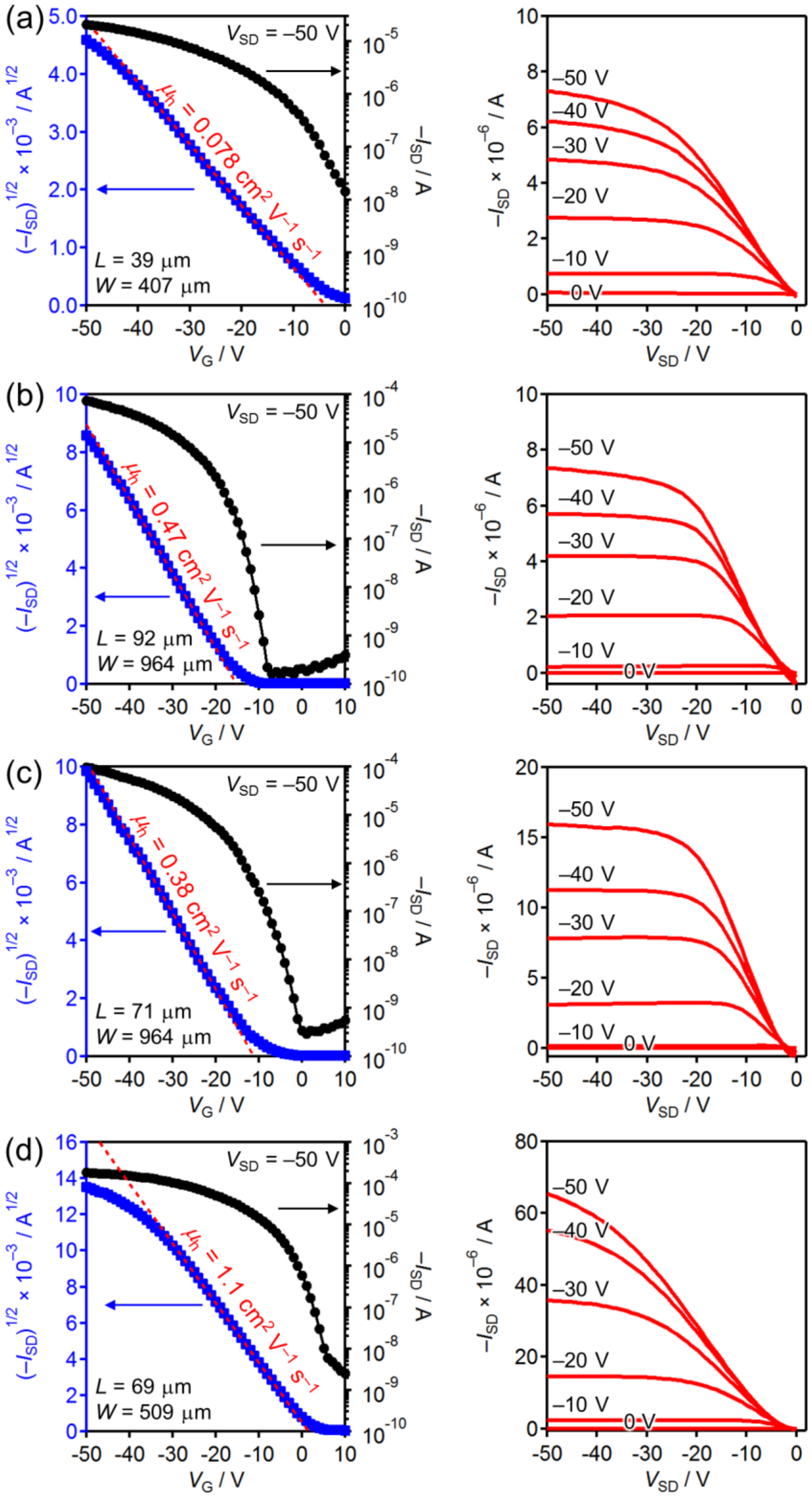

Figure S3-9. Transfer curve (left) and output curves (right) of OFETs fabricated by dip coating from (a) chloroform ($CHCl_3$), (b) dichloromethane (CH_2Cl_2), and (c) CH_2Cl_2:$CHCl_3$ = 9:1 solution on MODPA-modified substrates and from (d) CH_2Cl_2:$CHCl_3$ = 9:1 solution on CDPA-modified substrates.

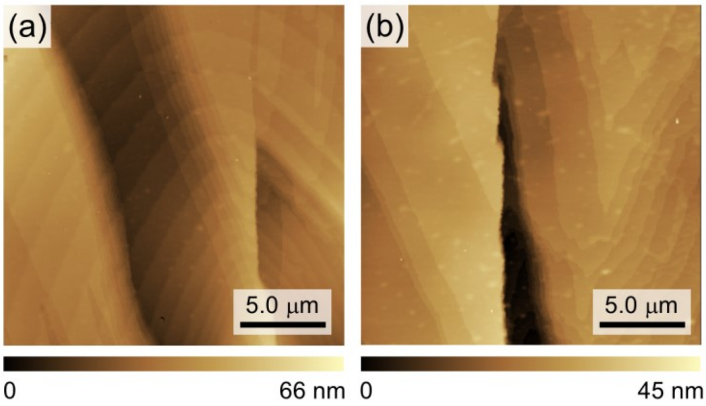

Figure S3-10. Tapping-mode AFM height images of TIPS-BP thin films prepared by dip coating using CH_2Cl_2 with 10% $CHCl_3$ as solvent: (a) on MODPA SAM (RMS roughness = 9.4 nm), (b) on CDPA SAM (RMS roughness = 6.1 nm). The two films are in general similar in terms of micron-scale surface topology, and the considerable improvement in hole mobility for the case of CDPA monolayer could not be explained based on these images.

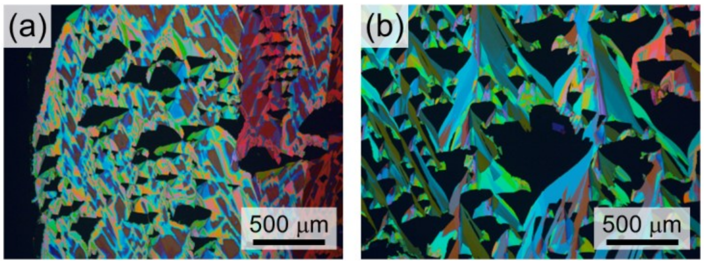

Figure S3-11. Polarized optical micrographs of TIPS-BP dip-coated using CH_2Cl_2 with 10% $CHCl_3$ as solvent: (a) on MODPA SAM, (b) on CDPA SAM. The MODPA-modified surface affords a higher surface coverage and smaller domains, while the CDPA-modified surface gives a lower surface coverage and larger domains. These observations are in accordance with the fact that CDPA gives lower surface energies as compared to MODPA.

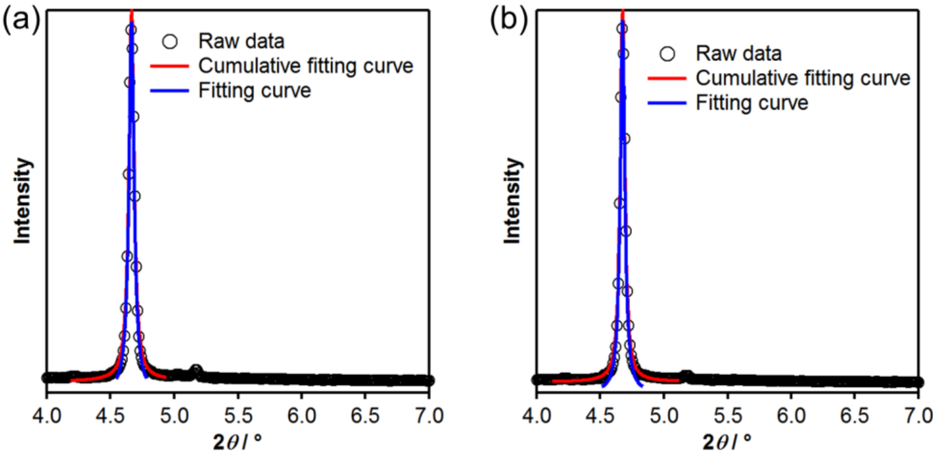

Figure S3-12. Profile analysis to determine FWHM values for primary XRD peaks and estimated crystallite sizes in dip-coated TIPS-BP; (a) on MODPA SAM (estimated average crystal size = 330 nm), (b) on CDPA SAM (375 nm).

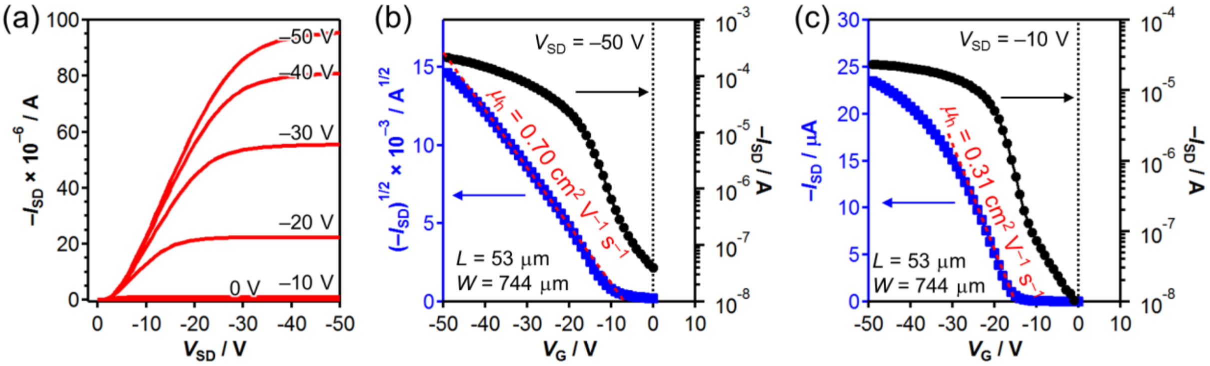

Figure S3-13. FET data of a TIPS-BP film deposited under the optimized conditions; (a) Output characteristics, (b,c) Transfer curves at V_{SD} = –50 V (saturation region) and –10 V (linear region at V_G = –20 V). Note that the saturation mobility can be overestimated. At the same time, the mobility derived from the linear regime might be underestimated owing to the strong influence by the contact resistance as commented by, for example, Bao et al.[10] With these considered, as well as the fact that the so-far reported field-effect mobilities for BP and its derivatives have been fitted from the saturation region, it would be reasonable to employ saturation mobilities for discussion and comparison purposes in the present work.

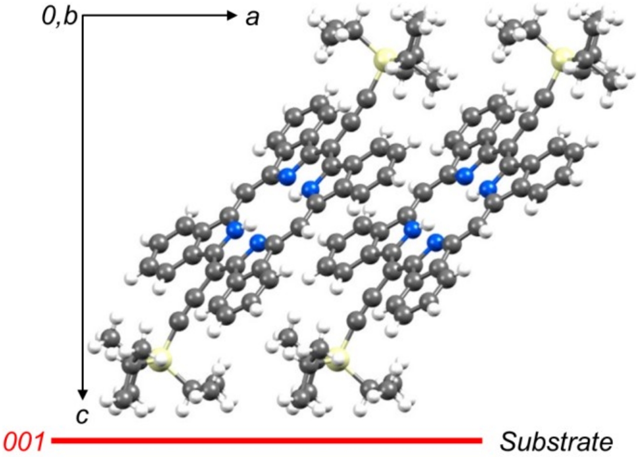

Figure S3-14. Relation between 2D π-stack crystallites and substrate.

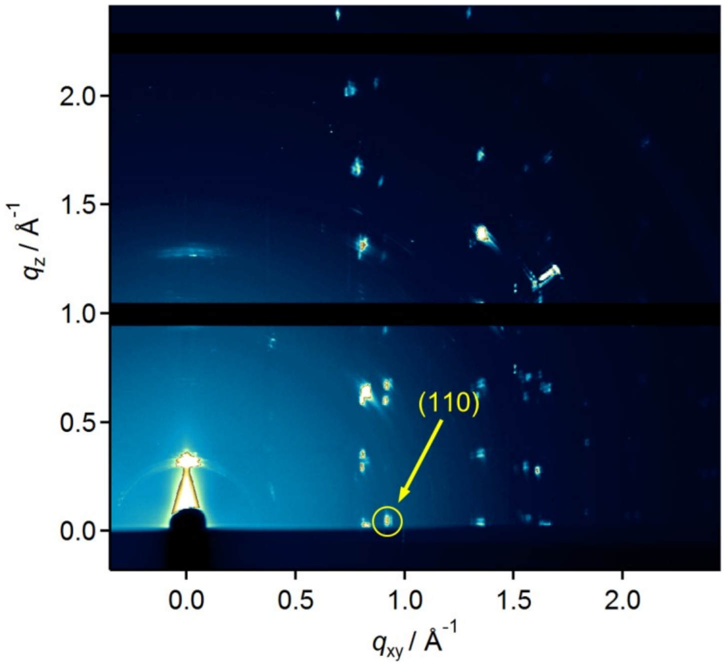

Figure S3-15. Integrated 2D-GIWAXD image of an OFET active layer deposited by dip coating from a dichloromethane/chloroform (9:1 vol) solution of TIPS-BP on a CDPA-modified substrate. The yellow arrow and circle indicate the 110 diffraction of the 2D π-stack motif.

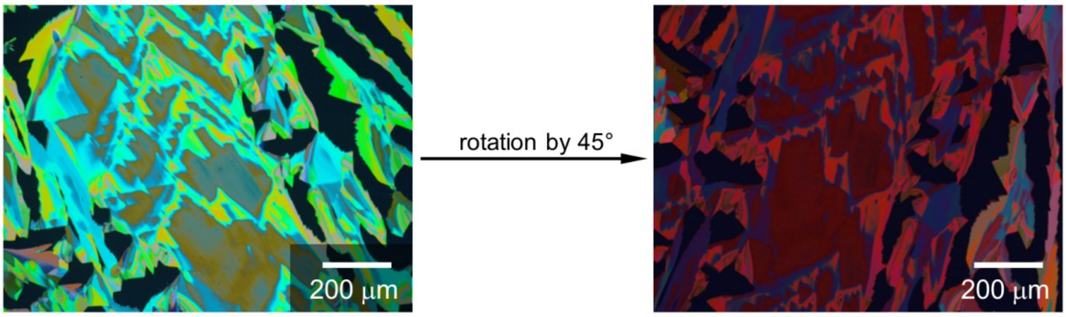

Figure S3-16. Polarized optical micrographs of 2D π-stack grown on a CDPA monolayer.

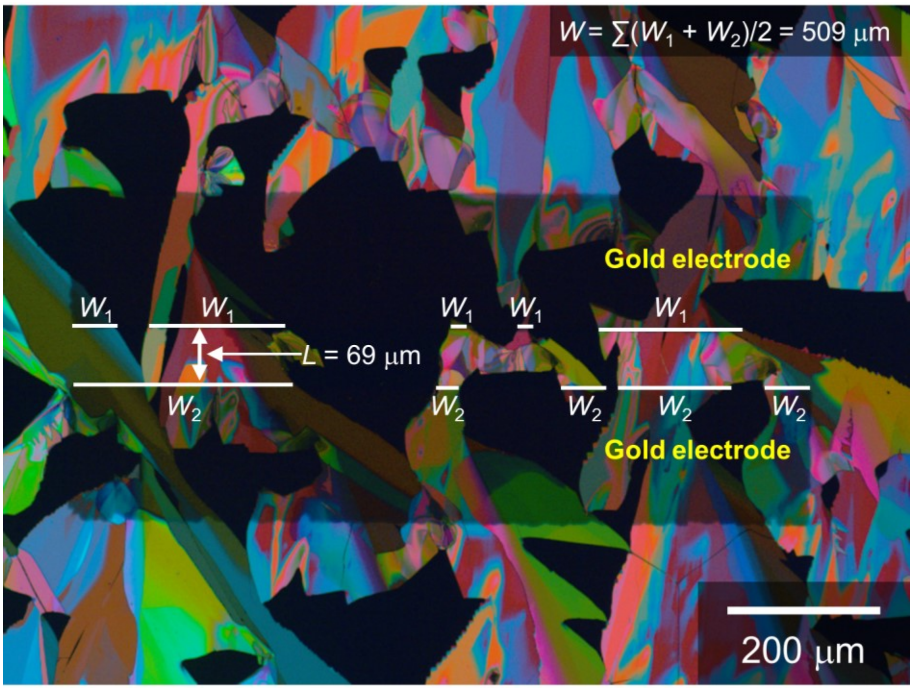

Figure S3-17. Reflected polarized-light micrograph for the best-performing OFET device which was fabricated via dip coating from a dichloromethane/chloroform (9:1 vol) solution of TIPS-BP on a CDPA-modified substrate. The white lines were measured directly from the images to calculate the effective channel widths (*W*) and lengths (*L*).

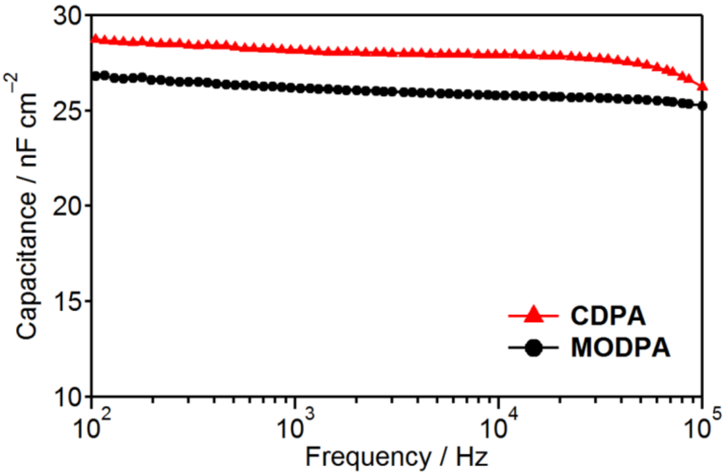

Figure S3-18. Capacitance density versus frequency under 0 V bias voltage of MOPDA and CDPA-modified SiO_2/Al_2O_3 dielectrics as measured from a metal–insulator–metal structure.

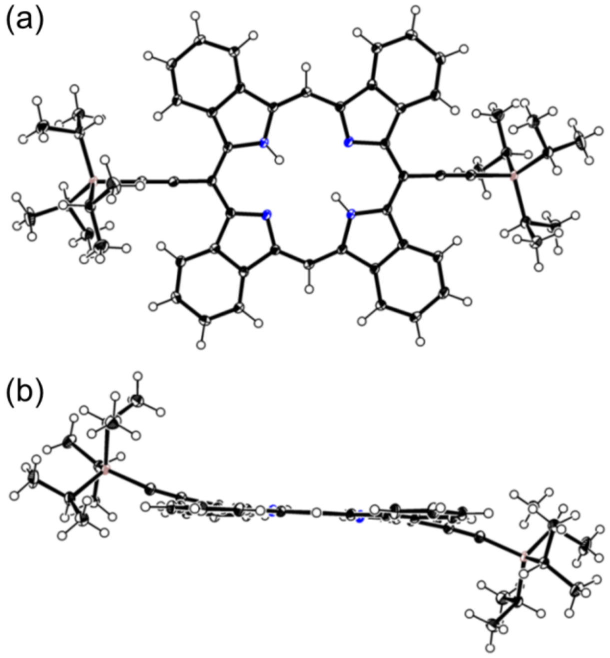

Figure S3-19. Crystal structure of TIPS-BP in 2D π-stack; (a) top view and (b) side view. Thermal ellipsoids represent the 50% probability.

Table S3-1. Crystal data and structure refinement for TIPS-BP of 2D π-stack motif.

Empirical formula	$C_{58}H_{62}N_4Si_2$	
Formula weight	871.33	
Temperature	103 K	
Wavelength	0.71075 Å	
Crystal system	triclinic	
Space group	*P*-1	
Unit cell dimensions	a = 8.21844(15) Å	α = 86.5438(7)°
	b = 8.23048(15) Å	β = 88.8447(7)°
	c = 18.9666(4) Å	γ = 67.9519(7)°
Volume	1186.95(4) $Å^3$	
Z	1	
Density (calculated)	1.219 g cm^{-3}	
Absorption coefficient	1.182 cm^{-1}	
$F(000)$	466	
Crystal size	0.20 × 0.08 × 0.04 mm	
Theta range for data collection	3.13 to 27.47°	
Index ranges	$-10 \leq h \leq 10$, $-10 \leq k \leq 10$, $-24 \leq l \leq 24$	
Reflections collected	20542	
Independent reflections	5428 [R(int) = 0.0257]	
Max. and min. transmission	0.995 and 0.888	
Refinement method	Full-matrix least-squares on F^2	
Data / restraints / parameters	5428 / 0 / 295	
Goodness-of-fit on F^2	1.144	
Final R indices [$I > 2\sigma(I)$]	R_1 = 0.0416, wR_2 = 0.1079	
R indices (all data)	R_1 = 0.0466, wR_2 = 0.1126	
Largest diff. peak and hole	0.663 and –0.314 e $Å^{-3}$	
CCDC No.	1441675	

3-7. Experimental Section

3-7-1. General

Materials for Device Fabrication

TIPS-BP,[16] MODPA,[24] and CDPA[25] were prepared according to the reported procedures.

Preparation of Dielectric Layers

The highly n-doped silicon wafers with a 100 nm-thick thermally grown SiO_2 layer were cleaned sequentially with acetone, isopropanol and ethanol for 10 min in an ultrasonic bath. After rinsing ethanol by deionized (DI) water, substrates were dried with a flow of nitrogen gas and then treated by oxygen plasma for 2 min. A solution of $Al(NO_3)_3 \cdot 9H_2O$ in ethanol (0.15 M) was spin-coated (5000 rpm, 40 s) on cleaned substrates and annealed at 300 °C for 30 min in air to form an Al_2O_3 layer, following the reported solution-based procedure to form dielectrics.[31] To form SAMs of MODPA and CDPA, Al_2O_3-coated substrates were treated by oxygen plasma for 1.5 min and then soaked in a solution of the MODPA or CDPA in isopropanol (1.5 mM) at room temperature for 12 hours. Lastly, substrates were rinsed with isopropanol in an ultrasonic bath and DI water, and then dried with a flow of nitrogen gas to afford SAM-modified substrates.

Preparation of Active Layers

To form drop-cast films, one drop of TIPS-BP solution (2.0 mg mL^{-1} in chlorobenzene (entry 1) or 0.5 mg mL^{-1} in toluene (entry 2)) was dropped onto a MODPA-modified substrate (12 mm × 12 mm) and then dried up solvent in air. To form dip-coated films, a SAM (MODPA or CDPA)-modified substrate (12 mm × 6 mm) was immersed vertically in a TIPS-BP solution (2.0 mg mL^{-1} in chloroform (entry 3) or 1.0 mg mL^{-1} in either dichloromethane (entry 4) or dichloromethane/chloroform (9:1 vol, entries 5 and 6)) and then pulled up at a constant speed of 0.1 mm min^{-1} as controlled by a Longer Pump TJ-3A syringe pump controller.

Deposition of Source and Drain Electrodes

Top contact source and drain electrodes were vacuum-deposited afterward through a shadow mask onto the active layer by an Edward Auto 306 vacuum coating system with a Turbomolecular pump at a pressure of 2.0×10^{-6} torr or lower, with a deposition rate of ca. 2 nm min^{-1} to a thickness about 30 nm as measured by a quartz crystal sensor.

Characterization of the Thin Films and OFETs

Polarized optical images of the thin films were obtained using Nikon 50IPOL microscope. Out-of-plane XRD measurements with θ–2θ scan mode were carried out on a SmartLab X-ray Refractometer. Tapping-mode AFM images were observed by an SPM-9700 (Shimazu). Azimuthal (ϕ) diffraction scan was conducted in beamline BL19B2 at SPring-8 (Hyogo, Japan) with a GIWAXD setup. The X-ray beam was monochromatized by a double-crystal Si(111) monochromator, and the X-ray energy was 12.398 keV (λ = 1 Å). The incident angle was set to 0.12° with a Huber diffractometer and the sample-to-detector distance was 175 mm. The sample for this experiment was the best performing OTFT device and located with the pull-up direction parallel to the incident X-ray. The direction of ϕ-scan was set as a clockwise rotation with a scan step of 0.2°. Diffracted X-rays from samples were recorded by an X-ray photon counting pixel detector (PILATUS 300 K, Dectris) for 1 s for every azimuthal angle at room temperature in air. The current–voltage measurements of OFETs were conducted using a probe station (4PROBES TECH, ST-102C) and a Keithley 4200 Semiconductor Characterization System in air. The field-effect hole mobilities in the devices were calculated in the saturation regime. The equation is listed as follows:

$$I_{DS} = (\mu W C\text{i}/2L)(V_G - V_{th})^2$$

where I_{DS} is the drain–source current, μ the field–effect mobility, W the channel width, L the channel length, V_G the gate voltage and V_{th} threshold voltage and C_i the capacitance per unit area of the gate dielectric layer. Effective W and L were measured by an optical microscope (see Figure S3-17). The frequency-dependent capacitance of SAM-modified SiO_2/Al_2O_3 were measured using a HP 4284A Precision LCR Meter in a frequency range of 100 Hz to 100 kHz from a metal–insulator–metal structure, which had vacuum-deposited gold (0.2 mm × 1 mm) as the top electrode and a highly doped silicon substrate as the bottom electrode. The capacitance per unit area of MODPA and CDPA-modified SiO_2/Al_2O_3 as taken at the lowest frequency (100 Hz) were 27 and 28 nF cm^{-2}, respectively (Figure S3-18). This measurement was conducted by Dr. Xiaomin Xu in the Prof. Miao's group of CUHK.

Single-Crystal X-ray Crystallography

Single crystals of 2D π-stacking motif of TIPS-BP were obtained from recrystallization of TIPS-BP in a $CHCl_3$ or chlorobenzene solution at room temperature. Single crystals of 1D π-stacking motif of TIPS-BP were obtained from slow diffusion of methanol into a $CHCl_3$ solution or slow diffusion of *n*-hexane into a chlorobenzene solution. Single-crystal X-ray diffraction data of 2D π-stacking motif of TIPS-BP were collected at 103 K on a Rigaku VariMax RAPID using Mo-Kα radiation. The structures were solved by direct methods and refined on F^2 by full-matrix least-squares using the CrystalClear and SHELXS-97 program (Table S3-1 and Figure S3-19). CCDC 1441675 contains the crystallographic data of 2D π-stack. This data can be obtained free of charge from The Cambridge Crystallographic Data Centre via https://summary.ccdc.cam.ac.uk/structure-summary-form.

Charge Transfer Integral Calculation

Charge transfer integrals were calculated by fragment orbital method with the GGA:BP/DZP level of theory using ADF program.[45]

2-8. References

(1) Brédas, J. L.; Calbert, J. P.; da Silva Filho, D. A.; Cornil, J. Organic Semiconductors: A Theoretical Characterization of the Basic Parameters Governing Charge Transport. *Proc. Natl. Acad. Sci. U. S. A.* **2002**, *99*, 5804–5809.

(2) Lee, J. Y.; Roth, S.; Park, Y. W. Anisotropic Field Effect Mobility in Single Crystal Pentacene. *Appl. Phys. Lett.* **2006**, *88*, 252106.

(3) Sundar, V. C.; Zaumseil, J.; Podzorov, V.; Menard, E.; Willett, R. L.; Someya, T.; Gershenson, M. E.; Rogers, J. A. Elastomeric Transistor Stamps: Reversible Probing of Charge Transport in Organic Crystals. *Science* **2004**, *303*, 1644–1646.

(4) Choi, S.; Chae, S. H.; Hoang, M. H.; Kim, K. H.; Huh, J. A.; Kim, Y.; Kim, S.-J.; Choi, D. H.; Lee, S. J. An Unsymmetrically π-Extended Porphyrin-Based Single-Crystal Field-Effect Transistor and Its Anisotropic Carrier-Transport Behavior. *Chem. – Eur. J.* **2013**, *19*, 2247–2251.

(5) Noh, Y.-Y.; Kim, J.-J.; Yoshida, Y.; Yase, K. Effect of Molecular Orientation of Epitaxially Grown Platinum(II) Octaethyl Porphyrin Films on the Performance of Field-Effect Transistors. *Adv. Mater.* **2003**, *15*, 699–702.

(6) Lim, J. A.; Lee, H. S.; Lee, W. H.; Cho, K. Control of the Morphology and Structural Development of Solution-Processed Functionalized Acenes for High-Performance Organic Transistors. *Adv. Funct. Mater.* **2009**, *19*, 1515–1525.

(7) Minemawari, H.; Yamada, T.; Matsui, H.; Tsutsumi, J.; Haas, S.; Chiba, R.; Kumai, R.; Hasegawa, T. Inkjet Printing of Single-Crystal Films. *Nature* **2011**, *475*, 364–367.

(8) Kang, B.; Jang, M.; Chung, Y.; Kim, H.; Kwak, S. K.; Oh, J. H.; Cho, K. Enhancing 2D Growth of Organic Semiconductor Thin Films with Macroporous Structures via a Small-Molecule Heterointerface. *Nat. Commun.* **2014**, *5*, 4752.

(9) Gundlach, D. J.; Royer, J. E.; Park, S. K.; Subramanian, S.; Jurchescu, O. D.; Hamadani, B. H.; Moad, A. J.; Kline, R. J.; Teague, L. C.; Kirillov, O.; Richter, C. A.;

Kushmerick, J. G.; Richter, L. J.; Parkin, S. R.; Jackson, T. N.; Anthony, J. E. Contact-Induced Crystallinity for High-Performance Soluble Acene-Based Transistors and Circuits. *Nat. Mater.* **2008**, *7*, 216–221.

(10) Yuan, Y.; Giri, G.; Ayzner, A. L.; Zoombelt, A. P.; Mannsfeld, S. C. B.; Chen, J.; Nordlund, D.; Toney, M. F.; Huang, J.; Bao, Z. Ultra-High Mobility Transparent Organic Thin Film Transistors Grown by an Off-Centre Spin-Coating Method. *Nat. Commun.* **2014**, *5*, 3005.

(11) Diao, Y.; Tee, B. C.-K.; Giri, G.; Xu, J.; Kim, D. H.; Becerril, H. A.; Stoltenberg, R. M.; Lee, T. H.; Xue, G.; Mannsfeld, S. C. B.; Bao, Z. Solution Coating of Large-Area Organic Semiconductor Thin Films with Aligned Single-Crystalline Domains. *Nat. Mater.* **2013**, *12*, 665–671.

(12) Mattheus, C. C.; Dros, A. B.; Baas, J.; Oostergetel, G. T.; Meetsma, A.; de Boer, J. L.; Palstra, T. T. M. Identification of Polymorphs of Pentacene. *Synth. Met.* **2003**, *138*, 475–481.

(13) Ito, S.; Murashima, T.; Uno, H.; Ono, N. A New Synthesis of Benzoporphyrins Using 4,7-Dihydro-4,7-Ethano-2*H*-Isoindole as a Synthon of Isoindole. *Chem. Commun.* **1998**, 1661–1662.

(14) Noguchi, N.; Junwei, S.; Asatani, H.; Matsuoka, M. Control of Morphology and Orientation of a Thin Film Tetrabenzoporphyrin (TBP) Organic Semiconductor by Solid-State Crystallization. *Cryst. Growth Des.* **2010**, *10*, 1848–1853.

(15) Shea, P. B.; Kanicki, J.; Pattison, L. R.; Petroff, P.; Kawano, M.; Yamada, H.; Ono, N. Solution-Processed Nickel Tetrabenzoporphyrin Thin-Film Transistors. *J. Appl. Phys.* **2006**, *100*, 34502.

(16) Takahashi, K.; Kuzuhara, D.; Aratani, N.; Yamada, H. Synthesis and Crystal Structures of 5,15-Bis(triisopropylsilylethynyl)-tetrabenzoporphyrins. *J. Photopolym. Sci. Technol.* **2013**, *26*, 213–216.

(17) Takahashi, K.; Yamada, N.; Kumagai, D.; Kuzuhara, D.; Suzuki, M.; Yamaguchi, Y.; Aratani, N.; Nakayama, K.; Yamada, H. Effect of Alkyl Substituents: 5,15-Bis(trimethylsilylethynyl)- vs. 5,15-Bis(triisopropylsilylethynyl)-tetrabenzoporphyrins and Their Metal Complexes. *J. Porphyrins Phthalocyanines* **2015**, *19*, 465–478.

(18) Anthony, J. E.; Brooks, J. S.; Eaton, D. L.; Parkin, S. R. Functionalized Pentacene: Improved Electronic Properties from Control of Solid-State Order. *J. Am. Chem. Soc.* **2001**, *123*, 9482–9483.

(19) Giri, G.; Verploegen, E.; Mannsfeld, S. C. B.; Atahan-Evrenk, S.; Kim, D. H.; Lee, S. Y.; Becerril, H. A.; Aspuru-Guzik, A.; Toney, M. F.; Bao, Z. Tuning Charge Transport in Solution-Sheared Organic Semiconductors Using Lattice Strain. *Nature* **2011**, *480*, 504–508.

(20) Kim, D. H.; Lee, D. Y.; Lee, H. S.; Lee, W. H.; Kim, Y. H.; Han, J. I.; Cho, K. High-Mobility Organic Transistors Based on Single-Crystalline Microribbons of Triisopropylsilylethynyl Pentacene via Solution-Phase Self-Assembly. *Adv. Mater.* **2007**, *19*, 678–682.

(21) Park, S. K.; Jackson, T. N.; Anthony, J. E.; Mourey, D. A. High Mobility Solution Processed 6,13-Bis(triisopropyl-Silylethynyl) Pentacene Organic Thin Film Transistors. *Appl. Phys. Lett.* **2007**, *91*, 63514.

(22) Tsutsui, Y.; Schweicher, G.; Chattopadhyay, B.; Sakurai, T.; Arlin, J.-B.; Ruzié, C.; Aliev, A.; Ciesielski, A.; Colella, S.; Kennedy, A. R.; Lemaur, V.; Olivier, Y.; Hadji, R.; Sanguinet, L.; Castet, F.; Osella, S.; Dudenko, D.; Beljonne, D.; Cornil, J.; Samorì, P.; Seki, S.; Geerts, Y. H. Unraveling Unprecedented Charge Carrier Mobility through Structure Property Relationship of Four Isomers of Didodecyl[1]benzothieno[3,2-*b*][1]benzothiophene. *Adv. Mater.* **2016**, *28*, 7106–7114.

(23) Xu, W.; Wang, H.; Ye, L.; Xu, J. The Role of Solution-Processed High-κ Gate

Dielectrics in Electrical Performance of Oxide Thin-Film Transistors. *J. Mater. Chem. C* **2014**, *2*, 5389–5396.

(24) Liu, D.; Xu, X.; Su, Y.; He, Z.; Xu, J.; Miao, Q. Self-Assembled Monolayers of Phosphonic Acids with Enhanced Surface Energy for High-Performance Solution-Processed n-Channel Organic Thin-Film Transistors. *Angew. Chem. Int. Ed.* **2013**, *52*, 6222–6227.

(25) Liu, D.; He, Z.; Su, Y.; Diao, Y.; Mannsfeld, S. C. B.; Bao, Z.; Xu, J.; Miao, Q. Self-Assembled Monolayers of Cyclohexyl-Terminated Phosphonic Acids as a General Dielectric Surface for High-Performance Organic Thin-Film Transistors. *Adv. Mater.* **2014**, *26*, 7190–7196.

(26) Anderson, P. A. Work Function of Gold. *Phys. Rev.* **1959**, *115*, 553–554.

(27) Rivière, J. C. The Work Function of Gold. *Appl. Phys. Lett.* **1966**, *8*, 172–172.

(28) Liman, C. D.; Choi, S.; Breiby, D. W.; Cochran, J. E.; Toney, M. F.; Kramer, E. J.; Chabinyc, M. L. Two-Dimensional GIWAXS Reveals a Transient Crystal Phase in Solution-Processed Thermally Converted Tetrabenzoporphyrin. *J. Phys. Chem. B* **2013**, *117*, 14557–14567.

(29) Youn, J.; Kewalramani, S.; Emery, J. D.; Shi, Y.; Zhang, S.; Chang, H.-C.; Liang, Y.; Yeh, C.-M.; Feng, C.-Y.; Huang, H.; Stern, C.; Chen, L.-H.; Ho, J.-C.; Chen, M.-C.; Bedzyk, M. J.; Facchetti, A.; Marks, T. J. Fused Thiophene Semiconductors: Crystal Structure–Film Microstructure Transistor Performance Correlations. *Adv. Funct. Mater.* **2013**, *23*, 3850–3865.

(30) Sele, C. W.; Kjellander, B. K. C.; Niesen, B.; Thornton, M. J.; van der Putten, J. B. P. H.; Myny, K.; Wondergem, H. J.; Moser, A.; Resel, R.; van Breemen, A. J. J. M.; van Aerle, N.; Heremans, P.; Anthony, J. E.; Gelinck, G. H. Controlled Deposition of Highly Ordered Soluble Acene Thin Films: Effect of Morphology and Crystal Orientation on Transistor Performance. *Adv. Mater.* **2009**, *21*, 4926–4931.

(31) Rogowski, R. Z.; Dzwilewski, A.; Kemerink, M.; Darhuber, A. A. Solution Processing of Semiconducting Organic Molecules for Tailored Charge Transport Properties. *J. Phys. Chem. C* **2011**, *115*, 11758–11762.

(32) Jang, J.; Nam, S.; Im, K.; Hur, J.; Cha, S. N.; Kim, J.; Son, H. B.; Suh, H.; Loth, M. A.; Anthony, J. E.; Park, J.-J.; Park, C. E.; Kim, J. M.; Kim, K. Highly Crystalline Soluble Acene Crystal Arrays for Organic Transistors: Mechanism of Crystal Growth During Dip-Coating. *Adv. Funct. Mater.* **2012**, *22*, 1005–1014.

(33) Gao, P.; Beckmann, D.; Tsao, H. N.; Feng, X.; Enkelmann, V.; Baumgarten, M.; Pisula, W.; Müllen, K. Dithieno[2,3-*d*;2′,3′-*d*′]benzo[1,2-*b*;4,5-*b*′]dithiophene (DTBDT) as Semiconductor for High-Performance, Solution-Processed Organic Field-Effect Transistors. *Adv. Mater.* **2009**, *21*, 213–216.

(34) Li, L.; Gao, P.; Schuermann, K. C.; Ostendorp, S.; Wang, W.; Du, C.; Lei, Y.; Fuchs, H.; Cola, L. D.; Müllen, K.; Chi, L. Controllable Growth and Field-Effect Property of Monolayer to Multilayer Microstripes of an Organic Semiconductor. *J. Am. Chem. Soc.* **2010**, *132*, 8807–8809.

(35) Nam, S.; Jang, J.; Anthony, J. E.; Park, J.-J.; Park, C. E.; Kim, K. High-Performance Triethylsilylethynyl Anthradithiophene Transistors Prepared without Solvent Vapor Annealing: The Effects of Self-Assembly during Dip-Coating. *ACS Appl. Mater. Interfaces* **2013**, *5*, 2146–2154.

(36) Xu, X.; Yao, Y.; Shan, B.; Gu, X.; Liu, D.; Liu, J.; Xu, J.; Zhao, N.; Hu, W.; Miao, Q. Electron Mobility Exceeding 10 cm^2 V^{-1} s^{-1} and Band-Like Charge Transport in Solution-Processed n-Channel Organic Thin-Film Transistors. *Adv. Mater.* **2016**, *28*, 5276–5283.

(37) Rivnay, J.; Jimison, L. H.; Northrup, J. E.; Toney, M. F.; Noriega, R.; Lu, S.; Marks, T. J.; Facchetti, A.; Salleo, A. Large Modulation of Carrier Transport by Grain-Boundary Molecular Packing and Microstructure in Organic Thin Films. *Nat. Mater.* **2009**, *8*,

952–958.

(38) Diao, Y.; Shaw, L.; Bao, Z.; Mannsfeld, S. C. B. Morphology Control Strategies for Solution-Processed Organic Semiconductor Thin Films. *Energy Environ. Sci.* **2014**, *7*, 2145–2159.

(39) Minari, T.; Kano, M.; Miyadera, T.; Wang, S.-D.; Aoyagi, Y.; Tsukagoshi, K. Surface Selective Deposition of Molecular Semiconductors for Solution-Based Integration of Organic Field-Effect Transistors. *Appl. Phys. Lett.* **2009**, *94*, 93307.

(40) Ho, C.-C.; Tao, Y.-T. Crystallization of Rubrene on a Nanopillar-Templated Surface by the Melt-Recrystallization Process and Its Application in Field-Effect Transistors. *Chem. Commun.* **2014**, *51*, 603–606.

(41) Diao, Y.; Zhou, Y.; Kurosawa, T.; Shaw, L.; Wang, C.; Park, S.; Guo, Y.; Reinspach, J. A.; Gu, K.; Gu, X.; Tee, B. C. K.; Pang, C.; Yan, H.; Zhao, D.; Toney, M. F.; Mannsfeld, S. C. B.; Bao, Z. Flow-Enhanced Solution Printing of All-Polymer Solar Cells. *Nat. Commun.* **2015**, *6*, 7955.

(42) Hiszpanski, A. M.; Baur, R. M.; Kim, B.; Tremblay, N. J.; Nuckolls, C.; Woll, A. R.; Loo, Y.-L. Tuning Polymorphism and Orientation in Organic Semiconductor Thin Films via Post-Deposition Processing. *J. Am. Chem. Soc.* **2014**, *136*, 15749–15756.

(43) Diao, Y.; Lenn, K. M.; Lee, W.-Y.; Blood-Forsythe, M. A.; Xu, J.; Mao, Y.; Kim, Y.; Reinspach, J. A.; Park, S.; Aspuru-Guzik, A.; Xue, G.; Clancy, P.; Bao, Z.; Mannsfeld, S. C. B. Understanding Polymorphism in Organic Semiconductor Thin Films through Nanoconfinement. *J. Am. Chem. Soc.* **2014**, *136*, 17046–17057.

(44) Giri, G.; Li, R.; Smilgies, D.-M.; Li, E. Q.; Diao, Y.; Lenn, K. M.; Chiu, M.; Lin, D. W.; Allen, R.; Reinspach, J.; Mannsfeld, S. C. B.; Thoroddsen, S. T.; Clancy, P.; Bao, Z.; Amassian, A. One-Dimensional Self-Confinement Promotes Polymorph Selection in Large-Area Organic Semiconductor Thin Films. *Nat. Commun.* **2014**, *5*, 3573.

(45) te Velde, G.; Bickelhaupt, F. M.; Baerends, E. J.; Fonseca Guerra, C.; van Gisbergen, S.

J. A.; Snijders, J. G.; Ziegler, T. Chemistry with ADF. *J. Comput. Chem.* **2001**, *22*, 931–967.

Chapter 4

Molecular Engineering on a Tetrabenzoporphyrin-Based Acceptor–Donor–Acceptor System for Efficient Photocurrent Generation in Bulk-Heterojunction Layers

---

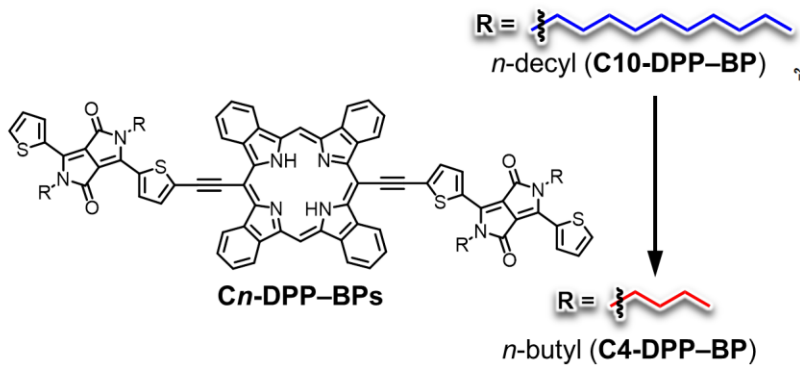

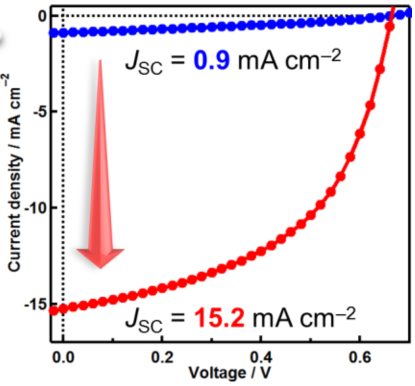

This chapter describes the synthesis, electronic properties, and photovoltaic performance of a series of new BP derivatives linking with dithienyldiketopyrrolopyrroles (DPPs) with different length of alkyl side-chains (C*n*-DPP–BPs). Systematical investigation of C*n*-DPP–BPs on the OPV performance reveals the significant substituent impact in J_{SC} ranging from 0.88 mA cm^{-2} with C10-DPP–BP to 15.19 mA cm^{-2} with C4-DPP–BP, resulting in PCEs of 0.2 and 5.2 %, respectively. The fluorescence decay measurements, AFM, and 2D-GIWAXD indicate that the introduction of shorter alkyl chains on a C*n*-DPP–BP framework induces better miscibility, finer grains, and π–π stacking.

4-1. Introduction

The aim of this chapter is to offer a high-performance BP-based molecular semiconductor that can be processed by the precursor approach for the photovoltaic application. The state-of-the-art OPVs have achieved PCEs of over 10%,[1–8] and many research groups are working toward even higher efficiencies in order for realizing practically useful devices. The author envisions that a high-performance p-type material may be obtained by exploiting the superior traits of BP such as the high absorption coefficient,[9,10] good hole transport capability,[11,12] and exceptional stability.[13,14] In addition, the precursor approach provides unique opportunities in controlling the molecular arrangement in blend films, which will enable construction of well-performing photovoltaic layers.[15,16]

One of the key tasks in this context is the expansion of photoabsorption range. BP has rather narrow absorption bands, being transparent at 500–600 nm and over 700 nm.[17,18] Accordingly, J_{SC} values in BP-based OPVs have been relatively low; for example, the p–i–n-type system reported by Matsuo et al. showed a J_{SC} of 10.5 mA cm^{-2} at maximum, while the current best cells typically afford J_{SC} of 15–20 mA cm^{-2}.[1,3–8] The most straightforward approach to extend the photoabsorption range of BP would be having it conjugated with other π-systems. However, systematic investigation for this purpose has been scarce probably because of the limited synthetic accessibility to BP derivatives. Meanwhile, the author investigated that 5,15-bis(trialkylsilyl)ethynylbenzoporphyrins could be formed in good yields via the corresponding CP-type precursors (i.e., via the precursor approach),[19,20] which can serve as useful intermediates in the construction of extended π-systems based on BP in Chapter 2.

Another important factor to be considered in improving J_{SC} is substituents of active-layer materials. It is well known that the photovoltaic performance of organic semiconductors largely depends not only on the main π-framework but also on the structure and position of peripheral substituents. For instance, Shin et al. reported that the difference in alkyl-chain length on a dithienyldiketopyrrolopyrrole (DPP)-based small-molecule system brought about a considerable variation in J_{SC} ranging from below 4 to over 8 mA cm^{-2} associated with a change in PCE from 1.1 to 4.2%.[21] This and many other examples have demonstrated the critical role of substituents in determining the p/n interface area and domain size, the two major morphological parameters that influence the charge-carrier generation and transport efficiencies in organic photovoltaic layers.[21–24] The two parameters are often related also to the FF and sometimes to the V_{OC} of OPVs, further enhancing the importance of the optimization of thin film morphology through substituent engineering.[23,25,26]

In this chapter, the author has designed a series of DPP–BP conjugates that can efficiently absorb at a wide range of wavelengths in the visible and near-infrared region. These conjugates have normal alkyl chains on the DPP units, and are denoted as C*n*-DPP–BP where *n* is 2, 4, 6, 8, or 10 depending on the length of alkyl chains (Figure 4-1). Note that C*n*-DPP–BPs are all insoluble in common organic solvents thus solution-deposited via the precursor approach from the corresponding CP derivatives.

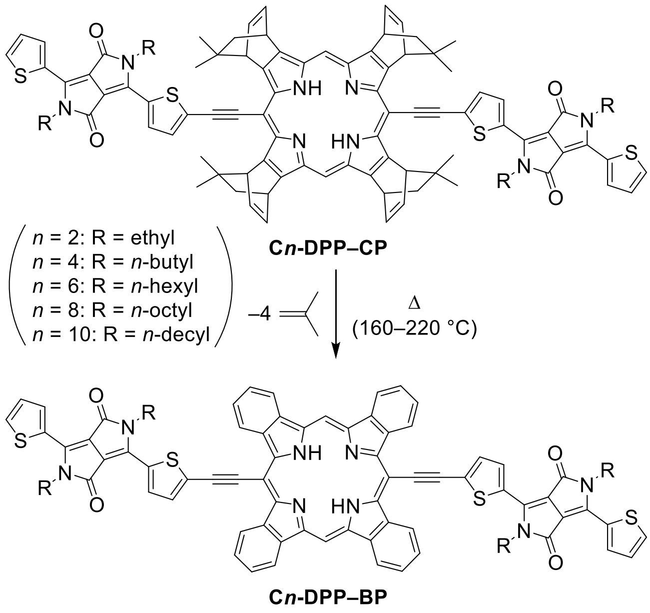

Figure 4-1. Formation of C*n*-DPP–BPs from the corresponding thermally convertible precursors C*n*-DPP–CPs. C*n*-DPP–BPs were isolated and used as mixtures of diastereomers.

The following sections compare BHJ OPVs comprising C*n*-DPP–BP and $PC_{61}BM$, revealing that alkyl-chain length greatly affects the photovoltaic parameters of C*n*-DPP–BP: $PC_{61}BM$ blends. Difference in J_{SC} is especially large, ranging from 0.88 mA cm^{-2} with C10-DPP–BP to 15.25 mA cm^{-2} with C4-DPP–BP, resulting in PCEs of 0.19 and 5.21%, respectively. The origin of this substituent impact is discussed based on morphological analyses by fluorescence decay measurements, AFM, and 2D-GIWAXD. The results reported herein will serve as a basis for the substituent-directed morphology control in blend films prepared through the thermo-precursor approach, and pave the way to BP-based high-performance OPVs.

4-2. Molecular Design and Synthesis

C*n*-DPP–BPs are designed to have an acceptor–donor–acceptor (A–D–A) configuration in which BP and DPP act as donor and acceptor units, respectively. Construction of the A–D–A structure has been a widely used molecular-design strategy to achieve desirable frontier-orbital energy levels and effective π-conjugation for many state-of-the-art OPV materials.[27] The DPP chromophore is chosen as a partner of BP, since DPP possesses a strong absorption band around 550 nm at which BP's absorption valley locates.[28] The BP and DPP units are connected through the sterically non-demanding ethynylene linkage in order to minimize the steric hindrance between the benzo moieties and the *meso* substituents of BP. Molecular geometry optimization by the DFT has predicted that C*n*-DPP–BPs have efficient π-conjugation within a relatively flat molecular conformation (Figure 4-2). Peripheral substituents in C*n*-DPP–BPs are kept minimal; namely, each C*n*-DPP–BP molecule is equipped with only four linear, relatively short alkyl chains at the nitrogen atoms of DPP moieties. Accordingly, C*n*-DPP–BPs are all insoluble in common organic solvents. This molecular design is made possible by employment of the precursor approach and beneficial in that large π-systems, such as C*n*-DPP–BPs, do not require heavy decoration with insulating

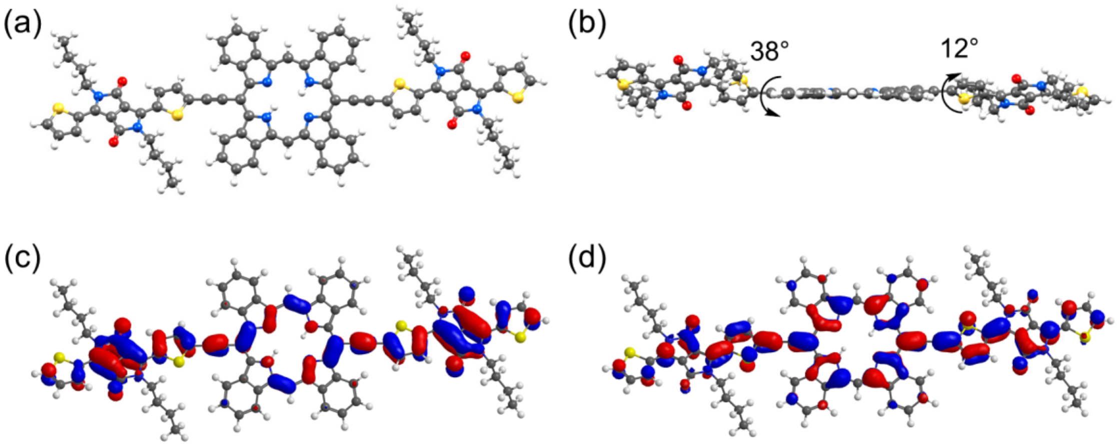

Figure 4-2. Optimized molecular structure of C4-DPP–BP (a) top view and (b) side view with the dihedral angles between BP and DPP planes. Geometry of (c) HOMO and (d) LUMO for the optimized structure of C4-DPP–BP. HOMO and LUMO are delocalized BP and DPP units indicate the effective expansion of π-conjugation through ethynyl spacers.

solubilizing groups which are unnecessary in terms of the optimization of thin-film morphology and molecular packing.

The precursors C*n*-DPP–CPs have dimethylethano bridges as thermally removable solubilizing units in order to ensure enough solubility for synthesis and solution deposition.[29–31] Thermally induced retro-Diels–Alder reactions of each C*n*-DPP–CP were confirmed by thermogravimetric analysis in the solid state (Figure 4-3). The mass loss of precursors starts at 131–136 °C and ends at 181–191 °C. The mass loss proportions of C2-, C4-, C6-, C8- and C10-DPP–CPs are 15.2, 14.0, 13.1, 12.3, and 11.6%, respectively, that are in good agreement with the elimination of four isobutene molecules (calculated values of mass loss are 15.0, 14.0, 13.1, 12.3 and 11.6%). The decomposition temperatures of C2-, C4-, C6-, C8-, and C10-DPP–CPs are 432, 403, 378, 359, and 354 °C, respectively. The thermal stability of C*n*-DPP–BPs is higher with the shorter alkyl chains than the longer chains. Note that the original CP has non-methylated ethano bridges which are often insufficient for solubilizing π-extended CP derivatives.

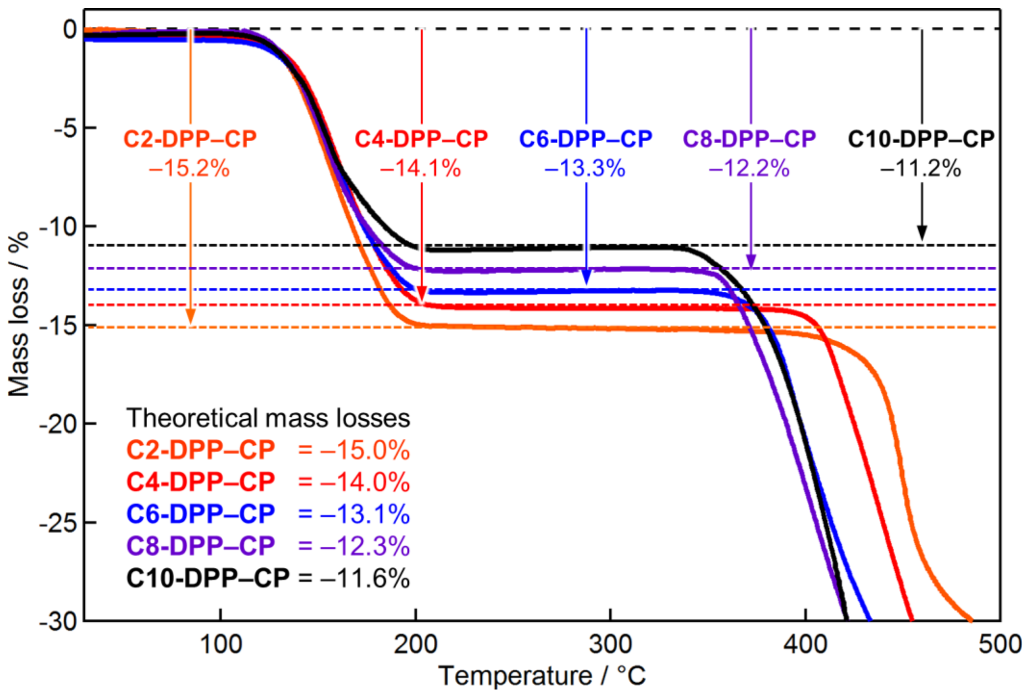

Figure 4-3. TGA curves of C*n*-DPP–CPs.

C*n*-DPP–CPs were synthesized via the corresponding ethynyl-substituted CP, which was obtained by a MacDonald-type condensation of two dipyrromethane subunits (Scheme 4-1 and Experimental Section).[19,20]

Here, while five diastereomers are possible to form depending on the relative orientation of four dimethylethano bridges against the porphyrin framework, only a mixture of two diastereomers were subjected to the following steps toward C*n*-DPP–CPs (see Experimental Section). The exact structure of other three diastereomers was experimentally confirmed by single-crystal X-ray structure analysis (Figure S4-1). The proper connectivity among the CP, DPP, and ethynylene units in the final product was confirmed by single-crystal X-ray diffraction analysis of C6-DPP–CP (Figure 4-4 and Table S4-1). The dihedral angles between the porphyrin and DPP planes in the crystal structure are 13.8° and 25.7°. Similar planarity is expected for C*n*-DPP–BPs after thermal conversion, because the steric hindrance between π-frameworks should not be much different before and after the extrusion of isobutylene units.

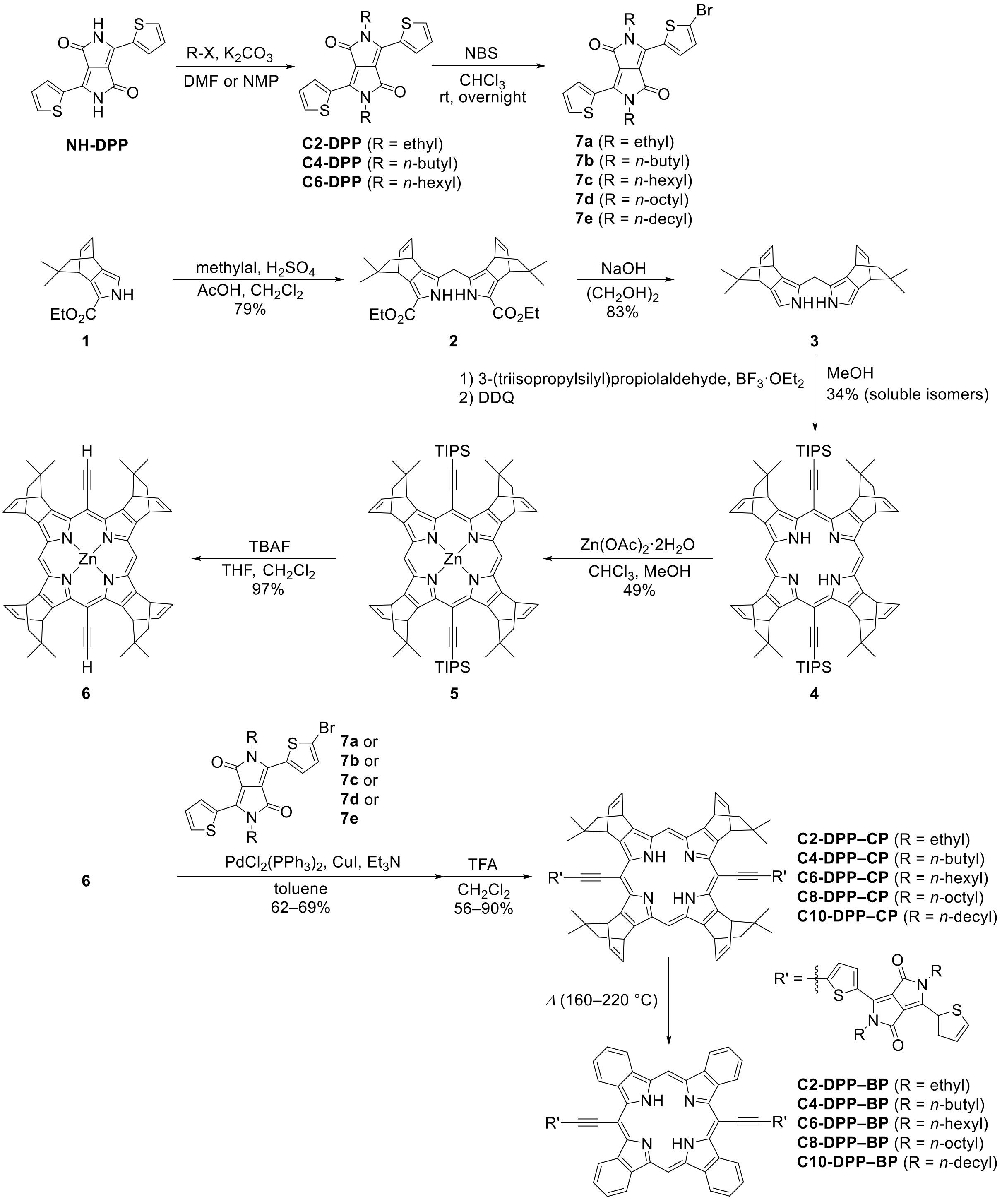

Scheme 4-1. Synthetic scheme of C*n*-DPP–BPs. (check the compound number and name)

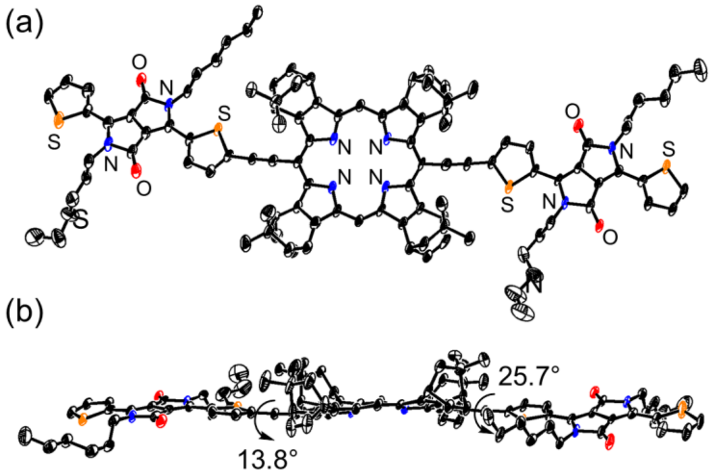

Figure 4-4. Crystal structure of C6-DPP–CP. (a) Top view and (b) side view. Solvents and hydrogen atoms are omitted for clarity. Thermal ellipsoids represent 50% probability.

4-3. Optical and Electronic Properties

The optical absorption spectra of BP and C*n*-DPP–BP films are shown in Figure 4-5 and their parameters are summarized in Table 4-1. The BP film shows large-Soret and Q bands at around 400 and 700 nm, respectively, but the absorption between these bands are weak and the absorption edge is at 716 nm. The C*n*-DPP–BP films show broader absorption spectra with longer absorption edge wavelengths reaching 846–868 nm. The absorption edges of C*n*-DPP–BP thin films are slightly different to each other, indicating that there are minor

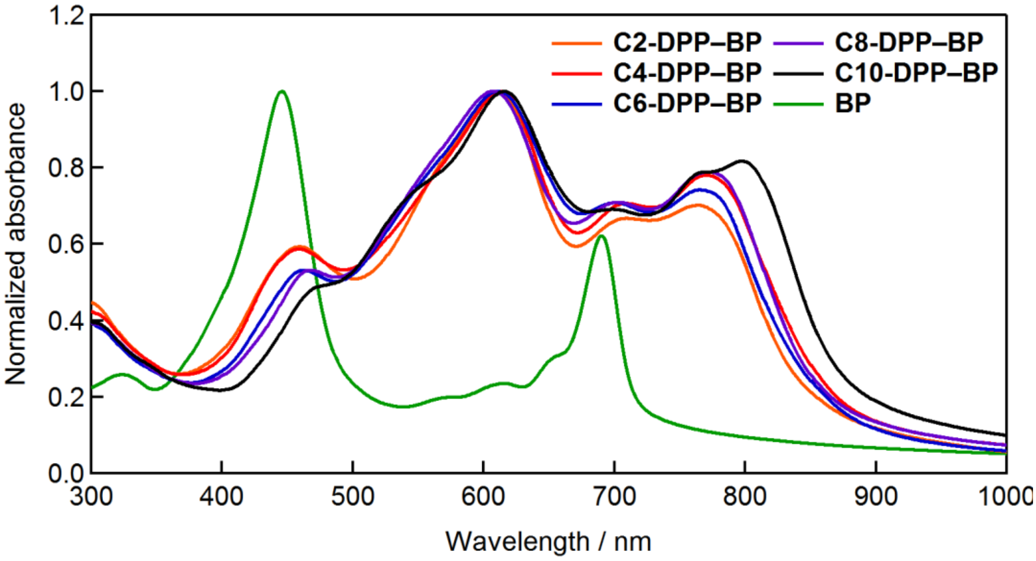

Figure 4-5. Absorption spectra of BP and C*n*-DPP–BP thin films.

deviations in the solid-state molecular arrangement depending on the length of alkyl chains.

The E_{HOMO}s of C*n*-DPP–BPs were determined by photoelectron spectrometry to be –5.0 to –5.1 eV. (Figure 4-6). The optical energy gaps were calculated from the absorption onsets of the thin films to be 1.44–1.47 eV, and the E_{LUMO}s were calculated to be –3.5 to –3.7 eV. The E_{HOMO}s and E_{LUMO}s of all C*n*-DPP–BPs are summarized in Table 4-1. The E_{HOMO}s and E_{LUMO}s of C*n*-DPP–BPs are 0.1 and 0.4 eV lower than those of a BP film (E_{HOMO} = –4.9 eV and E_{LUMO} = –3.2 eV), respectively.[32] Considering the relationship between V_{OC} of OPV and the energy gap between the E_{HOMO} of the donor and the E_{LUMO} of the acceptor, V_{OC} of the C*n*-DPP–BPs:PC$_{61}$BM system was expected to be improved than that of the BP:PC$_{61}$BM system.

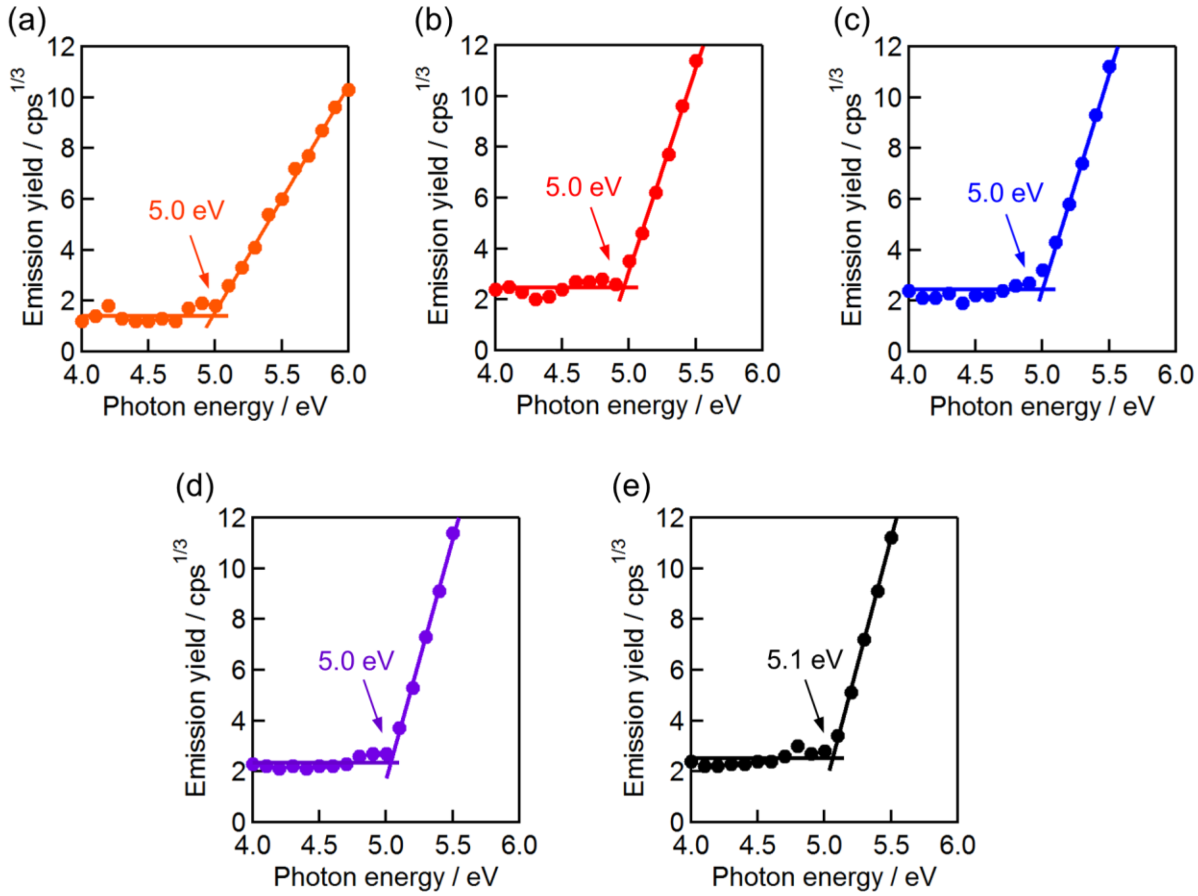

Figure 4-6. Photoelectron spectra in air of the thin films based on (a) C2-DPP–BP, (b) C4-DPP–BP, (c) C6-DPP–BP, (d) C8-DPP–BP, and (e) C10-DPP–BP on ITO-coated glass substrates.

Table 4-1. Electronic properties of C*n*-DPP–BPs and BP.

Materials	$\lambda_{\mathrm{onset}}{}^{a}$ / nm	$E_g{}^{b}$ / eV	$E_{\mathrm{HOMO}}{}^{c}$ / eV	$E_{\mathrm{LUMO}}{}^{d}$ / eV
C2-DPP–BP	846	1.47	–5.0	–3.5
C4-DPP–BP	862	1.44	–5.0	–3.6
C6-DPP–BP	857	1.45	–5.0	–3.6
C8-DPP–BP	855	1.45	–5.0	–3.5
C10-DPP–BP	868	1.43	–5.1	–3.7
BP	716	1.73	–4.9	–3.2

[a] As thin films, [b] Calculated from λ_{onset}. [c] Determined by photoelectron spectroscopy in air, [d] $E_{\mathrm{LUMO}} = E_{\mathrm{HOMO}} + E_g$,

4-4. Photovoltaic Performance

Solution-processed BHJ OPVs with a general device structure of [ITO/PEDOT:PSS/C*n*-DPP–BP:$PC_{61}BM$/Ca/Al] were fabricated by the precursor approach using C*n*-DPP–CPs as precursors of C*n*-DPP–BPs. Fabrication and evaluation of OPV devices was conducted by Mr. Naoya Yamada and Mr. Daichi Kuamgai Prof. Nakayama's group in Yamagata University. The weight ratios of C*n*-DPP–BPs and $PC_{61}BM$, annealing conditions (duration and temperatures), and the concentration of solutions (thickness of the films) were optimized for each C*n*-DPP–BP (Table S4-2–S4-13). Because of the low solubility, thin films containing C2-DPP–BP were too rough to be evaluated for OPV performance. Thus, C2-DPP–BP was not studied further (Figure 4-7).

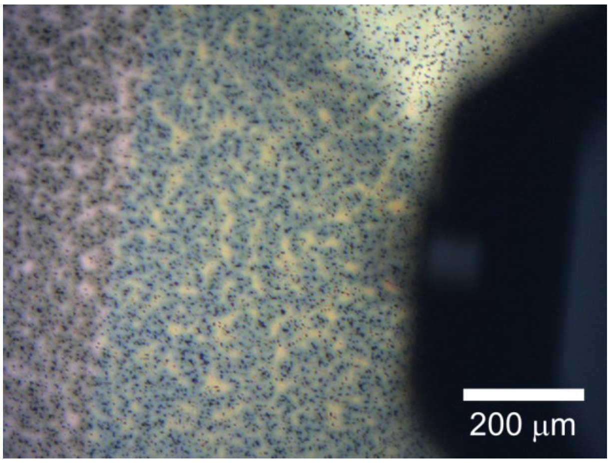

Figure 4-7. An optical microscope image of the thin films of C2-DPP–BP:$PC_{61}BM$ (2:1) on a PEDOT:PSS-modified ITO substrate.

J–V curves and EQE spectra of the best performing cells are shown in Figure 4-8a,b and the photovoltaic parameters are summarized in Table 4-2. The optimum active-layer thicknesses of C4-, C6-, C8-, and C10-DPP–BP:$PC_{61}BM$ systems were experimentally determined as 105, 115, 115, and 115 nm, respectively. The best performance was obtained with C4-DPP–BP affording the highest PCE of 5.2% (J_{SC} = 15.2 mA cm^{-2}, V_{OC} = 0.67 V, FF = 0.52). This PCE is much higher than those of BP:$PC_{61}BM$ and BP:PCBNB (≤ 0.1%).[32,33] Moreover, it is close to the best efficiencies so far reported for BP-based OPVs (5.2–5.4%) which have been achieved by using carefully designed n-type materials SIMEF[17] and SIMEF-Ph, *o*-An[34] in p–i–n-type active layers. Notably, the J_{SC} obtained with the C4-DPP–BP:$PC_{61}BM$ system (15.2 mA cm^{-2}) is considerably higher than those of the BP:$PC_{61}BM$ (5.7–7.0 mA cm^{-2})[12,17] and BP:SIMEF systems (10.2–10.5 mA cm^{-2}).[17,34] In EQE spectra (Figure 4-8c), photovoltaic response extends beyond 700 and reaches 850 nm where pristine BP does not absorb. The V_{OC}s of a C*n*-DPP–BP:$PC_{61}BM$ systems (0.64–0.70 V) are slightly increased from those of the BP:$PC_{61}BM$ devices (0.44–0.61 V),[12,35] reflecting the lower E_{HOMO} of C*n*-DPP–BPs (–5.0 eV) as compared to BP (–4.9 eV). On the other hand, FF of the C4-DPP–BP:$PC_{61}BM$ system (0.52) is lower than the p–i–n-type OPV based on BP:$PC_{61}BM$ (0.61).[12] It is known that FF of BHJ system is lower than that of p–i–n system.[33,36] Figure 2d shows the plots of normalized OPV parameters against the length of alkyl chains. The PCE is improved together with J_{SC}

Table 4-2. Photovoltaic parameters of optimized C*n*-DPP–BP:$PC_{61}BM$ OPVs.[a]

Materials	Thickness[b] / nm	J_{SC} / mA cm^{-2}	V_{OC} / V	FF	PCE[c] / %
C4-DPP–BP	105	15.19 (± 0.18)	0.67 (± 0.00)	0.52 (± 0.01)	5.24 (5.03 ± 0.14)
C6-DPP–BP	115	13.56 (± 0.25)	0.69 (± 0.00)	0.49 (± 0.00)	4.52 (4.39 ± 0.08)
C8-DPP–BP	115	9.12 (± 0.09)	0.70 (± 0.00)	0.48 (± 0.01)	3.06 (2.95 ± 0.10)
C10-DPP–BP	115	0.88 (± 0.01)	0.66 (± 0.01)	0.33 (± 0.00)	0.19 (0.18 ± 0.01)

[a]Showing the parameters of the best-performing cell with standard deviation of four devices in parentheses, [b]Active layer thickness, [c]Highest values followed by averages and standard deviation of four devices in parentheses.

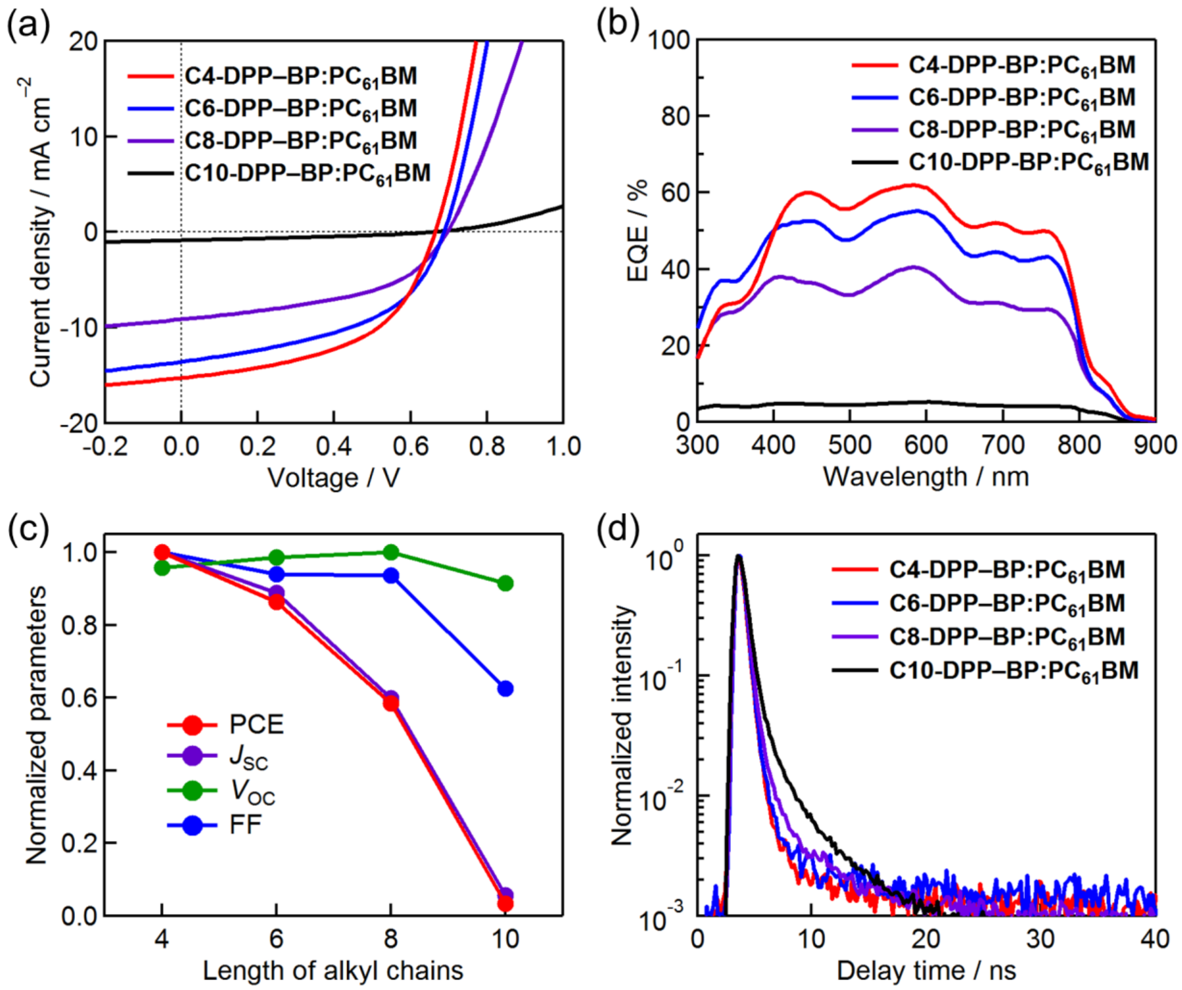

Figure 4-8. (a) *J*–*V* curves, (b) EQE spectra, (c) normalized photovoltaic parameters, and (d) fluorescence lifetime decay curves of OPV based on C*n*-DPP–BP:PC$_{61}$BM blend.

when alkyl chains become shorter. The V_{OC} values are similar for all C*n*-DPP–BPs. By making the alkyl chains on DPP units shorter from C10 to C4, the FF values are increased from 0.33 to 0.52.

To investigate the relationship between the photovoltaic performance and the alkyl-chain length, the charge-transfer efficiency, charge-carrier mobility, and charge-recombination efficiency of each blend film were investigated. The charge-transfer efficiency was evaluated using a picosecond-pulsed laser excitation at 470 nm followed by measuring the average fluorescence lifetime (τ_{f}) (Figure 4-8d). This measurement was conducted by Prof. Sadahiro Masuo in Kwansei Gakuin University. The obtained τ_{f}s are shorter with shorter alkyl chains;

namely, 0.45 ns for C4-DPP–BP:$PC_{61}BM$, 0.48 ns for C6-DPP–BP:$PC_{61}BM$, 0.54 ns for C8-DPP–BP:$PC_{61}BM$, and 0.70 ns for C10-DPP–BP:$PC_{61}BM$. This result suggests more effective fluorescence quenching via charge separation occurs with shorter alkyl chains.[16,37] In other words, C*n*-DPP–BPs are more finely mixed with $PC_{61}BM$ when alkyl substituents are shorter.

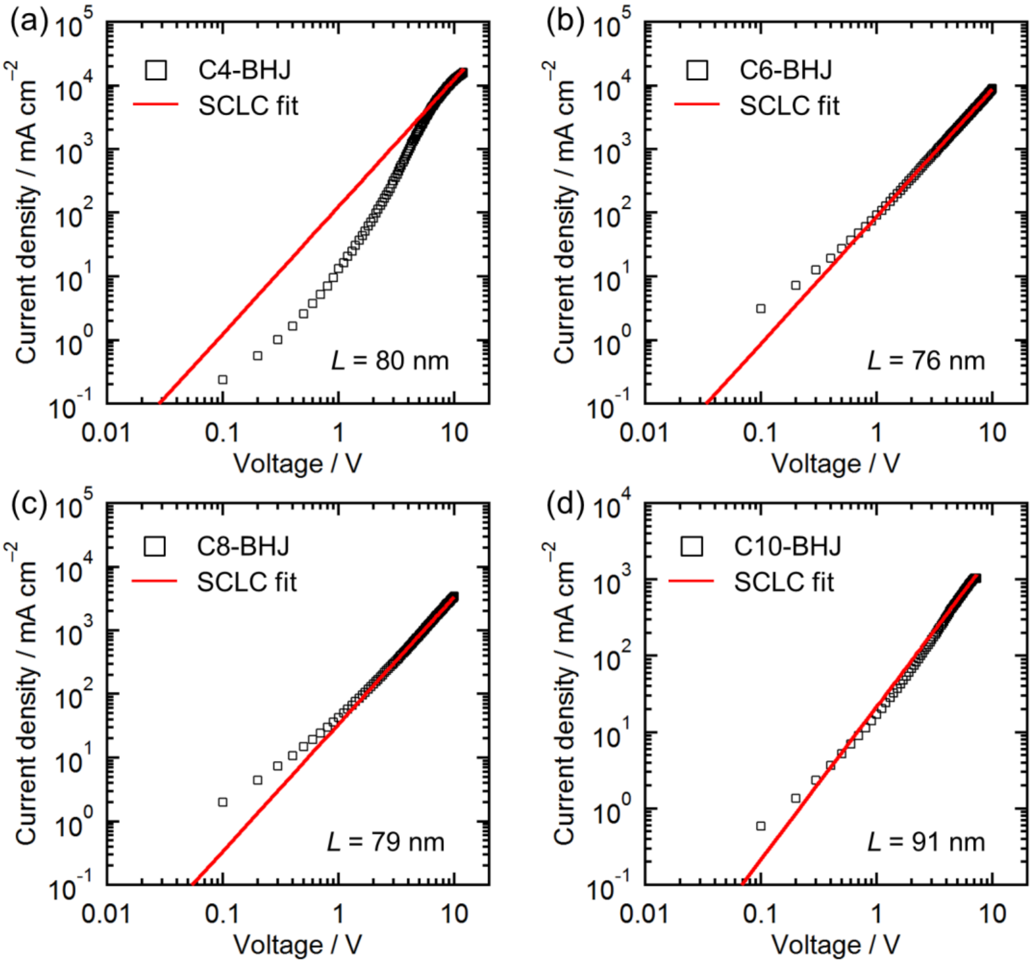

Figure 4-9. *J*–*V* curves and fitting lines to the Mott-Gurney Low for the hole-only devices of blend films. (a) C4-DPP–BP:$PC_{61}BM$ ($\mu_h = 2.18 \times 10^{-4}$ cm^2 V^{-1} s^{-1}), (b) C6-DPP–BP:$PC_{61}BM$ ($\mu_h = 1.31 \times 10^{-4}$ cm^2 V^{-1} s^{-1}), C8-DPP–BP:$PC_{61}BM$ ($\mu_h = 5.64 \times 10^{-5}$ cm^2 V^{-1} s^{-1}), and C10-DPP–BP:$PC_{61}BM$ ($\mu_h = 5.55 \times 10^{-5}$ cm^2 V^{-1} s^{-1}).

Next, the charge-carrier hole mobility (μ_h) in the blend films were measured by the space-charge-limited current (SCLC) method with the general device structure of [ITO/PEDOT:PSS/C*n*-DPP–BP:$PC_{61}BM$/MoO_3/Al] (Figure 4-9). The organic layers were deposited under the same conditions as those optimized for the BHJ OPV devices. The measuments revealed that the μ_h increases from 5.55×10^{-5} to 2.18×10^{-4} cm^2 V^{-1} s^{-1} as the alkyl substituents become shorter form C10 to C4. This observation indicates that the C4-DPP–BP:PC$_{61}$BM system is the best in terms of the charge-carrier transport property of the holes reaching to the electrodes. Improvement in the μ_h generally leads to a higher J_{SC} and FF, which is also the case for the present C*n*-DPP–BP:PC$_{61}$BM system.[3,38,39]

Then, the variation of J_{SC} as a function of illumination intensity was studied to evaluate the charge-recombination characteristics.[40,41] The data are plotted on a log–log scale and fitted to a power law (Figure 4-10). In general, a power law dependence of J_{SC} upon light intensity is observed in OPV; namely, $J_{SC} \propto I^{\alpha}$ where α is an exponential factor, and $\alpha = 1$ indicates the efficient sweep-out of carriers prior to recombination. The value of α are high for the C4, C6, and C8-DPP–BP:PC$_{61}$BM devices, being 1, 1, and 0.98, respectively. On the other hand, the C10-DPP–BP:PC$_{61}$BM device showed an α of 0.88 suggesting that bimolecular charge recombination is promoted in C10-DPP–BP:PC$_{61}$BM compared to other systems with shorter alkyl chains. Namely, non-geminate charge recombination is suppressed when alkyl groups are shorter.

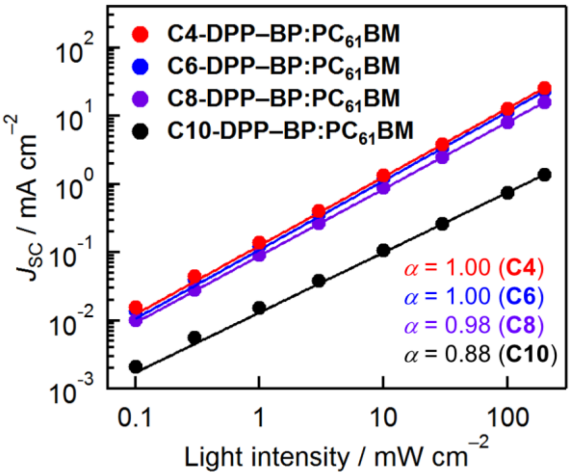

Figure 4-10. Light intensity dependency on J_{SC} of C*n*-DPP–BP:PC$_{61}$BM-based OPVs.

4-5. Film Morphology

The surface morphology of C*n*-DPP–BP:$PC_{61}BM$ films was probed by AFM (Figure 4-11). Pinholes, which have been reported to lower the performance and stability of OPVs,[42,43] were observed in all cases, although their depth and appearance frequency were largely dependent on the length of alkyl substituents. The depth of the deepest pinhole in each AFM image is about 10, 12, 37, and 34 nm for the C4-, C6-, C8-, and C10-DPP–BP blend films, respectively (Figure S4-2). The best-performing system, C4-DPP–BP:$PC_{61}BM$ has the shallowest pinholes (Figure 4-11a–d). Pinholes or cracks were also observed in C*n*-DPP–BP neat films (Figure S4-3) and TIPS-BP films deposited by the precursor approach in Chapter 2 (Figure 2-17f and S2-15). In all cases, pinholes or cracks became more obvious when longer or larger alkyl groups were introduced as substituents. These observations suggest that the formation of such large structural defects in thin films would be facilitated as molecules become more mobile and easier to rearrange owing to the higher flexibility of longer or larger alkyl substituents.

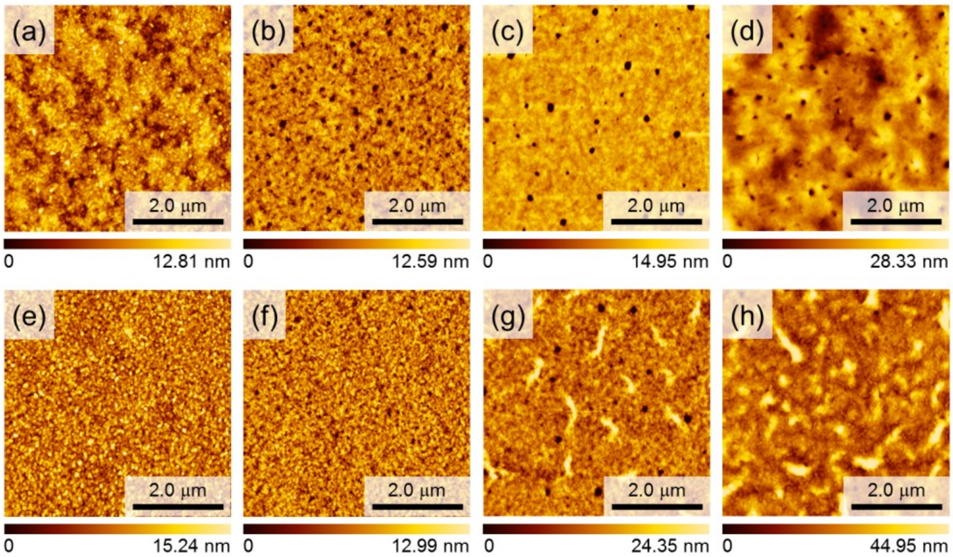

Figure 4-11. Tapping-mode AFM images. (a) C4-DPP–BP:$PC_{61}BM$, (b) C6-DPP–BP:$PC_{61}BM$, (c) C8-DPP–BP:$PC_{61}BM$, (d) C10-DPP–BP:$PC_{61}BM$, (e) rinsed C4-DPP–BP: $PC_{61}BM$, (f) C6-DPP–BP:$PC_{61}BM$, (g) rinsed C8-DPP–BP:$PC_{61}BM$, and (h) rinsed C10-DPP–BP:$PC_{61}BM$.

The author also observed the surface morphology of blend films after rinsing with toluene. Since the C*n*-DPP–BPs are insoluble in toluene (Figure S4-4), it is possible to selectively wash away $PC_{61}BM$ from the blend films and directly observe the morphology of C*n*-DPP–BP domains by AFM (Figure 4-11e–h).[12,17] In the cases of C8- and C10-DPP–BPs, micrometer-sized grains were observed, whereas the grain size is around 100 nm or smaller in the cases of C4- and C6-DPP–BPs. These observations are in accordance with the above postulation that longer alkyl chains would lead to higher molecular mobility during the deposition–thermal conversion process, which can result in more significant self-aggregation forming larger domains and less domain boundaries. Considering that the exciton diffusion lengths in molecular organic materials are within the range of only a few to dozens of nanometers,[44] the grain sizes in C8- and C10-DPP–BP films are too large to enable efficient photovoltaic processes.

4-6. Molecular Orientation and Crystallinity

The molecular arrangement in C*n*-DPP–BP neat films and C*n*-DPP–BP:$PC_{61}BP$ blend films were observed by 2D-GIWAXD measurements.[45] Figure 4-12a–h and Figure 4-12i,j show the 2D-GIWAXD images, and their out-of-plane profiles of the films, respectively (see also Figure S4-5 and S4-6). For the C4- and C6-DPP–BP neat films, a low wavenumber diffraction in the in-plane direction (q_{xy} = 0.47–0.48 $Å^{-1}$, d = 13.1–13.4 Å) and a high wavenumber diffraction in the out-of-plane direction (q_z = 1.79 $Å^{-1}$, d = 3.51 Å) are observed. Here, the former corresponds roughly to the minor axis of a DPP–BP framework (Figure 4-13), and the latter corresponds to π–π stacking. Thus, this combination of diffraction peaks indicates that molecules of C4- and C6-DPP–BP in neat films are arranged in face-on geometries which is favorable for OPV.[4] The C8-DPP–BP neat films showed arc-shaped diffraction patterns at q = 0.35 $Å^{-1}$ (d = 18.0 Å) and 1.73–1.77 $Å^{-1}$ (d = 3.55–3.63 Å) indicating a random arrangement of crystallites.[46] The C10-DPP–BP neat film showed a combination of a primary peak in the out-of-plane direction (q_z = 0.33 $Å^{-1}$, d = 19.0 Å) and a peak from π–π stacking in the in-plane direction (q_{xy} = 1.74 $Å^{-1}$, d = 3.61 Å) indicating that C10-DPP–BP molecules adopt

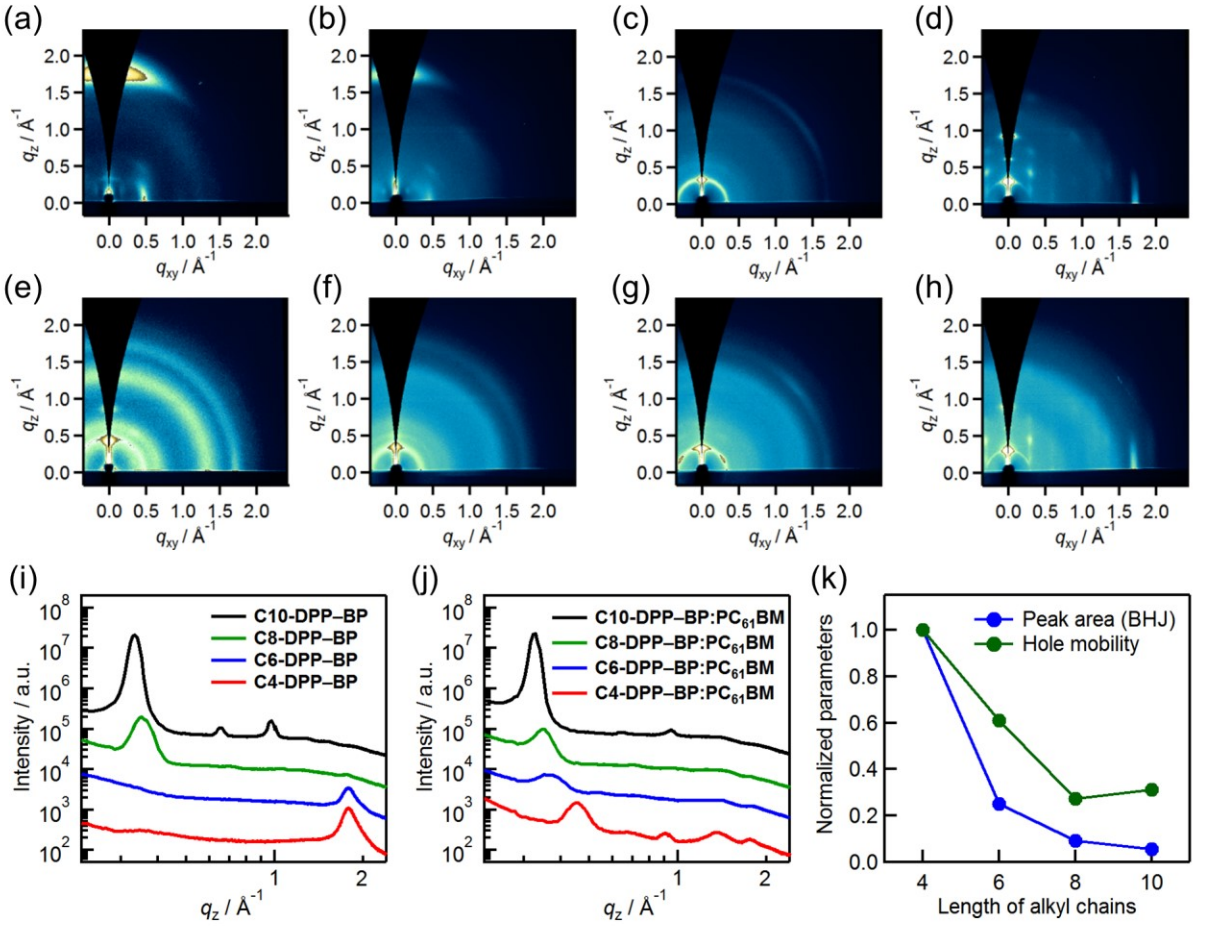

Figure 4-12. 2D-GIWAXD images of (a) C4-DPP–BP, (b) C6-DPP–BP, (c) C8-DPP–BP, (d) C10-DPP–BP, (e) C4-DPP–BP:PC$_{61}$BM, (f) C6-DPP–BP:PC$_{61}$BM, (g) C8-DPP–BP:PC$_{61}$BM, and (h) C10-DPP–BP:PC$_{61}$BM. Out-of-plane profiles of 2D-GIWAXD images of the (i) C*n*-DPP–BP neat films and (j) C*n*-DPP–BP:PC$_{61}$BM blend films. (k) Correlation of the lengths of alkyl chains, the peak area in the out-of-plane direction, and hole mobility of the blend films.

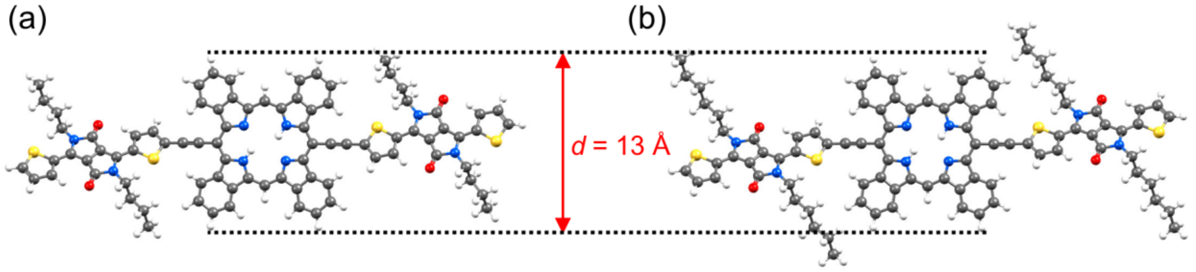

Figure 4-13. Optimized molecular structures of (a) C4-DPP–BP and (b) C6-DPP–BP.

an edge-on orientation. The C10-DPP–BP neat film also direction (q_z = 0.65 Å^{-1} and 0.94 Å^{-1}) indicating a higher crystallinity as compared to the other neat films.

It is noteworthy that the molecular orientation in C*n*-DPP–BP neat films is drastically changed only by the difference of alkyl-chain length. This observation made the author to focus on the aspect ratio of major and minor axis of molecules. The aspect ratio of C*n*-DPP–BP system increases by shorter alkyl chains from 1.5 (C10), 1.8 (C8), 2.4 (C6), and 2.9 (C4) (Figure 4-14) and the molecular orientation changes from edge-on to face-on orientation.

Same tendency in solution processable small molecular OPV materials was reported by Cheng et al.[3,47] and Bazan et al.[48,49] For both studies, the molecular orientation of neat films changes from edge-on to face-on orientation by increasing the major axis of molecules via elongating the molecular backbone as well as the aspect ratio (Figure S4-7 and S4-8). Thus, the author presumed that the aspect ratio of molecules is one of the key factors to decide molecular orientation.

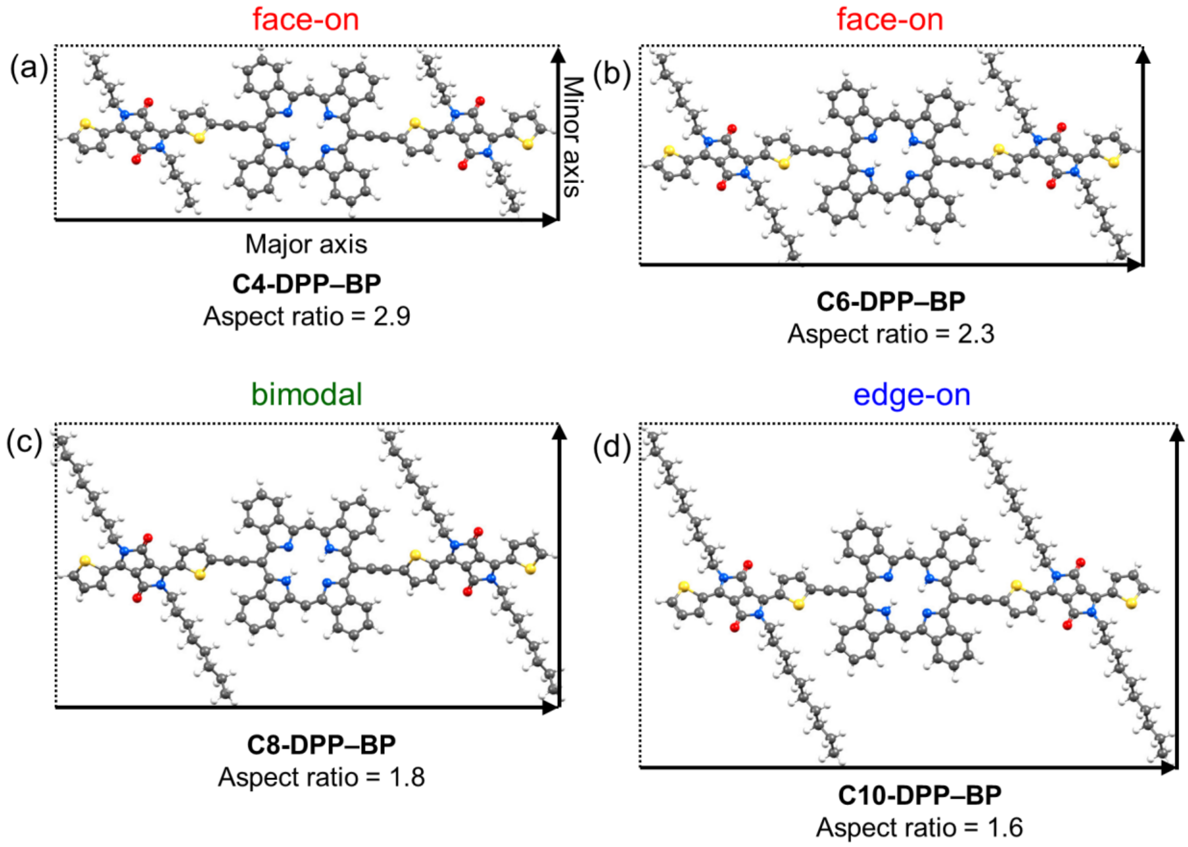

Figure 4-14. Optimized molecular structures of (a) C4-DPP–BP, (b) C6-DPP–BP, (c) C8-DPP–BP, and (d) C10-DPP–BP with their aspect ratios and molecular orientations in neat films.

On the other hand, the edge-on geometry was found to be a major molecular arrangement in all the blend films. Specifically, the C10-DPP–BP:$PC_{61}BM$ blend showed strong peaks in the out-of-plane direction (q_z = 0.33 Å^{-1}, 0.65 Å^{-1}, and q_z = 0.94 Å^{-1}) and a strong π–π stacking peak in the in-plane direction (q_{xy} = 1.72 Å^{-1}) indicating that the edge-on geometry is the dominant molecular orientation within crystallites. Thus, out-of-plane carrier transport should be inefficient in the C10-DPP–BP:$PC_{61}BM$ blend, which is reflected to the low J_{SC} and FF in corresponding OPV.[50] In the case of the C8-DPP–BP:$PC_{61}BM$ system, the peak corresponds to the π–π stacking of C8-DPP–BP is considerably weaker than that of C10-DPP–BP along the q_{xy} axis (Figure S4-6c). Instead, a relatively strong π–π stacking peak (q = 1.74 Å^{-1}, d = 3.61 Å) is observed at 20–60° from the q_{xy} axis, indicating that the effective

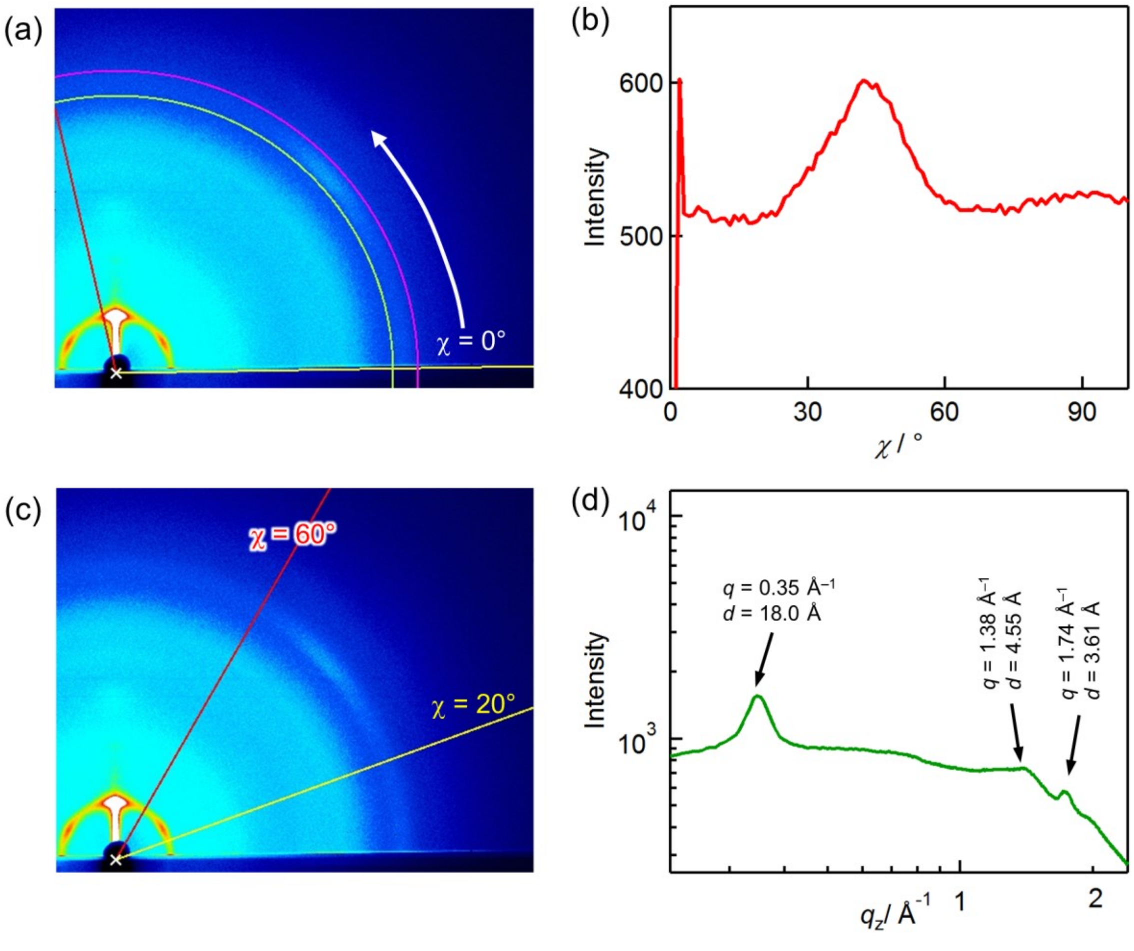

Figure 4-15. (a) Pole figure analysis of the peak from π–π stacking and (b) its profile of the C8-DPP–BP:$PC_{61}BM$ blend film. (c) 2D-GIWAXD image and (d) its profile from 20–60° of polar angles of a C8-DPP–BP:$PC_{61}BM$ blend film.

charge-carrier pathway based on C8-DPP–BP molecule is directed diagonally to the substrates (Figure 4-15). This orientation is less favorable for the charge extraction than the face-on orientation but better than the edge-on orientation, since the charge carrier pathway in OPVs is vertical to the substrates.

In the C6-DPP–BP:$PC_{61}BM$ blend film, diffraction peaks are generally weaker indicating a lower crystallinity as compared to the C8- and C10-DPP–BP:$PC_{61}BM$ systems. The π–π stacking diffraction of the C6-DPP–BP:$PC_{61}BM$ system is arc-shaped indicating that the charge-carrier transport via C6-DPP–BP molecules do not have preferred orientation in the blend film. This type of molecular arrangement is often observed in efficient small-molecule BHJ OPVs.[3,51] The C4-DPP–BP blend showed a similar diffraction pattern to the C6-DPP–BP blend, while the diffraction intensities are higher for the case of C4-DPP–BP.

In order to compare the relative populations of effective charge-carrier paths along the out-of-plane direction among the C*n*-DPP–BP:$PC_{61}BM$ systems, the peak areas corresponding to the π–π stacking of C*n*-DPP–BP were calculated (Figure 4-12k). The peak area is a relative measure of the crystallite volume within the film.[52] The peak areas were obtained by applying the Gaussian fitting to the out-of-plane profiles of 2D-GIWAXD images (Figure 4-16).[53] The extracted peak areas of π–π stacking of C*n*-DPP–BPs in blend films are larger with decreasing the length of alkyl side-chain along with the hole-mobility of blend films (Figure 4-12k). These results suggest that the charge-carrier paths to the vertical direction in blend films are improved with shorter alkyl side-chains due to the larger population of the π–π stacking crystallites for C*n*-DPP–BP. This trend is presumed to originate from the nature of C*n*-DPP–BPs neat films that tends to arrange face-on orientation with shorter alkyl chains. Thus, introducing shorter alkyl side-chains induces the better charge-carrier transport to improve the J_{SC} and FF, which is also indicated by the light intensity dependence of J_{SC}.

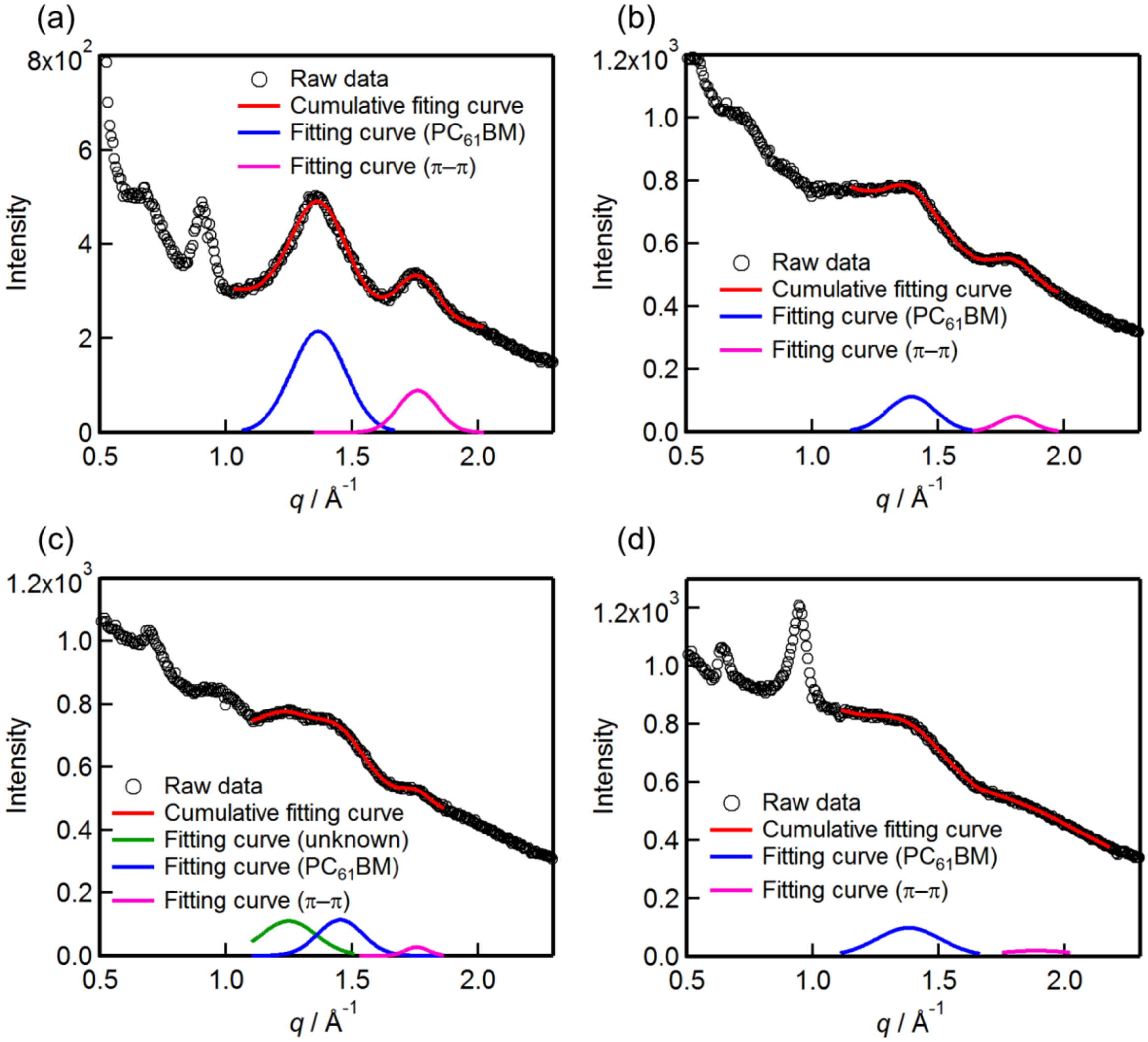

Figure 4-16. Out-of-plane profiles and Gaussian fitting of (a) C4-DPP–BP:$PC_{61}BM$, (b) C6-DPP–BP:$PC_{61}BM$, (c) C8-DPP–BP:$PC_{61}BM$, and (d) C10-DPP–BP:$PC_{61}BM$ blend films.

4-7. Summary

This work has demonstrated that BP frameworks can be modified to improve the absorption capability, miscibility, crystallinity, and molecular orientation for BHJ OPV. It is shown that the alkyl chain length has a strong impact on the OPV performance, with J_{SC} and PCE values ranging from 0.9–15.2 mA cm^{-2} and 0.2–5.2%, respectively. A BHJ OPV device of C4-DPP–BP:$PC_{61}BM$ shows the best J_{SC} of 15.2 mA cm^{-2} among BP based OPV. The GIWAXD measurements suggested that the C*n*-DPP–BPs with shorter alkyl chains in blend films tend to have larger amount of crystallites derived from π–π stacking in the out-of-plane direction which is suitable for charge-carrier transport of OPV. On the other hand, the C*n*-DPP–BP with longer alkyl chains tends to orient edge-on against the substrate. Notably, the drastic change of molecular orientation of C*n*-DPP–BPs provides a clue that the aspect ratio of molecules is one of the key factors to decide molecular orientation. Since a BHJ OPV based on C4-DPP–BP:$PC_{61}BM$ shows 5.2% of PCE by only a single active layer, further improvement of the OPV performance can be expected by utilizing p–i–n[17,36] architectures using the precursor approach.

4-8. Outlook

The OPV devices based on C4-DPP–BP:$PC_{61}BM$ blend showed the PCE of 5.24% with the great J_{SC} value of 15.19 mA cm^{-2} as a BP derivatives. However, that PCE value is still much lower than the state-of-the-art OPV and even much far away from the practical use. C4-DPP–BP still has two drawbacks for the p-type material for OPV. The first is high E_{HOMO} of C4-DPP–BP. The E_{HOMO} of C4-DPP–BP (–5.0 eV) is still higher than ideal E_{HOMO} (–5.4~–5.2 eV) in the case of using $PC_{61}BM$ as an n-type material reflecting the obtained V_{OC} is 0.65 V which is much lower than that of DRCN5T (0.92 V) which show the PCE over 10%.[3] The second is long synthesis steps. The preparation of C4-DPP–CP needs 12 steps and 18 reactions indicating the practical application is almost impossible.

In this regard, the author designed and synthesized 5,15-bis(trifluoromethyl)tetrabenzoporphyrins (CF_3BP) from a corresponding soluble precursor (CF_3CP). The number of synthesis steps of CF_3CP is 8 which is much shorter than that of C4-DPP–BP. The E_{HOMO} of CF_3BP film is –5.3 eV indicating the V_{OC} of OPV comprising CF_3BP would be comparable with those of state-of-the-art OPV. The p-n type OPV[35] comprising CF_3BP as a p-type and $PC_{61}BM$ as an n-type material were fabricated by a precursor approach for the initial evaluation to probe the potential of CF_3BP. As a result, the

V_{OC} and FF of 0.96 V and 0.68 were obtained, respectively indicating the energy levels and electrical property of $\mathrm{CF_3BP}$ are comparable with those of DRCN5T (Table 4-3).

Table 4-3. Comparison of E_{HOMO}s OPV performance of C4-DPP–BP, DRCN5T and $\mathrm{CF_3BP}$.

p-type materials	E_{HOMO}	J_{SC} / mA cm^{-2}	V_{OC} / V	FF	PCE / %
C4-DPP–BP^{a}	–5.0	15.19	0.65	0.52	5.24
DRCN5T^{b}	–5.2	15.66	0.92	0.68	10.0
$\mathrm{CF_3BP}^{c}$	–5.3	3.57	0.96	0.66	2.24

^{a}BHJ OPV with $\mathrm{PC_{61}BM}$. ^{b}BHJ OPV with $\mathrm{PC_{71}BM}$. ^{c}p–n type OPV with $\mathrm{PC_{61}BM}$.

In addition, the edge of photovoltaic response of $\mathrm{CF_3BP}$ reaches 800 nm in which BP and DRCN5T don't have photovoltaic response. Since the $\mathrm{CF_3BP}$ has enough insolubility to fabricate multi-layered p–i–n-type OPV by precursor approach, further improvement of J_{SC} to achieve PCE over 10% could be expected.

4-9. Supporting Figures and Tables

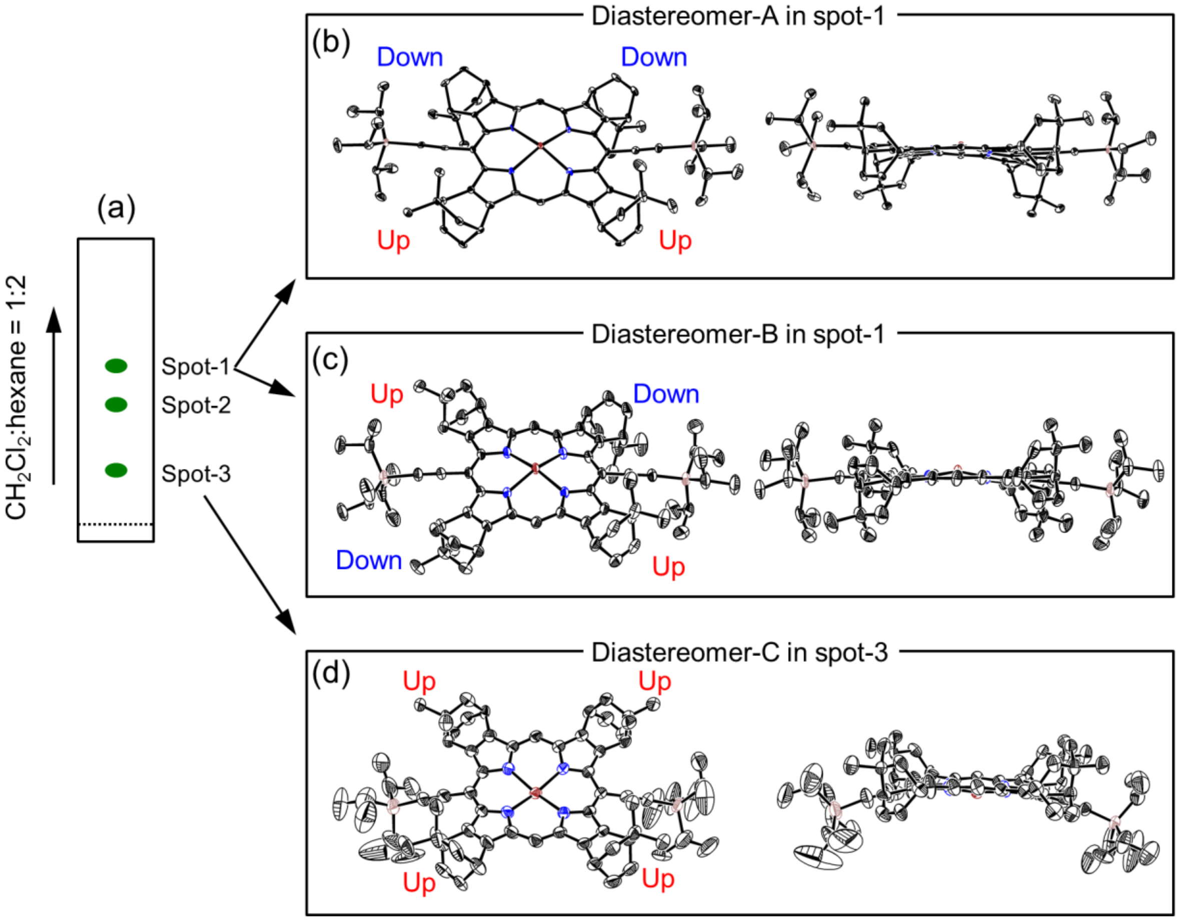

Figure S4-1. (a) Schematic drawing of analytical TLC and single-crystal structures of three diastereomers of compound **7**. (b) and (c): Two diastereomers in spot-1. (d): Diastereomer in spot-3. Up and Down mean the relative relationship of the direction of dimethyl groups. Solvents and hydrogen atoms are omitted for clarity. Thermal ellipsoids represent 50% probability.

Table S4-1. Crystal data and structure refinement for C6-DPP–CP

Empirical formula	$C_{117}H_{132}Cl_9N_8O_4S_4$	
Formula weight	2161.59	
Temperature	90 K	
Wavelength	0.71073 Å	
Crystal system	Triclinic	
Space group	P-1	
Unit cell dimensions	a = 17.452(10) Å	α = 106.590(8)°
	b = 17.834(10) Å	β = 100.966(9)°
	c = 20.187(11) Å	γ = 109.185(7)°
Volume	5400(5) $Å^3$	
Z	2	
Density (calculated)	1.330 g cm^{-3}	
Absorption coefficient	0.368 mm^{-1}	
F(000)	2278	
Crystal size	0.300 × 0.100 × 0.050 mm	
Theta range for data collection	1.301 to 23.500°	
Index ranges	$-19 \leq h \leq 19, -20 \leq k \leq 18, -18 \leq l \leq 22$	
Reflections collected	23951	
Independent reflections	15747 [R(int) = 0.0693]	
Completeness to theta = 27.48°	98.6 %	
Max. and min. transmission	0.982 and 0.641	
Refinement method	Full-matrix least-squares on F^2	
Data/restraints/parameters	15747 / 6 / 1290	
Goodness-of-fit on F^2	1.047	
Final R indices [$I > 2\sigma(I)$]	$R_1 = 0.1093$, $wR_2 = 0.2730$	
R indices (all data)	$R_1 = 0.1978$, $wR_2 = 0.3568$	
Largest diff. peak and hole	0.893 and –0.872 e $Å^{-3}$	
CCDC No.	1491998	

Table S4-2. Photovoltaic performance of BHJ OPVs based on C4-DPP–BP:$PC_{61}BM$ with different D:A weight ratios of 2:1, 1:1, and 1:2. (10 mg mL^{-1}, $CHCl_3$, 800 rpm, 40 s, annealed at 200 °C for 10 min)

D : A ratio	J_{SC} / mA cm^{-2}	V_{OC} / V	FF	PCE / %
2 : 1	14.49	0.64	0.43	3.99
1 : 1	**14.20**	**0.66**	**0.47**	**4.38**
1 : 2	4.19	0.61	0.40	1.02

The optimum D:A ratio was assumed as 1:1.

Table S4-3. Photovoltaic performance of BHJ OPVs based on C4-DPP–BP:$PC_{61}BM$ with different solution concentrations of 8, 10, 12, and 15 mg mL^{-1}. (D:A = 1:1, $CHCl_3$, 800 rpm, 40 s, annealed at 200 °C for 10 min)

Concentration / mg mL^{-1}	J_{SC} / mA cm^{-2}	V_{OC} / V	FF	PCE / %
8	**14.77**	**0.65**	**0.46**	**4.39**
10	14.20	0.66	0.47	4.38
12	13.96	0.63	0.39	3.46
15	11.79	0.65	0.38	2.92

The optimum concentration of solution was assumed as 8 mg mL^{-1}.

Table S4-4. Photovoltaic performance of BHJ OPVs based on C4-DPP–BP:$PC_{61}BM$ with different D:A weight ratios of 4:3 and 3:4. (8 mg mL^{-1}, $CHCl_3$, 800 rpm, 40 s, annealed at 200 °C for 10 min)

D : A ratio	J_{SC} / mA cm^{-2}	V_{OC} / V	FF	PCE / %
4 : 3	**13.98**	**0.67**	**0.51**	**4.82**
3 : 4	10.11	0.61	0.49	3.02

The optimum D:A ratio was assumed as 4:3.

Table S4-5. Photovoltaic performance of BHJ OPVs based on C4-DPP–BP:$PC_{61}BM$ with different additive (CS_2 v/v) ratios in $CHCl_3$ of 0%, 5%, 10% and 20%. (8 mg mL^{-1}, 800 rpm, 40 s, annealed at 220 °C for 10 min)

CS_2 ratio / %	J_{SC} / mA cm^{-2}	V_{OC} / V	FF	PCE / %
0	13.98	0.67	0.51	4.82
5	13.35	0.67	0.51	4.60
10	**14.54**	**0.67**	**0.51**	**4.98**
20	15.44	0.67	0.48	4.89

The optimum CS_2 ratio in $CHCl_3$ was assumed as 10% v/v.

Table S4-6. Photovoltaic performance of BHJ OPVs based on C4-DPP–BP:$PC_{61}BM$ with different solution concentrations of 8, 8.5 and 9 mg mL^{-1}. (D:A = 4:3, $CHCl_3$ (10% v/v CS_2), 800 rpm, 40 s, annealed at 220 °C for 10 min)

Concentration / mg mL^{-1}	J_{SC} / mA cm^{-2}	V_{OC} / V	FF	PCE / %
8	14.54	0.67	0.51	4.98
8.5	**15.19**	**0.67**	**0.52**	**5.24**
9	15.63	0.66	0.49	5.05

The optimum concentration of solution was assumed as 8.5 mg mL^{-1}. The thickness of active layer was 105 nm.

Table S4-7. Photovoltaic performance of BHJ OPVs based on C6-DPP–BP:$PC_{61}BM$ with different D:A weight ratios of 4:1, 3:1, 2:1, 1:1, and 1:2. (10 mg mL^{-1}, $CHCl_3$, 800 rpm, 40 s, annealed at 180 °C for 30 min)

D : A ratio	J_{SC} / mA cm^{-2}	V_{OC} / V	FF	PCE / %
4 : 1	10.81	0.68	0.39	2.84
3 : 1	11.85	0.69	0.43	3.49
2 : 1	**12.87**	**0.69**	**0.43**	**3.86**
1 : 1	8.50	0.73	0.40	2.45
1 : 2	6.15	0.70	0.38	1.64

The optimum D:A ratio was assumed as 2:1.

Table S4-8. Photovoltaic performance of BHJ OPVs based on C6-DPP–BP:$PC_{61}BM$ with different annealing temperature at 160 (30 min), 180 (30 min), 200 (10 min) and 220 (10 min). (D:A = 2:1, 10 mg mL^{-1}, $CHCl_3$, 800 rpm, 40 s)

Temperature / °C	J_{SC} / mA cm^{-2}	V_{OC} / V	FF	PCE / %
160	9.77	0.66	0.34	2.17
180	12.87	0.69	0.43	3.86
200	**13.56**	**0.69**	**0.49**	**4.52**
220	12.99	0.68	0.48	4.25

The optimum annealing temperature was assumed as 200 °C.

Table S4-9. Photovoltaic performance of BHJ OPVs based on C6-DPP–BP:$PC_{61}BM$ with different solution concentrations of 8, 10 and 12 mg mL^{-1}. (D:A = 2:1, $CHCl_3$, 800 rpm, 40 s, annealed at 200 °C for 10 min)

Concentration / mg mL^{-1}	J_{SC} / mA cm^{-2}	V_{OC} / V	FF	PCE / %
8	10.06	0.68	0.46	2.92
10	**13.56**	**0.69**	**0.49**	**4.52**
12	8.52	0.67	0.35	1.97

The optimum concentration of solution was assumed as 10 mg mL^{-1}. The thickness of active layer was

115 nm.

Table S4-10. Photovoltaic performance of BHJ OPVs based on C8-DPP–BP:PC$_{61}$BM with different D:A weight ratios of 2:1, 1:1, and 1:2. (10 mg mL^{-1}, CHCl$_3$, 800 rpm, 40 s, annealed at 180 °C for 30 min)

D : A ratio	J_{SC} / mA cm^{-2}	V_{OC} / V	FF	PCE / %
2 : 1	**2.41**	**0.55**	**0.25**	**0.33**
1 : 1	0.29	0.44	0.28	0.04
1 : 2	0.29	0.45	0.31	0.04

The optimum D:A ratio was assumed as 2:1.

Table S4-11. Photovoltaic performance of BHJ OPVs based on C8-DPP–BP:PC$_{61}$BM with different annealing temperature at 160 (30 min), 180 (30 min), and 200 °C (10 min) . (D:A = 2:1, 10 mg mL^{-1}, CHCl$_3$, 800 rpm, 40 s)

Temperature / °C	J_{SC} / mA cm^{-2}	V_{OC} / V	FF	PCE / %
160	**9.12**	**0.70**	**0.48**	**3.06**
180	2.41	0.55	0.25	0.33
200	2.53	0.52	0.24	0.32

The optimum annealing temperature was assumed as 160 °C. The thickness of active layer was 115 nm.

Table S4-12. Photovoltaic performance of BHJ OPVs based on C10-DPP–BP:PC$_{61}$BM with different D:A weight ratios of 2:1, 1:1, and 1:2. (10 mg mL^{-1}, CHCl$_3$, 800 rpm, 40 s, annealed at 180 °C for 30 min)

D : A ratio	J_{SC} / mA cm^{-2}	V_{OC} / V	FF	PCE / %
2 : 1	**0.88**	**0.66**	**0.33**	**0.19**
1 : 1	0.61	0.64	0.34	0.13
1 : 2	0.30	0.55	0.31	0.05

The optimum D:A ratio was assumed as 2:1.

Table S4-13. Photovoltaic performance of BHJ OPVs based on C10-DPP–BP:PC$_{61}$BM with different annealing temperature at 160 (30 min), 180 (30 min) and 200 (10 min). (D:A = 2:1, 10 mg mL^{-1}, CHCl$_3$, 800 rpm, 40 s)

Temperature / °C	J_{SC} / mA cm^{-2}	V_{OC} / V	FF	PCE / %
160	0.42	0.39	0.30	0.05
180	**0.88**	**0.66**	**0.33**	**0.19**
200	0.72	0.66	0.32	0.15

The optimum annealing temperature was assumed as 180 °C. The thickness of active layer was 115 nm.

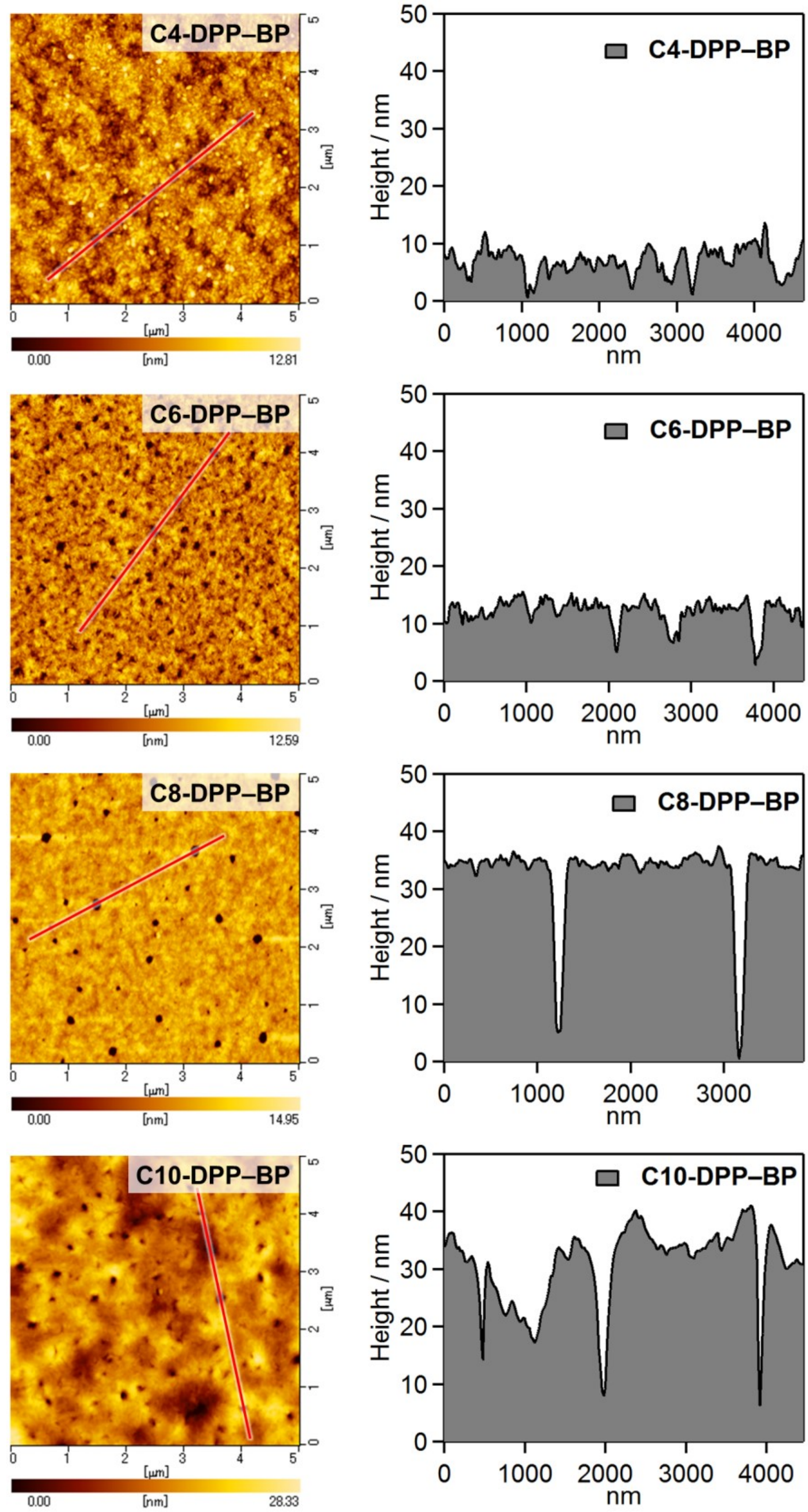

Figure S4-2. Tapping-mode AFM images (left) and cross-sectional profiles of blend films (right). Red lines indicate the places that the profiles were extracted. The location with the deepest pinhole in each film was chosen for the profile.

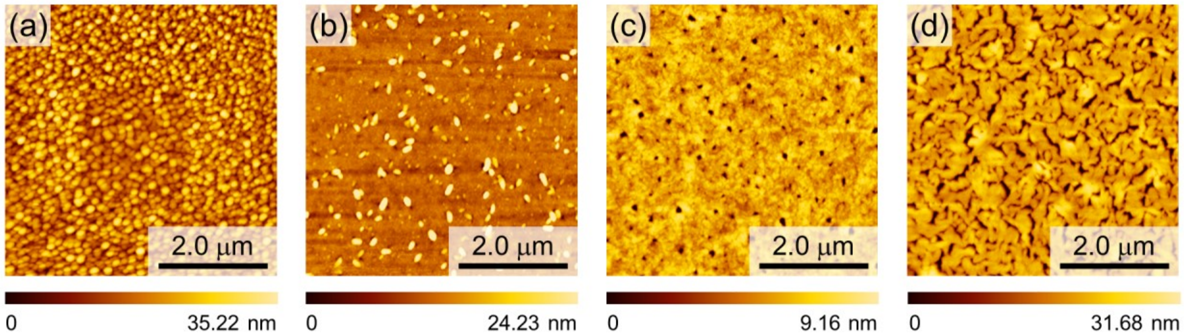

Figure S4-3. Tapping-mode AFM images of neat films based on (a) C4-DPP–BP (RMS = 5.61 nm), (b) C6-DPP–BP (RMS = 3.69 nm) (c) C8-DPP–BP (RMS = 1.23 nm), and (d) C10-DPP–BP (RMS = 5.20 nm) on PEDOT:PSS-modified glass substrates.

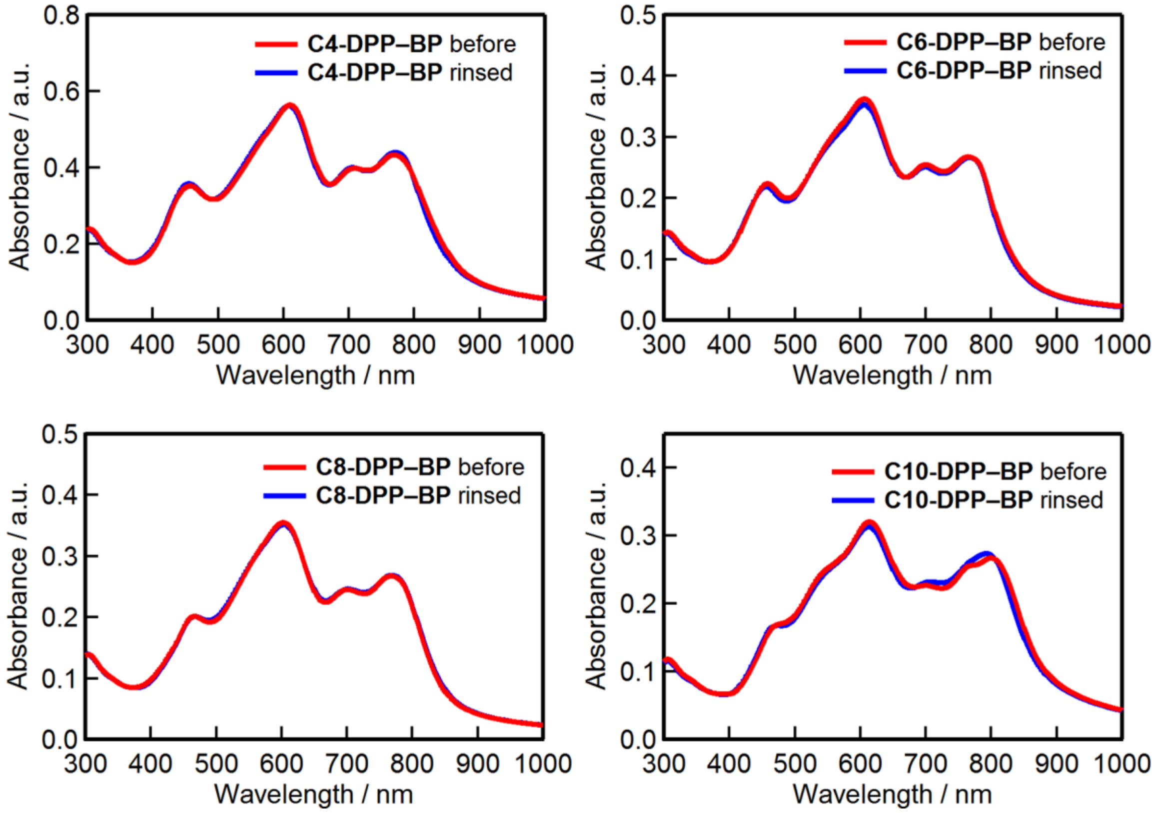

Figure S4-4. Absorption spectra of C4, C6, C8, and C10-DPP–BP neat films on glass substrates before (red) and after (blue) soaking in toluene for 5 min.

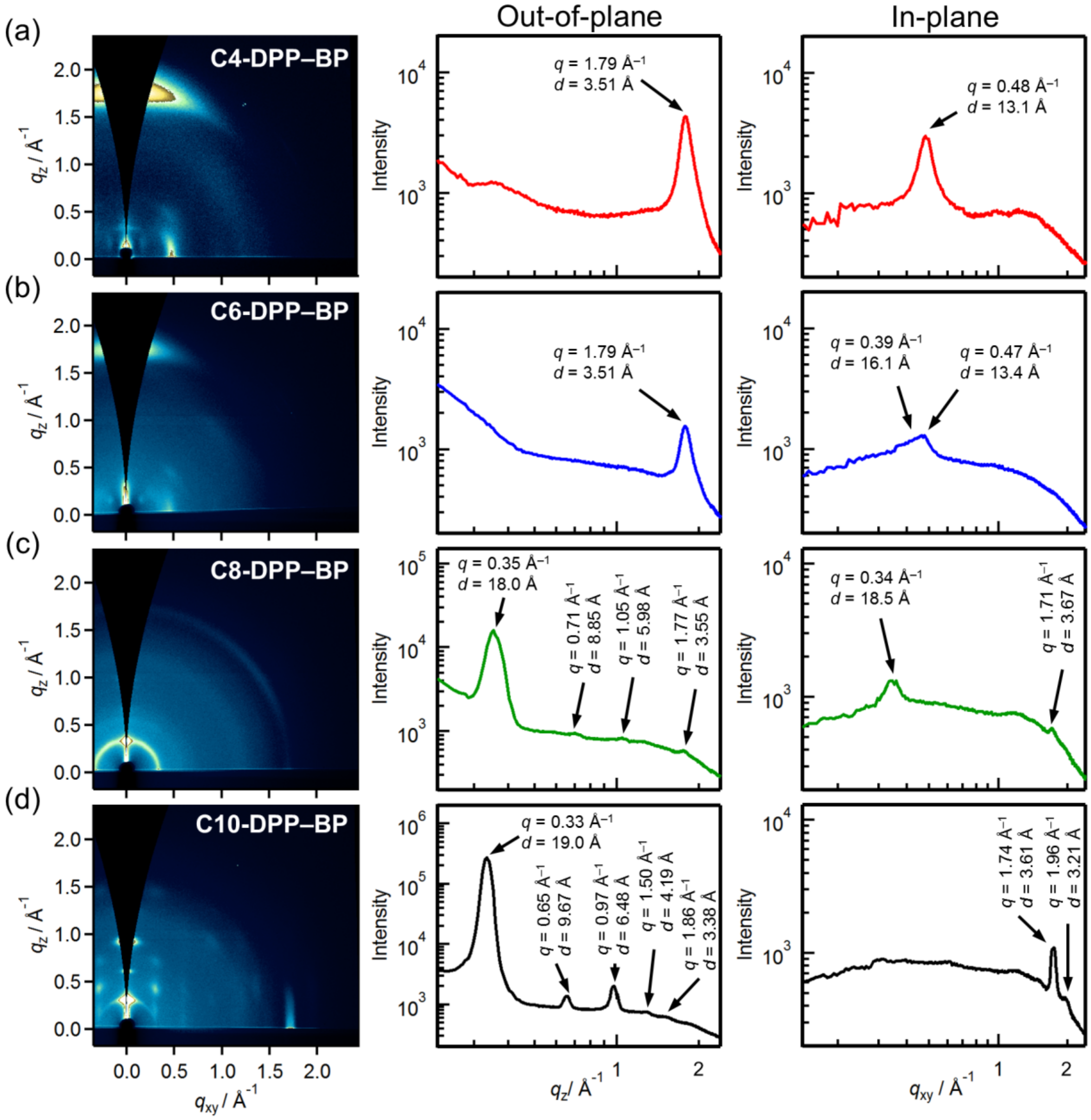

Figure S4-5. 2D-GIWAXD images (left), out-of-plane (middle), and in-plane (right) profiles with peak labels of neat films based on (a) C4-, (b) C6-, (c) C8-, and (d) C10-DPP–BP on PEDOT:PSS modified-Si substrates.

Table S4-14. Summary of peaks from C*n*-DPP–BP extracted in 2D-GIWAXD images of neat films.

	Out-of-plane				In-plane			
	Primary peak		π–π stacking peak		Primary peak		π–π stacking peak	
Materials	q / Å^{-1}	d / Å	q / Å^{-1}	d / Å	q / Å^{-1}	d / Å	q / Å^{-1}	d / Å
C4-DPP–BP	–	–	1.79	3.51	0.48	13.1	–	–
C6-DPP–BP	–	–	1.79	3.51	0.47	13.4	–	–
C8-DPP–BP	0.35	18.0	1.77	3.55	0.34	18.5	1.71	3.67
C10-DPP–BP	0.33	19.0	1.86	3.38	–	–	1.74	3.61

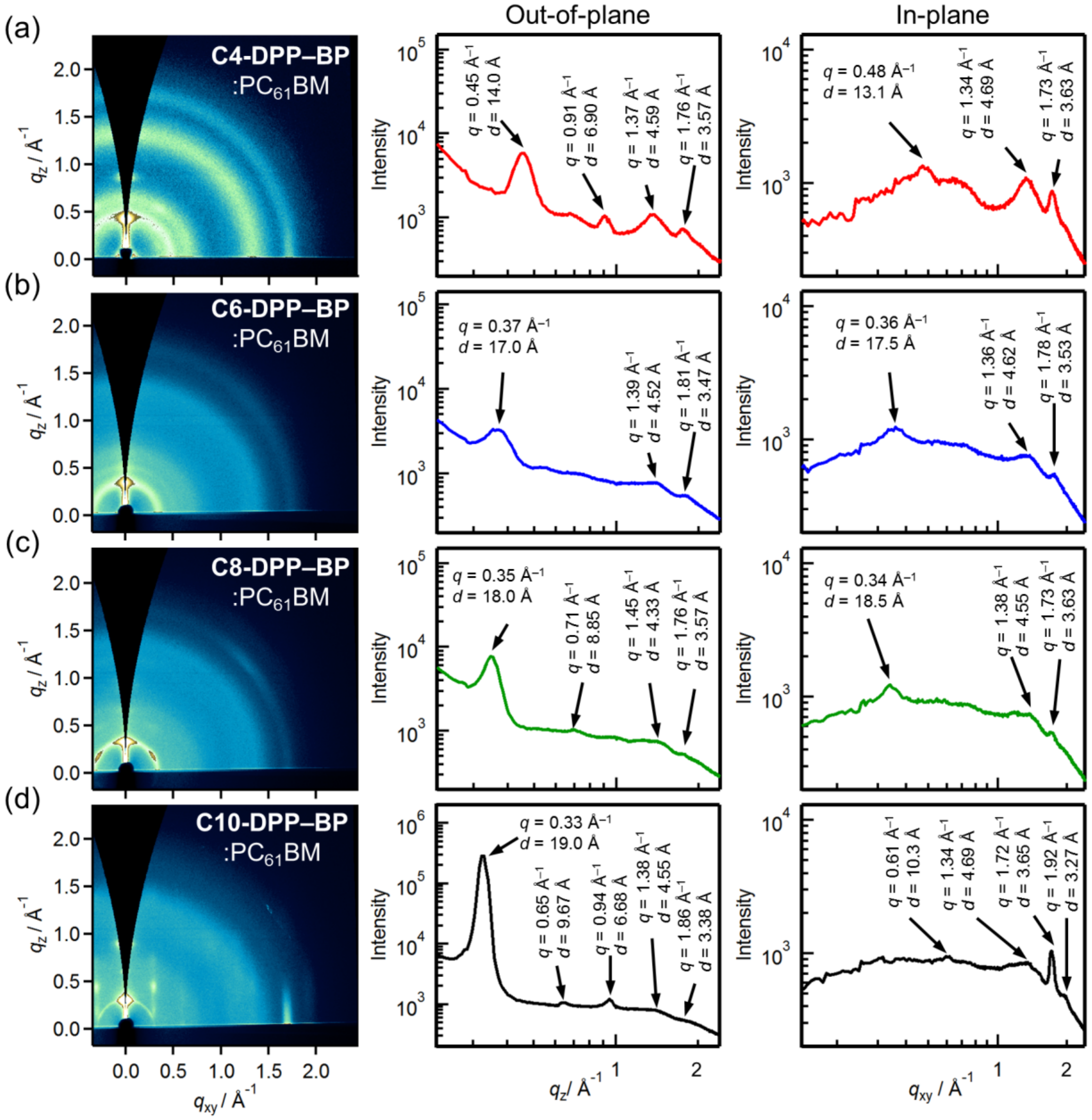

Figure S4-6. 2D-GIWAXD images (left), out-of-plane (middle), and in-plane (right) profiles with peak labels of blend films based on (a) C4-, (b) C6-, (c) C8-, and (d) C10-DPP–BP:$PC_{61}BM$ on PEDOT:PSS modified-Si substrates.

Table S4-15. Summary of peaks from C*n*-DPP–BP extracted in 2D-GIWAXD images of blend films.

	Out-of-plane				In-plane			
	Primary peak		π–π stacking peak		Primary peak		π–π stacking peak	
Materials	q / Å^{-1}	d / Å	q / Å^{-1}	d / Å	q / Å^{-1}	d / Å	q / Å^{-1}	d / Å
C4-DPP–BP	0.45	14.0	1.76	3.57	0.48	13.1	1.73	3.63
C6-DPP–BP	0.37	17.0	1.81	3.47	0.36	17.5	1.78	3.53
C8-DPP–BP	0.35	18.0	1.76	3.57	0.34	18.5	1.73	3.63
C10-DPP–BP	0.33	19.0	1.86	3.38	–	–	1.72	3.65

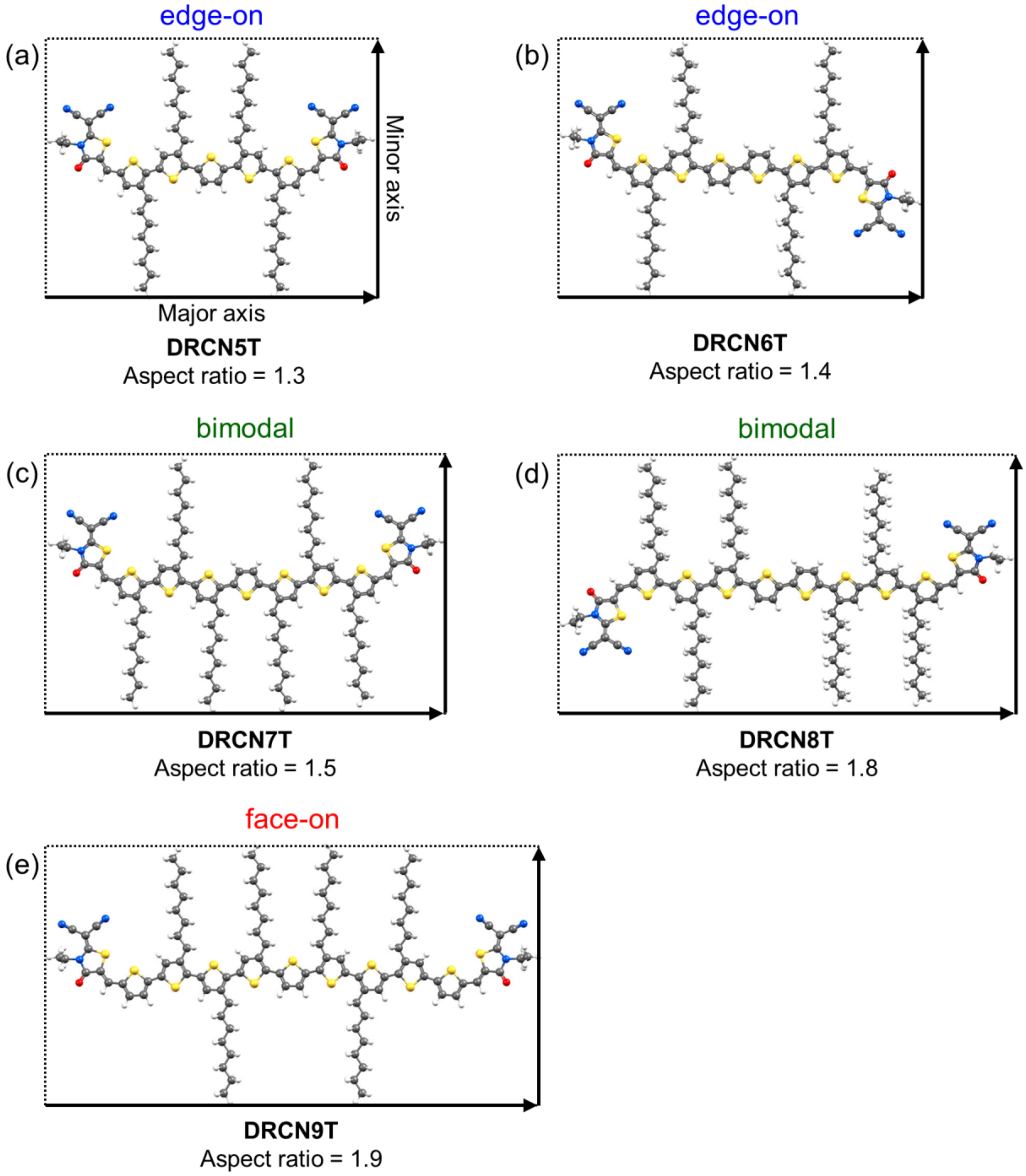

Figure S4-7. Optimized molecular structures of (a) DRCN5T, (b) DRCN6T, (c) DRCN7T, (d) DRCN8T, and (e) DRCN9T with their aspect ratio and molecular orientations in neat films.[3,47]

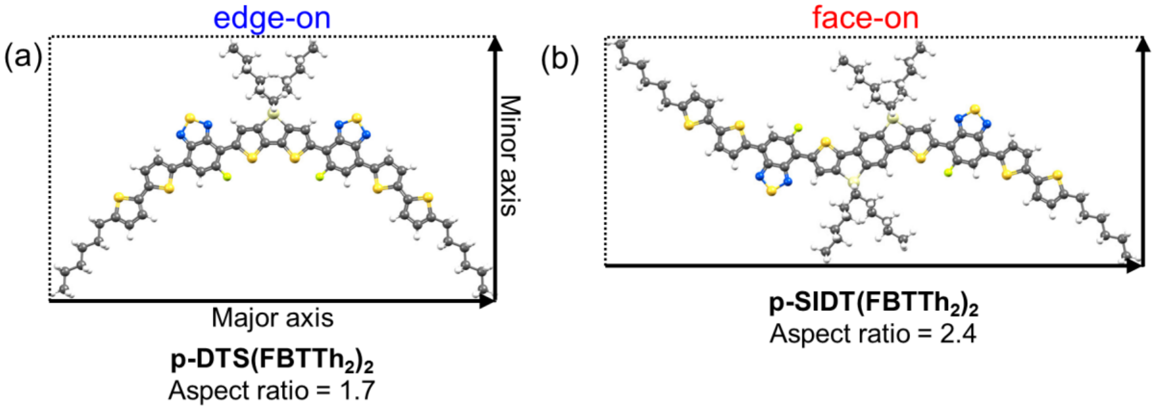

Figure S4-8. Optimized molecular structures of (a) p-DTS$(FBTTh_2)_2$, and (b) p-SIDT$(FBTTh_2)_2$ with their aspect ratio and molecular orientations in neat films.[48,49] 2-Ethylhexyl groups were simplified as hexyl groups.

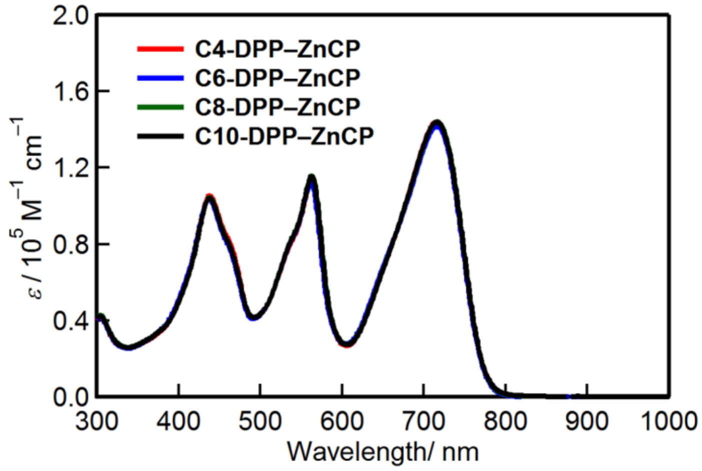

Figure S4-9. Absorption spectra of C4, C6, C8, and C10-DPP–ZnCP in $CHCl_3$.

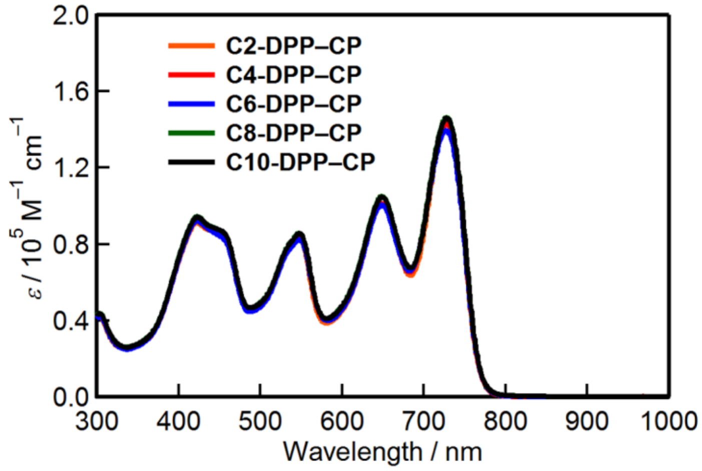

Figure S4-10. Absorption spectra of C2, C4, C6, C8, and C10-DPP–CP in $CHCl_3$.

4-10. Experimental Section

4-10-1. General

Materials for Synthesis

Solvents and chemical reagents were reagent grade quality, obtained from commercial sources and used without further purification. Dehydrated CH_2Cl_2 and toluene were purchased from Kanto Chemical used as received. NBS was recrystallized from hot water. 3,6-Dithiophen-2-yl-2,5-dihydropyrrolo[3,4-*c*]pyrrole-1,4-dione (NH-DPP),[54] 2,5-dibutyl-3,6-dithiophen-2-yl-pyrrolo[3,4-*c*]pyrrole-1,4-dione (C4-DPP),[55] 2,5-dihexyl-3,6-dithiophen-2-yl-pyrrolo[3,4-*c*]pyrrole-1,4-dione (C6-DPP),[28] 3-(5-bromothiophene-2-yl)-2,5-dioctyl-6-(thiophene-2-yl)-pyrrolo[3,4-*c*]pyrrole-1,4-dione (7d),[56] 3-(5-bromothiophene-2-yl)-2,5-didecyl-6-(thiophene-2-yl)-pyrrolo[3,4-*c*]pyrrole-1,4-dione (7e),[57] 3-(triisopropylsilyl)propiolaldehyde,[58] and ethyl 4,7-dihydro-8,8-dimethyl-4,7-ethano-2*H*-isoindole-1-carboxylate (1)[29] were prepared as described in literatures.

Purification and Characterization of Materials

Material purification by flash column chromatography was conducted on silica gel purchased from Kanto Chemical (Silica Gel 60N, 60 Å, 40–50 μm) and by GPC was conducted with a JAI LC-9225NEXT (JAIGEL-2H-40/JAIGEL-1H-40) at room temperature using $CHCl_3$ as an eluent. Analytical TLC was conducted on Merck 200-μm thickness silica gel plates with a fluorescent indicator. Visualization was accomplished with UV light at 254 nm and 365 nm. ^{1}H NMR and ^{13}C NMR spectra were recorded on a JEOL ECX 400P (400 MHz) or ECA 600 (600 MHz) spectrometer at 294 K using tetramethylsilane as an internal standard. High resolution ESI mass spectra were measured on a JEOL AccuTOF/JMS-T100LC mass spectrometer. High resolution MALDI mass spectrum was measured on a JEOL SpiralTOF^{TM}/JMS-S3000 mass spectrometer. UV−vis–NIR absorption spectra in solutions and thin films were measured on a JASCO V-670 and V-650 spectrophotometer, respectively. For spectral measurements, spectral grade solvents were purchased from Nacalai Tesque Inc. TGA were carried out on a Seiko Exstar 6000 TG/DTA 6200 instrument under nitrogen gas flow with a heating rate of 10 °C min^{-1}.

DFT Calculation

DFT calculation was carried out using a Gaussian 09 package based on B3LYP/6-31G(d) level of theory.

Single-Crystal X-ray Crystallography

The sample for making single-crystals of C6-DPP–CP was synthesized from a stereoisomer of compound **5** (spot-3) by the same reaction scheme. Single-crystals of C6-DPP–CP were obtained from diffusion of hexane into a dichloroethane solution. Single-crystal X-ray diffraction data of C6-DPP–CP were collected at 90 K on a Bruker APEX II X-ray diffractometer equipped with a large area CCD detector by using graphite monochromated Mo-Kα radiation (λ = 0.71073 Å). The diffraction data were solved with the SIR-97 program and refined with the SHELX-97 program. CCDC 1491998 contains the supplementary crystallographic data for this paper. This data can be obtained free of charge for The Cambridge Crystallographic Data Centre via www.ccdc.cam.ac.uk/data_request/cif.

Materials for Device Fabrication

Semico Clean 53 was purchased from Furuuchi Chemical. $PC_{61}BM$ was purchased from Luminescence Technology Crop. and used as received. For OPV device fabrication, solvents were purchased from Sigma-Aldrich and used as received.

OPV Device Fabrication and Evaluation

ITO-patterned glass substrates (20 × 25 mm, 15 Ω per square) were cleaned by gentle rubbing with an acetone-soaked wipe for ca. 5 s, sonication in acetone and isopropanol for 10 min each, and exposure to boiling isopropanol for 10 min. The cleaned substrates were further treated in a UV–O_3 cleaner (UV253 V8, Filgen) for 20 min, and the PEDOT:PSS (Clevious P VP AI4083) layer was spin-coated at 5000 rpm for 40 s, followed by thermal annealing at 120 °C for 20 min in air. The thickness of the resulting PEDOT:PSS layer was about 30 nm. The substrates were then transferred to a N_2-filled glovebox (<0.5 ppm of O_2 and H_2O) for preparation of the active layers. C*n*-DPP–BP:$PC_{61}BM$ blend films were prepared by spin-coating of a C*n*-DPP–CP:$PC_{61}BM$ solution, followed by thermal annealing on a hot plate in a glovebox. Finally, Ca (10 nm, 1 Å s^{-1}) and Al (90 nm, 10 Å s^{-1}) were vapor-deposited at high vacuum (~10^{-5} Pa) through a shadow mask that defined an active area of 4.0 mm^2. The general device structure was [ITO/PEDOT:PSS (30 nm)/ C*n*-DPP–BP:$PC_{61}BM$/Ca (10 nm)/Al (90 nm)]. *J*–*V* curves were measured using a Keithley 2400 source measurement unit under AM 1.5G illumination at an intensity of 100 mW cm^{-2} using a solar simulator (CEP-2000TF, Bunko-keiki). The EQE spectra were obtained under illumination of monochromatic light using the same system. Thickness of active layers was measured using a surface profiler (DektakXT, Bruker) after the OPV measurements.

Hole-only Device Fabrication and Evaluation

ITO-patterned glass substrates (20 × 20 mm, 15 Ω per square) were first pre-cleaned sequentially by sonicating in a detergent bath with Semico Clean 53, distilled water and isopropanol at room temperature for 10 min each, and then subjected to a UV–O_3 treatment at room temperature for 20 min. The PEDOT:PSS (Clevios P VP AI4083) layer was spin-coated at 3000 rpm for 30 s in air followed by a thermal annealing treatment at 130 °C for 10 min in air. The thickness of the resulting PEDOT:PSS layer was about 30 nm. The substrates were then transferred to a N_2-filled glovebox (<0.5 ppm of O_2 and H_2O) for preparation of the organic layers. The active layers were then fabricated by spin-coating from $CHCl_3$ (10 mg mL^{-1}, D:A = 2:1 (w/w)) for C6-, C8- and C10-DPP–BP and $CHCl_3$ (10% v/v CS_2) solution for

C4-DPP–BP (8.5 mg mL^{-1}, D:A = 4:3 (w/w)) with respective amount of PC$_{61}$BM at 800 rpm for 40 s. The substrates were heated at 160–220 °C (C4-DPP–BP (220 °C, 10 min), C6-DPP–BP (200 °C, 10 min), C8-DPP–BP (160 °C, 30 min) and C10-DPP–BP (180 °C, 30 min)) on a hot plate to convert precursors to corresponding C*n*-DPP-BPs. The thin films were transferred into a vacuum evaporator connected to the glove box, and the MoO$_3$ layer (15 nm, 0.5 Å s^{-1}) and the Al layer (80 nm, 1 Å s^{-1}) were vapor-deposited at high vacuum (~10^{-5} Pa) through a shadow mask that defined an active area of 1.0 mm^2. Resulting devices were sealed by glass plates with epoxy resin followed by irradiation of UV light. Thickness of the films was measured using a surface profiler (ET200, Kosaka Laboratory) after the SCLC measurements. (C4-DPP–BP:PC$_{61}$BM = 80 nm, C6-DPP–BP:PC$_{61}$BM = 76 nm C8-DPP–BP:PC$_{61}$BM = 79 nm and C10-DPP–BP:PC$_{61}$BM = 91 nm). *J*–*V* characteristics were measured in the range of 0−10 V using a Keithley 2400 source-measure unit in air, and fitting the results to a space charge limited model, where described as below:

$$J = \frac{8}{9} \cdot \frac{\varepsilon\varepsilon_0 \mu V^3}{L^3}$$

where ε is the dielectric constant, ε_0 is the permittivity of free space, μ is the hole mobility, V is the applied voltage, and L is the thickness of the active layer. The dielectric constant ε is assumed to be 3, which is a typical value for organic semiconductors.

Fluorescence Decay Measurement[37]

The laser beam from a picosecond-diode laser (470 nm, 10 MHz, 100 ps FWHM, Picoquant) was introduced to an inverted microscope (IX71, Olympus) and focused onto the active layer of the OPV by an objective lens (× 60, N.A.:0.7, LUCPlanFLN, Olympus). The fluorescence from the active layer of the OPV device was collected by the same objective lens and passed through a confocal pinhole (100 μm) and suitable filters.

Characterization of Thin Films

Thin films for the absorption measurement and the photoelectron spectrometry were prepared by spin-coating of precursors on glass substrates, followed by heating at 160–220 ºC for 10–30 min. Details as follows (precursor: concentration of solution, solvent, spin rate, heating temperature and duration): CP (20 mg mL^{-1}, $CHCl_3$:chlorobenzene = 1:2 v/v, 1500 rpm for 30 s, 180 °C for 20 min), C2-DPP–CP (3 mg mL^{-1}, $CHCl_3$, 800 rpm for 30 s, 200 °C for 10 min), C4-DPP–CP (4.6 mg mL^{-1}, $CHCl_3$ (10% CS_2 v/v), 800 rpm for 30 s, 220 °C for 10 min), C6-DPP–CP (6.7 mg mL^{-1}, $CHCl_3$, 800 rpm for 30 s, 200 °C for 10 min), C8-DPP–CP (6.7 mg mL^{-1}, $CHCl_3$, 800 rpm for 30 s, 160 °C for 30 min), C10-DPP–CP (6.7 mg mL^{-1}, $CHCl_3$, 800 rpm for 30 s, 180 °C for 30 min). Ionization energies of the thin films were determined from the onset of photoelectron spectra measured by a photoelectron spectrometer in air (AC-3, Riken Keiki). The surface morphology of organic films was observed by an SII SPA400/SPI3800N atomic force microscope in tapping mode using a silicon probe with a resonant frequency of 138 kHz and a force constant of 16 N m^{-1} (SII, SI-DF20).

GIWAXD Experiment

GIWAXD experiments were conducted in beamline BL19B2 at SPring-8 (Hyogo, Japan). The X-ray beam was monochromatized by a double-crystal Si(111) monochromator, and the X-ray energy was 12.398 keV (λ = 1 Å). The incident angle was set to 0.12° with a Huber diffractometer and the sample-to-detector distance was about 174 mm. Diffracted X-rays from samples were recorded by an X-ray photon counting pixel detector (PILATUS 300K, Dectris) for 30 s at room temperature. Samples for GIWAXD measurements were prepared by the same conditions with OPV devices on the PEDOT:PSS-modified Si substrates (Si/PEDOT:PSS/Cn-DPP–BP:$PC_{61}BM$).

4-10-2. Synthesis

2,5-Diethyl-3,6-di(thiophen-2-yl)-pyrrolo[3,4-*c*]pyrrole-1,4-dione (C2-DPP)

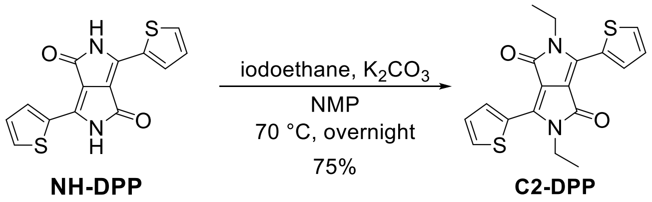

A solution of **NH-DPP**[54] (0.166 mmol, 500 mg, 1.0 eq) and potassium carbonate (6.64 mmol, 0.92 g, 4 eq) in 53 ml dehydrated NMP was brought under argon atmosphere. Then, iodoethane (21.2 mmol, 1.7 mL, 12.8 eq) were added in one portion. The mixture was stirred and heated at 70 °C and 10 additional equivalents of iodoethane (16.6 mmol, 1.3 mL, 10 eq) was added. The mixture was stirred at 70 °C for 2 h and then another 10 equivalents of iodoethane (16.6 mmol, 1.3 mL, 10 eq) was added and the mixture was stirred overnight (21 h) at 70 °C. The mixture was cooled to room temperature, added distilled water (80 ml) and filtered to remove NMP. The residue was washed with MeOH (15 mL × 3) and precipitated with CH_2Cl_2/hexane to give a target compound **C2-DPP** as red solid in 75% yield (446 mg, 1.25 mmol). ^{1}H NMR (400 MHz, $CDCl_3$, δ): 8.88 (dd, *J* = 4.0, 1.0 Hz, 2H), 7.64 (dd, *J* = 5.0, 1.0 Hz, 2H), 7.29 (dd, *J* = 5.0, 4.0 Hz), 4.16 (q, *J* = 7.0 Hz, 4H), 1.38 (t, *J* = 7.0 Hz, 6H); ^{13}C NMR (100 MHz, $CDCl_3$, δ): 161.25, 139.88, 135.06, 130.72, 129.68, 128.66, 107.78, 37.07, 15.13; HRMS (EI): *m*/*z*: $[M]^+$ calcd for $C_{18}H_{16}BrN_2O_2S_2$, 356.0653; found, 356.0651. (Experimental note-6, page 61–62, reaction No. 6-30)

3-(5-Bromothiophen-2-yl)-2,5-diethyl-6-(thiophen-2-yl)-pyrrolo[3,4-*c*]pyrrole-1,4-dione (7a)

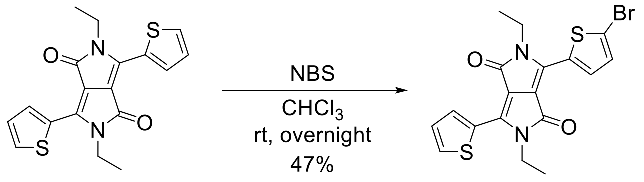

Protected from light, a solution of NBS (150 mg, 0.842 mmol, 1.0 eq) in $CHCl_3$ (25 mL) was added dropwise to a solution of **C2-DPP** (300 mg, 0.842 mmol, 1.0 eq) in $CHCl_3$ (25 mL) at 0 °C for 1 h. The reaction was stirred at room temperature overnight and the solvent was removed under reduced pressure. The residue was purified by column chromatography on silica gel (CH_2Cl_2:hexane = 2:1) and reprecipitation (CH_2Cl_2/hexane) to give a target compound **7a** as a purple solid in 47% yield (171 mg, 0.393 mmol). ^{1}H NMR (400 MHz, $CDCl_3$, δ): 8.89 (dd, *J* = 4.0, 1.0 Hz, 1H), 8.64 (d, *J* = 4.2 Hz, 1H), 7.66 (dd, *J* = 5.0, 1.0 Hz, 1H), 7.29 (dd, *J* = 5.0, 4.0 Hz, 1H), 7.24 (d, *J* = 4.2 Hz, 1H), 4.15 (q, *J* = 7.2 Hz, 2H), 4.09 (q, *J* = 7.2 Hz, 2H), 1.37 (t, *J* = 7.2 Hz, 3H), 1.37 (t, *J* = 7.2 Hz, 3H); ^{13}C NMR (100 MHz,

$CDCl_3$, δ): 161.15, 160.97, 140.32, 138.39, 135.32, 134.93, 131.61, 131.09, 131.01, 129.60, 128.74, 118.82, 108.01, 107.65, 37.13, 37.08, 15.18, 15.10; HRMS (EI): *m*/*z*: $[M]^+$ calcd for $C_{18}H_{15}BrN_2O_2S_2$, 433.9758; found, 433.9757.
(Experimental note-6, page 65–66, reaction No. 6-32)

3-(5-Bromothiophen-2-yl)-2,5-dibutyl-6-(thiophen-2-yl)-pyrrolo[3,4-*c*]pyrrole-1,4-dione (7b)

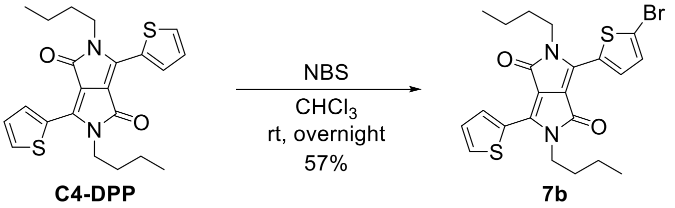

Protected from light, a solution of NBS (215 mg, 1.21 mmol, 1.0 eq) in $CHCl_3$ (25 mL) was added dropwise to a solution of **C4-DPP**[55] (500 mg, 1.21 mmol, 1.0 eq) in $CHCl_3$ (25 mL) at 0 °C for 1 h. The reaction was stirred at room temperature overnight and the solvent was removed under reduced pressure. The residue was purified by flash column chromatography on silica gel (CH_2Cl_2:hexane = 2:1) and then reprecipitation (CH_2Cl_2/hexane) to give a target compound **7b** as a purple solid in 57% yield (337 mg, 0.686 mmol). ^1H NMR (400 MHz, $CDCl_3$, δ): 8.94 (dd, *J* = 4.0, 1.0 Hz, 1H), 8.67 (d, *J* = 4.0 Hz, 1H), 7.65 (dd, *J* = 5.0, 1.0 Hz, 1H), 7.28 (dd, *J* = 5.0, 4.0 Hz, 1H), 7.23 (d, *J* = 4.0 Hz, 1H), 4.07 (t, *J* = 7.8 Hz, 2H), 4.00 (t, *J* = 7.8 Hz, 2H), 1.76–1.67 (m, 4H), 1.49–1.40 (m, 4H), 0.98 (t, *J* = 7.4 Hz, 3H), 0.97 (t, *J* = 7.4 Hz, 3H); ^{13}C NMR (100 MHz, $CDCl_3$, δ): 161.25, 161.09, 140.41, 138.52, 135.52, 135.08, 131.53, 131.16, 130.96, 129.66, 128.66, 118.76, 107.86, 107.51, 42.00, 41.96, 32.05, 31.96, 20.15, 13.73; HRMS (EI): *m*/*z*: $[M]^+$ calcd for $C_{24}H_{23}BrN_2O_2S_2$, 490.0384; found, 490.0381.
(Experimental note-6, page 1–2, reaction No. 6-1)

3-(5-Bromothiophen-2-yl)-2,5-dihexyl-6-(thiophen-2-yl)-pyrrolo[3,4-*c*]pyrrole-1,4-dione (7c)

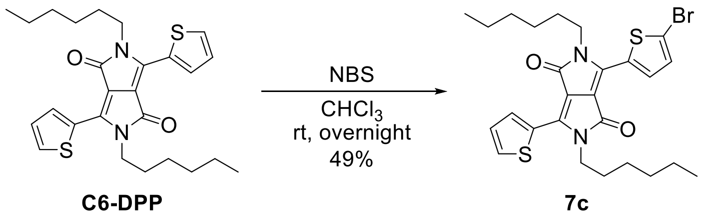

Protected from light, a solution of NBS (178 mg, 1.00 mmol, 1.0 eq) in $CHCl_3$ (17 mL) was added dropwise to a solution of **C6-DPP**[28] (469 mg, 1.00 mmol, 1.0 eq) in $CHCl_3$ (17 mL) at 0 °C for 1 h. The reaction was stirred at room temperature overnight and the solvent was removed under reduced pressure. The residue was purified by flash column chromatography on silica gel (CH_2Cl_2:hexane = 7:3) and then reprecipitation (CH_2Cl_2/hexane) to give a target compound **7c** as a purple solid in 49% yield (270 mg, 0.493 mmol). ^1H NMR (400 MHz,

$CDCl_3$, δ): 8.94 (dd, J = 4.0, 1.0 Hz, 1H), 8.67 (d, J = 4.0 Hz), 7.66 (dd, J = 5.0, 1.0 Hz), 7.29 (dd, J = 5.0, 4.0 Hz, 1H), 7.24 (d, J = 4.0 Hz, 1H), 4.06 (t, J = 8.0 Hz, 2H), 3.99 (t, J =8.0 Hz, 2H), 1.78–1.68 (m, 4H), 1.45–1.27 (m, 12H), 0.91–0.87 (m, 6H); ^{13}C NMR (100 MHz, $CDCl_3$, δ): 161.29, 161.12, 140.46, 138.56, 135.54, 135.10, 131.57, 131.20, 130.00, 129.77, 128.70, 118.79, 107.91, 107.55, 42.28, 42.23, 31.40, 31.38, 29.97, 29.90, 26.54, 26.52, 22.56, 22.53, 14.02; HRMS (MALDI): *m*/*z*: $[M]^+$ calcd for $C_{26}H_{32}N_2O_2S_2Br$, 547.1084; found, 547.1083.
(Experimental note-4, page 108–109, reaction No. 4-54)

Bis(3-ethoxycarbonyl-4,7-dihydro-8,8-dimethyl-4,7-ethano-2*H*-isoindol-1-yl)methane (2)

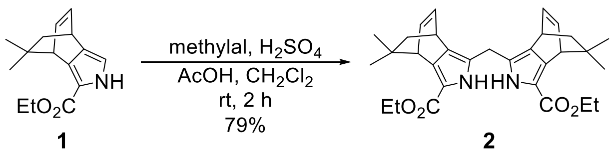

Methylal (4.24 mL, 48.0 mmol, 0.6 eq) and acetic acid (240 mL) were added to a solution of compound **1**[29] (19.63 g, 80.0 mmol, 1.0 eq) in CH_2C1_2 (120 mL). After the addition of conc.H_2SO_4 (80 drops, 1 drop mmol^{-1}), the resulting mixture was stirred for 1 h at room temperature. The reaction mixture was poured into water to quench, and extracted with CH_2Cl_2. The Organic layer was washed with saturated $NaHCO_3$ aq, and brine, then dried over Na_2SO_4. The solvent was removed under reduced pressure. The residue was purified by recrystallization in hexane to give a target compound **2** as white powder in 79% yield (15.88 g, 31.6 mmol). ^{1}H NMR (400 MHz, $CDCl_3$, δ): 8.43−8.35 (m, 2H, NH), 6.54–6.50 (m, 2H, olefine), 6.46–6.42 (m, 2H, olefine), 4.37−4.20 (m, 4H, OCH_2), 3.96–3.82 (m, 2H, *meso*), 3.79–3.77 (m, 2H, bridgeheads), 3.51–3.48 (m, 2H, bridgeheads), 1.36–1.32 (m, 8H, ester-CH_3+bridge), 1.18–1.14 (m, 2H, bridge), 1.05 (s, 6H, bridge-CH_3), 0.73–0.72 (m, 6H, bridge-CH_3); ^{13}C NMR spectrum (100 MHz, $CDCl_3$, δ) was measured, but the number of peaks were insufficient due to the presence of stereoisomers: 162.10, 137.68, 137.61, 136.04, 135.14, 135.11, 127.21, 127.03, 124.15, 123.94, 114.76, 59.81, 59.79, 46.61, 43.58, 43.58, 37.64, 37.62, 33.64, 30.77, 30.74, 30.31, 30.22, 23.51, 23.46, 14.50; HRMS (ESI): *m*/*z*: $[M + Na]^+$ calcd for $C_{31}H_{38}N_2NaO_4$, 525.2729; found, 525.2722.
(Experimental note-4, page 148–149, reaction No. 4-74)

Bis(4,7-dihydro-8,8-dimethyl-4,7-ethano-2*H*-isoindol-1-yl)methane (3)

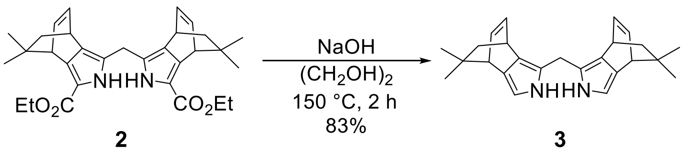

A solution of compound **2** (7.54 g, 15.0 mmol, 1.0 eq.), NaOH (7.34 g, 184 mmol, 12 eq.), and $(CH_2OH)_2$ (150 mL) was heated at 150 °C for 2 h under argon atmosphere in the dark.

The reaction mixture was cooled to room temperature by using ice bath, added water, and extracted with EtOAc. The organic layer was washed with water and brine, dried over Na_2SO_4, and concentrated under reduced pressure. The residue was purified by flash column chromatography on silica gel (CH_2Cl_2) to give a target compound **3** as a brown solid in 83% (4.45 g, 12.4 mmol). ^{1}H NMR (400 MHz, $CDCl_3$, δ): 7.11 (br, 2H), 6.56–6.52 (m, 2H), 6.45–6.41 (m, 2H), 6.34–6.34 (m, 2H), 3.92–3.78 (m, 2H), 3.47–3.43 (m, 2H), 3.17–3.15 (m, 2H), 1.37−1.34 (m, 2H), 1.20−1.17 (m, 2H), 1.03 (s, 6H), 0.76 (s, 6H); ^{13}C NMR spectrum (100 MHz, $CDCl_3$, δ) was measured, but the number of peaks were insufficient due to the presence of stereoisomers: 136.99, 136.89, 135.07, 135.04, 128.46, 128.33, 124.51, 124.28, 118.50, 118.82, 108.82, 108.60, 45.99, 44.05, 37.02, 33.24, 33.20, 30.86, 30.63, 30.54, 23.14, 22.95; HRMS (ESI): *m*/*z* $[M + Na]^+$ calcd for $C_{25}H_{30}N_2$, 381.2307; found, 381.2304.
(Experimental note-4, page 42–43, reaction No. 4-21)

5,15-Bis(triisopropylsilylethynyl)tetrakis(dimethylBCOD)porphyrin (4)

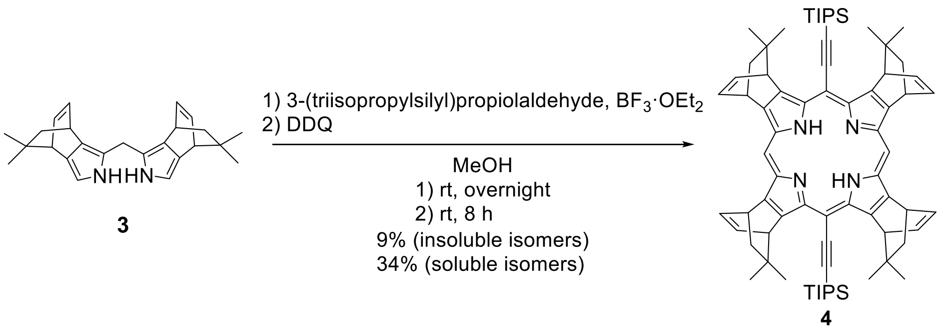

A solution of compound **3** (6.21g, 17.1 mmol, 1.0 eq) in methanol (1710 mL) was deoxygenated by bubbling of argon gas for 20 min. 3-(Triisopropylsilyl)propiolaldehyde[S10] (5.0 ml, 13.8 mmol, 1.1 eq) was added to a solution of compound **5** and then the reaction system was covered with aluminum foil. Boron trifluoride etherate ($BF_3 . OEt_2$) (0.29 ml, 2.35 mmol, 1.4 mM) was added dropwise to the solution and the resulting mixture was stirred overnight at room temperature. 2,3-Dichloro-5,6-dicyano-*p*-benzoquinone (7.76 g, 34.2 mmol, 2.0 eq) was added to the solution and stirred for 8 h at room temperature. Then, the solvent was removed under reduced pressure. The residue was purified by flash column chromatography (CH_2Cl_2) on silica gel and the solvent was removed under reduced pressure. The resulting solid was washed and filtered with CH_2Cl_2 (200 mL) to give poorly soluble stereoisomers of a target compound **4** as purple powder in 9% yield (0.798 g, 0.729 mmol). The filtrate was reprecipitated (CH_2Cl_2/MeOH) to give soluble stereoisomers of a target compound **4** as a purple powder in 34% (3.16 g, 3.61 mmol). The soluble stereoisomers of **4** were only used for the next reaction. ^{1}H NMR (400 MHz, $CDCl_3$, δ): 10.20–10.17 (m, 2H), 7.21–7.10 (m, 8H), 6.08–6.01 (m, 4H), 5.59–5.54 (m, 4H), 2.05–1.96 (m, 4H), 1.78–1.43 (m, 58H), 0.72–0.57 (m, 12H), –2.62~ –2.72 (m, 2H); ^{13}C NMR spectrum (100 MHz, $CDCl_3$, δ) was measured, but the number of peaks were insufficient due to the presence of

stereoisomers: 150.37, 150.35, 150.33, 150.28, 150.21, 149.28, 149.25, 149.19, 149.16, 144.05, 143.94, 143.80, 138.17, 138.11, 138.08, 136.21, 136.12, 136.03, 136.01, 135.27, 135.23, 135.09, 135.05, 109.49, 100.28, 98.84, 98.79, 97.62, 97.42, 50.86, 50.82, 50.80, 50.77, 44.39, 40.54, 40.51, 40.49, 40.46, 40.42, 40.38, 37.58, 31.05, 31.00, 30.94, 30.91, 30.63, 30.54, 30.42, 30.37, 30.22, 19.26, 19.10, 19.08, 12.63, 12.59, 12.34, 12.30, 12.27; UV−vis (CH_2Cl_2): λ_{max} ($\varepsilon \times 10^4$) = 663 (1.79), 605 (0.847), 578 (4.91), 537 (1.20), 423 (23.5); HRMS (ESI): *m*/*z*: $[M + H]^+$ calcd for $C_{74}H_{95}N_4Si_2$, 1095.7095; found, 1095.7090.
(Experimental note-6, page 24–25, reaction No. 6-11)

[5,15-Bis(triisopropylsilylethynyl)tetrakis(dimethylBCOD)porphyrinato]zinc(II) (5)

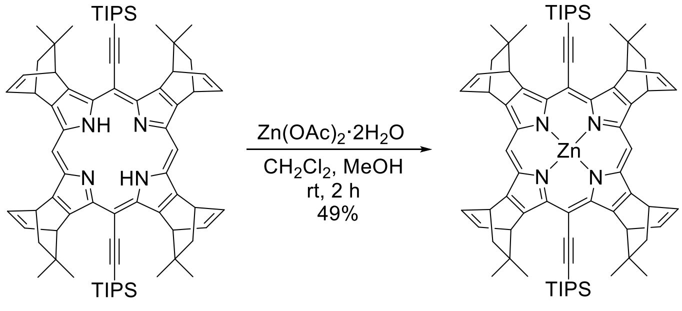

4 **5**

A solution of $Zn(OAc)_2·2H_2O$ (2.52 g, 11.5 mmol, 5.0 eq) in methanol (25 ml) was added to a solution of **4** (2.51 g, 2.29 mmol, 1.0 eq) in CH_2Cl_2 (200 ml). After stirring for 2 h at room temperature, the reaction mixture was washed with saturated $NaHCO_3$ aq. and water. The mixture was then dried over Na_2SO_4, and the solvent was removed under reduced pressure. The residue was purified by flash column chromatography on silica gel (CH_2Cl_2:hexane = 1:2, R_f = 0.42, green band, spot-2)* and reprecipitation (CH_2Cl_2/MeOH) to give a target compound **5** as purple powder in 49% (1.31 g, 1.13 mmol). *There are other two spots of target compound **5** during column chromatography (R_f = 0.55, spot-1 and R_f = 0.19, spot-3, green bands), but they showed lower solubility than spot-2 and their amount were small. Therefore, the target compound **5** of spot-2 was only used for the next reaction. ^1H NMR (400 MHz, $CDCl_3$, δ): 10.18 (s, 2H), 7.24–7.12 (m, 8H), 6.24–6.16 (m, 4H), 5.58–5.52 (m, 4H), 2.03–1.96 (m, 4H), 1.81–1.42 (m, 58H), 0.71–0.48 (m, 12H); ^{13}C NMR spectrum (100 MHz, $CDCl_3$, δ) was measured, but the number of peaks were insufficient due to the presence of stereoisomers: 151.33, 151.21, 151.12, 151.05, 150.61, 150.58, 150.54, 146.71, 146.65, 146.49, 146.46, 140.58, 140.54, 140.52, 138.42, 138.38, 138.33, 135.39, 135.32, 135.07, 135.05, 110.79, 110.25, 102.20, 99.78, 99.51, 99.47, 98.90, 98.48, 51.73, 51.67, 44.55, 44.46, 40.59, 40.51, 40.49, 40.41, 37.56, 37.53, 37.49, 31.09, 31.05, 30.94, 30.88, 30.67, 30.52, 30.50, 30.43, 19.31, 19.11, 12.68, 12.39; UV−vis ($CHCl_3$): λ_{max} ($\varepsilon \times 10^4$) = 613 (3.68), 572 (1.52), 438 (39.7); HRMS (ESI): *m*/*z*: $[M + H]^+$ calcd for $C_{74}H_{93}N_4Si_2Zn$, 1157.6230; found, 1157.6229.

(Experimental note-6, page 56–58, reaction No. 6-28)

[5,15-Diethynyltetrakis(dimethylBCOD)porphyrinato]zinc(II) (6)

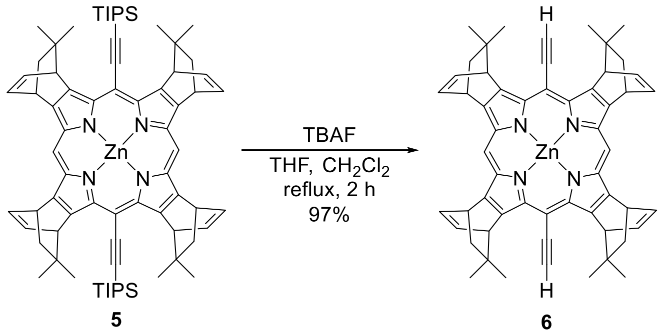

Tetrabutylammonium fluoride (1.0 M in THF, 3.6 mL, 3.6 mmol, 6.0 eq) was added to a solution of compound **5** (700 mg, 0.604 mmol, 1.0 eq) in dehydrated CH_2Cl_2 (60 ml) under argon atmosphere. After refluxing with stirring the reaction mixture for 2 h, the mixture was washed with saturated $NaHCO_3$ aq. and water. Then organic layer was dried over Na_2SO_4, and the solvent was removed under reduced pressure. The residue was purified by flash silica gel column chromatography on silica gel (CH_2Cl_2) and reprecipitation (CH_2Cl_2/hexane) to give a target compound **6** as purple powder in 97% (496 mg, 0.586 mmol). ^{1}H NMR (600 MHz, $CDCl_3$, δ): 10.23–10.22 (m, 2H, *meso*), 7.21–7.08 (m, 8H, olefine), 6.14–6.12 (m, 4H, bridgeheads), 5.60–5.53 (m, 4H, bridgeheads), 4.41–4.40 (m, 2H, acetylene), 2.08–2.05 (m, 4H, bridge), 1.80–1.75 (m, 4H, bridge), 1.52–1.48 (m, 12H, CH_3), 0.83–0.78 (m, 12H, CH_3); ^{13}C NMR spectrum (150 MHz, $CDCl_3$, δ) was measured, but the number of peaks were insufficient due to the presence of stereoisomers: 151.24, 151.20, 151.18, 151.15, 150.91, 150.89, 150.87, 150.82, 146.24, 146.22, 146.19, 146.16, 140.95, 140.92, 140.90, 140.88, 138.53, 135.34, 135.29, 99.37, 96.97, 96.89, 88.18, 88.05,. 87.19, 86.90, 52.20, 52.17, 52.10, 52.07, 44.25, 44.20, 40.65, 40.64, 40.62, 37.53, 31.61, 31.57, 30.84, 30.78, 30.74, 30.71; HRMS (ESI) *m*/*z*: $[M + H]^+$ calcd for $C_{56}H_{53}N_4Zn$, 1157.6230; found, 845.3554.

(Experimental note-6, page 9–10, reaction No. 6-5)

5,15-Bis(2,5-diethyl-3,6-dithienyl-2-yl-pyrrolo[3,4-*c*]pyrrole-1,4-dione-5'-yl-ethynyl)tetrakis(dimethylBCOD)porphyrin (C2-DPP–CP)

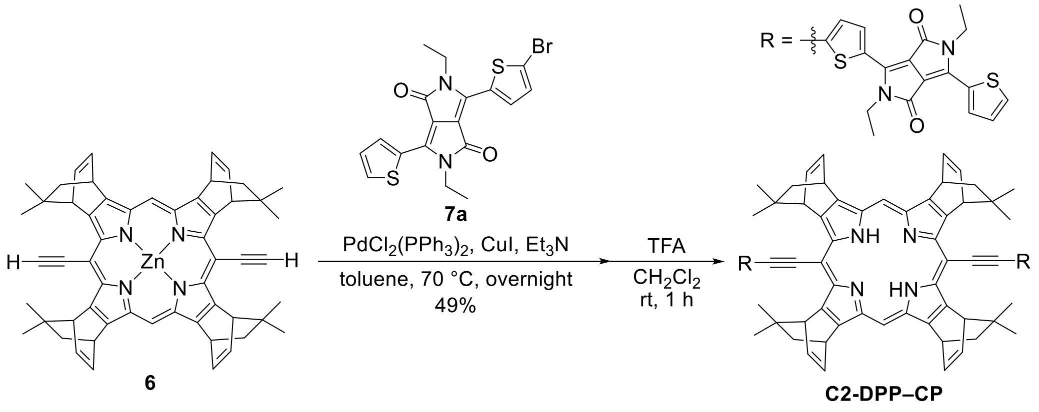

A solution of compound **6** (100 mg, 118 μmol, 1.0 eq) and compound **7a** (103 mg, 236 μmol, 2.0 eq) in dehydrated toluene (20 mL) and Et_3N (10 mL) was deoxygenated by freeze–pump–thaw (FPT) cycle for three times followed by the addition of $PdCl_2(PPh_3)_2$ (16.6 mg, 23.6 μmol, 0.2 eq) and CuI (9.0 mg, 47.2 μmol, 0.4 eq) under the protection of argon atmosphere. After stirring and heating at 70 °C for overnight (23 h), the solvent was removed under reduced pressure. The residue was purified by flash column chromatography on silica gel ($CHCl_3$, $R_f = 0.23$, black band) to give crude product of **C2-DPP–ZnCP** (127 mg). Since the crude product of **C2-DPP–ZnCP** was too poorly soluble to isolate by any purification methods, the dezincification reaction was conducted directly. Trifluoroacetic acid (1 mL, 13.1 mmol, excess) was added to a solution of crude product of **C2-DPP–ZnCP** (127 mg) in CH_2Cl_2. After stirring at room temperature for 2 h, the mixture was washed with $NaHCO_3$ aq. (× 2). Then the organic layer was dried over Na_2SO_4, and the solvent was removed under reduced pressure. The residue was purified by flash silica gel column chromatography on silica gel (EtOAc:hexane = 3:7, $R_f = 0.17$, black band) and reprecipitation ($CHCl_3$/hexane) to give a target compound **C2-DPP–CP** as black powder in 49% (86.6 mg, 58.0 μmol). ^{1}H NMR (400 MHz, $CDCl_3$, δ): 10.21 (s, 2H), 9.35–9.34 (m, 2H), 9.00–8.98 (m, 2H), 7.98–7.96 (m, 2H), 7.71–7.69 (m, 2H), 7.36–7.33 (m, 2H), 7.22–7.10 (m, 8H), 5.95–5.93 (m, 4H), 5.60–5.56 (m, 4H), 4.39–4.34 (m, 4H), 4.29–4.23 (m, 4H), 2.13–2.10 (m, 4H), 1.86–1.80 (m, 4H), 1.60–1.55 (m, 18H), 1.47–1.44 (m, 6H), 0.93–0.91 (m, 12H), –2.50~ –2.52 (m, 2H); ^{13}C NMR spectrum was not available due to low solubility; UV−vis ($CHCl_3$): $\lambda_{\max}$ ($\varepsilon \times 10^4$) = 728 (14.6), 649 (10.1), 547 (8.34), 423 (9.14), 303 (4.24); HRMS (ESI) *m*/*z*: $[M + H]^+$ calcd for $C_{92}H_{83}N_8O_4S_4$, 1491.5420; found: 1491.5415.
(Experimental note-6, page 79–80 and 92–93, reaction No. 6-38 and 6-43)

General procedure for Sonogashira coupling reactions for C4-, C6-, C8-, and C10-DPP–ZnCP

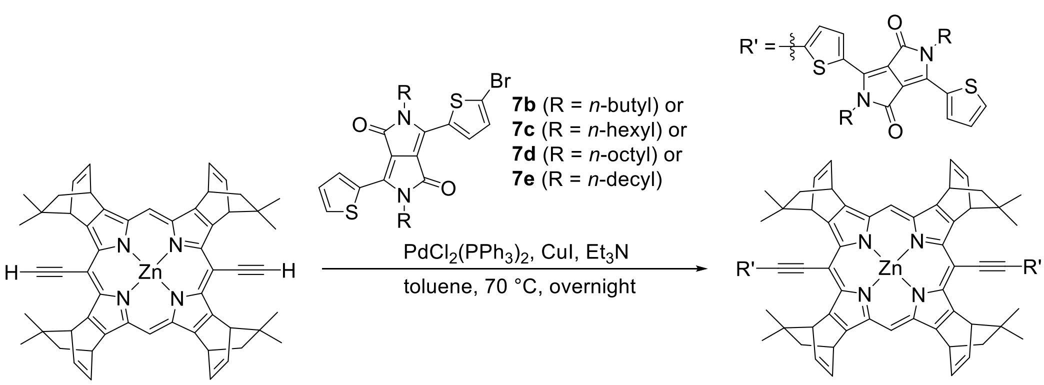

6

C4-DPP–ZnCP (R = *n*-butyl)
C6-DPP–ZnCP (R = *n*-hexyl)
C8-DPP–ZnCP (R = *n*-octyl)
C10-DPP–ZnCP (R = *n*-decyl)

A solution of compound **6** (1.0 eq) and compound **7b–e** (2.0 eq) in dehydrated toluene:Et_3N = 2:1 was deoxygenated by freeze–pump–thaw (FPT) cycle for three times or bubbling of argon gas for 20 min followed by the addition of $PdCl_2(PPh_3)_2$ (0.2 eq) and CuI (0.4 eq) under the protection of argon atmosphere. After stirring and heating at 70 °C overnight, the solvent was removed under reduced pressure. The residue was purified by flash column chromatography on silica gel and reprecipitation ($CHCl_3$/hexane) to give target compounds (**C4-**, **C6-**, **C8-** or **C10-DPP–ZnCP**).

[5,15-Bis(2,5-dibutyl-3,6-dithienyl-2-yl-pyrrolo[3,4-*c*]pyrrole-1,4-dione-5'-yl-ethynyl)tetrakis(dimethylBCOD)porphyrinato]zinc(II) (C4-DPP–ZnCP)

The reaction of compound **6** (180 mg, 213 μmol, 1.0 eq), **7b** (209 mg, 426 μmol, 2.0 eq), $PdCl_2(PPh_3)_2$ (29.9 mg, 42.6 μmol, 0.1 eq) and CuI (16.2 mg, 85.2 μmol, 0.2 eq) in dehydrated toluene (36 mL) and Et_3N (18 mL) following general procedure and purified by flash column chromatography on silica gel ($CHCl_3$, *R*f = 0.16, black band) and reprecipitation to give a target compound **C4-DPP–ZnCP** with a small amount of impurities as black solid in 69% yield (244 mg, 146 μmol). Since these impurities could not be removed by flash column chromatography, GPC and reprecipitation, it was used for the next reaction without further purification. ^{1}H NMR (400 MHz, THF-d_8, δ): 10.21 (s, 2H), 9.45–9.43 (m, 2H), 9.17–9.15 (m, 2H), 8.04–8.03 (m, 2H), 7.85–7.82 (m,2H), 7.33–7.30 (m, 2H), 7.24–7.20 (m, 4H), 7.10–7.06 (m, 4H), 6.08–6.07 (m, 4H), 5.61–5.55 (m, 4H), 4.29–4.26 (m, 4H), 4.20–4.15 (m, 4H), 2.07–2.04 (m, 4H), 1.93–1.86 (m, 4H), 1.75–1.71 (m, 12H), 1.16–1.54 (m, 16H), 1.08–1.02 (m, 6H), 0.99–0.95 (m, 6H), 0.87–0.83 (m, 12H); UV−vis ($CHCl_3$): λ_{max} ($\varepsilon \times 10^4$) = 715 (14.4), 562 (11.4), 438 (10.5), 304 (4.18); HRMS (ESI) *m*/*z*: $[M]^+$ calcd for $C_{100}H_{96}N_8O_4S_4Zn$, 1664.5729; found, 1664.5700.
(Experimental note-6, page 36–37, reaction No. 6-17)

[5,15-Bis(2,5-dihexyl-3,6-dithienyl-2-yl-pyrrolo[3,4-*c*]pyrrole-1,4-dione-5'-yl-ethynyl)tetrakis(dimethylBCOD)porphyrinato]zinc(II) (C6-DPP–ZnCP)

The reaction of compound **6** (200 mg, 236 μmol, 1.0 eq), **7c** (258 mg, 472 μmol, 2.0 eq), $PdCl_2(PPh_3)_2$ (16.6 mg, 23.6 μmol, 0.1 eq) and CuI (9.0 mg, 47.2 μmol, 0.2 eq) in dehydrated toluene (40 mL) and Et_3N (20 mL) following general procedure and purified by flash column chromatography on silica gel (CH_2Cl_2:hexane = 2:1, $R_f = 0.31$, black band) and reprecipitation to give a target compound **C6-DPP–ZnCP** with a small amount of impurities as black solid in 67% yield (281 mg, 158 μmol). Since these impurities could not be removed by flash column chromatography, GPC and reprecipitation, it was used for the next reaction without further purification. ^1H NMR (400 MHz, $CDCl_3$ (1 drop pyridine), δ): 10.66 (s, 2H), 9.82–9.80 (m, 2H), 9.52–9.50 (m, 2H), 8.28–8.24 (m, 2H), 7.99–7.98 (m, 2H), 7.49–7.41 (m, 4H), 7.40–7.37 (m, 2H), 7.29–7.24 (m, 4H), 6.46–6.40 (m, 4H), 5.76–5.73 (m, 4H), 4.46–4.42 (m, 4H), 4.30–4.27 (m, 4H), 2.15–2.06 (m, 8H), 1.93–1.78 (m, 8H), 1.73–1.62 (m, 16H), 1.48–1.37 (m, 12H), 1.33–1.26 (m, 8H), 1.09–1.05 (m, 12H), 0.95–0.85 (m, 12H); UV−vis ($CHCl_3$): λ_{max} ($\varepsilon \times 10^4$) = 712 (14.1), 564 (11.5), 441 (10.4), 304 (4.16); HRMS (ESI) *m*/*z*: $[M]^+$ calcd for $C_{108}H_{112}N_8O_4S_4Zn$, 1776.6981; found, 1776.6989.
(Experimental note-5, page 70–71, reaction No. 5-35)

[5,15-Bis(2,5-dioctyl-3,6-dithienyl-2-yl-pyrrolo[3,4-*c*]pyrrole-1,4-dione-5’-yl-ethynyl)tetrakis(dimethylBCOD)porphyrinato]zinc(II) (C8-DPP–ZnCP)

The reaction of compound **6** (100 mg, 118 μmol, 1.0 eq), **7d** (142 mg, 236 μmol, 2.0 eq), $PdCl_2(PPh_3)_2$ (16.6 mg, 23.6 μmol, 0.1 eq) and CuI (9.0 mg, 47.3 μmol, 0.2 eq) in dehydrated toluene (20 mL) and Et_3N (10 mL) purified by flash column chromatography on silica gel (CH_2Cl_2:hexane = 2:1 to CH_2Cl_2), GPC ($CHCl_3$) and reprecipitation following general procedure to give a target compound **C8-DPP–ZnCP** with a small amount of impurities as black solid in 65% yield (145 mg, 76.4 μmol). Since these impurities could not be removed by flash column chromatography, GPC and reprecipitation, it was used for the next reaction without further purification. ^1H NMR (600 MHz, THF-d_8, δ): 10.21 (s, 2H), 9.45–9.44 (m, 2H), 9.17–9.16 (m, 2H), 8.04 (m, 4H), 7.85–7.83 (m, 2H), 7.32–7.30 (m, 4H), 7.10–7.70 (m, 4H), 6.08–6.07 (m, 4H), 5.59–5.57 (m, 4H), 4.28–4.25 (m, 4H), 4.17–4.15 (m, 4H), 2.06–2.04 (m, 4H), 1.94–1.88 (m, 4H), 1.79–1.72 (m, 8H), 1.58–1.53 (m, 16H), 1.47–1.24 (m, 36H), 0.88–0.82 (m, 24 H); UV−vis ($CHCl_3$): λ_{max} ($\varepsilon \times 10^4$) = 716 (14.4), 563 (11.6), 438 (10.4), 304 (4.28); HRMS (ESI) *m*/*z*: $[M]^+$ calcd for $C_{116}H_{128}N_8O_4S_4Zn$, 1888.8233; found, 1888.8175.
(Experimental note-5, page 122–125, reaction No. 5-59)

[5,15-Bis(2,5-didecyl-3,6-dithienyl-2-yl-pyrrolo[3,4-*c*]pyrrole-1,4-dione-5’-yl-ethynyl)tetrakis(dimethylBCOD)porphyrinato]zinc(II) (C10-DPP–ZnCP)

The reaction of compound **6** (70 mg, 82.7 μmol, 1.0 eq), **7e** (109 mg, 165 μmol, 2.0 eq), $PdCl_2(PPh_3)_2$ (11.6 mg, 16.5 μmol, 0.1 eq) and CuI (6.3 mg, 33.1 μmol, 0.2 eq) in dehydrated toluene (14 mL) and Et_3N (7 mL) purified by flash column chromatography on silica gel

(CH_2Cl_2:hexane = 2:1, *R*f = 0.23, black band to CH_2Cl_2) and reprecipitation following general procedure to give a target compound **C10-DPP–ZnCP** with a small amount of impurities as black solid in 62% yield (103 mg, 51.4 μmol). Since these impurities could not be removed by flash column chromatography, GPC and reprecipitation, it was used for the next reaction without further purification. ^1H NMR (400 MHz, THF-d_8, δ): 10.21 (s, 2H), 9.46–9.44 (m, 2H), 9.18–9.17 (m, 2H), 8.05–8.04 (m, 2H), 7.85–7.83 (m, 2H) 7.33–7.30 (m, 2H), 7.23–7.20 (m, 4H), 7.10–7.06 (m, 4H), 6.08–6.07 (m, 4H), 5.61–5.55 (m, 4H), 4.29–4.25 (m, 4H), 4.18–4.15 (m, 4H), 2.07–2.04 (m, 4H), 1.96–1.87 (m, 4H), 1.80–1.70 (m, 8H), 1.61–1.51 (m, 12H), 1.49–1.19 (m, 56H), 0.87–0.79 (m, 24H); HRMS (ESI) *m*/*z*: $[M + Na]^+$ calcd for $C_{124}H_{144}N_84_6S_4ZnNa$, 2023.9383; found, 2023.9432.
(Experimental note-5, page 96–97, reaction No. 5-48)

General procedure for dezincification reactions for C4-, C6-, C8-, and C10-DPP–CP

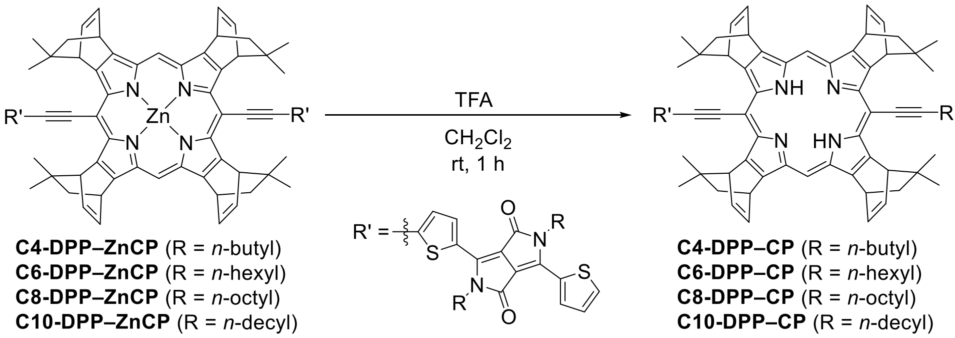

Trifluoroacetic acid (excess) was added to a solution of compounds **C4-**, **C6-**, **C8-** or **C10-DPP–ZnCP** (1.0 eq) in CH_2Cl_2. After stirring at room temperature for 1 h, the mixture was washed with $NaHCO_3$ aq. (× 2). Then the organic layer was dried over Na_2SO_4, and the solvent was removed under reduced pressure. The residue was purified by flash silica gel column chromatography on silica gel and reprecipitation ($CHCl_3$/hexane) to give a target compounds **C4-**, **C6-**, **C8-** or **C10-DPP–CP**.

5,15-Bis(2,5-dibutyl-3,6-dithienyl-2-yl-pyrrolo[3,4-*c*]pyrrole-1,4-dione-5'-yl-ethynyl)tetrakis(dimethylBCOD)porphyrin (C4-DPP–CP)

The reaction of trifluoroacetic acid (0.5 mL, 6.53 mmol, excess) and compound **C4-DPP–ZnCP** (100 mg, 60.0 μmol, 1.0 eq) in CH_2Cl_2 (20 mL) purified by flash column chromatography on silica gel ($CHCl_3$, R_f = 0.32, black band) and reprecipitation following general procedure to give a target compound **C4-DPP–CP** as a black solid in 56% yield (53.5 mg, 33.4 μmol). ^1H NMR (400 MHz, $CDCl_3$, δ): 10.21 (s, 2H), 9.40–9.38 (m, 2H), 9.04–9.01 (m, 2H), 7.98–7.97 (m, 2H), 7.70–7.68 (m, 2H), 7.35–7.32 (m, 2H), 7.22–7.11 (m, 8H), 5.93–5.91 (m, 4H), 5.61–5.55 (m, 4H), 4.29–4.25 (m, 4H), 4.20–4.14 (m, 4H), 2.13–2.09 (m, 4H), 1.98–1.89 (m, 4H), 1.86–1.77 (m, 8H), 1.67–1.47 (m, 20H), 1.10–1.07 (m, 6H), 1.05–1.01 (m,

6H), 0.92–0.89 (m, 12H), –2.50~ –2.52 (m, 2H); ^{13}C NMR spectrum (150 MHz, $CDCl_3$, δ) was measured, but the number of peaks were insufficient due to the presence of stereoisomers: 161.45, 161.37, 161.35, 150.81, 150.78, 149.11, 143.01, 140.33, 139.04, 138.01, 136.85, 136.62, 136.59, 135.66, 135.65, 135.39, 135.23, 132.16, 131.08, 130.49, 130.46, 129.81, 129.65, 128.76, 108.77, 107.99, 103.48, 100.11, 92.21, 91.89, 51.56, 51.52, 51.44, 51.42, 43.94, 43.94, 43.90, 43.88, 42.13, 40.72, 40.70, 40.68, 37.56, 32.50, 32.48, 32.08, 31.60, 31.58, 31.55, 31.03, 30.93, 30.90, 20.39, 20.23, 13.93, 13.82; UV−vis ($CHCl_3$): λ_{max} ($\varepsilon \times 10^4$) = 725 (12.7), 655 (10.4), 551 (9.69), 457 (9.46), 432 (9.01), 303 (4.58); HRMS (ESI) *m*/*z*: $[M + H]^+$ calcd for $C_{100}H_{99}N_8O_4S_4$, 1603.6672; found, 1603.6666.
(Experimental note-6, page 20–21, reaction No. 6-9)

5,15-Bis(2,5-dihexyl-3,6-dithienyl-2-yl-pyrrolo[3,4-*c*]pyrrole-1,4-dione-5'-yl-ethynyl)tetrakis(dimethylBCOD)porphyrin (C6-DPP–CP)

The reaction of trifluoroacetic acid (1.0 mL, 13.1 mmol, excess) and compound **C6-DPP–ZnCP** (150 mg, 84.3 μmol, 1.0 eq) in CH_2Cl_2 (50 mL) following general procedure and purified by flash column chromatography on silica gel (CH_2Cl_2), GPC ($CHCl_3$) and reprecipitation to give a target compound **C6-DPP–CP** as a black solid in 72% yield (105 mg, 61.2 μmol). ^{1}H NMR (400 MHz, $CDCl_3$, δ): 10.21 (s, 2H), 9.40–9.38 (m, 2H), 9.04–9.01 (m, 2H), 7.98–7.97 (m, 2H), 7.70–7.68 (m, 2H), 7.35–7.32 (m, 2H), 7.22–7.11 (m, 8H), 5.93–5.92 (m, 4H), 5.61–5.55 (m, 4H), 4.28–4.24 (m, 4H), 4.18–4.13 (m, 4H), 2.13–2.10 (m, 4H), 1.98–1.91 (m, 4H), 1.86–1.80 (m, 8H), 1.62–1.55 (m, 16H), 1.51–1.36 (m, 20H), 0.95–0.89 (m, 24H), –2.50~ –2.52 (m, 2H); ^{13}C NMR spectrum (100 MHz, $CDCl_3$, δ) was measured, but the number of peaks were insufficient due to the presence of stereoisomers: 161.33, 161.22, 161.12, 161.05, 150.83, 150.76, 150.70, 149, 06, 149.04, 149.02, 149.00, 143.07, 142.98, 140.23, 140.02, 138.93, 138.75, 138.05, 137.97, 137.96, 137.92, 136.84, 136.77, 136.69, 136.59, 136.55, 135.63, 135.52, 135.39, 135.36, 135.27, 135.21, 132.14, 131.03, 130.91, 130.49, 130.43, 129.71, 129.60, 129.55, 128.71, 128.63, 108.70, 108.55, 107.87, 107.68, 103.51, 103.35, 100.12, 96.80, 96.74, 92.24, 91.91, 51.53 51.51, 51.44, 51.42, 43.96, 43.94, 43.91, 42.56, 42.32, 42.19, 40.73, 40.69, 40.67, 37.56, 31.63, 31.58, 31.43, 31.41, 31.16, 31.00, 30.86, 30.45, 30.42, 29.93, 29.86, 26.83, 26.57, 26.53, 22.69, 22.57, 14.10, 14.05; UV−vis ($CHCl_3$): λ_{max} ($\varepsilon \times 10^4$) = 727 (14.4), 650 (10.6), 549 (8.94), 424 (9.57), 304 (4.53); HRMS (ESI) *m*/*z*: $[M + H]^+$ calcd for $C_{108}H_{115}N_8O_4S_4$, 1715.7924; found, 1715.7910.
(Experimental note-5, page 78–79, reaction No. 5-39)

5,15-Bis(2,5-dioctyl-3,6-dithienyl-2-yl-pyrrolo[3,4-*c*]pyrrole-1,4-dione-5'-yl-ethynyl)tetrakis(dimethylBCOD)porphyrin (C8-DPP–CP)

The reaction of trifluoroacetic acid (1.0 mL, 13.1 mmol, excess) and compound **C8-DPP–ZnCP** (100 mg, 52.9 μmol, 1.0 eq) in CH_2Cl_2 (20 mL) purified by flash column chromatography on silica gel (CH_2Cl_2:hexane = 2:1) following general procedure to give a target compound **C8-DPP–CP** as a black solid in 87% yield (83.9 mg,45.9 μmol). ^{1}H NMR (400 MHz, $CDCl_3$, δ): 10.21 (s, 2H), 9.40–9.37 (m, 2H), 9.03–8.99 (m, 2H), 7.98–7.97 (m, 2H), 7.70–7.67 (m, 2H), 7.34–7.31 (m, 2H), 7.22–7.11 (m, 8H), 5.93–5.91 (m, 4H), 5.61–5.55 (m, 4H), 4.28–4.23 (m, 4H), 4.18–4.11 (m, 4H), 2.13–2.10 (m, 4H), 1.99–1.88 (m, 4H), 1.88–1.75 (m, 8H), 1.58–1.29 (m, 52H), 0.93–0.85 (m, 24H), –2.50~ –2.52 (m, 2H); ^{13}C NMR spectrum (100 MHz, $CDCl_3$, δ) was measured, but the number of peaks were insufficient due to the presence of stereoisomers: 161.40, 161.32, 161.23, 150.87, 150.75, 149.12, 149.08, 149.04, 143.09, 142.98, 140.21, 139.01, 138.93, 138.04, 138.01, 137.96, 136.85, 136.79, 136.70, 136.61, 136.58, 135.65, 135.61, 135.39, 135.37, 135.29, 135.22, 132.15, 131.06, 131.01, 130.51, 130.46, 129.78, 129.71, 129.63, 129.62, 128.76, 128.72, 108.75, 108.70, 107.96, 107.89, 103.50, 103.38, 100.12, 96.78, 92.23, 91.91, 51.55, 51.52, 51.44, 51.42, 43.97, 43.94, 43.91, 42.59, 42.38, 42.32, 40.72, 40.70, 40.68, 37.57, 31.86, 31.81, 31.62, 31.60, 31.58, 31.08, 31.02, 30.91, 30.88, 30.51, 30.01, 29.99, 29.47, 29.34, 29.23, 27.18, 26.94, 26.92, 22.67, 14.14, 14.11; UV−vis ($CHCl_3$): $\lambda_{\max}$ ($\varepsilon \times 10^4$) = 728 (14.6), 649 (10.5), 548 (8.58), 423 (9.45), 304 (4.38); HRMS (ESI) *m*/*z*: $[M + H]^+$ calcd for $C_{116}H_{131}N_8O_4S_4$, 1827.9176; found,1827.9180.

(Experimental note-5, page 126–129, reaction No. 5-60)

5,15-Bis(2,5-didecyl-3,6-dithienyl-2-yl-pyrrolo[3,4-*c*]pyrrole-1,4-dione-5’-yl-ethynyl)tetrakis(dimethylBCOD)porphyrin (C10-DPP–CP)

The reaction of trifluoroacetic acid (0.5 mL, 6.53 mmol, excess) and compound **C10-DPP–ZnCP** (40.0 mg, 20.0 μmol, 1.0 eq) in CH_2Cl_2 (4 mL) following general procedure to give a target compound **C10-DPP–CP** as a black solid in 90% yield (35.0 mg, 18.0 μmol). ^{1}H NMR (400 MHz, $CDCl_3$, δ): 10.22 (s, 2H), 9.40–9.37 (m, 2H), 9.03–9.00 (m, 2H), 7.98–7.97 (m, 2H), 7.70–7.68 (m, 2H), 7.35–7.31 (m, 2H), 7.22–7.11 (m, 8H), 5.93–5.92 (m, 4H), 5.61–5.56 (m, 4H), 4.28–4.23 (m, 4H), 4.18–4.12 (m, 4H), 2.13–2.09 (m, 4H), 1.98–1.89 (m, 4H), 1.86–1.77 (m, 8H), 1.58–1.25 (m, 68H), 0.93–0.92 (m, 24H), –2.44~ –2.59 (m, 2H); ^{13}C NMR spectrum (100 MHz, $CDCl_3$, δ) was measured, but the number of peaks were insufficient due to the presence of stereoisomers: 161.42, 161.33, 161.29, 161.26, 150.88, 150.78, 150.76, 149.13, 149.10, 149.08, 149.05, 143.09, 143.01, 140.32, 140.23, 139.04, 138.96, 138.05, 138.01, 137.96, 136.86, 136.80, 136.73, 136.61, 136.58, 135.65, 135.62, 135.40, 135.38, 135.29, 135.23, 132.15, 131.06, 131.01, 130.51, 130.48, 129.80, 129.74, 129.65, 129.63, 128.75, 128.73, 108.77, 108.72, 107.98, 107.92, 103.50, 103.39, 100.12, 96.79, 92.23, 91.92, 51.56, 51.52, 51.45, 43.99, 43.96, 43.91, 42.59, 42.39, 42.34, 40.73, 40.68, 37.58, 31.91, 31.88, 31.63, 31.61, 31.59, 31.09, 31.02, 30.92, 30.90, 30.54, 30.51, 30.01, 29.99, 29.69, 29.61, 29.56, 29.51, 29.34, 29.29, 27.19, 26.92, 22.70, 22.66, 14.15, 14.11; UV−vis ($CHCl_3$): $\lambda_{\max}$ ($\varepsilon \times 10^4$) = 728 (14.6), 649 (10.5), 548 (8.57), 423 (9.42), 304 (4.36); HRMS (ESI) *m*/*z*: $[M + H]^+$ calcd for $C_{124}H_{147}N_8O_4S_4$, 1940.0428; found, 1940.0435.

(Experimental note-6, page 54–55, reaction No. 6-27)

General procedure for retro-Diels−Alder reactions of precursors

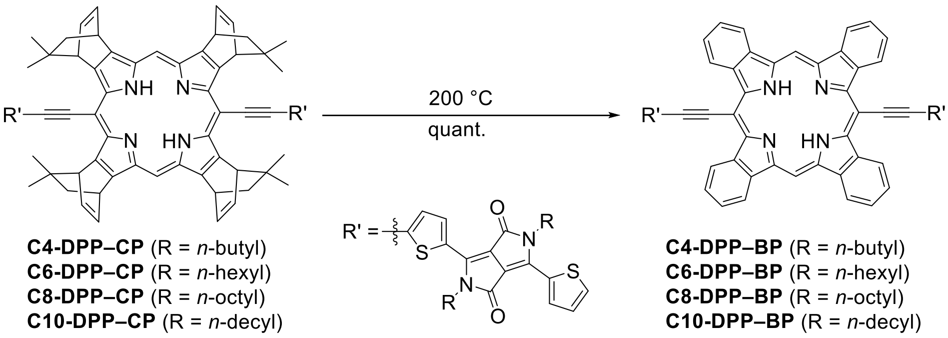

C4-DPP–CP (R = *n*-butyl)
C6-DPP–CP (R = *n*-hexyl)
C8-DPP–CP (R = *n*-octyl)
C10-DPP–CP (R = *n*-decyl)

C4-DPP–BP (R = *n*-butyl)
C6-DPP–BP (R = *n*-hexyl)
C8-DPP–BP (R = *n*-octyl)
C10-DPP–BP (R = *n*-decyl)

Precursors (**C2-**, **C4-**, **C6-**, **C8-**, and **C10-DPP–CP**) were heated at 200 °C for 1 h in sample tubes under reduced pressure to give corresponding products (**C2-**, **C4-**, **C6-**, **C8-**, and **C10-DPP–BP**) quantitatively as black solids.

5,15-Bis(2,5-diethyl-3,6-dithienyl-2-yl-pyrrolo[3,4-*c*]pyrrole-1,4-dione-5'-yl-ethynyl)tetrabenzoporphyrin (C2-DPP–BP)

^{1}H and ^{13}C NMR spectra were not available due to low solubility; HRMS (MALDI) *m*/*z*: $[M + H]^+$ calcd for $C_{76}H_{50}N_8O_4S_4$, 1266.2832; found, 1266.2832.

5,15-Bis(2,5-dibutyl-3,6-dithienyl-2-yl-pyrrolo[3,4-*c*]pyrrole-1,4-dione-5'-yl-ethynyl)tetrabenzoporphyrin (C4-DPP–BP)

^{1}H and ^{13}C NMR spectra were not available due to low solubility; HRMS (MALDI) *m*/*z*: $[M + H]^+$ calcd for $C_{84}H_{66}N_8O_4S_4$, 1378.4084; found, 1378.4089.

5,15-Bis(2,5-dihexyl-3,6-dithienyl-2-yl-pyrrolo[3,4-*c*]pyrrole-1,4-dione-5'-yl-ethynyl)tetrabenzoporphyrin (C6-DPP–BP)

^{1}H and ^{13}C NMR spectra were not available due to low solubility; HRMS (MALDI) *m*/*z*: $[M + H]^+$ calcd for $C_{92}H_{82}N_8O_4S_4$, 1490.5336; found, 1490.5331.

5,15-Bis(2,5-dioctyl-3,6-dithienyl-2-yl-pyrrolo[3,4-*c*]pyrrole-1,4-dione-5'-yl-ethynyl)tetrabenzoporphyrin (C8-DPP–BP)

^{1}H and ^{13}C NMR spectra were not available due to low solubility; HRMS (MALDI) *m*/*z*: $[M + H]^+$ calcd for $C_{100}H_{98}N_8O_4S_4$, 1602.6588; found, 1602.6586.

5,15-Bis(2,5-didecyl-3,6-dithienyl-2-yl-pyrrolo[3,4-c]pyrrole-1,4-dione-5'-yl-ethynyl)tetrabenzoporphyrin (C10-DPP–BP)

^{1}H and ^{13}C NMR spectra were not available due to low solubility; HRMS (MALDI) *m*/*z*: $[M + H]^+$ calcd for $C_{108}H_{114}N_8O_4S_4$, 1714.7840; found, 1714.7830.

4-10-4. NMR Spectra

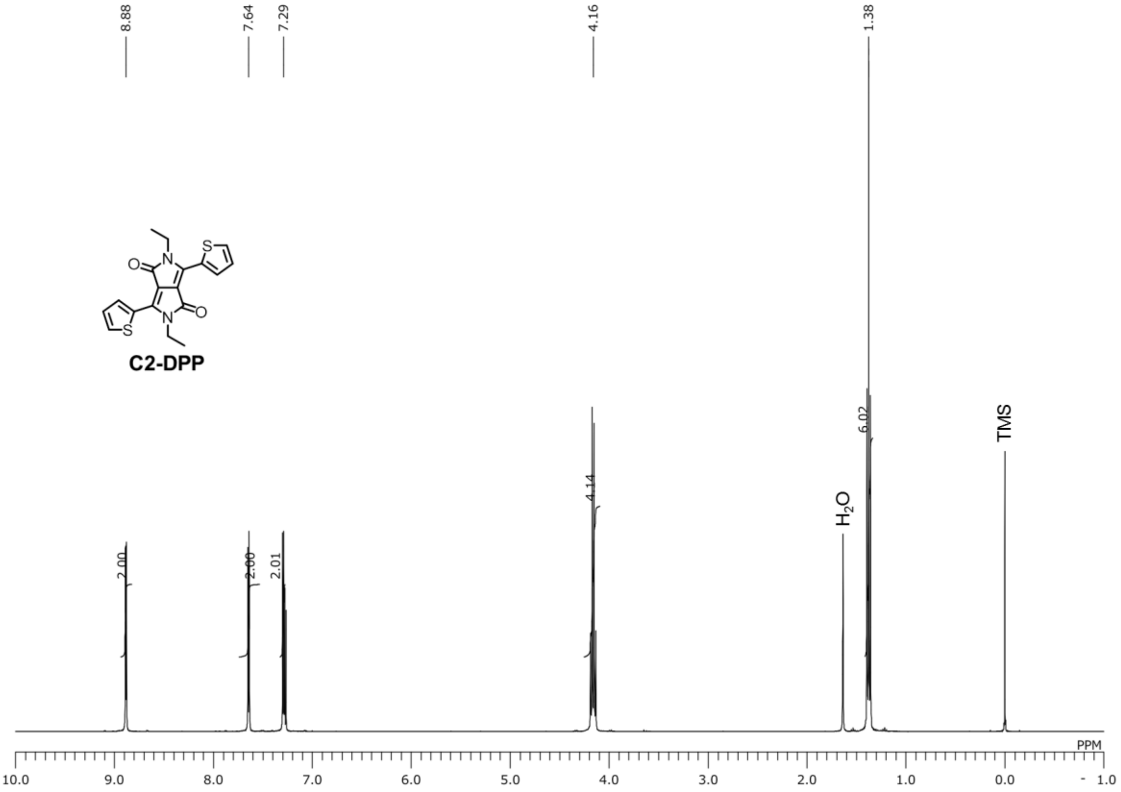

Figure S4-11. ^{1}H NMR spectrum of **C2-DPP** in CDCl$_3$.

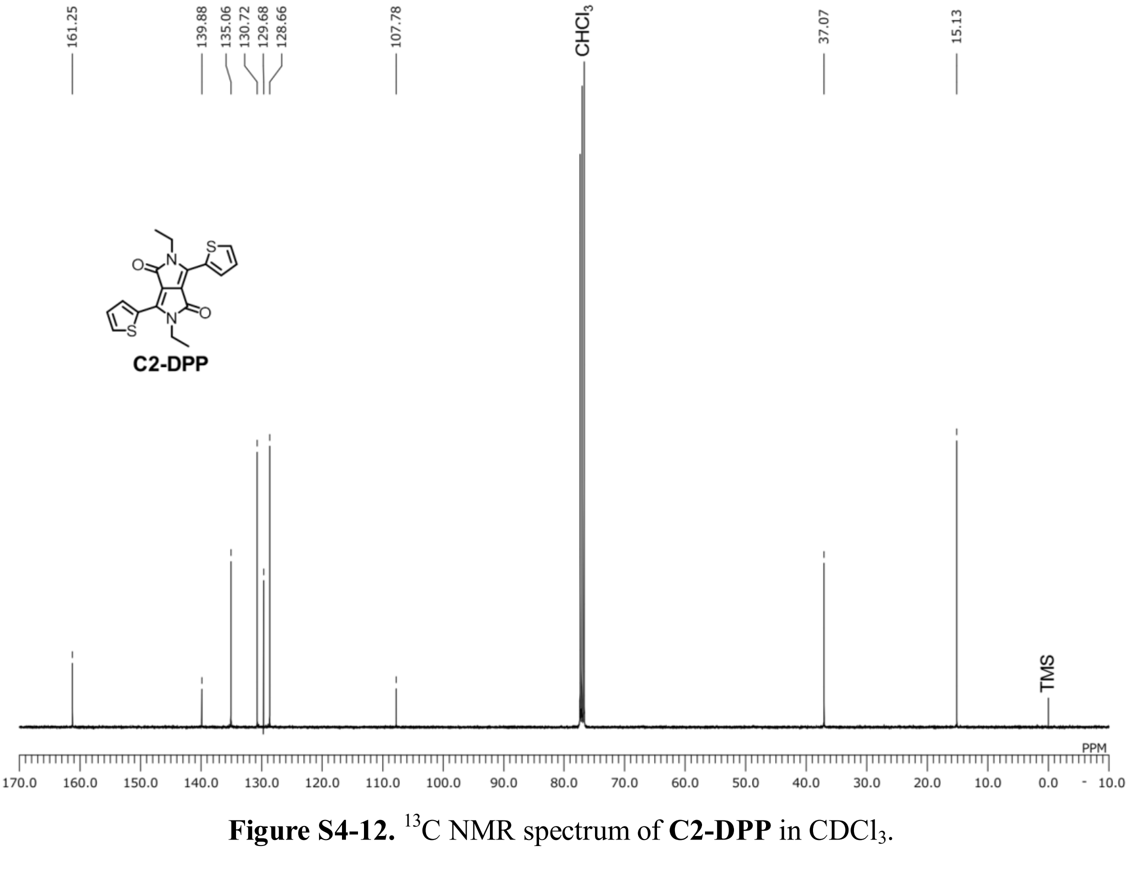

Figure S4-12. ^{13}C NMR spectrum of **C2-DPP** in CDCl$_3$.

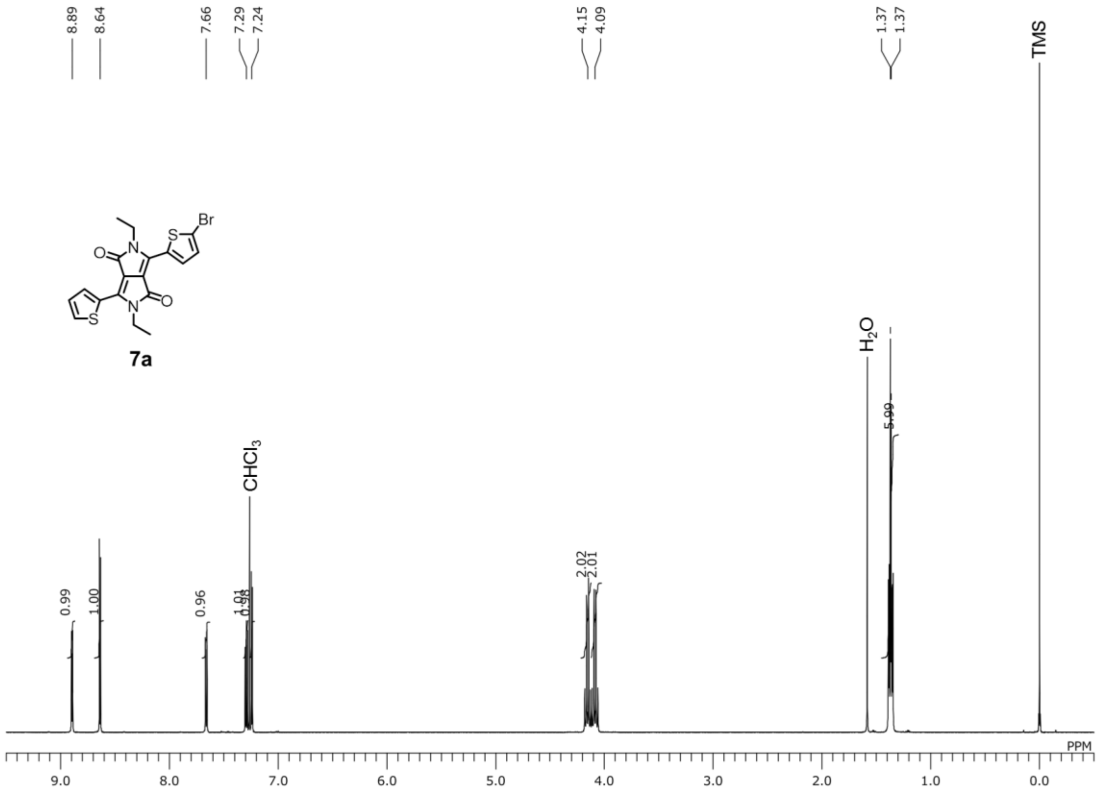

Figure S4-13. ^{1}H NMR spectrum of **7a** in CDCl$_3$.

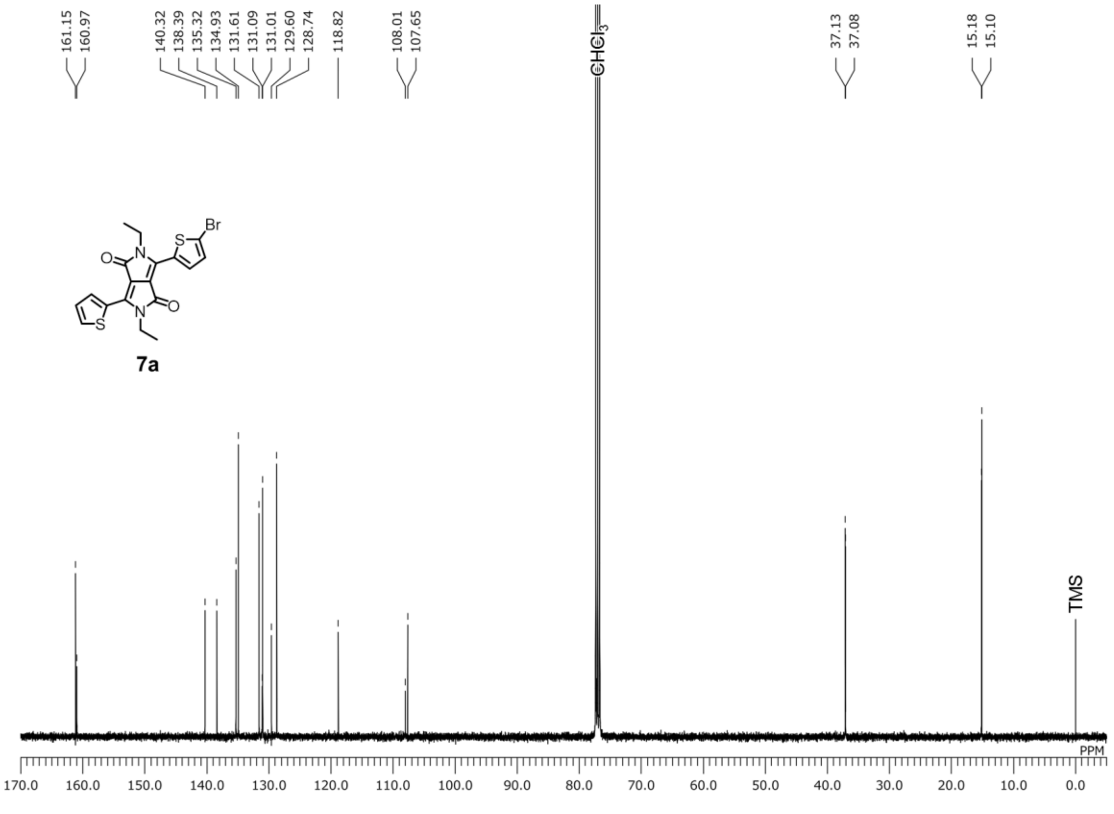

Figure S4-14. ^{13}C NMR spectrum of **7a** in CDCl$_3$.

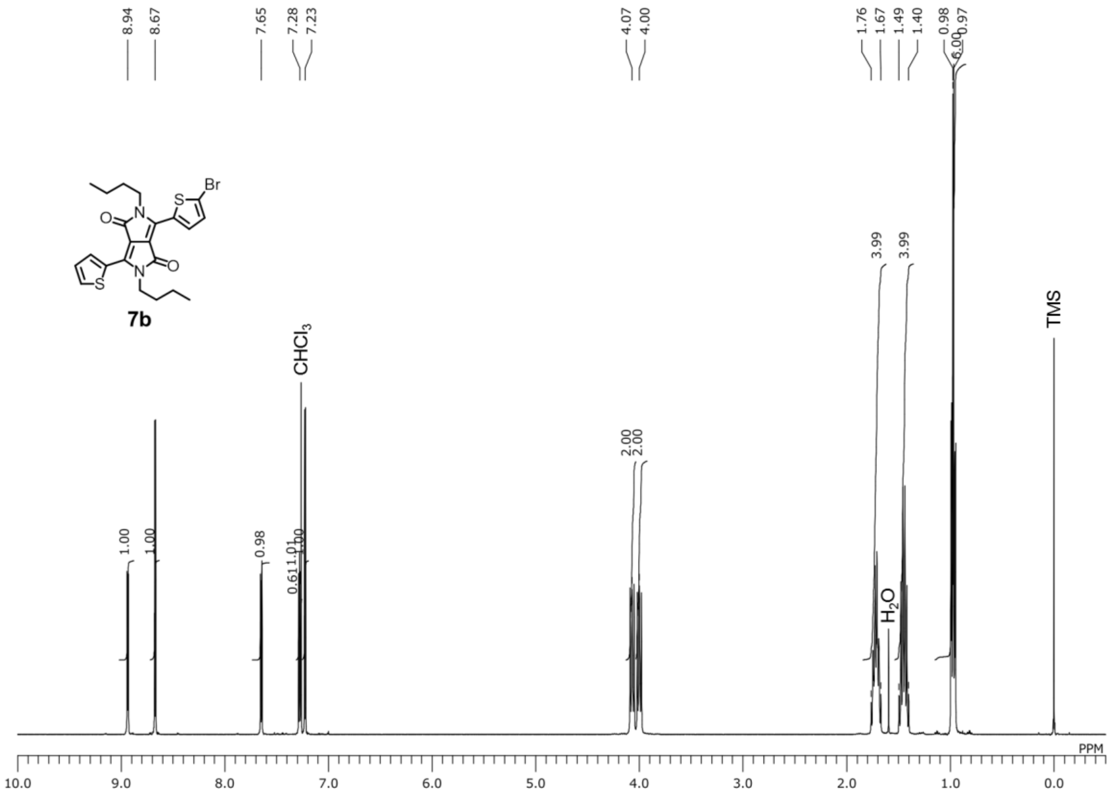

Figure S4-15. ^{1}H NMR spectrum of **7b** in CDCl$_3$.

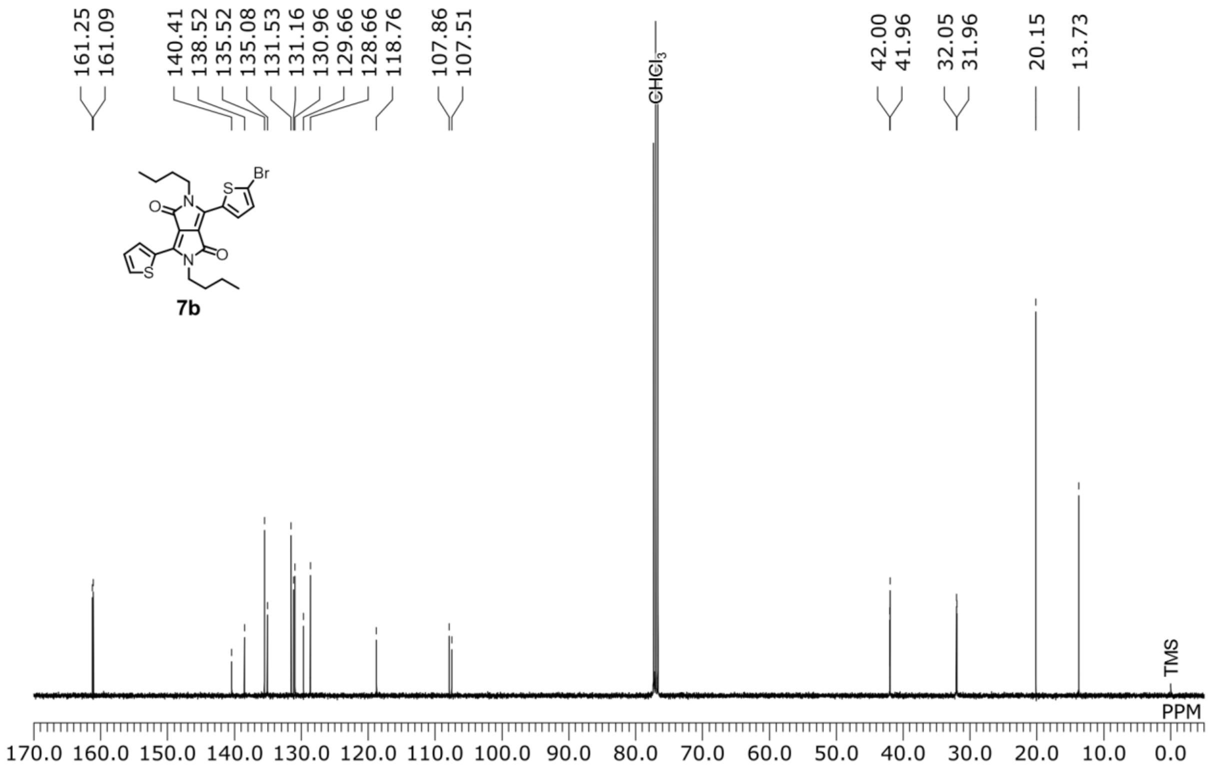

Figure S4-16. ^{13}C NMR spectrum of **7b** in CDCl$_3$.

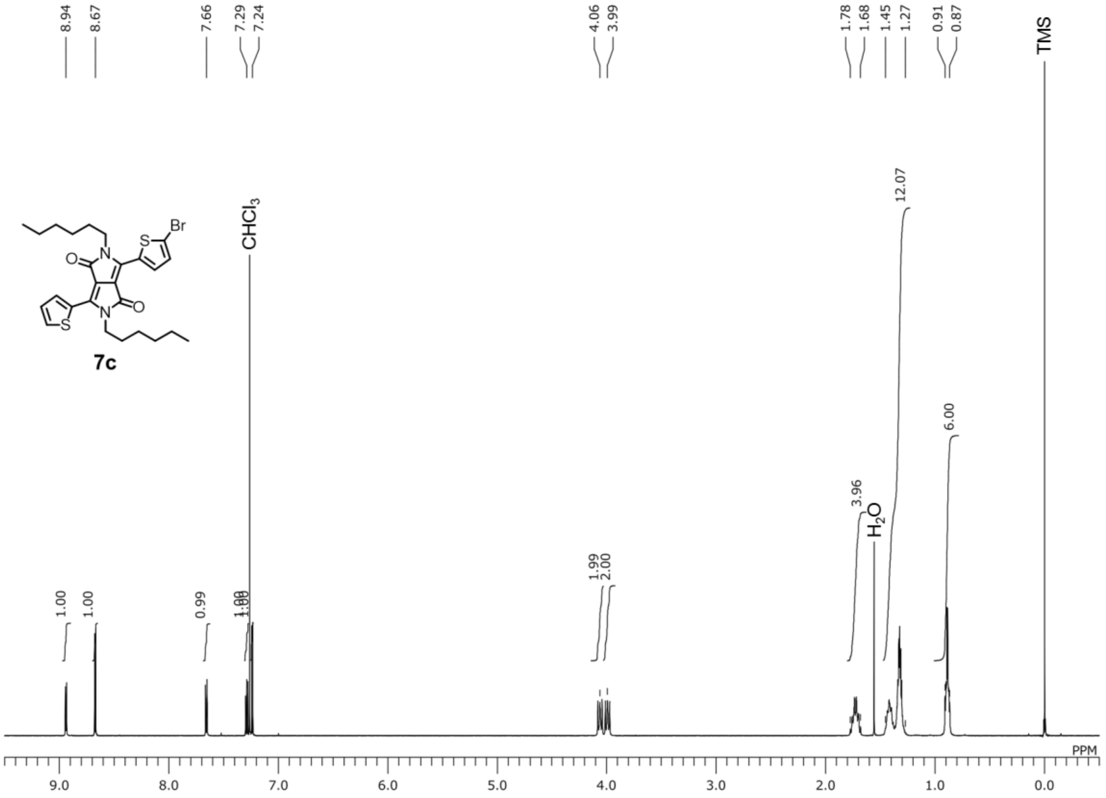

Figure S4-17. ^{1}H NMR spectrum of **7c** in CDCl$_3$.

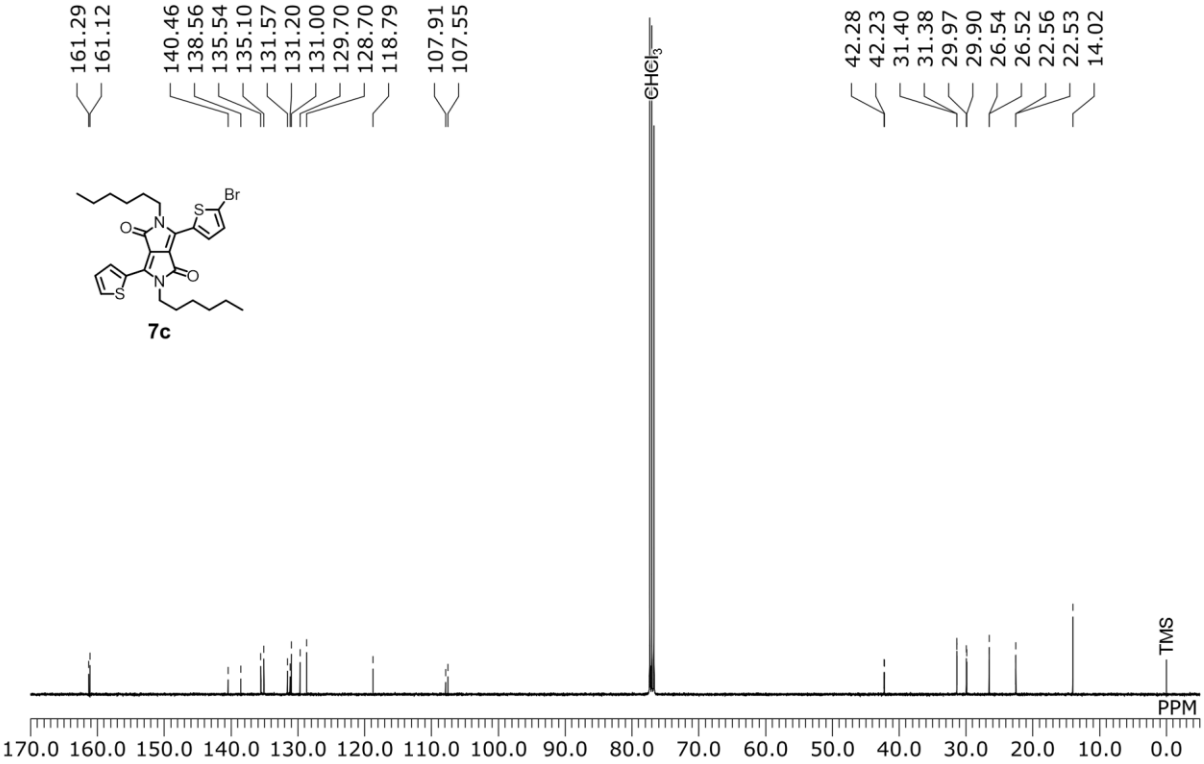

Figure S4-18. ^{13}C NMR spectrum of **7c** in CDCl$_3$.

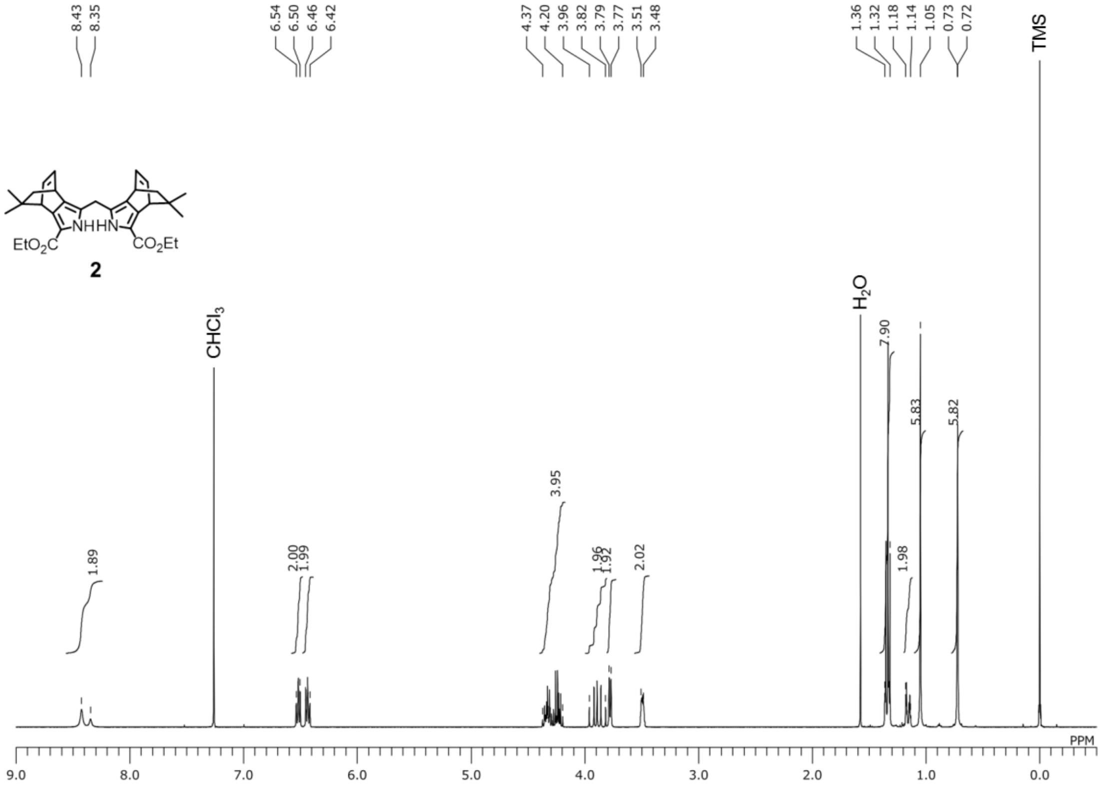

Figure S4-19. ^{1}H NMR spectrum of **2** in $CDCl_3$.

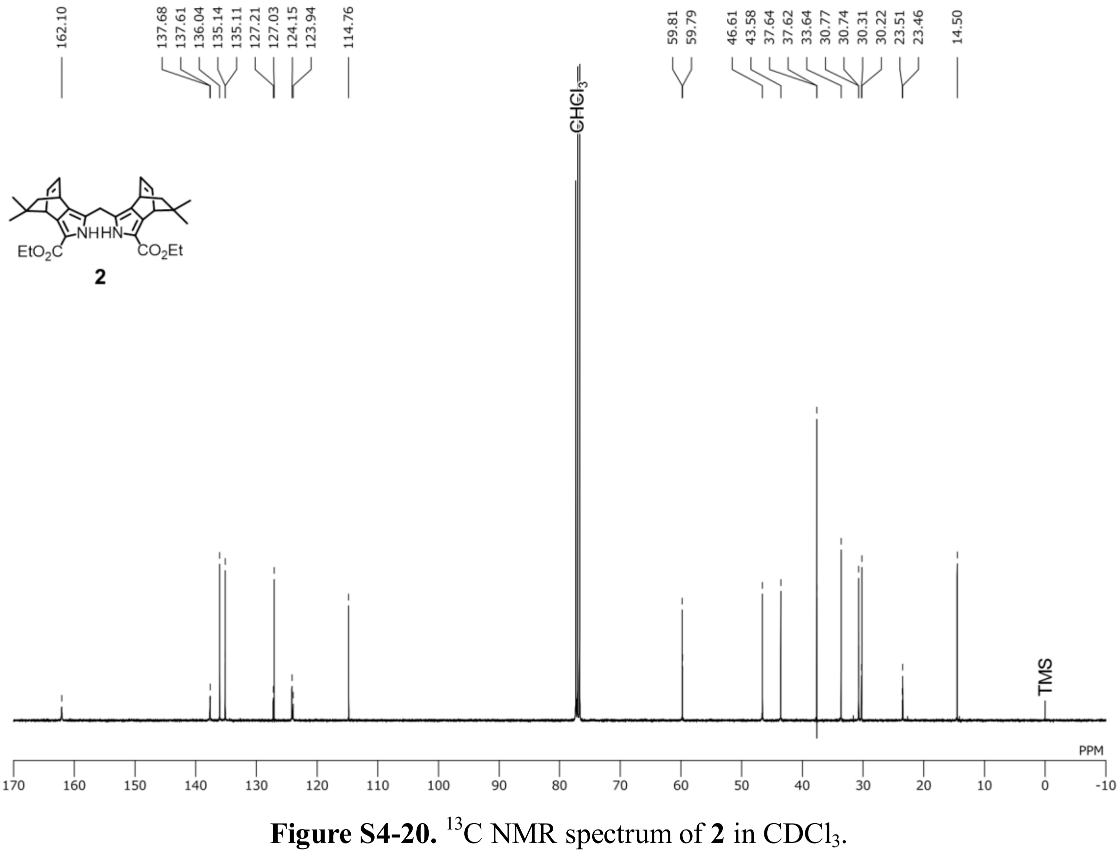

Figure S4-20. ^{13}C NMR spectrum of **2** in $CDCl_3$.

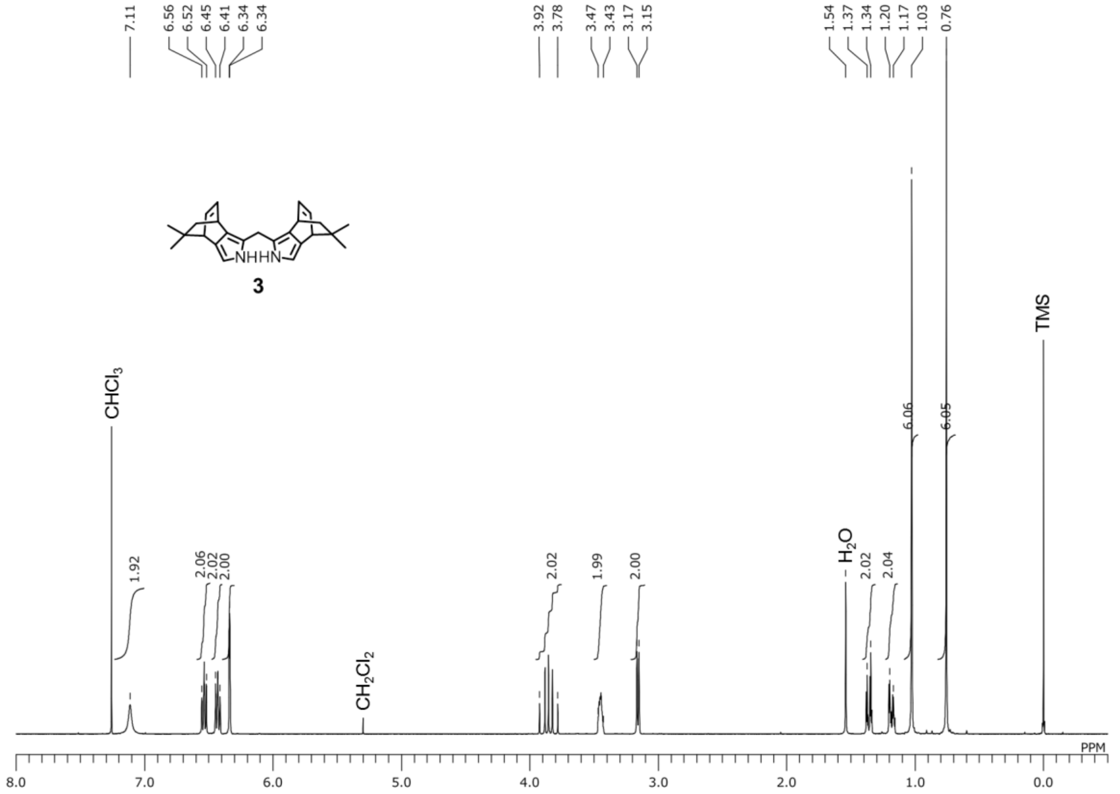

Figure S4-21. ^{1}H NMR spectrum of **3** in CDCl$_3$.

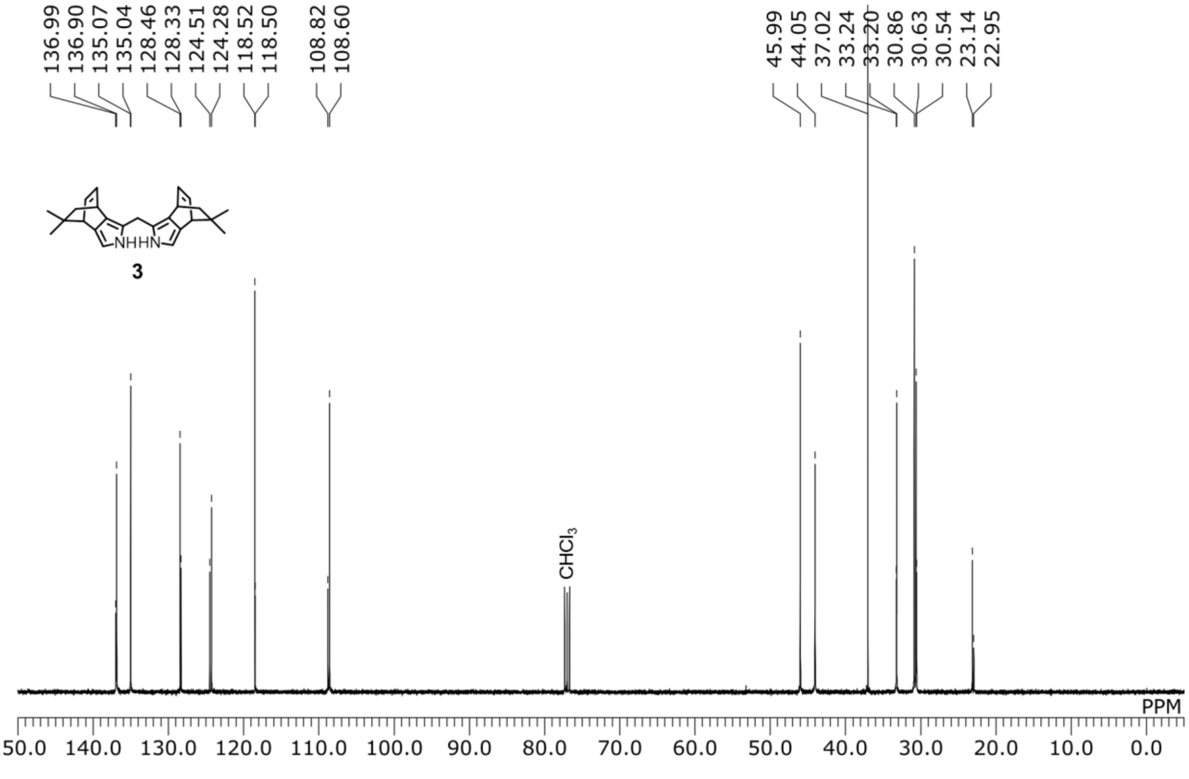

Figure S4-22. ^{13}C NMR spectrum of **3** in CDCl$_3$.

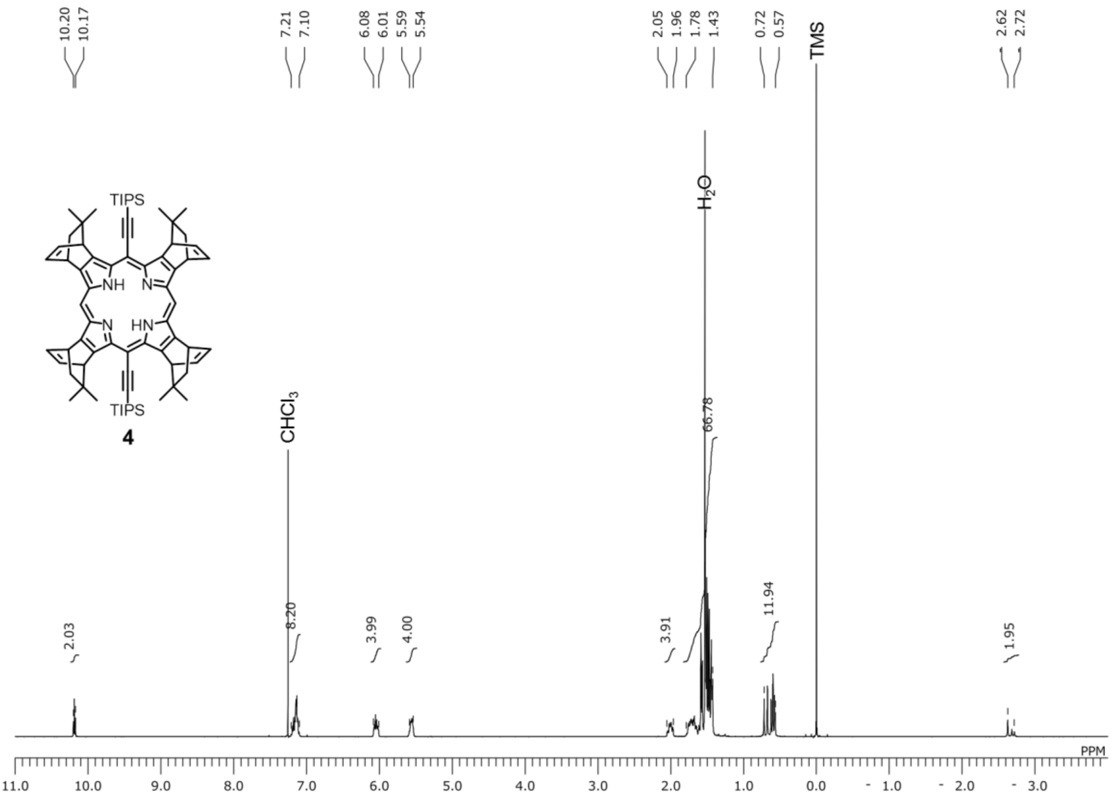

Figure S4-23. ^{1}H NMR spectrum of **4** in CDCl$_3$.

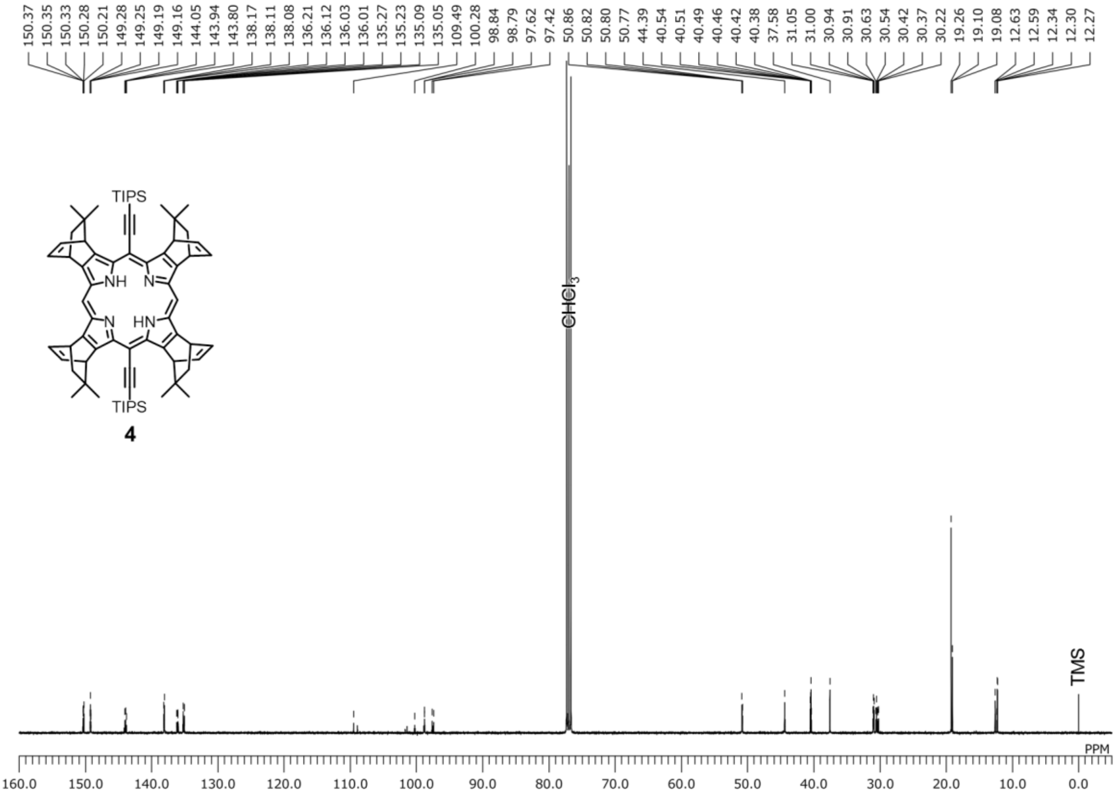

Figure S4-24. ^{13}C NMR spectrum of **4** in CDCl$_3$.

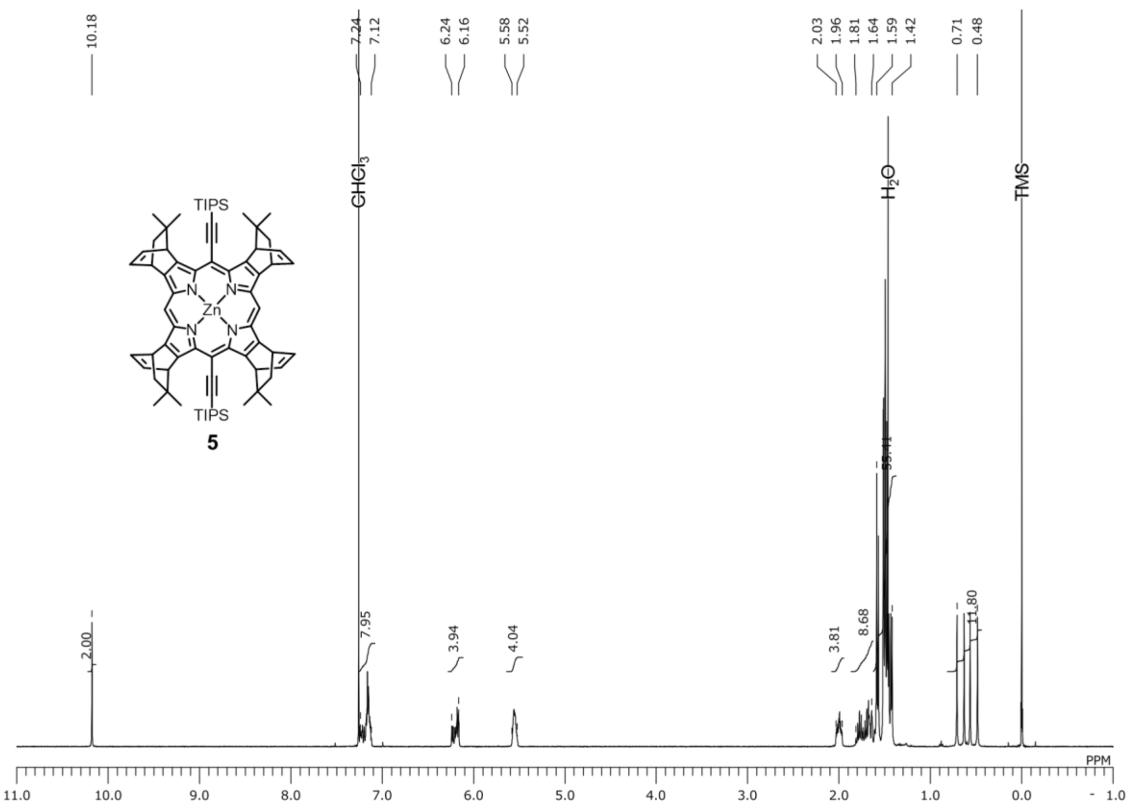

Figure S4-25. ^{1}H NMR spectrum of **5** in CDCl$_3$.

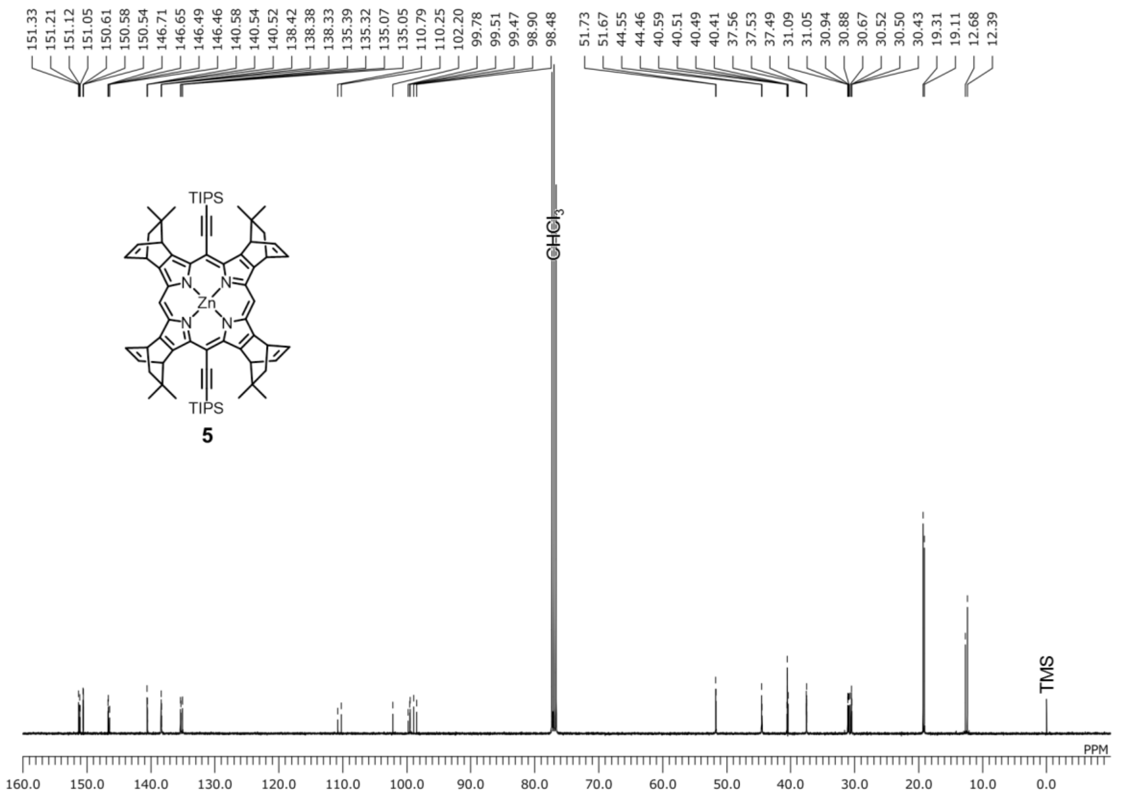

Figure S4-26. ^{13}C NMR spectrum of **5** in CDCl$_3$.

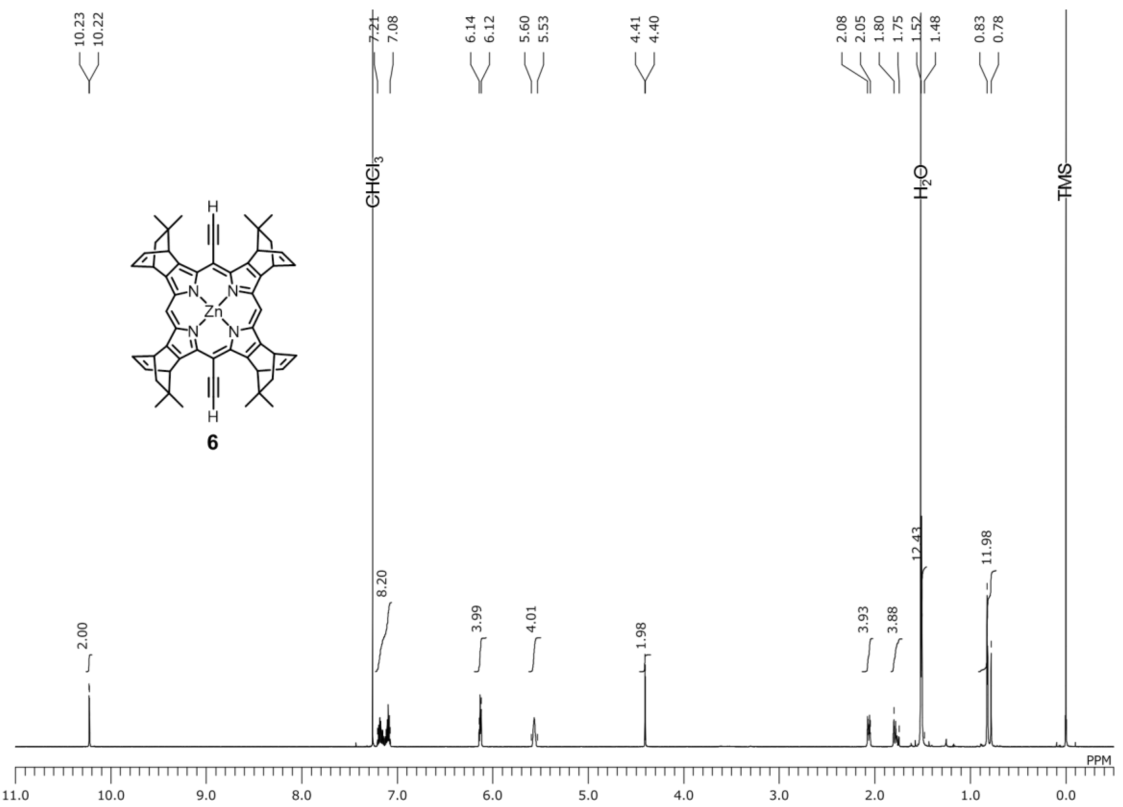

Figure S4-27. ^{1}H NMR spectrum of **6** in $CDCl_3$.

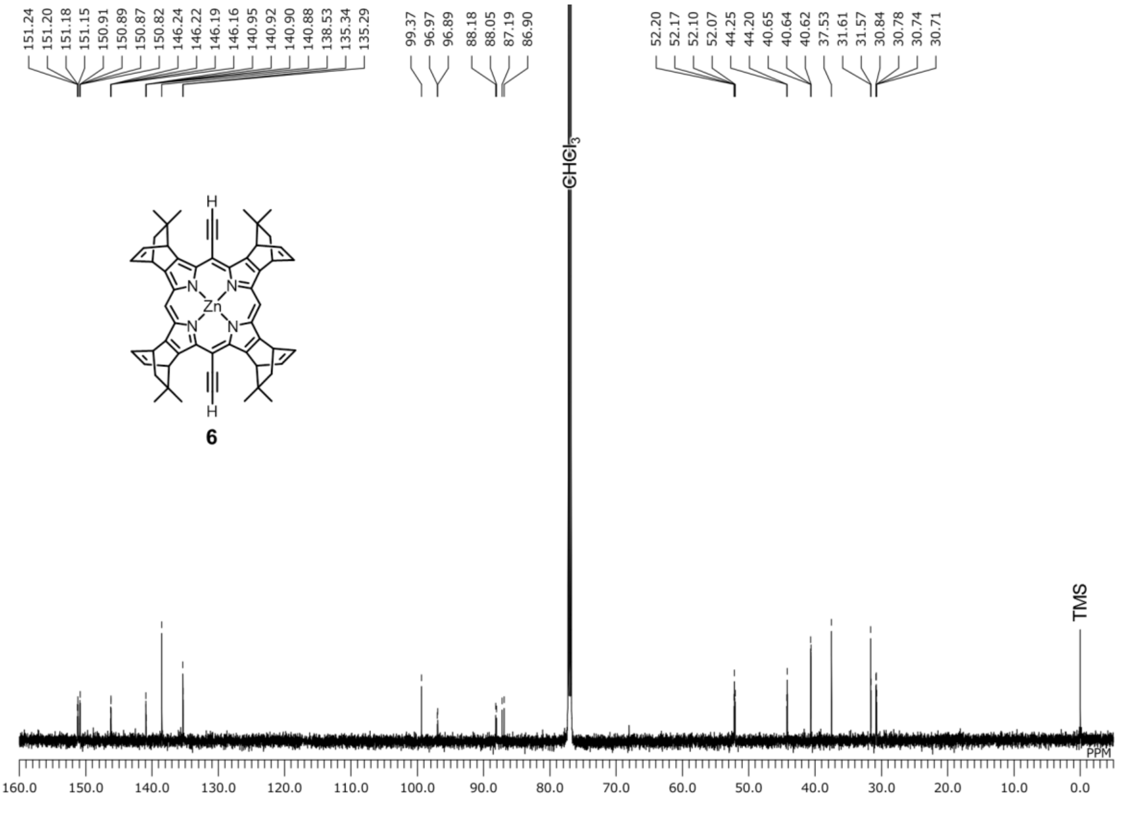

Figure S4-28. ^{13}C NMR spectrum of **6** in $CDCl_3$.

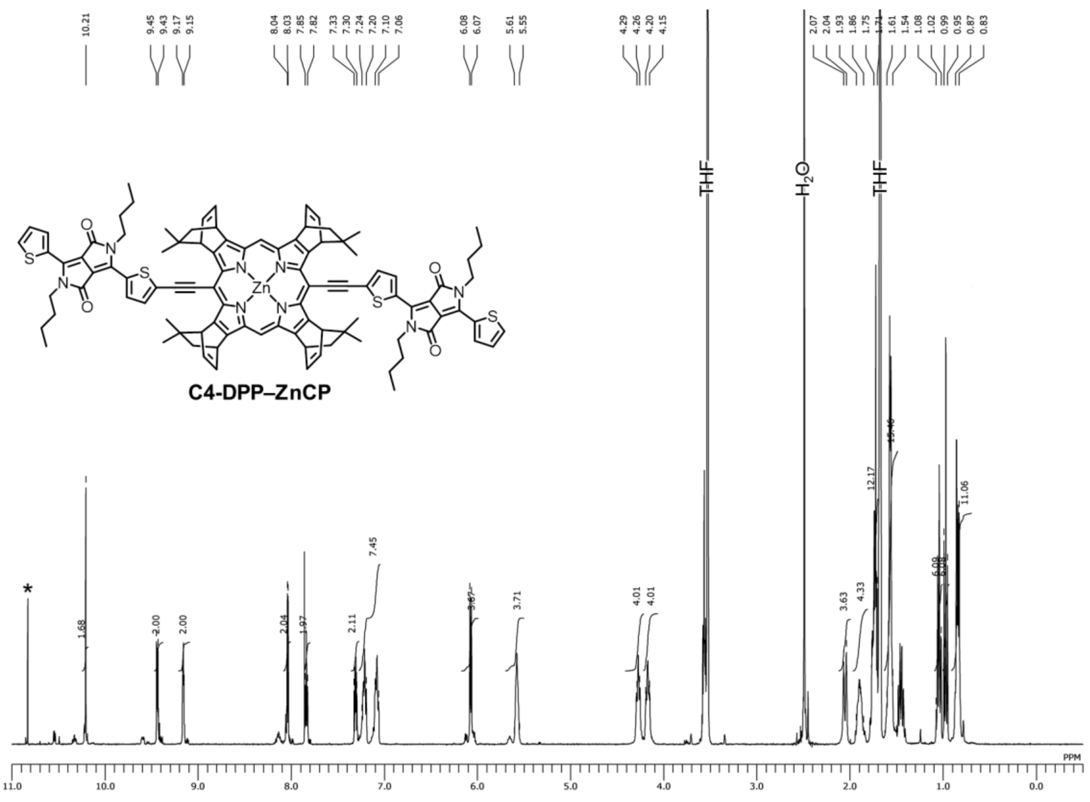

Figure S4-29. ^{1}H NMR spectrum of **C4-DPP–ZnCP** in THF-d_8.

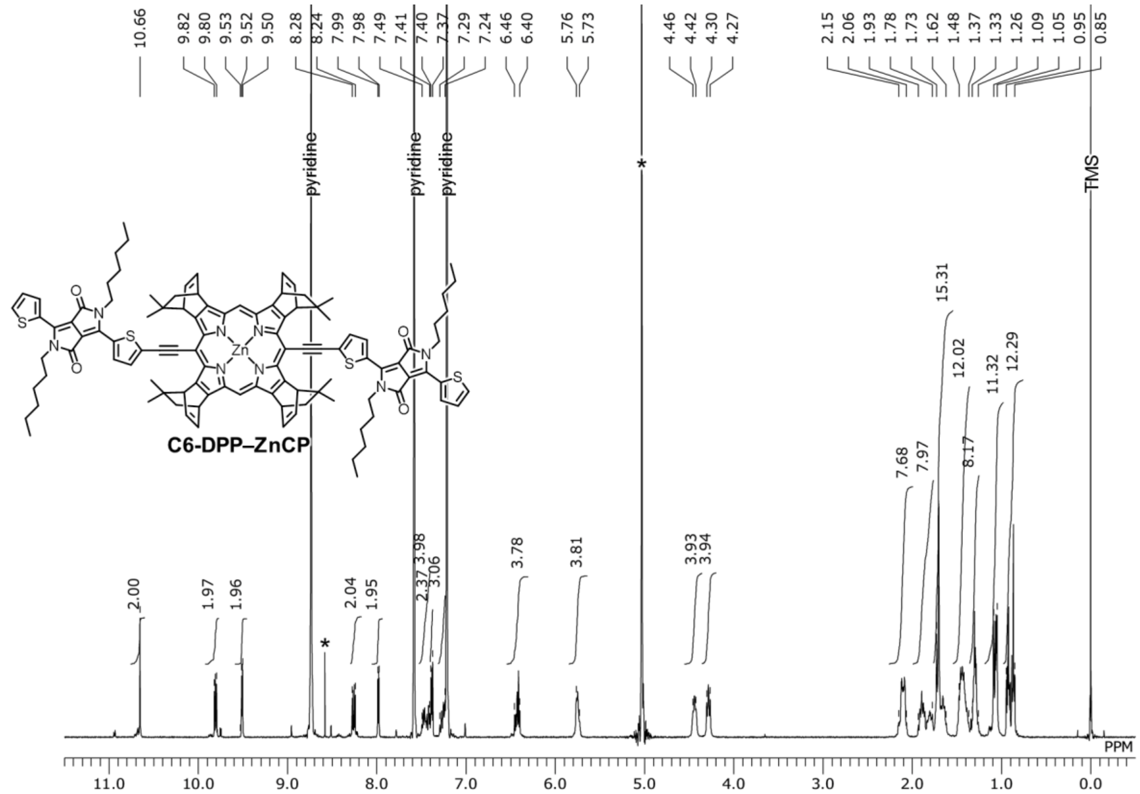

Figure S4-30. ^{1}H NMR spectrum of **C6-DPP–ZnCP** in $CDCl_3$ (1 drop pyridine).

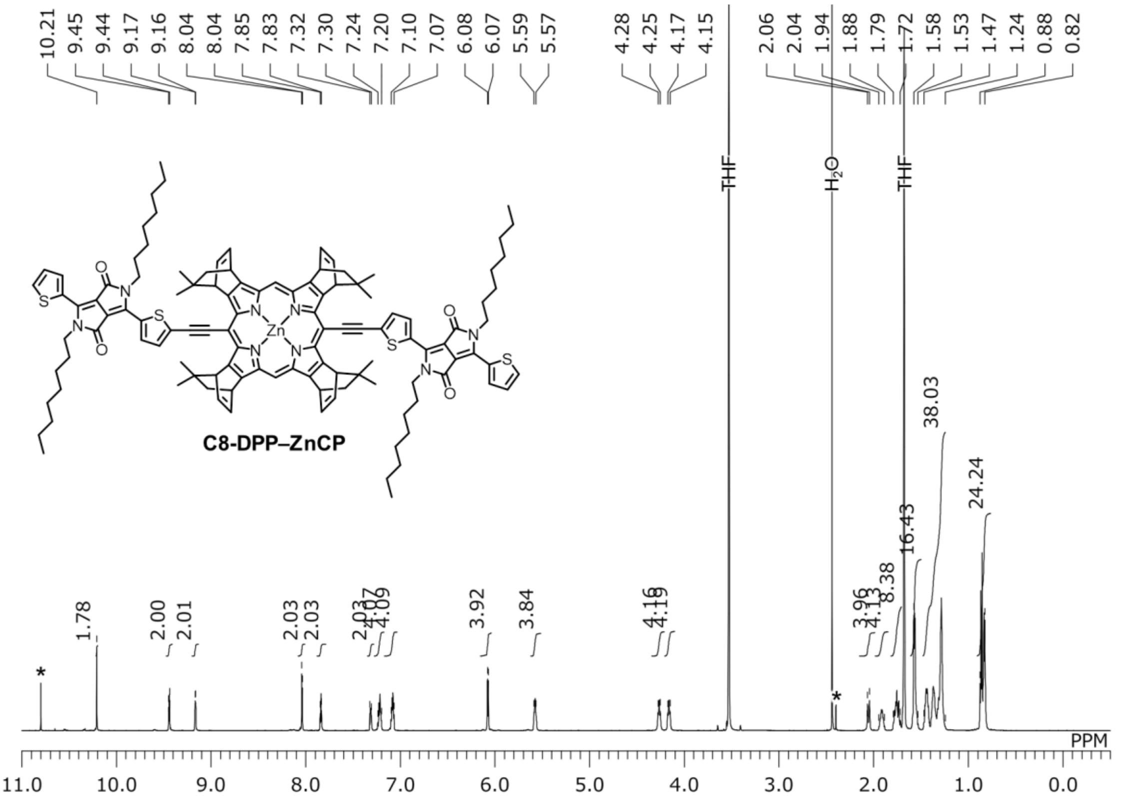

Figure S4-31. ^{1}H NMR spectrum of **C8-DPP–ZnCP** in THF-d_8.

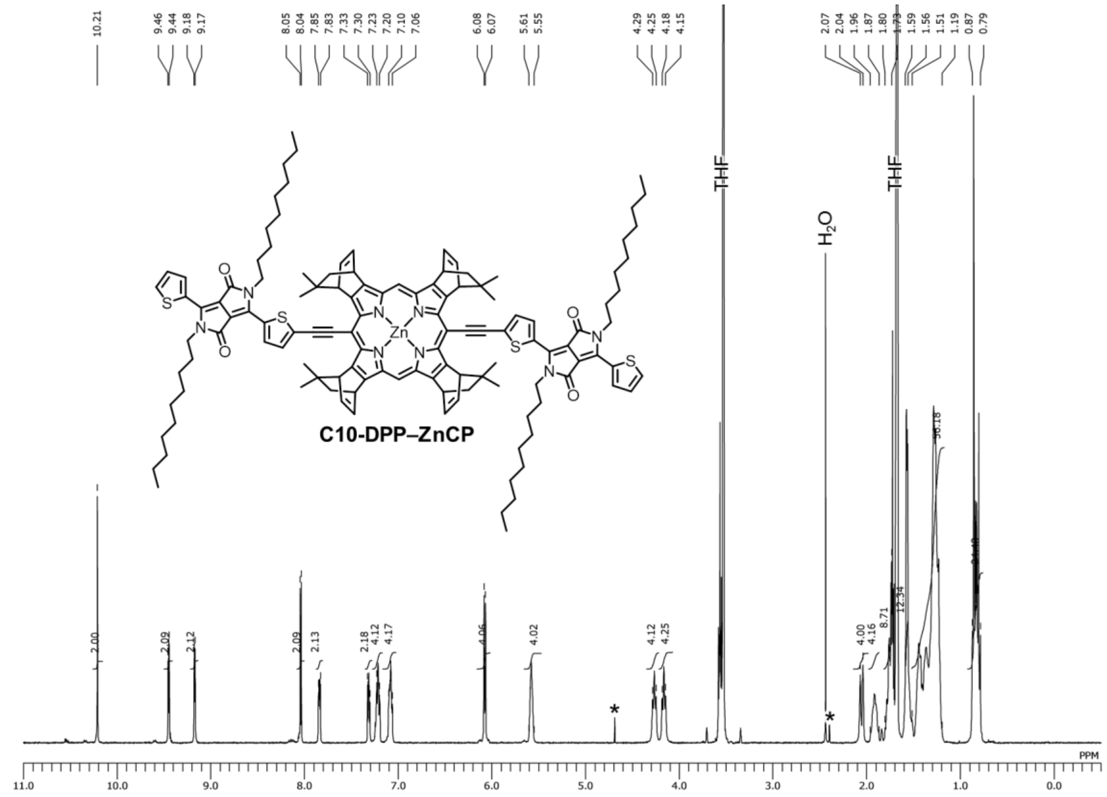

Figure S4-32. ^{1}H NMR spectrum of **C10-DPP–ZnCP** in CDCl$_3$.

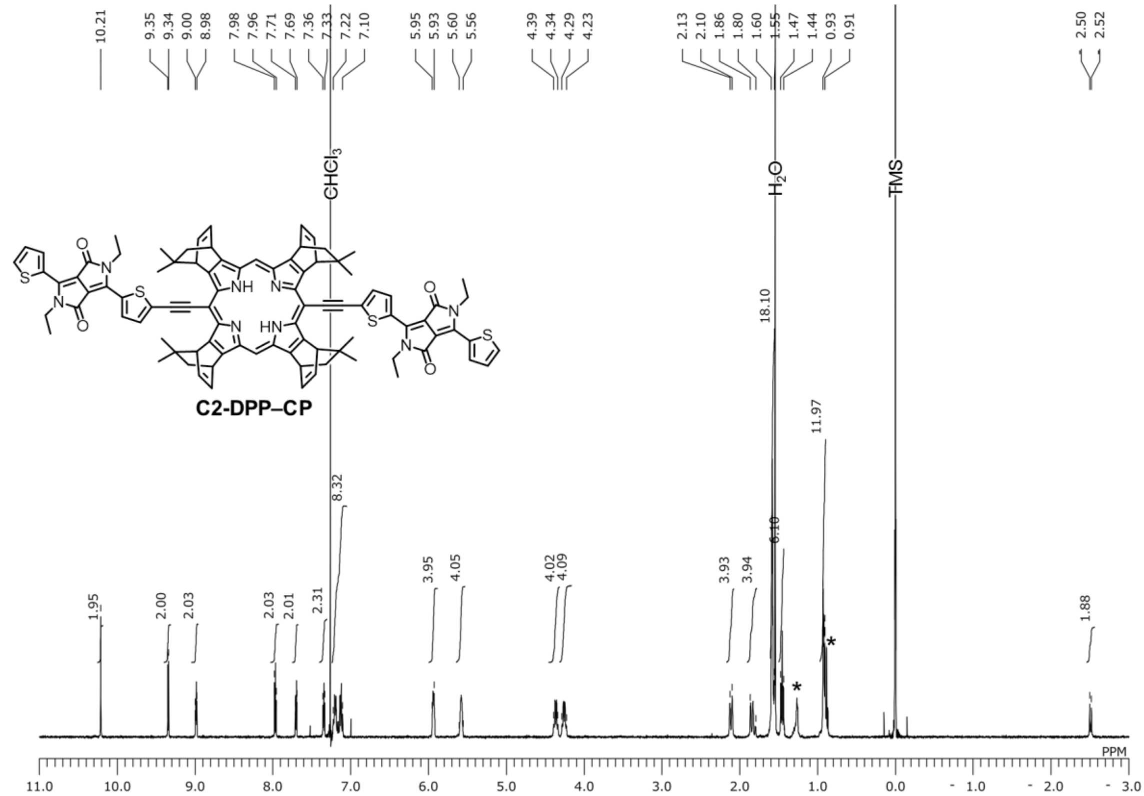

Figure S4-33. ^{1}H NMR spectrum of **C2-DPP–CP** in $CDCl_3$.

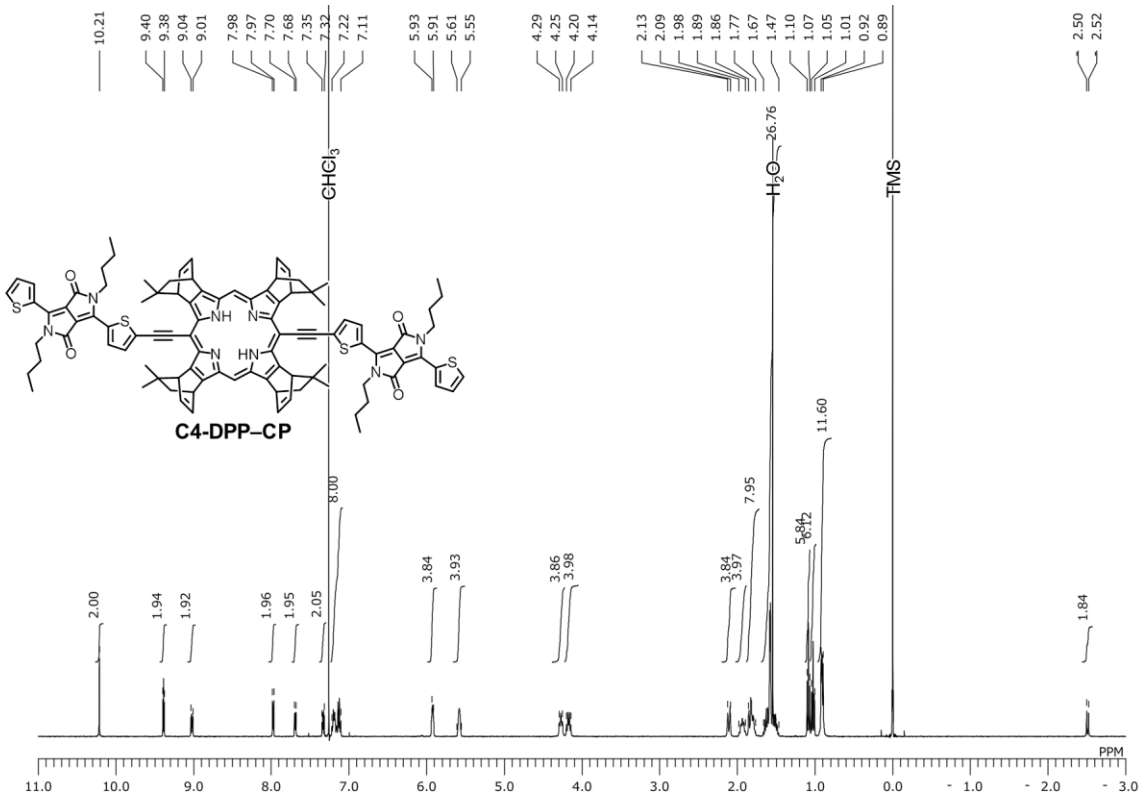

Figure S4-34. ^{1}H NMR spectrum of **C4-DPP–CP** in $CDCl_3$.

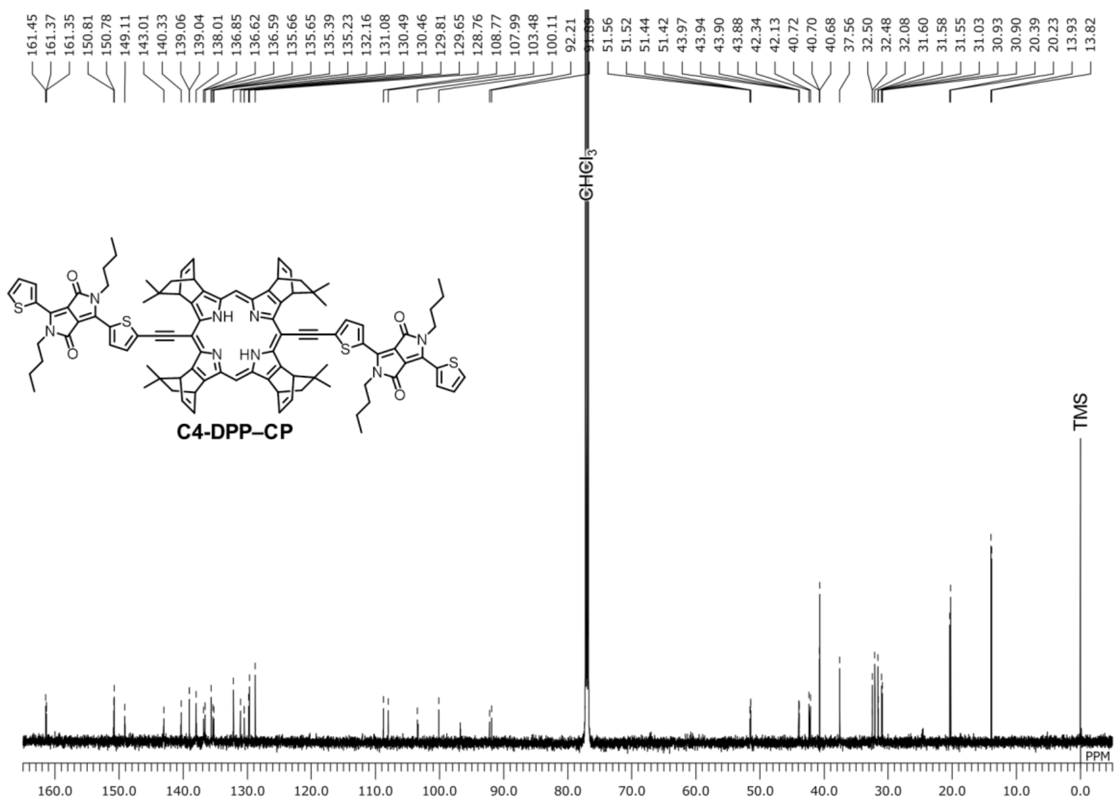

Figure S4-35. ^{13}C NMR spectrum of **C4-DPP–CP** in CDCl$_3$.

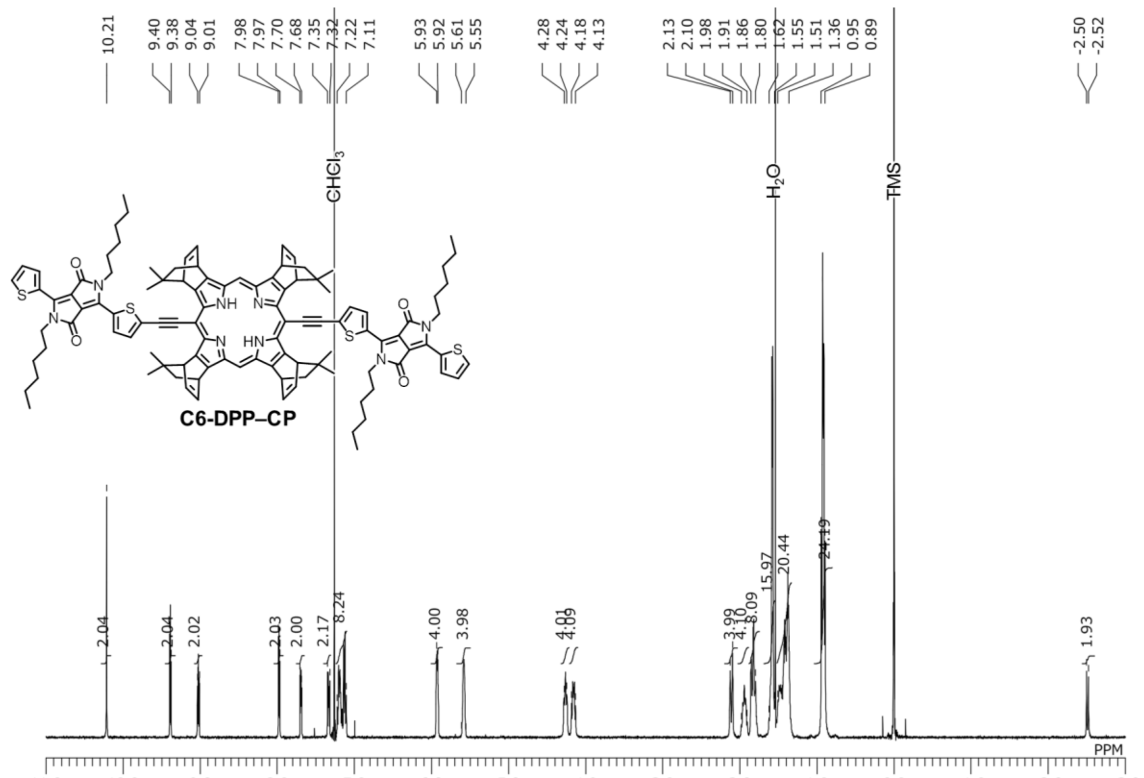

Figure S4-36. ^{1}H NMR spectrum of **C6-DPP–CP** in CDCl$_3$.

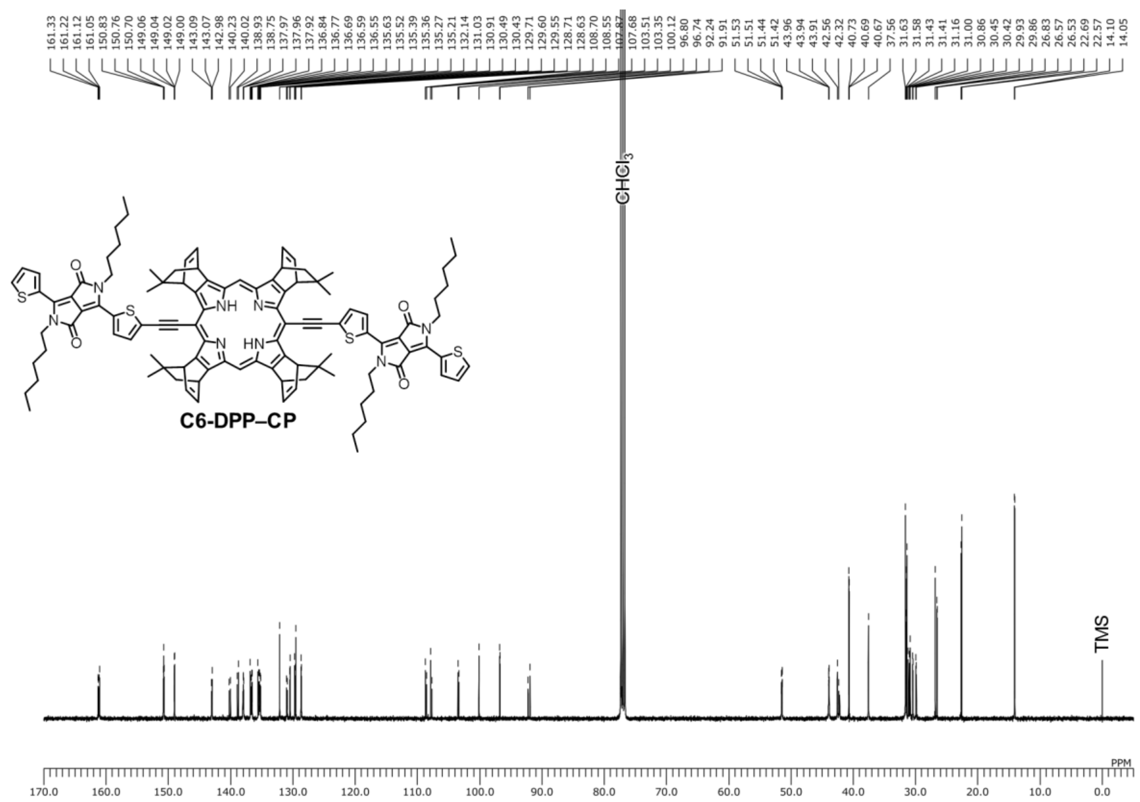

Figure S4-37. ^{13}C NMR spectrum of **C6-DPP–CP** in CDCl$_3$.

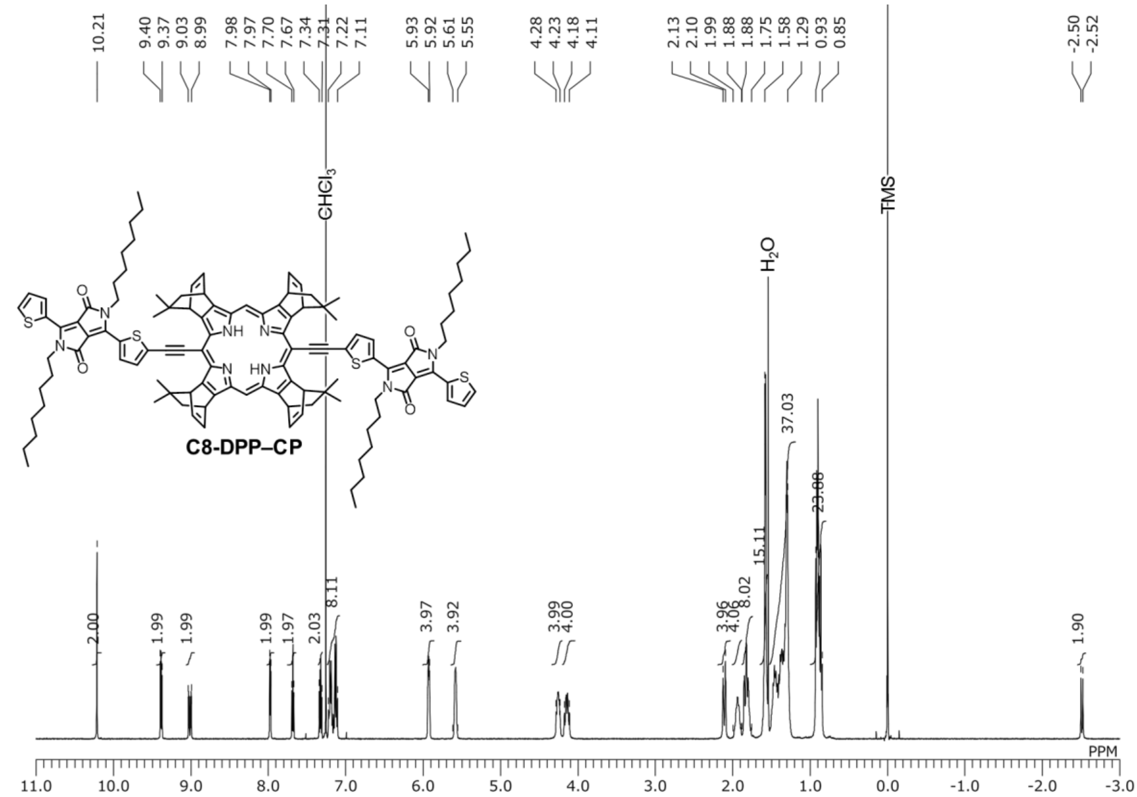

Figure S4-38. ^{1}H NMR spectrum of **C8-DPP–CP** in CDCl$_3$.

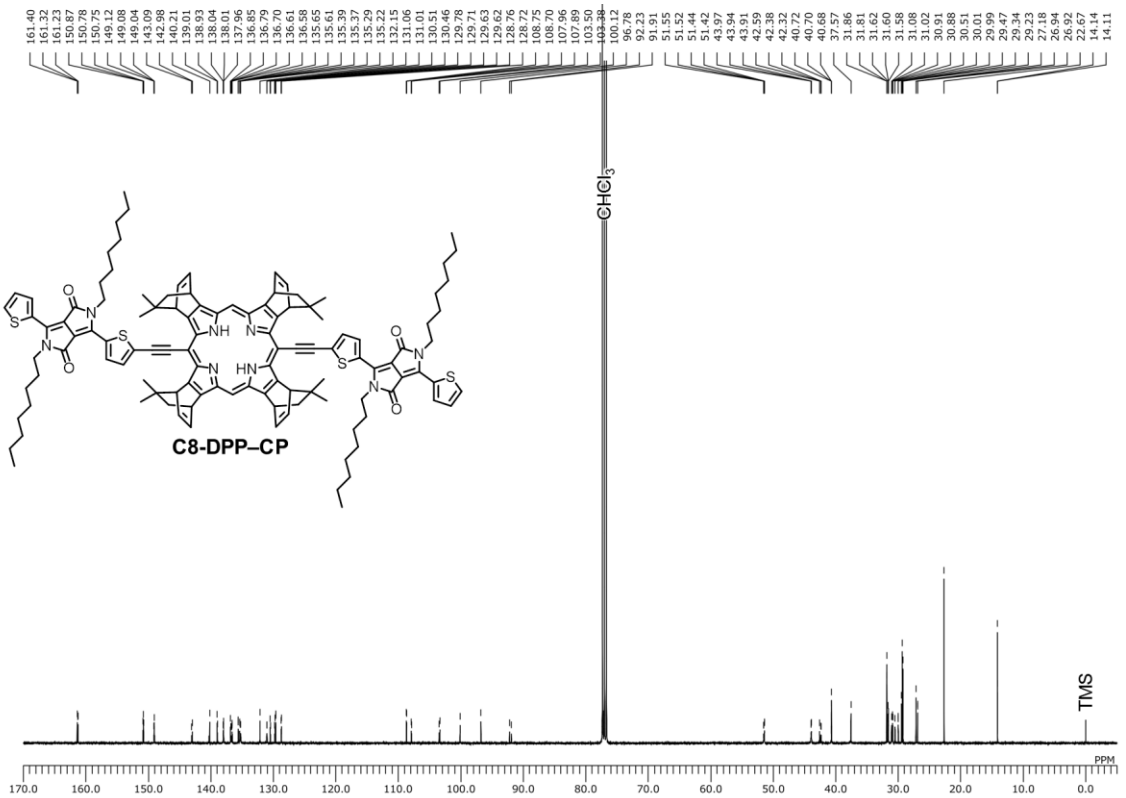

Figure S4-39. ^{13}C NMR spectrum of **C8-DPP–CP** in $CDCl_3$.

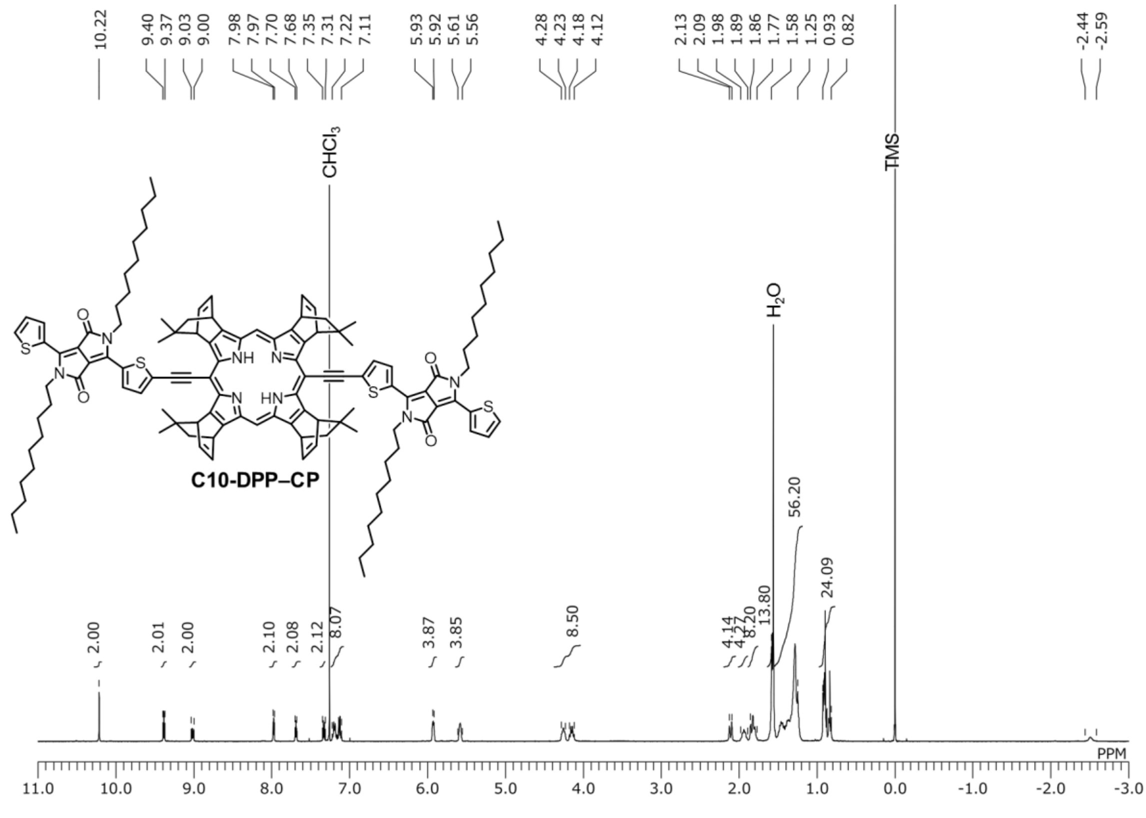

Figure S4-40. ^{1}H NMR spectrum of **C10-DPP–CP** in $CDCl_3$.

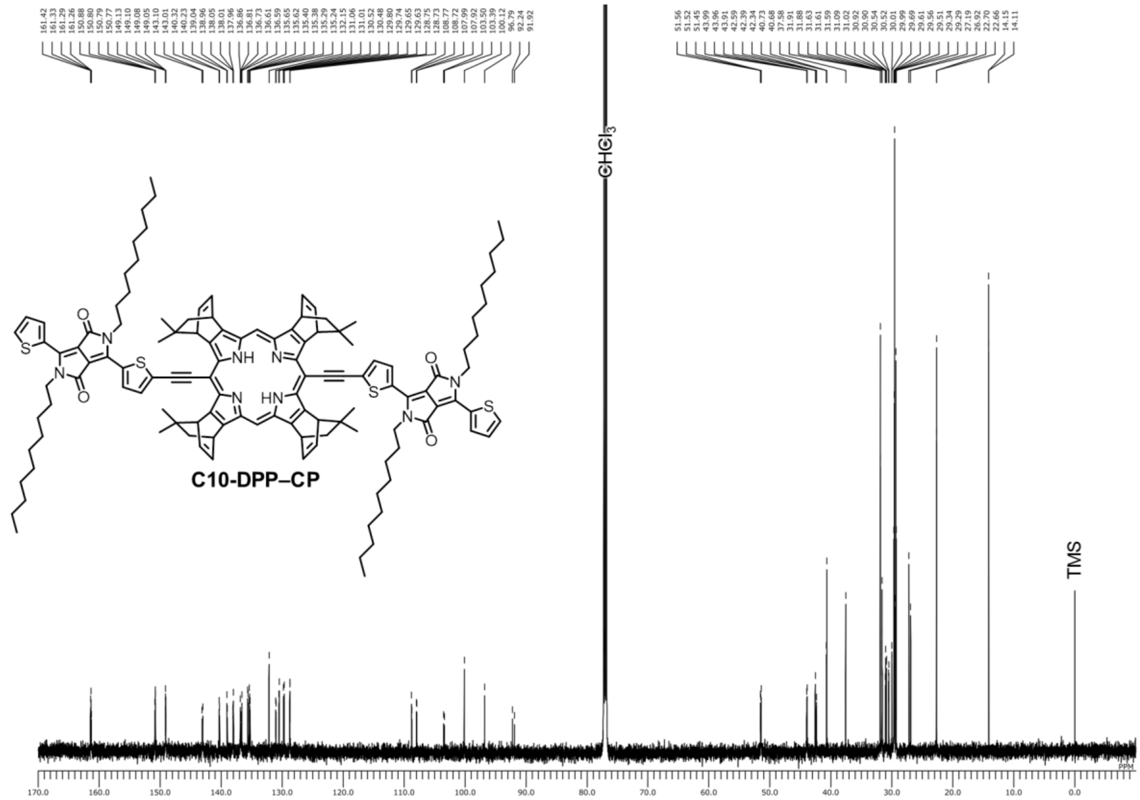

Figure S4-41. ^{13}C NMR spectrum of **C10-DPP–CP** in $CDCl_3$.

4-11. References

(1) Liu, Y.; Zhao, J.; Li, Z.; Mu, C.; Ma, W.; Hu, H.; Jiang, K.; Lin, H.; Ade, H.; Yan, H. Aggregation and Morphology Control Enables Multiple Cases of High-Efficiency Polymer Solar Cells. *Nat. Commun.* **2014**, *5*, 5293.

(2) Chen, J.-D.; Cui, C.; Li, Y.-Q.; Zhou, L.; Ou, Q.-D.; Li, C.; Li, Y.; Tang, J.-X. Single-Junction Polymer Solar Cells Exceeding 10% Power Conversion Efficiency. *Adv. Mater.* **2015**, *27*, 1035–1041.

(3) Kan, B.; Li, M.; Zhang, Q.; Liu, F.; Wan, X.; Wang, Y.; Ni, W.; Long, G.; Yang, X.; Feng, H.; Zuo, Y.; Zhang, M.; Huang, F.; Cao, Y.; Russell, T. P.; Chen, Y. A Series of Simple Oligomer-like Small Molecules Based on Oligothiophenes for Solution-Processed Solar Cells with High Efficiency. *J. Am. Chem. Soc.* **2015**, *137*, 3886–3893.

(4) Vohra, V.; Kawashima, K.; Kakara, T.; Koganezawa, T.; Osaka, I.; Takimiya, K.; Murata, H. Efficient Inverted Polymer Solar Cells Employing Favourable Molecular Orientation. *Nat. Photonics* **2015**, *9*, 403–408.

(5) Zhao, W.; Qian, D.; Zhang, S.; Li, S.; Inganäs, O.; Gao, F.; Hou, J. Fullerene-Free Polymer Solar Cells with over 11% Efficiency and Excellent Thermal Stability. *Adv. Mater.* **2016**, *28*, 4734–4739.

(6) Jin, Y.; Chen, Z.; Dong, S.; Zheng, N.; Ying, L.; Jiang, X.-F.; Liu, F.; Huang, F.; Cao, Y. A Novel Naphtho[1,2-*c*:5,6-*c*′]Bis([1,2,5]Thiadiazole)-Based Narrow-Bandgap π-Conjugated Polymer with Power Conversion Efficiency Over 10%. *Adv. Mater.* **2016**, *28*, 9811–9818.

(7) Li, S.; Ye, L.; Zhao, W.; Zhang, S.; Mukherjee, S.; Ade, H.; Hou, J. Energy-Level Modulation of Small-Molecule Electron Acceptors to Achieve over 12% Efficiency in Polymer Solar Cells. *Adv. Mater.* **2016**, *28*, 9423–9429.

(8) Berezin, D. S.; Toldina, O. V.; Kudrik, E. V. Complex Formation and Spectral

Properties of *meso*-Phenyltetrabenzoporphyrins in Pyridine and *N*,*N*-Dimethylformamide. *Russ. J. Gen. Chem.* **2003**, *73*, 1309–1314.

(9) Keawsongsaeng, W.; Gasiorowski, J.; Denk, P.; Oppelt, K.; Apaydin, D. H.; Rojanathanes, R.; Hingerl, K.; Scharber, M.; Sariciftci, N. S.; Thamyongkit, P. Systematic Investigation of Porphyrin-Thiophene Conjugates for Ternary Bulk Heterojunction Solar Cells. *Adv. Energy Mater.* **2016**, *6*, 1600957.

(10) Noguchi, N.; Junwei, S.; Asatani, H.; Matsuoka, M. Control of Morphology and Orientation of a Thin Film Tetrabenzoporphyrin (TBP) Organic Semiconductor by Solid-State Crystallization. *Cryst. Growth Des.* **2010**, *10*, 1848–1853.

(11) Guide, M.; Dang, X.-D.; Nguyen, T.-Q. Nanoscale Characterization of Tetrabenzoporphyrin and Fullerene-Based Solar Cells by Photoconductive Atomic Force Microscopy. *Adv. Mater.* **2011**, *23*, 2313–2319.

(12) Gottumukkala, V.; Ongayi, O.; Baker, D. G.; Lomax, L. G.; Vicente, M. G. H. Synthesis, Cellular Uptake and Animal Toxicity of a Tetra(carboranylphenyl)-tetrabenzoporphyrin. *Bioorg. Med. Chem.* **2006**, *14*, 1871–1879.

(13) Hutter, L. H.; Müller, B. J.; Koren, K.; Borisov, S. M.; Klimant, I. Robust Optical Oxygen Sensors Based on Polymer-Bound NIR-Emitting platinum(II)–benzoporphyrins. *J. Mater. Chem. C* **2014**, *2*, 7589–7598.

(14) Liman, C. D.; Choi, S.; Breiby, D. W.; Cochran, J. E.; Toney, M. F.; Kramer, E. J.; Chabinyc, M. L. Two-Dimensional GIWAXS Reveals a Transient Crystal Phase in Solution-Processed Thermally Converted Tetrabenzoporphyrin. *J. Phys. Chem. B* **2013**, *117*, 14557–14567.

(15) Suzuki, M.; Yamaguchi, Y.; Takahashi, K.; Takahira, K.; Koganezawa, T.; Masuo, S.; Nakayama, K.; Yamada, H. Photoprecursor Approach Enables Preparation of Well-Performing Bulk-Heterojunction Layers Comprising a Highly Aggregating

Molecular Semiconductor. *ACS Appl. Mater. Interfaces* **2016**, *8*, 8644–8651.

(16) Matsuo, Y.; Sato, Y.; Niinomi, T.; Soga, I.; Tanaka, H.; Nakamura, E. Columnar Structure in Bulk Heterojunction in Solution-Processable Three-Layered p-i-n Organic Photovoltaic Devices Using Tetrabenzoporphyrin Precursor and Silylmethyl[60]fullerene. *J. Am. Chem. Soc.* **2009**, *131*, 16048–16050.

(17) Aramaki, S.; Sakai, Y.; Yoshiyama, R.; Sugiyama, K.; Ono, N.; Mizuguchi, J. Tetrabenzoporphyrin Semiconductor for Transistor Applications. *Proc. SPIE* **2004**, *5522*, 27–35.

(18) Yamada, H.; Kushibe, K.; Okujima, T.; Uno, H.; Ono, N. Novel One-Pot Synthesis of 5-Alkenyl-15-alkynylporphyrins and Their Derivatisation to a Butadiyne-Linked Benzoporphyrin Dimer. *Chem. Commun.* **2006**, *4*, 383–385.

(19) Takahashi, K.; Kuzuhara, D.; Aratani, N.; Yamada, H. Synthesis and Crystal Structures of 5,15-Bis(triisopropylsilylethynyl)-tetrabenzoporphyrins. *J. Photopolym. Sci. Technol.* **2013**, *26*, 213–216.

(20) Shin, W.; Yasuda, T.; Watanabe, G.; Yang, Y. S.; Adachi, C. Self-Organizing Mesomorphic Diketopyrrolopyrrole Derivatives for Efficient Solution-Processed Organic Solar Cells. *Chem. Mater.* **2013**, *25*, 2549–2556.

(21) Choi, Y. S.; Shin, T. J.; Jo, W. H. Small Molecules Based on Thieno[3,4-*c*]pyrrole-4,6-dione for High Open-Circuit Voltage (V_{OC}) Organic Photovoltaics: Effect of Different Positions of Alkyl Substitution on Molecular Packing and Photovoltaic Performance. *ACS Appl. Mater. Interfaces* **2014**, *6*, 20035–20042.

(22) Mishra, A.; Popovic, D.; Vogt, A.; Kast, H.; Leitner, T.; Walzer, K.; Pfeiffer, M.; Mena-Osteritz, E.; Bäuerle, P. A–D–A-Type *S*,*N*-Heteropentacenes: Next-Generation Molecular Donor Materials for Efficient Vacuum-Processed Organic Solar Cells. *Adv. Mater.* **2014**, *26*, 7217–7223.

(23) Hoang, Q. V.; Song, C. E.; Kang, I.-N.; Moon, S.-J.; Lee, S. K.; Lee, J.-C.; Shin, W. S. Low Band Gap Diketopyrrolopyrrole-Based Small Molecule Bulk Heterojunction Solar Cells: Influence of Terminal Side Chain on Morphology and Photovoltaic Performance. *RSC Adv.* **2016**, *6*, 28658–28665.

(24) Jung, M.; Yoon, Y.; Park, J. H.; Cha, W.; Kim, A.; Kang, J.; Gautam, S.; Seo, D.; Cho, J. H.; Kim, H.; Choi, J. Y.; Chae, K. H.; Kwak, K.; Son, H. J.; Ko, M. J.; Kim, H.; Lee, D.-K.; Kim, J. Y.; Choi, D. H.; Kim, B. Nanoscopic Management of Molecular Packing and Orientation of Small Molecules by a Combination of Linear and Branched Alkyl Side Chains. *ACS Nano* **2014**, *8*, 5988–6003.

(25) Takahashi, K.; Yamada, N.; Kumagai, D.; Kuzuhara, D.; Suzuki, M.; Yamaguchi, Y.; Aratani, N.; Nakayama, K.; Yamada, H. Effect of Alkyl Substituents: 5,15-Bis(trimethylsilylethynyl)- vs. 5,15-Bis(triisopropylsilylethynyl)-Tetrabenzoporphyrins and Their Metal Complexes. *J. Porphyrins Phthalocyanines* **2015**, *19*, 465–478.

(26) Ni, W.; Wan, X.; Li, M.; Wang, Y.; Chen, Y. A–D–A Small Molecules for Solution-Processed Organic Photovoltaic Cells. *Chem. Commun.* **2015**, *51*, 4936–4950.

(27) Tamayo, A. B.; Tantiwiwat, M.; Walker, B.; Nguyen, T.-Q. Design, Synthesis, and Self-Assembly of Oligothiophene Derivatives with a Diketopyrrolopyrrole Core. *J. Phys. Chem. C* **2008**, *112*, 15543–15552.

(28) Okujima, T.; Hashimoto, Y.; Jin, G.; Yamada, H.; Uno, H.; Ono, N. Synthesis of Extremely Soluble Precursors of Tetrabenzoporphyrins. *Tetrahedron* **2008**, *64*, 2405–2411.

(29) Saeki, H.; Kurimoto, O.; Nakaoka, H.; Misaki, M.; Kuzuhara, D.; Yamada, H.; Ishida, K.; Ueda, Y. Effect of Crystallinity in Small Molecular Weight Organic Heterojunction Solar Cells. *J. Mater. Chem. C* **2014**, *2*, 5357–5364.

(30) Zhen, Y.; Tanaka, H.; Harano, K.; Okada, S.; Matsuo, Y.; Nakamura, E. Organic Solid Solution Composed of Two Structurally Similar Porphyrins for Organic Solar Cells. *J. Am. Chem. Soc.* **2015**, *137*, 2247–2252.

(31) Tamura, Y.; Saeki, H.; Hashizume, J.; Okazaki, Y.; Kuzuhara, D.; Suzuki, M.; Aratani, N.; Yamada, H. Direct Comparison of a Covalently-Linked Dyad and a 1:1 Mixture of Tetrabenzoporphyrin and Fullerene as Organic Photovoltaic Materials. *Chem. Commun.* **2014**, *50*, 10379–10381.

(32) Sato, Y.; Niinomi, T.; Hashiguchi, M.; Matsuo, Y.; Nakamura, E. Organic Photovoltaics Based on Solution-Processed Benzoporphyrin. *Proc. SPIE* **2007**, *6656*, 66560U.

(33) Tanaka, H.; Abe, Y.; Matsuo, Y.; Kawai, J.; Soga, I.; Sato, Y.; Nakamura, E. An Amorphous Mesophase Generated by Thermal Annealing for High-Performance Organic Photovoltaic Devices. *Adv. Mater.* **2012**, *24*, 3521–3525.

(34) Guide, M.; Lin, J. D. A.; Proctor, C. M.; Chen, J.; García-Cervera, C.; Nguyen, T.-Q. Effect of Copper Metalation of Tetrabenzoporphyrin Donor Material on Organic Solar Cell Performance. *J. Mater. Chem. A* **2014**, *2*, 7890–7896.

(35) Yamaguchi, Y.; Suzuki, M.; Motoyama, T.; Sugii, S.; Katagiri, C.; Takahira, K.; Ikeda, S.; Yamada, H.; Nakayama, K. Photoprecursor Approach as an Effective Means for Preparing Multilayer Organic Semiconducting Thin Films by Solution Processes. *Sci. Rep.* **2014**, *4*, 7151.

(36) Masuo, S.; Sato, W.; Yamaguchi, Y.; Suzuki, M.; Nakayama, K.; Yamada, H. Evaluation of the Charge Transfer Efficiency of Organic Thin-Film Photovoltaic Devices Fabricated Using a Photoprecursor Approach. *Photochem. Photobiol. Sci.* **2015**, *14*, 883–890.

(37) Qin, H.; Li, L.; Guo, F.; Su, S.; Peng, J.; Cao, Y.; Peng, X. Solution-Processed Bulk Heterojunction Solar Cells Based on a Porphyrin Small Molecule with 7% Power

Conversion Efficiency. *Energy Environ. Sci.* **2014**, *7*, 1397–1401.

(38) Xiao, L.; Chen, S.; Gao, K.; Peng, X.; Liu, F.; Cao, Y.; Wong, W.-Y.; Wong, W.-K.; Zhu, X. New Terthiophene-Conjugated Porphyrin Donors for Highly Efficient Organic Solar Cells. *ACS Appl. Mater. Interfaces* **2016**, *8*, 30176–30183.

(39) Cowan, S. R.; Roy, A.; Heeger, A. J. Recombination in Polymer-Fullerene Bulk Heterojunction Solar Cells. *Phys. Rev. B* **2010**, *82*, 245207.

(40) Kyaw, A. K. K.; Wang, D. H.; Gupta, V.; Leong, W. L.; Ke, L.; Bazan, G. C.; Heeger, A. J. Intensity Dependence of Current–Voltage Characteristics and Recombination in High-Efficiency Solution-Processed Small-Molecule Solar Cells. *ACS Nano* **2013**, *7*, 4569–4577.

(41) Kippelen, B.; Brédas, J.-L. Organic Photovoltaics. *Energy Environ. Sci.* **2009**, *2*, 251–261.

(42) Hains, A. W.; Liang, Z.; Woodhouse, M. A.; Gregg, B. A. Molecular Semiconductors in Organic Photovoltaic Cells. *Chem. Rev.* **2010**, *110*, 6689–6735.

(43) Mikhnenko, O. V.; Blom, P. W. M.; Nguyen, T.-Q. Exciton Diffusion in Organic Semiconductors. *Energy Environ. Sci.* **2015**, *8*, 1867–1888.

(44) Müller-Buschbaum, P. The Active Layer Morphology of Organic Solar Cells Probed with Grazing Incidence Scattering Techniques. *Adv. Mater.* **2014**, *26*, 7692–7709.

(45) Osaka, I.; Takimiya, K. Backbone Orientation in Semiconducting Polymers. *Polymer* **2015**, *59*, A1–A15.

(46) Zhang, Q.; Kan, B.; Liu, F.; Long, G.; Wan, X.; Chen, X.; Zuo, Y.; Ni, W.; Zhang, H.; Li, M.; Hu, Z.; Huang, F.; Cao, Y.; Liang, Z.; Zhang, M.; Russell, T. P.; Chen, Y. Small-Molecule Solar Cells with Efficiency over 9%. *Nat. Photonics* **2015**, *9*, 35–41.

(47) Love, J. A.; Proctor, C. M.; Liu, J.; Takacs, C. J.; Sharenko, A.; van der Poll, T. S.; Heeger, A. J.; Bazan, G. C.; Nguyen, T.-Q. Film Morphology of High Efficiency Solution-Processed Small-Molecule Solar Cells. *Adv. Funct. Mater.* **2013**, *23*, 5019–

5026.

(48) Love, J. A.; Nagao, I.; Huang, Y.; Kuik, M.; Gupta, V.; Takacs, C. J.; Coughlin, J. E.; Qi, L.; van der Poll, T. S.; Kramer, E. J.; Heeger, A. J.; Nguyen, T.-Q.; Bazan, G. C. Silaindacenodithiophene-Based Molecular Donor: Morphological Features and Use in the Fabrication of Compositionally Tolerant, High-Efficiency Bulk Heterojunction Solar Cells. *J. Am. Chem. Soc.* **2014**, *136*, 3597–3606.

(49) Osaka, I.; Kakara, T.; Takemura, N.; Koganezawa, T.; Takimiya, K. Naphthodithiophene–Naphthobisthiadiazole Copolymers for Solar Cells: Alkylation Drives the Polymer Backbone Flat and Promotes Efficiency. *J. Am. Chem. Soc.* **2013**, *135*, 8834–8837.

(50) Gao, K.; Li, L.; Lai, T.; Xiao, L.; Huang, Y.; Huang, F.; Peng, J.; Cao, Y.; Liu, F.; Russell, T. P.; Janssen, R. A. J.; Peng, X. Deep Absorbing Porphyrin Small Molecule for High-Performance Organic Solar Cells with Very Low Energy Losses. *J. Am. Chem. Soc.* **2015**, *137*, 7282–7285.

(51) Sharenko, A.; Kuik, M.; Toney, M. F.; Nguyen, T.-Q. Crystallization-Induced Phase Separation in Solution-Processed Small Molecule Bulk Heterojunction Organic Solar Cells. *Adv. Funct. Mater.* **2014**, *24*, 3543–3550.

(52) Szarko, J. M.; Guo, J.; Liang, Y.; Lee, B.; Rolczynski, B. S.; Strzalka, J.; Xu, T.; Loser, S.; Marks, T. J.; Yu, L.; Chen, L. X. When Function Follows Form: Effects of Donor Copolymer Side Chains on Film Morphology and BHJ Solar Cell Performance. *Adv. Mater.* **2010**, *22*, 5468–5472.

(53) Huo, L.; Hou, J.; Chen, H.-Y.; Zhang, S.; Jiang, Y.; Chen, T. L.; Yang, Y. Bandgap and Molecular Level Control of the Low-Bandgap Polymers Based on 3,6-Dithiophen-2-yl-2,5-dihydropyrrolo[3,4-*c*]pyrrole-1,4-dione toward Highly Efficient Polymer Solar Cells. *Macromolecules* **2009**, *42*, 6564–6571.

(54) Zhou, E.; Wei, Q.; Yamakawa, S.; Zhang, Y.; Tajima, K.; Yang, C.; Hashimoto, K.

Diketopyrrolopyrrole-Based Semiconducting Polymer for Photovoltaic Device with Photocurrent Response Wavelengths up to 1.1 μm. *Macromolecules* **2010**, *43*, 821–826.

(55) Lafleur-Lambert, A.; Rondeau-Gagné, S.; Soldera, A.; Morin, J.-F. Synthesis and Characterization of a New Ethynyl-Bridged C_{60} Derivative Bearing a Diketopyrrolopyrrole Moiety. *Tetrahedron Lett.* **2011**, *52*, 5008–5011.

(56) Tang, A.; Lu, Z.; Bai, S.; Huang, J.; Chen, Y.; Shi, Q.; Zhan, C.; Yao, J. Photocurrent Enhancement in Diketopyrrolopyrrole Solar Cells by Manipulating Dipolar Anchoring Terminals on Alkyl-Chain Spacers. *Chem. – Asian J.* **2014**, *9*, 883–892.

(57) Robles, O.; McDonald, F. E. Modular Synthesis of the C9−C27 Degradation Product of Aflastatin A via Alkyne−Epoxide Cross-Couplings. *Org. Lett.* **2008**, *10*, 1811–1814.

Chapter 5

General Conclusion

This dissertation focused on the development of new BP derivatives toward efficient organic semiconductor devices. The relationship between chemical structures and bulk properties such as thin-film absorptions, crystal packings, energy levels, morphologies, molecular orientations as well as device performances of new BP derivatives were investigated.

As general conclusions of this dissertation, introduction of substituents through ethynyl-spacers at 5,15-positons of a BP framework are effective for the extension of π-conjugation as well as absorption rage. Free-base BP derivatives are suitable for both OFET and OPV applications compared with that of metal complexes. When the thin-films based on BP derivatives deposited by the precursor approach, introduced substituents should be as small as possible to reduce the formation of cracks and large aggregation and domains. Direct solution-deposition methods using soluble BP derivatives are effective to improve the μ_h of OFET. From the systematical investigation of the molecular structure and orientation of BP derivatives, it is suggested that the aspect ratio of molecular structures is one of the key factor to decide molecular orientations. This suggestion would be applicable not only for BP derivatives but also the solution-processable small molecular materials. These comprehensive findings and knowledges of this study suggest that a basis for the molecular engineering of BP derivatives, and pave the way to achieve BP-based high-performance organic semiconductor devices.

List of Achievements

List of Publications

1. Synthesis and Crystal Structures of 5,15-Bis(triisopropylsilylethynyl)-tetrabenzo porphyrins
   Kohtaro Takahashi, Daiki Kuzuhara, Naoki Aratani, Hiroko Yamada
   Journal of Photopolymer Science and Technology, **2013**, *26*, 213–216.

2. Effect of Alkyl Substituents: 5,15-Bis(trimethylsilylethynyl)- vs. 5,15-Bis(triisopropylsilylethynyl)-tetrabenzoporphyrins and their Metal Complexes
   Kohtaro Takahashi, Naoya Yamada, Daichi Kumagai, Daiki Kuzuhara, Mitsuharu Suzuki, Yuji Yamaguchi, Naoki Aratani, Ken-ichi Nakayama, Hiroko Yamada
   Journal of Porphyrins and Phthalocyanines, **2015**, *19*, 465–478.

3. Engineering Thin Films of a Tetrabenzoporphyrin toward Efficient Charge-Carrier Transport: Selective Formation of a Brickwork Motif
   Kohtaro Takahashi, Bowen Shan, Xiaomin Xu, Shuaijun Yang, Tomoyuki Koganezawa, Daiki Kuzuhara, Naoki Aratani, Mitsuharu Suzuki, Qian Miao, Hiroko Yamada
   ACS Applied Materials & Interfaces, (Accepted on 10th February, 2017).

4. Molecular Engineering on a Tetrabenzoporphyrin-Based Acceptor–Donor–Acceptor System for Efficient Photocurrent Generation in Bulk-Heterojunction Layers
   Kohtaro Takahashi, Daichi Kumagai, Naoya Yamada, Mitsuharu Suzuki, Daiki Kuzuhara, Yuji Yamaguchi, Naoki Aratani, Tomoyuki Koganezawa, Sota Koshika, Noriyuki Yoshimoto, Sadahiro Masuo, Ken-ichi Nakayama, Hiroko Yamada
   Manuscript in preparation.

International Conferences

1. Materials for Organic Solar Cells: Synthesis of *meso*-Substituted Tetrabenzoporphyrins
   Kohtaro Takahashi, Naoya Yamada, Mitsuharu Suzuki, Daiki Kuzuhara, Naoki Aratani, Ken-ichi Nakayama, Hiroko Yamada
   GIST–NCTU–NAIST International Joint Symposium 2013, Nara Japan, November, 2013

2. Materials for Organic Solar Cells: Diketopyrrolopyrrole-linked Tetrabenzoporphyrin
   Kohtaro Takahashi, Naoya Yamada, Daiki Kuzuhara, Naoki Aratani, Ken-ichi Nakayama, Hiroko Yamada
   8th International Conference on Porphyrins & Phthalocyanines (ICPP8), Istanbul, Turkey, June, 2014

3. Solution-Processed Organic Field-Effect Transistors of Soluble Tetrabenzoporphyrins
   Kohtaro Takahashi, Bowen Shan, Xiaomin Xu, Daiki Kuzuhara, Mitsuharu Suzuki, Naoki Aratani, Tomoyuki Koganezawa, Qian Miao, Hiroko Yamada
   2015 MRS Fall Meeting & Exhibit, Boston, USA, December, 2015.

4. Solution-Processed Organic Field-Effect Transistors of Soluble a Tetrabenzoporphyrin
   Kohtaro Takahashi, Bowen Shan, Xiaomin Xu, Daiki Kuzuhara, Mitsuharu Suzuki, Naoki Aratani, Tomoyuki Koganezawa, Qian Miao, Hiroko Yamada
   International Conference on Organic and Hybrid Thermoelectronics (ICOT2016), Kyoto, Japan, January, 2016

5. Orientation, Morphology, and Performance of Organic Photovoltaics based on Diketopyrrolopyrrole-linked Tetrabenzoporphyrins
   Kohtaro Takahashi, Daichi Kumagai, Naoya Yamada, Yuji Yamaguchi, Tomoyuki Koganezawa, Daiki Kuzuhara, Mitsuharu Suzuki, Naoki Aratani, Sadahiro Masuo, Ken-ichi Nakayama, Hiroko Yamada
   International Conference on Hybrid and Organic Photovoltaics (HOPV16), Swansea, UK, July, 2016

6. Engineering Electronic Structure of Tetrabenzoporphyrin toward Improved Performance in Organic Solar Cells: Trifluoromethyl-Substituted Tetrabenzoporphyrin Prepared by a Thermo-Precursor Approach
   Kohtaro Takahashi, Mitsuharu Suzuki, Hiroko Yamada
   KJF International Conference on Organic Materials for Electronics and Photonics 2016 (KJF-ICOMEP 2016), Fukuoka, Japan, September, 2016

Domestic Conferences

1. メソ置換ベンゾポルフィリンの合成と有機デバイスへの応用
   高橋功太郎，山田直也，葛原大軌，荒谷直樹，中山健一，山田容子
   日本化学会第９３春季年会，立命館大学，２０１３年３月

2. ベンゾチアゾール置換ベンゾポルフィリンの合成と物性
   高橋功太郎，山田直也，葛原大軌，荒谷直樹，中山健一，山田容子
   第２４回 基礎有機化学討論会，学習院大学，２０１３年９月

3. ベンゾチアゾール置換ベンゾポルフィリンの合成と物性
   高橋功太郎，山田直也，葛原大軌，荒谷直樹，中山健一，山田容子

大阪府立大学２１世紀科学研究機構「分子エレクトロニックデバイス研究所」第１４回研究会　RIMED シーズ発掘講演会，大阪府立大学，２０１３年１１月

4. メソ置換ベンゾポルフィリンの合成と物性
   高橋功太郎，山田直也，佐伯宏之，葛原大軌，荒谷直樹，中山健一，山田容子
   第７回 有機π電子系シンポジウム，高崎ビューホテル，群馬，２０１３年１２月

5. 有機薄膜太陽電池材料を指向したジケトピロロピロール連結ベンゾポルフィリンの合成と物性
   高橋功太郎，山田直也，佐伯宏之，鈴木充朗，葛原大軌，荒谷直樹，中山健一，山田容子
   日本化学会第９４春季年会，名古屋大学，２０１４年３月

6. ジケトピロロピロール連結テトラベンゾポルフィリンの合成と有機薄膜太陽電池への応用
   高橋功太郎，山田直也，葛原大軌，荒谷直樹，中山健一，山田容子
   ２０１４年光化学討論会，北海道大学，２０１４年１０月

7. 可溶性テトラベンゾポルフィリンの溶液塗布による有機薄膜トランジスタ特性
   高橋功太郎, Bowen Shan, 葛原大軌, 鈴木充朗, 荒谷直樹, 小金澤智之, Qian Miao, 山田容子
   第２６回基礎有機化学討論会，愛媛大学，２０１５年９月

8. 2D-GIWAXD による熱変換型有機半導体材料の分子配向と有機薄膜太陽電池性能との相関
   高橋功太郎，熊谷大地，山田直也，小鹿曹汰，山口裕二，小金澤智之，葛原大軌，鈴木充朗，荒谷直樹，増尾貞弘，吉本則之，中山健一，山田容子
   第１３回 SPring-8 産業利用報告会，兵庫県民会館，２０１６年９月

Award

1. 優秀学生発表賞
   Mid-Term Student Research Evaluation Symposium 2014, 奈良先端科学技術大学院大学，２０１４年１１月

List of Foundations

1. 平成２５年度 競争的研究支援（１０万円）
2. 平成２６年度 競争的研究支援（４０万円）

3. 平成２７年度 競争的研究支援（３０万円）
4. 平成２７年度 奈良先端科学技術大学院大学支援財団支援事業 教育研究活動助成（１００万円）
5. 平成２８年度科学研究費助成事業（特別研究員奨励費）（９０万円）

List of Bulletins

1. 溶液プロセスによる積層型有機薄膜太陽電池材料の開発
   高橋功太郎
   公益財団法人 奈良先端科学技術大学院大学支援財団，機関紙「シーエンス 財団設立２５周年記念号」，Vol. 15, 8–9, 2016 年

Patent

1. 熱電変換材料及び熱電変換素子，WO 2015129877 A1，２０１５年２月２７日（出願）

Others

1. 平成２８年度日本学術振興会特別研究員（DC-2）
2. 2015A 期 SPring-8 利用課題採択，課題番号：2015A1842，ビームライン：BL19B2
3. 2015B 期 SPring-8 利用課題採択，課題番号：2015B1769，ビームライン：BL19B2

Acknowledgements

The studies in this dissertation were accomplished by the author and with several research collaborators under the direction of Prof. Hiroko Yamada at Nara Institute of Science and Technology (NAIST).

First of all, the author would like to appreciate Prof. Hiroko Yamada, Prof. Naoki Aratani, Dr. Daiki Kuzuhara, Dr. Mitsuharu Suzuki, and Dr. Hironobu Hayashi of NAIST for the precious guidance and encouragement throughout my doctoral course.

The author is truly grateful to Prof. Ken-ichi Nakayama, Dr. Yuji Yamaguchi, Mr. Naoya Yamada, and Mr. Daichi Kumagai in Yamagata University for fabricating and evaluating OPV and OFET devices in Chapter 2 and 4.

The author would like to acknowledge Prof. Hidemitsu Uno of Ehime University, for his invaluable guidance during the fourth year of undergraduate studies.

The author is truly grateful to Prof. Qian Miao and his lab members for allowing work in his laboratory and for supporting the research in Chapter 3 during my internship in The Chinese University of Hong Kong. This has been one of the best memories yet and no word is enough to describe the appreciation.

The author would like to appreciate Prof. Sadahiro Masuo in Kwansei Gakuin University for measuring fluorescence decay curves and calculating fluorescence lifetimes of OPV devices in Chapter 4.

The author would also like to express the appreciation to Prof. Tadaaki Ikoma in Niigata University for helpful discussion.

The author appreciates the Grant-in-Aid for the Japan Society for the Promotion of Science (JSPS) Research Fellow (16J04335), NAIST Presidential Special Fund, and Foundation for NAIST for the financial support.

The author acknowledges Dr. Tomoyuki Koganezawa (Japan Synchrotron Radiation Research Institute (JASRI), Mr. Ryo Abe (NAIST) and Mr. Sota Koshika (Iwate University) for the technical support and helpful discussions in GIWAXD analysis.

The author also acknowledges Prof. Noriyuki Yoshimoto (Iwate University) and Dr. Tomoyuki Koganezawa (JASRI, SPring-8) for giving the chance to conduct GIWAXD measurement in SPring-8.

The author would like to thank Mr. Shohei Katao and Ms. Yoshiko Nishikawa in NAIST for measuring and analyzing single-crystal X-ray analysis and high-resolution mass spectrometry, respectively. The author also appreciates all technical staffs in NAIST for giving lectures and continuous maintenance of research facilities.

The author would like to thank The Nippon Synthetic Chemical Industry Co., Ltd. (Osaka, Japan) for a gift of ethyl isocyanoacetate which was used for the preparation of the starting pyrroles.

Finally, the author can never be grateful enough for the continued support of family.

Kohtaro Takahashi